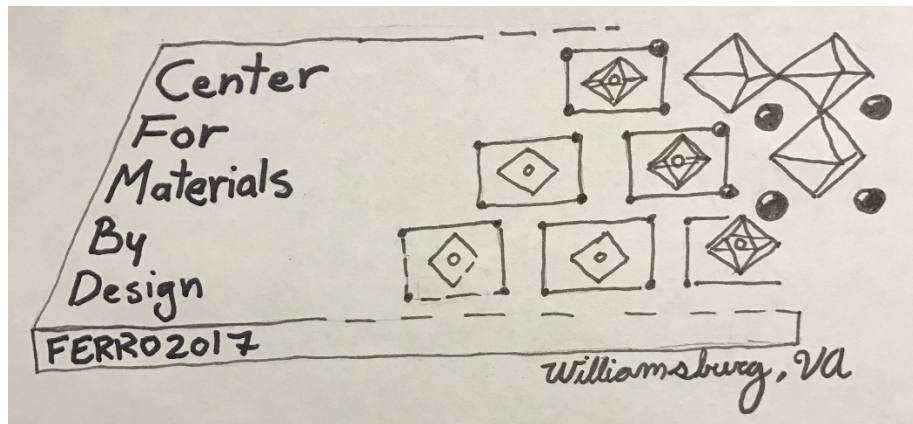


Fundamental Physics of Ferroelectrics and Related Materials 2017

29 January – 1 February, 2017



Williamsburg Woodlands Hotel & Suites

Williamsburg, Virginia

Organizers:

Ronald Cohen, Extreme Materials Initiative, Geophysical Laboratory,
Carnegie Institution for Science and LMU Munich

William Ratcliff, National Institute of Standards and Technology

Xifan Wu, Temple University

Albina Borisevich, Oak Ridge National Laboratory

SPONSORS:

Carnegie Institution for Science

CDAC

National Institute of Standards and Technology

Temple University

Radiant Technologies, Inc.



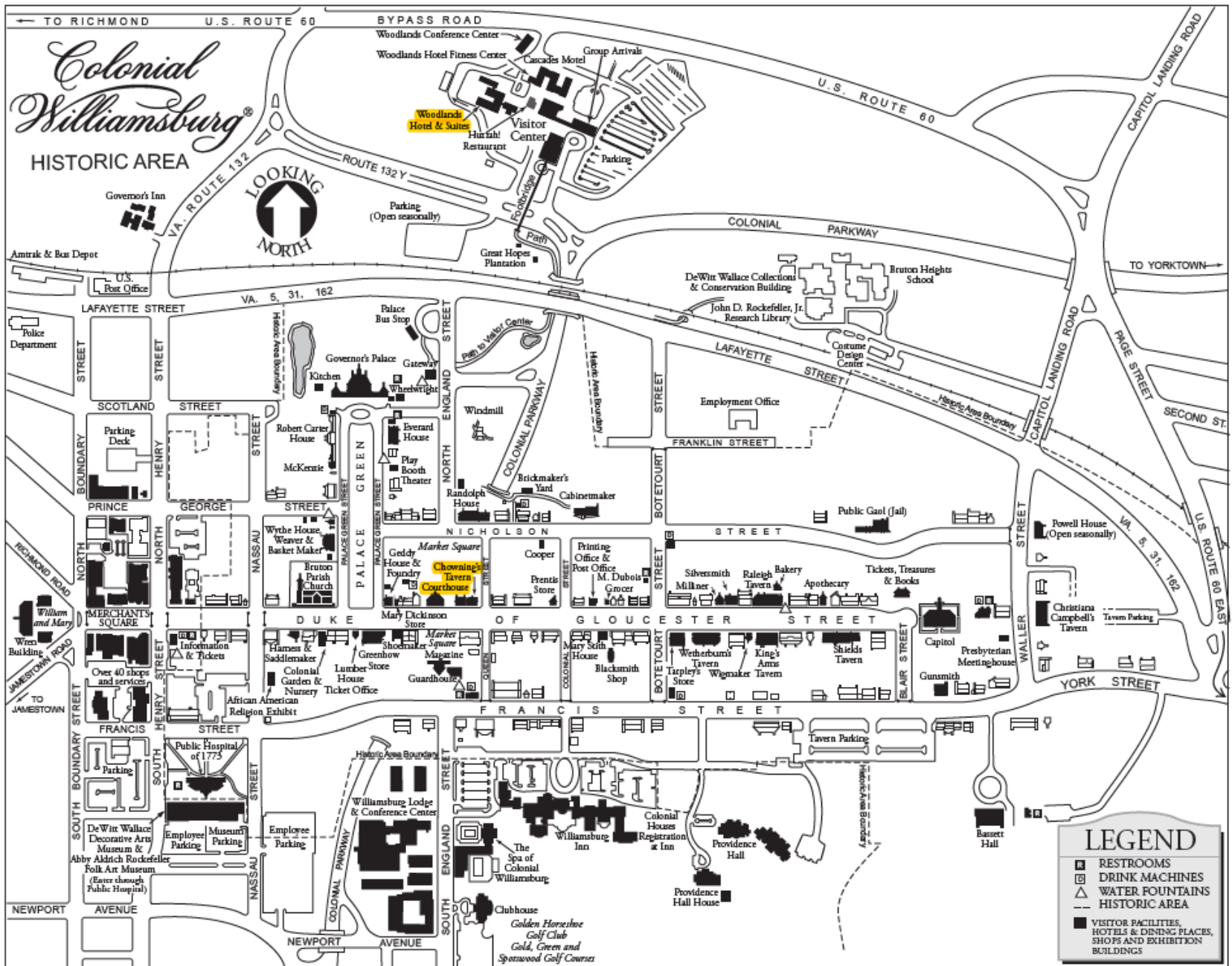
CARNEGIE
SCIENCE

NIST
National Institute of
Standards and Technology
U.S. Department of Commerce

RADIANT
TECHNOLOGIES, INC.



YOUR GATEWAY TO
FERROELECTRIC/MULTIFERROIC/PIEZOELECTRIC
TESTING & DEVICES



2017 Workshop on the Fundamental Physics of Ferroelectrics and
Related Materials

29 January – 1 February, 2017

PROGRAM

Williamsburg Woodlands Hotel & Suites
105 Visitor Center Drive
Williamsburg, VA 23185
(757)220-7960

Registration (Dogwood)

Reception, Lunch, Dinner (Oak)

Coffee Breaks (Dogwood)

Banquet Dinner (Chownings Tavern)

Talks (Cascade)

Posters (Dogwood)

WiFi Access

Network=Autograph_Guest

(no password required)

Sunday, January 29

18:00 Registration (Dogwood)

18:30-20:30 Reception (Oak)

Monday, January 30

8:00 Welcome (Cascades)

R. E. Cohen (Chair)

8:10 Raffaele Resta (Keynote)

The quantum-mechanical position operator tamed: Polarization, orbital magnetization, and more

- 9:00 Andrew Rappe
A new model for the dynamic polar response of $\text{PbMg}_{1/3}\text{Nb}_{2/3}\text{O}_3\text{-PbTiO}_3$ and its connections to piezoelectricity
- 9:20 Sang-Wook Cheong (invited)
Hybrid Improper Ferroelectricity
- 9:50 Kinnary Patel
Effect of Trilinear Couplings on Dynamical Properties of Perovskites
- 10:10 Break (Dogwood)**
- 10:30 (Cascades)
Hongjun Xiang (invited)
Origin of Distinct Pressure Effects on Octahedral Tilting in Perovskite Oxides
- 11:00 Shi Liu
Origin of Defect Dipole Enhanced Electromechanical Coupling
- 11:20 S. Omid Sayedaghaee
The effect of time-dependent magnetic field on polarization in multiferroics
- 11:40 Sebastian Reyes-Lillo
An Automated Ab Initio Framework for Identifying New Ferroelectrics
- 12:00 -13:00 Lunch (Oak)**
- 13:00 Chair: Xifan Wu (Cascades)
- 13:00 Xiaoshan Xu (invited)
Effects of biaxial strain on the improper multiferroicity in h-LuFeO₃ films
- 13:30 Santosh KC
First-principles and neutron diffraction investigation of polarization in tetragonal BiCoO₃
- 13:50 Jeffrey Lynn
Complex magnetic incommensurability and electronic charge transfer through the ferroelectric transition in multiferroic Co₃TeO₆

14:10 Steven Disseler (invited)

Atomic Scale Engineering of Multiferroicity in LuFeO₃/LuFe₂O₄ Superlattices

14:40 Bin Xu

Intrinsic polarization switching mechanisms in BiFeO₃

15:00 Break (Dogwood)

15:30 (Cascades)

Ye Cao (invited)

Emergence of coupled surface electrochemistry-bulk ferroelectricity state on the nanoscale --- a combined study of thermodynamics, phase-field and experimental demonstration

16:00 Huaxiang Fu

Persistence of strong and switchable ferroelectricity despite vacancies

16:20 Dustin Gilbert

Structural and Magnetic Depth Profiles of Magneto-Ionic Heterostructures Beyond the Interface Limit

16:40 Jacob Chapman (invited)

Switching Dynamics and Mechanisms in Morphotropic PbZr_xTi_{1-x}O₃ from Atomistic Modelling

17:10 Brian Abbett

Antiferroelectric switching pathways and the relation between nonpolar and polar states in PbZrO₃ from first principles

17:30 Bo Wang

Deterministic Domain Switching in Ferroelectric Thin Films by Mechanical Probe: Synergy of Piezoelectricity and Flexoelectricity

18:30-20:00 Dinner (Oak)

Poster Session

20:00-22:00

(Dogwood)

Posters Should not exceed 8 feet wide by 4 feet high (243 cm x 121 cm). Pins will be provided.

**** ALL posters should remain up from Monday morning through Tuesday 6:00 pm. ****

1. Charles Paillard Photostriction in bismuth ferrite from first principles
2. Zhijun Jiang Electrocaloric effect in relaxor Ba(Zr,Ti)O₃ from atomistic simulations
3. Yurong Yang Defect-engineering: the case of LaBaCo₂O₅+? compounds
4. Jun Ouyang Increasing energy storage capabilities of space-charge dominated ferroelectric thin films using interlayer coupling
5. Shinya Tsukada Local and Macroscopic Properties of BaTi₂O₅
6. Pavan Nukala Atomic scale structural complexities in antiferroelectric Pb(Yb_{0.5}Nb_{0.5})O₃ and its solid solutions with PbTiO₃ revealed using high resolution electron microscopy
7. Michael S. Richman Ferroelectric film dynamics simulated by a second-order time-dependent Landau model
8. Moustafa Nasser Speckle Photography with LiNbO₃ Crystal for the Measurement of In-Plane Displacement Field Distribution of Distant Objects
9. Abdullah Al-Barakaty Structure and properties of Pb(Mg_{1/4}Nb_{1/2}Ti_{1/4})O₃ Nanodot from first principles based effective Hamiltonian approach
10. Eric Cockayne Temperature dependence of Ti 1s near-edge spectra in two perovskites: theory and experiment
11. Cyrus E. Dreyer Towards a current-density implementation for calculating flexoelectric coefficients
12. Stanislav Kamba Soft-mode driven nonferroic phase transition in multiferroic BaMnO₃

13. Axiel Ya'el Birenbaum "Striped" lanthanum cobaltite films: How strain orders oxygen defects
14. Timothy Morgan Ferroelectric Properties of Off-Stoichiometrically Grown Barium Titanate via Molecular Beam Epitaxy
15. Sinisa Coh An alternative structure of TiO₂ with higher energy valence band edge
16. Hiroyuki Takenaka First Principles studies in Oxynitrides at High Pressure
17. Harold C. Robinson ONR's Research Program on Acoustic Transduction Materials and Devices
18. Md Aftabuzzaman Electric Field Effect on Lead Free Uniaxial Relaxor Sr_{0.4}Ba_{0.6}Nb₂O₆ single crystal Studied by Brillouin Scattering
29. Hiroyuki Takenaka New model of structures and dynamics in perovskite oxide relaxor ferroelectrics
20. Matthew Krogstad Single Crystal Diffuse Scattering from Ferroelectric PbZr_{0.54}Ti_{0.46}O₃
21. Chengtao Luo Super-lattice point linking diffuse scattering network and its dynamical mechanism in lead-free NBT-xBT single crystals
22. Jacob Chapman Atomistic Modelling of Ageing in Ferroelectrics

Tuesday, January 31

8:00 Chair: William Ratcliff (Cascades)

8:00 James Scott (invited)

Palladium-based Ferroelectrics and Multiferroics

8:30 Michelle Jamer

Effective control of magnetization rotation as a function of applied electric field in FeGa/NiFe multilayers on PMN-PT

8:50 Sergey Prosandeev

Effects of atomic short-range order on properties of the $\text{PbMg}_{1/3}\text{Nb}_{2/3}\text{O}_3$ relaxor ferroelectric

9:10 Fei Li

The Origin of Ultrahigh Piezoelectricity in Relaxor-Ferroelectric Solid Solution Crystals

9:30 Benjamin Burton

The PNR Relaxor Transitions in PSN with nearest neighbor [Pb-O] divacancies $[\text{Pb}1 - \text{X}(\text{Sc}_{1/2}\text{Nb}_{1/2})\text{O}_3 - \text{X}]$ and PMN $[\text{Pb}(\text{Mg}_{1/3}, \text{Nb}_{2/3})\text{O}_3]$

9:50 Break (Dogwood)

10:10 Cascades

Christopher Nelson (invited)

Observation of ferroelectric vortices in oxide superlattice

10:40 Meng Ye

Domain walls and ferroelectric reversal in corundum derivatives

11:00 Weida Wu (invited)

Direct visualization of magnetoelectric domains

11:30 Nicholas Barrett

Surface potential imaging of polar ferroelastic domain walls

11:50 Group Photo

12:00 Lunch (Oak)

13:00 Chair: Albina Borisevich (Cascades)

- 13:00 Chang-Beom Eom (invited)
Polar Metals by Geometric Design
- 13:30 Kesong Yang
Ab-initio Design of Two-Dimensional Electron Gas in Nonpolar/Nonpolar Oxide Interface via Polarization Discontinuity
- 13:50 Michele Kotiuga
Electron Doping and Charge Ordering of SmNiO₃ from First Principles
- 14:10 Saurabh Ghosh
Engineering a ferroelectric superlattice from metallic components
- 14:30 Nicole Benedek (invited)
'Ferroelectric' metals reexamined: Fundamental mechanisms and design considerations for new materials
- 15:00 Break (Dogwood)**
- 15:30 Xifan Wu (Cascades)
Electronic origin of spin-phonon coupling effect in transition-metal perovskites
- 15:50 Elizabeth Nowadnick
Domains and ferroelectric switching pathways in Ca₃Ti₂O₇
- 16:10 Anna Grunebohm
Optimizing the electrocaloric effect by ab initio simulations
- 16:30 Vladimir Fridkin (invited)
Ballistic Photovoltaic Effect in Ferroelectric Barium Titanate
- 17:00 Annette Busmann-Holder
Transparent EuTiO₃ films: a possible two-dimensional magneto-optical device
- 17:20 Henry Krakauer
The insulating phases of VO₂ are Mott-Hubbard insulators.
- 17:40 Ronald Cohen
Ferroelectricity in PbTiO₃ at high pressures?
- 19:30 Conference Banquet Chownings Tavern**

Wednesday, February 1

8:00 Chair: Peter Gehring (Cascades)

8:00 Seiji Kojima (Invited)

Brillouin Scattering Spectroscopy on Crossover from Strong to Weak Relaxor Behaviors of Uniaxial Tungsten Bronze Ferroelectrics

8:30 Mehmet Dogan

Ab initio study of doping and strain in ferroelectric HfO₂

8:50 Xiaohui Liu

Polarization Controlled Modulation Doping in Ferroelectric Semiconductor Heterostructures

9:10 Hiroki Moriwake (invited)

Mechanism of polarization switching in wurtzite-structured zinc oxide thin films

9:40 Jiri Hlinka

212 species of macroscopic symmetry breaking revisited

10:00 Break (Dogwood)

10:30 Cascades

M.A. Helal (invited)

Inelastic light scattering studies on relaxor ferroelectric 0.83Pb(Mg_{1/3}Nb_{2/3})O₃-0.17PbTiO₃ single crystals

11:00 Changsong Xu

Pressure-induced multiferroics via pseudo Jahn-Teller effects and novel couplings

11:20 Bartomeu Monserrat (invited)

Antiferroelectric topological insulators in ABC compounds

12:00 Lunch (Oak)

Monday's Abstracts

The quantum-mechanical position operator tamed: Polarization, orbital magnetization, and more

Raffaele Resta

Dipartimento di Fisica, Università di Trieste, Italy,

Condensed matter physics addresses unbounded samples within periodic boundary conditions, where the quantum-mechanical position operator \mathbf{r} is ill defined. Physical observables based on it—like electrical polarization \mathbf{P} and orbital magnetization \mathbf{M} —require therefore a somewhat exotic definition. Other observables are very close relatives of them; they are all expressed as Brillouin-zone (BZ) integrals, where the integrand is rooted in the geometry of the manifold of the occupied Bloch states.

The electronic ground state is uniquely determined by the projector \mathcal{P} ; I then define the projected position $\tilde{\mathbf{r}}$ as the Hermitian operator

$$\tilde{\mathbf{r}} = -[\mathcal{P}, [\mathbf{r}, \mathcal{P}]] = \mathcal{P}\mathbf{r}\mathcal{Q} + \mathcal{P}\mathbf{r}\mathcal{Q}, \quad \mathcal{Q} = \mathcal{I} - \mathcal{P}.$$

It is well defined even for unbounded samples; for a crystalline system $\tilde{\mathbf{r}}$ is lattice periodical. In terms of $\tilde{\mathbf{r}}$ several observables will be expressed by a compact formula which is the same for bounded and unbounded samples. Results are provided here for “spinless electrons”.

Polarization: The case of \mathbf{P} is special with respect to the other observables dealt with below, in that it is defined modulo a “quantum”. Polarization *differences* between two states related by an adiabatic transformation (which does not close the gap) can be expressed as

$$\Delta\mathbf{P}_{\text{electronic}} = -e \int_0^{\Delta t} dt \text{Tr}_V \{ \partial_t \mathcal{P} \mathbf{r} \} = -e \int_0^{\Delta t} dt \text{Tr}_V \{ \partial_t \mathcal{P} \tilde{\mathbf{r}} \},$$

where Tr_V indicates the trace per unit volume. The first form makes sense only for bounded samples, while the second one can be adopted for unbounded ones as well; in the crystalline case Tr_V acts on a lattice periodical operator. I will show that the explicit expression as a BZ integral leads to the famous King-Smith and Vanderbilt formula.

I will then discuss four other observables, all of them involving (non-commutative) operator products $\tilde{r}_\alpha \tilde{r}_\beta$. For each of the observables I am going to provide two formulas: the first one is valid—as it stands—for either

bounded or unbounded samples; the second one is the corresponding explicit expression—for crystalline systems only—as a BZ integral.

Anomalous Hall conductivity (both metals and insulators):

$$\sigma_{\alpha\beta} = \frac{2e^2}{h} \text{Im Tr}_V \{ \mathcal{P} \tilde{r}_\alpha \tilde{r}_\beta \} = \frac{2e^2}{h} \sum_j \int_{\text{BZ}} [d\mathbf{k}] \text{Im } \mathcal{F}_{\alpha\beta}(\mathbf{k}).$$

Marzari-Vanderbilt quadratic spread (insulators only):

$$\Omega_I/V_{\text{cell}} = \sum_\alpha \text{Tr}_V \{ \mathcal{P} \tilde{r}_\alpha \tilde{r}_\alpha \} = \sum_\alpha \sum_j \int_{\text{BZ}} [d\mathbf{k}] \mathcal{F}_{\alpha\alpha}(\mathbf{k}).$$

Orbital magnetization (both metals and insulators):

$$M_\gamma = -\frac{e}{2\hbar c} \varepsilon_{\gamma\alpha\beta} \text{Im Tr}_V \{ |\mathcal{H} - \mu| \tilde{r}_\alpha \tilde{r}_\beta \} = -\frac{e}{2\hbar c} \varepsilon_{\gamma\alpha\beta} \int_{\text{BZ}} [d\mathbf{k}] \text{Im } \mathcal{G}_{\alpha\beta}(\mathbf{k}).$$

Drude weight (trivially zero in insulators):

$$\begin{aligned} D_{\alpha\beta} &= \pi e^2 \frac{n}{m} \delta_{\alpha\beta} - \frac{2\pi e^2}{\hbar^2} \text{Re Tr}_V \{ |\mathcal{H} - \mu| \tilde{r}_\alpha \tilde{r}_\beta \} \\ &= \pi e^2 \frac{n}{m} \delta_{\alpha\beta} - \frac{2\pi e^2}{\hbar^2} \sum_j \int_{\text{BZ}} [d\mathbf{k}] \mathcal{G}_{\alpha\beta}(\mathbf{k}). \end{aligned}$$

In the above equations n is the electron density, μ is the Fermi level, $[d\mathbf{k}] = d\mathbf{k}/(2\pi)^d$, and the geometrical tensors $\mathcal{F}_{\alpha\beta}(\mathbf{k})$ and $\mathcal{G}_{\alpha\beta}(\mathbf{k})$ are defined in terms of the Hamiltonian $\mathcal{H}_{\mathbf{k}}$ and its periodic eigenstates $|u_{j\mathbf{k}}\rangle$ as:

$$\begin{aligned} \mathcal{F}_{\alpha\beta}(\mathbf{k}) &= \text{Tr} \{ \mathcal{P}_{\mathbf{k}} (\partial_{k_\alpha} \mathcal{P}_{\mathbf{k}}) (\partial_{k_\beta} \mathcal{P}_{\mathbf{k}}) \}, \quad \mathcal{G}_{\alpha\beta}(\mathbf{k}) = \text{Tr} \{ |\mathcal{H}_{\mathbf{k}} - \mu| (\partial_{k_\alpha} \mathcal{P}_{\mathbf{k}}) (\partial_{k_\beta} \mathcal{P}_{\mathbf{k}}) \}, \\ \mathcal{P}_{\mathbf{k}} &= \theta(\mu - \mathcal{H}_{\mathbf{k}}) = \sum_j \theta(\mu - \epsilon_{j\mathbf{k}}) |u_{j\mathbf{k}}\rangle \langle u_{j\mathbf{k}}|, \end{aligned}$$

$$|\mathcal{H}_{\mathbf{k}} - \mu| = \mathcal{H}_{\mathbf{k}} - \mu - 2 \mathcal{P}_{\mathbf{k}} (\mathcal{H}_{\mathbf{k}} - \mu) \mathcal{P}_{\mathbf{k}}.$$

Notice that, when a smooth gauge is chosen, $\partial_{k_\alpha} \mathcal{P}_{\mathbf{k}}$ is smooth in whole BZ for insulators; for metals instead $\partial_{k_\alpha} \mathcal{P}_{\mathbf{k}}$ is piecewise continuous, and additionally has a δ singularity at the Fermi surface. The singularity is harmless in $\mathcal{G}_{\alpha\beta}(\mathbf{k})$ and in the imaginary part of $\mathcal{F}_{\alpha\beta}(\mathbf{k})$, but it does make harm to the real part of $\mathcal{F}_{\alpha\beta}(\mathbf{k})$, which indeed is ill defined for metals.

Acknowledgments: Work supported by the ONR Grant N00014-11-1-0145.

A new model for the dynamic polar response of PbMg_{1/3}Nb_{2/3}O₃-PbTiO₃ and its connections to piezoelectricity

Hiroyuki Takenaka^{1,2}, Shi Liu^{1,2}, Ilya Grinberg^{1,3} and Andrew M. Rappe¹

¹ Dept of Chemistry, University of Pennsylvania, Philadelphia, PA, 19104–6323 rappe@sas.upenn.edu

² Geophysical Laboratory, Carnegie Institution of Washington, Washington DC

³ Department of Chemistry, Bar-Ilan University, Ramat Gan, Israel

Despite considerable research, it has proven difficult to make clear predictive relationships between new compositions and enhanced piezoelectric response. In large part, this is because the piezoelectric response of perovskite oxides does not relate simply to their low- T or high-symmetry structures. The fact that the optimal piezoelectric response appears in complex multi-component materials such as PbMg_{1/3}Nb_{2/3}O₃-PbTiO₃ (PMN-PT) with large distortions and at moderate T makes piezoelectricity an emergent property that demands study that incorporates the full complexity of the system.

Relaxor ferroelectrics were first discovered in the 1960s and have been a focus of intense research due to their intriguing properties.¹ In particular the so-called butterfly shape of the diffuse scattering (DS) has been identified as the structural signature of relaxor behavior.² While the widely used current model^{3,4} of polar nanoregions (PNR) inside a non-polar matrix has been used to explain the temperature dependence of relaxor behavior observed with several experimental techniques since 1983, this model is essentially a post-hoc justification of the experimental results and has not been used predictively.

To provide a conceptual picture of the changes in the relaxor structure and polar response, we perform first-principles based molecular dynamics^{5–7} and analyze the polar fluctuations with a correlation function approach (Fig. 1).

We use large (1,000,00–2,000,000 million atom) MD supercells and long simulation times to capture the emergent behavior and to solve for the relaxor structure in a wide range of T . To confirm that the structures obtained by our simulations are valid, we calculate diffuse scattering patterns from MD trajectories using $64 \times 64 \times 64$ and $72 \times 72 \times 72$ supercells. We find that the agreement with experimental DS is very good for calculations from the trajectories of large cell simulations; the DS shows the correct butterfly and rod shapes around the (100) and (110) Bragg spots, implying that our simulations correctly reproduce the dynamic local structure of PMN-PT.

Direct visualization (Fig. 2) and analysis of the local P changes of our MD-obtained PMN-PT shows that multiple domains are present in the material, with the average domain size of 4–6 nm depending on T and low angle ($45\text{--}90^\circ$) P changes at the domain walls (DWs) enabled by the small energy differences between the (100), (110) and (111) orientations of the local P . Thus, for $T < 400$ K, PMN-PT assumes a multi-domain state with a variety of low-angle DWs separating small polar domains without a non-polar matrix. In contrast to the previously accepted picture of PNR growth inside a non-polar matrix on cooling, the main change during the transitions at T_b and T_f is a higher correlation inside the domains and reduced rotation of domain P , while the size of the polar domains grows only slightly. The relaxor structure below T_b and T_f is characterized by strong but incomplete correlations inside the domains and weak correlations between the domains (Fig. 1). This is due to the presence of a mixture of unit cells with ferroelectric- and paraelectric-like behavior, with the paraelectric-like Mg-rich cells decoupling the polarization between the domains and giving rise to the nano-domain structure.

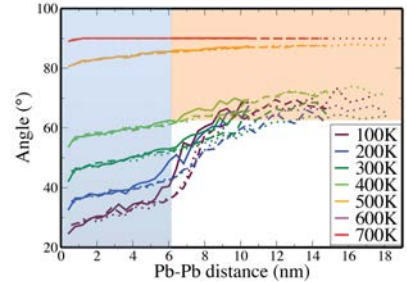


Figure 1: Angle correlation function for Pb displacements in Pb(Mg_{1/3}Nb_{2/3})O₃-PbTiO₃ shows the size and intensity of polar nanoregions. $\max_{\theta} P(\theta, r, T)$ plotted vs. r shows smaller angles (stronger dipole alignment) for small r and low T , but lack of alignment for $r > 8$ nm for all T .

Our model of relaxor structure explains several different physical properties of relaxors. First, the addition of Ti leads to the eventual suppression of relaxor behavior, while lower Ti content increases the strength of the relaxor phase. This is due to the lesser (greater) content of the $\text{Pb}(\text{Mg}_{1/2}\text{Nb}_{1/2})\text{O}_3$ wall sites that make the domain size larger (smaller) as Ti fraction increases (decreases) and is in agreement with the observed weaker DS patterns at higher Ti content. Eventually, the increased domain size leads to the relaxor to ferroelectric phase transition. Second, the mixture of the FE and PE states at the sub-nm scale is the origin of the phase instability due to their crossover and the phonon Anderson localization due to inhomogeneous phonon propagation. Third, the breaking up of the system into small domains and the decoupling of P fluctuations of each domain naturally leads to the Kohlrausch-Williams-Watts dielectric relaxation and the Vögel-Fulcher characteristics of the dielectric response observed in relaxors. Fourth, the high P values reached during the fluctuation of the finite- and small-size domains create strong local electric fields that smear the ferroelectric transition and result in diffuse phase transition.

The new understanding of relaxor structure also has important implications for the design of new piezoelectrics. It is known that the FE DW region exhibits a high permittivity that can dramatically enhance the high-frequency intrinsic dielectric response relative to a bulk single domain material. The extremely high density of DWs and the presence of a mixture of FE- and PE-like unit cells in relaxors give rise to a greater flexibility for P rotations over a wide T range and the ultrahigh piezoelectric response in relaxors. Our recent work has also shown that DW energy and orientation is a crucial determinant of the coercive field⁸ that is an important parameter of the piezoelectric materials, with higher DW energies favoring higher coercive fields. These findings point to the direction of seeking materials with enhanced density of higher energy DWs, where the higher DW energy provides the higher coercive field, while the higher DW density provides the higher dielectric and piezoelectric response. The authors thank ONR for support N00014-12-1-1033.

References

- [1] A. A. Bokov and Z.-G. Ye, "Recent progress in relaxor ferroelectrics with perovskite structure," *J. Mater. Sci.* **41**, 31–52 (2006).
- [2] M. Matsuura, K. Hirota, P. Gehring, Z.-G. Ye, W. Chen, and G. Shirane, "Compositional dependence of the diffuse scattering in the relaxor ferroelectric compound $(1-x)\text{Pb}(\text{Mg}_{1/3}\text{Nb}_{2/3})\text{O}_3-x\text{PbTiO}_3$ ($0 \leq x \leq 0.40$)," *Phys. Rev. B* **74**, 144107 (1–10) (2006).
- [3] G. Burns and F. H. Dacol, "Glassy polarization in relaxor ferroelectrics," *Solid State Commun.* **48**, 853–856 (1983).
- [4] V. Westphal, W. Kleemann, and M. Glinchuk, "Diffuse Phase Transitions and Random-Field-Induced Domain States of the "Relaxor" Ferroelectric $\text{PbMg}_{1/3}\text{Nb}_{2/3}\text{O}_3$," *Phys. Rev. Lett.* **68**, 847–850 (1992).
- [5] I. Grinberg, V. R. Cooper, and A. M. Rappe, "Relationship between local structure and phase transitions of a disordered solid solution," *Nature* **419**, 909–911 (2002).
- [6] Y.-H. Shin, V. R. Cooper, I. Grinberg, and A. M. Rappe, "Development of a bond-valence molecular-dynamics model for complex oxides," *Phys. Rev. B* **71**, 054104 (1–4) (2005).
- [7] S. Liu, I. Grinberg, H. Takenaka, and A. M. Rappe, "Reinterpretation of the bond-valence model with bond-order formalism: An improved bond-valence-based interatomic potential for PbTiO_3 ," *Phys. Rev. B* **88**, 104102 1–7 (2013).
- [8] S. Liu, I. Grinberg, and A. M. Rappe, "Intrinsic ferroelectric switching from first principles," *Nature* **534**, 360–363 (2016).

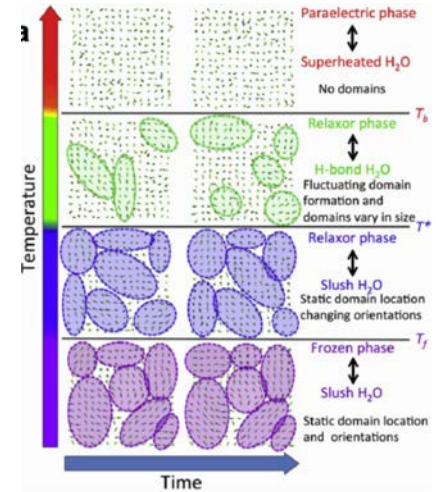


Figure 2: Angle correlation function for Pb displacements in $\text{Pb}(\text{Mg}_{1/3}\text{Nb}_{2/3})\text{O}_3\text{-PbTiO}_3$ shows the size and intensity of polar nanoregions. $\max_{\theta} P(\theta, r, T)$ plotted vs. r shows smaller angles (stronger dipole alignment) for small r and low T but lack of alignment for $r > 8$ nm for all T .

Hybrid Improper Ferroelectricity

S.-W. Cheong^{1,2}, F.-T. Huang¹, B. Gao¹, Y. S. Oh¹, Y. Wang¹, J.-W. Kim¹, S.-J. Lim¹, F. Xue³, L. H. Wang², X. Luo², W. Cai¹, X.-Z. Lu⁴, L. Q. Chen³ and J. M. Rondinelli⁴

¹Rutgers Center for Emergent Materials, Department of Physics and Astronomy, Rutgers University, Piscataway, New Jersey 08854, USA;

²Laboratory for Pohang Emergent Materials and Max Plank POSTECH Center for Complex Phase Materials, Pohang University of Science and Technology, Pohang 790-784, Korea;

³Department of Materials Science and Engineering, The Pennsylvania State University, University Park, Pennsylvania 16802, USA;

⁴Department of Materials Science and Engineering, Northwestern University, Evanston, Illinois 60208, USA.

Hybrid improper ferroelectricity (HIF), which describes a state with the polarization induced by a hybridization of two non-polar lattice instabilities, holds great promise toward the realization of room-temperature multiferroelectricity. The key idea is to design new materials in which ferroelectricity and (anti)ferromagnetism can be coupled by the same lattice instability, therefore providing an indirect but strong coupling between polarization and magnetism. Exemplary compounds with HIF include the double-layered Ruddlesden-Popper (RP) perovskites with the chemical formula of $A_3B_2O_7$ (A^{2+} = alkali metal; B^{4+} = transition metal), $PbTiO_3/SrTiO_3$ superlattice and $AA'B_2O_6$ double perovskites. In addition, the presence of related polar space groups has been reported in Dion-Jacobson compounds $ABiNb_2O_7$ ($A = Rb, Cs$), RP-phase ferrite composites and $Ca_3Mn_2O_7$.

We have, for the first time, grown single crystals of $(Ca,Sr)_3Ti_2O_7$, and experimentally confirmed the existence of hybrid improper ferroelectricity in the crystals [1]. Furthermore, we found that charged ferroelectric domain walls (FE DWs), some of which are highly conducting, are mysteriously abundant in the recently discovered $(Ca,Sr)_3Ti_2O_7$ crystals [1]. Head-to-head and tail-to-tail 180° FE DWs exhibit an approximately 100 times conduction difference in the conductive atomic force microscopy (c-AFM) measurements (FIG. 1a top). We also discover a zipper-like nature of domain walls with high energy; they are the reversible creation/annihilation centers of ferroelectric wall pairs for the process of 90° and 180° polarization switching (FIG. 1a bottom) [2]. Note that we have also prepared high-quality $Sr_3Sn_2O_7$ specimens [3], and experimentally proved the presence of HIF in $Sr_3Sn_2O_7$ (FIG. 1b).

RP-phase $Ca_3Mn_2O_7$ has been proposed as a prototypical HIF magnet. In addition, a relative large, possibly questionable, magnetoelectric (ME) effect (72 ps/m) has been reported in polycrystalline $Ca_3Mn_2O_7$ at 4 K. However, no measurable FE polarization has been reported in $Ca_3Mn_2O_7$. We have, for the first time, grown single crystals of $Ca_3Mn_2O_7$ and confirmed the presence of polar domains in $Ca_3Mn_2O_7$ [2,4]. However, we discovered that our $Ca_3Mn_2O_7$ crystals exhibit highly-irregular orthorhombic twin structures (FIG. 1c), distinct from the prototypical straight twin structure. We also

found that the polarization of $\text{Ca}_3\text{Mn}_2\text{O}_7$ is non-switchable in the electric field range that we can apply. We will discuss the origin of the unprecedented twin structure in $\text{Ca}_3\text{Mn}_2\text{O}_7$, and also its interrelationship with non-switchability of polarization [4]. Our results on a number of HIF materials pave a new avenue to design new ferroelectrics with enhanced functionalities and also novel multiferroics with room-temperature magnetoelectricity.

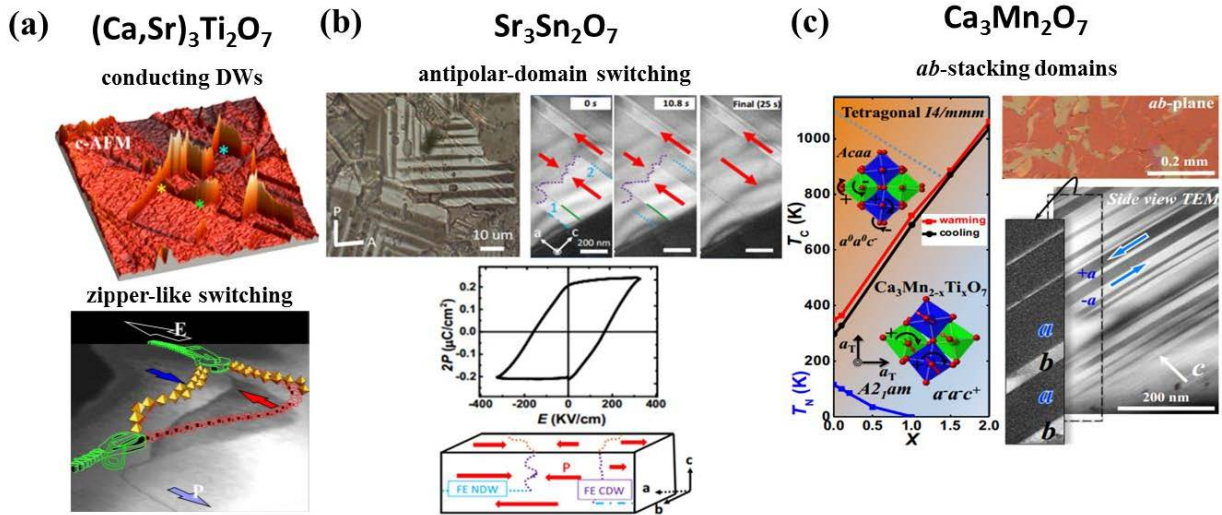


Figure 1 Bulk hybrid improper ferroelectrics. (a) conductive atomic force microscopy (c-AFM) image of $\text{Ca}_{2.46}\text{Sr}_{0.54}\text{Ti}_2\text{O}_{7.6}$ crystal shows abundant charged domain walls that conduct electricity at room temperature. DF-TEM images show in-situ 180° (as well as 90° -type) ferroelectric switching via zipper-like channels in which high-energy domain walls can be reversibly split into or merged by other ferroelectric domain walls with low energy. (b) Orthorhombic straight ferroelastic domains and switchable electric polarization of $\text{Sr}_3\text{Sn}_2\text{O}_7$ at room temperature. DF-TEM images show in-situ 180° -type ferroelectric switching via antipolar domain structures along the c -axis. (c) Phase diagram of $\text{Ca}_3\text{Mn}_{2-x}\text{Ti}_x\text{O}_7$ ($0 \leq x \leq 2$). Irregular in-plane ferroelastic domains combined with a high-density stacking of a - and b -domains along the c -axis of $\text{Ca}_3\text{Mn}_2\text{O}_7$ magnet appear to prevent polarization switching and lead to negligible ME coupling.

Ref: [1] Oh, Y. S., Luo, X., Huang, F.-T., Wang, Y. & Cheong, S.-W. *Nat. Mater.* **14**, 407–413 (2015). [2] Wang, Y., Huang, F.-T., Luo, X., Gao, B. & Cheong, S.-W. *Adv. Mater.* DOI:10.1002/adma.201601288. [3] Huang, F.-T., Xue, F., Gao, B., Wang, L.H., Luo, X., Cai, W., Lu, X.-Z., Rondinelli, J. M., Chen, L.Q. & Cheong, S.-W. *Nat. Commun.* **7**, 11602 (2016). [4] Gao, B., Huang, F.-T., Wang, Y., Kim, J.-W., Wang, L.H., Lim, S.-J. & Cheong, S.-W. under review.

Effect of Trilinear Couplings on Dynamical Properties of Perovskites

Kinnary Patel¹, Sergey Prosdandeev^{1,2}, and L. Bellaiche¹

¹Physics Department and Institute for Nanoscience and Engineering, University of Arkansas, Fayetteville, Arkansas 72701, USA

²Institute of Physics and Physics Department of Southern Federal University, Rostov-na-Donu 344090, Russia.

Trilinear energetic couplings have been intensively investigated in perovskites in recent years [1-7], especially static properties related to them. On the other hand, very little is known about dynamical properties of perovskites exhibiting trilinear couplings. Here, we wish to study such properties by focusing on BiFeO₃ under pressure, since this system is known to adopt a *Pnma* structure at high enough pressure that possesses a trilinear coupling between antiferroelectricity and two oxygen tilts. The effective Hamiltonian approach of Refs. [8-11] is presently used in order to investigate properties of BFO at finite temperature and under hydrostatic pressure, with the total energy being the sum of the following three terms

$$\begin{aligned}
 E_{\text{total}} = & E_1(\{u_i\}, \{\eta_H\}, \{\eta_i\}) + E_2(\{m_i\}, \{u_i\}, \{\eta_H\}, \{\eta_i\}, \{\omega_i\}) \\
 & + E_3(\{u_i\}, \{\eta_H\}, \{v_i\}, \{\omega_i\}) \quad \text{where} \\
 E_3(\{u_i\}, \{\eta_H\}, \{v_i\}, \{\omega_i\}) = & \sum_i \kappa_A \omega_i^4 + \sum_i [\gamma_A (\omega_{i,x}^2 \omega_{i,y}^2 \\
 & + \omega_{1ti,y}^2 \omega_{i,z}^2 + \omega_{i,x}^2 \omega_{i,z}^2)] + \sum_i \sum_{\alpha,\beta} C_{i,\alpha\beta} \eta_l(i) \omega_{i,\alpha} \omega_{i,\beta} \\
 & + \sum_{i,j} \sum_{\alpha} \omega_{i,\alpha}^3 (\omega_{i+\alpha,\alpha} + \omega_{i-\alpha,\alpha}) \\
 & + \sum_{i,j} \sum_{\alpha,\beta} D_{ij,\alpha\beta} \omega_{i,\alpha} \omega_{i,\beta} u_{j,\alpha} \quad (1)
 \end{aligned}$$

The degrees of freedoms are (i) the local soft mode u_i centered on Bi sites (such centering allows, e.g., to reproduce the Bi-driven antiferroelectricity associated the *Pnma* phase of BFO [11]); (ii) η_H -homogenous strain tensor; (iii) the pseudo-vector ω_i which is centered on Fe ions and characterizes the antiferrodistortive (AFD) distortions in unit cell i ; (iv) the magnetic dipole moment m_i which is centered on Fe ions too and whose magnitude is equal to $4\mu_B$, as consistent with first principles and measurements; and (v) inhomogeneous strain characterized by dimensionless variables, v_i . E_1 represents the energy associated with the local modes, elastic strain interactions, and coupling between the local modes and strain; E_2 is the term that gathers the energies related to magnetic degrees of freedom and their couplings with the local modes, elastic strains and AFD distortions; E_3 describes the AFD interactions and

their coupling with the local modes and strains. Analytical expressions for E_1 and E_2 are provided in Refs. [12] and [8], respectively. The expression for E_3 has been described in Ref. [11]. Note that the last term of E_3 is precisely a trilinear energy coupling between cation motions and two AFD modes. We first employed this effective Hamiltonian to perform Monte-Carlo (MC) simulation, as in Ref. [11], to compute finite temperature properties of BFO system under a simulated hydrostatic pressure of about 8.2GPa or 10.4GPa in $12 \times 12 \times 12$ supercells using 40,000 MC sweeps. We then performed MD calculations by using 4×10^5 MD steps with a time step of 0.5fs as similar to what was done in Ref. [13], except that the effective Hamiltonian used here has local modes that are centered on Bi ions (and not on Fe ions like in Ref. [13]). We computed different high-frequency responses related to different order parameters [14, 15].

We focused on the three following physical quantities: (i) the X_5^+ antiferroelectric mode that is defined via the u_x vector characterizing antiferroelectric Bi displacements at the X-point of the Brillouin zone, and that is given by $u_x = \frac{1}{N} \sum_i u_i (-1)^{n_z(i)}$, where N is the number of the Fe ions in the supercell; (ii) The M_3^+ mode that characterizes in-phase oxygen octahedral tilting around Fe sites, and that is quantified by $\omega_M = \frac{1}{N} \sum_i \omega_i (-1)^{n_x(i)+n_y(i)}$, and (iii) The R_4^+ mode representing antiphase-tilting of the oxygen octahedral and for which the corresponding order parameter is $\omega_R = \frac{1}{N} \sum_i \omega_i (-1)^{n_x(i)+n_y(i)+n_z(i)}$, where the sum runs over the N sites i and $n_x(i), n_y(i),$ and $n_z(i)$ are integers locating the cell i [16]. We decided to study these three particular modes because their order parameters are all coupled via a trilinear energy of the form $E_{\text{trilinear}} = D u_x \omega_M \omega_R$. Figure 1 shows the temperature dependence of the resonant frequencies (cm^{-1}) of different modes in BFO subject to a pressure of 8.2 GPa. The vertical dashed

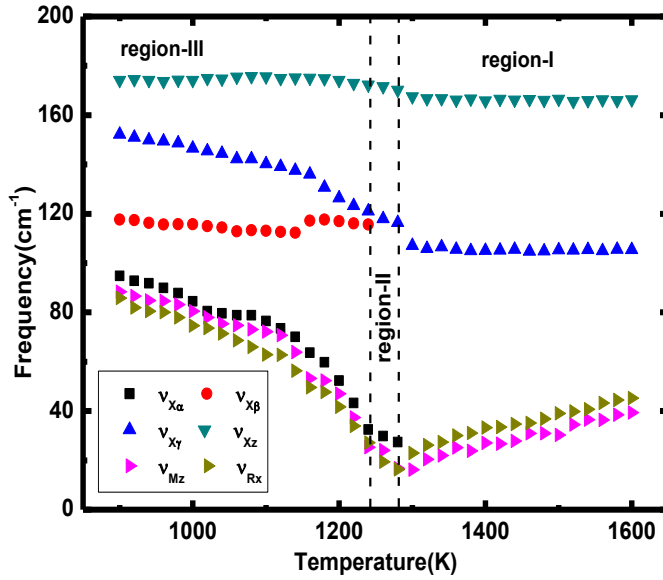


Fig. 1. Temperature dependence of resonant frequencies for X, R and M modes at 8.2 GPa pressure for BFO. See text for the notations on this figure.

lines delimit different structural phases of BFO obtained in the calculations: the cubic paraelectric state (region-I), an intermediate phase for which the in-phase tilting condenses (region-II), and the Pnma phase (region-III). The notations of the modes in the figure are the following: v_{Xz} is the resonant frequency of the X mode with fluctuations being along the z

direction, $v_{R_{x,y}}$ and v_{M_z} are the resonant frequencies associated with the R and M AFD modes, with fluctuations being along the x, y and z directions, respectively; $v_{X\alpha}$, $v_{X\beta}$, $v_{X\gamma}$ are three frequencies associated with X mode with fluctuations being in the XY plane. Only three of the X modes exist in the cubic phase: v_{Xz} is at 166 cm^{-1} and two degenerate X_γ and X_β modes locate at 105 cm^{-1} . These three modes are hard in the whole interval of the cubic phase and thus do not have any tendency to soften. In contrast to this, $R_{x,y}$ and M_z modes soften on decreasing the temperature, even more M_z than $R_{x,y}$. The softening of the M_z mode results in a phase transition from the cubic to the intermediate state at about 1300K. In this intermediate state, the M_z mode slightly hardens when decreasing temperature and R_x and $X_{\beta,\gamma}$ modes become strongly dynamically correlated. This correlation results in emergence of an X_α mode located at the frequency denoted as $v_{X\alpha}$. We numerically and analytically found that such new and soft X mode is due to the aforementioned trilinear energy that dynamically couples the fluctuations of the X and R modes via the condensation of the M mode. For temperatures below 1240K, both the R and X modes condense, which makes BFO adopting the Pnma symmetry. The trilinear coupling in BiFeO_3 has therefore a strong effect on the number of the phonon modes, their mixing, as well on the temperature-behavior of their resonant frequencies.

Acknowledgment: This work is supported by the ARO grant W911NF-16-1-0227 and ONR Grant N00014-12-1-1034.

References:

- [1] N. A. Benedek and C. J. Fennie, Phys. Rev. Lett. 106, 107204 (2011).
- [2] J. M. Rondinelli and C. J. Fennie, Adv. Mater. 24, 1961 (2012).
- [3] B. Xu, D. Wang, HJ. Zhao, J. X.M. Chen, and L. Bellaiche, Adv. Funct. Mater., 25-24 (2015) 3626-3633.
- [4] A. T. Mulder, N. A. Benedek, J. M. Rondinelli, and C. J. Fennie, Adv. Funct. Mater. 23, 4810 (2013).
- [5] Z. Zanolli, J. C. Wojdel, J. Iniguez, and P. Ghosez, Phys. Rev. B 88, 060102(R) (2013).
- [6] L. Bellaiche and J. Iniguez, Phys. Rev. B 88, 014104 (2013).
- [7] HJ. Zhao, J. Iniguez, W. Ren, XM. Chen, L. Bellaiche, Phys. Rev. B 89, 174101 (2014).
- [8] D. Albrecht, S. Lisenkov, Wei Ren, D. Rahmedov, Igor A Kornev, L. Bellaiche, Phys. Rev. B 2010, 81, 140401.
- [9] I. A. Kornev, S. Lisenkov, R. Haumont, B. Dkhil, L. Bellaiche, Phys. Rev. Lett. 2007, 99, 227602.
- [10] a) S. Lisenkov, Igor A. Kornev, L. Bellaiche, Phys. Rev. B 2009, 79, 012101; b) S. Lisenkov, Igor A. Kornev, L. Bellaiche, Phys. Rev. B 2009, 79, 219902.
- [11] S. Prosandeev, D. Wang, Wei Ren, J. Iniguez, L. Bellaiche, Adv. Funct. Mater. 2013, 23, 234-240.
- [12] a) W. Zhong, D. Vanderbilt, K. M. Rabe, Phys. Rev. Lett. 1994, 73, 1861; b) W. Zhong, D. Vanderbilt, K. M. Rabe, Phys. Rev. B 1995, 52, 6301.
- [13] D. Wang, J. Weerasinghe, and L. Bellaiche, Phys. Rev. Lett. 109, 067203 (2012).
- [14] J. Weerasinghe, D. Wang, and L. Bellaiche, Phys. Rev. B 85, 014301 (2012).
- [15] D. Wang, J. Hlinka, A.A. Bokov, Z.-G. Ye, P. Ondrejko, J. Petzelt, and L. Bellaiche, Nature communication, DOI: 10.1038/ncomms6100
- [16] I. A. Kornev, L. Bellaiche, P. E. Janolin, B. Dkhil, E. Suard, Phys. Rev. Lett. 2006, 97, 157601.

Origin of Distinct Pressure Effects on Octahedral Tilting in Perovskite Oxides

H. J. Xiang^{1,2*}, Mael Guennou³, Jorge Iniguez³, Jens Kreisel³, Laurent Bellaiche^{2*}

¹*Department of Physics, Fudan University, Shanghai 200433, P. R. China*

²*Department of Physics, University of Arkansas, Fayetteville, Arkansas 72701, USA*

⁴*Materials Research and Technology Department, Luxembourg Institute of Science and Technology (LIST), 5 avenue des Hauts-Fourneaux, L-4362 Esch/Alzette, Luxembourg*

*email: hxiang@fudan.edu.cn, laurent@uark.edu

Abstract

Octahedral tilting is common in perovskites and relevant to many physical properties, such as electronic and magnetic properties, and improper ferroelectricity. Pressure has become an efficient way to tune the octahedral tiltings. However, the richness of the pressure behavior remains a mystery. For example, the magnitude of the octahedral tilting increases with pressure in orthorhombic CaSnO_3 [1] and CaTiO_3 [2], while, in contrast, rhombohedral LaAlO_3 [3] and orthorhombic GdFeO_3 [4] perovskites become less distorted under high-pressure conditions. In this work, we formulate a rule for the pressure effect on octahedral tiltings. In particular, we find that pressure may enhance the in-phase octahedral rotation, but suppress the out-of-phase octahedral rotation (see Fig. 1b for the case of LuFeO_3) besides the above mentioned behaviors (see Figs. 1a and 1c). This unexpected behavior in, e.g., LuFeO_3 is found to arise from the tri-linear coupling between the two octahedral rotations and the anti-polar A-site mode. Moreover, we also numerically found that the octahedral rotations in ABO_3 perovskites with empty low-lying d states on the B-site will be greatly enhanced by pressure (see Figs. 1c and 1d) because these rotations can help to lower the electronic kinetic energy. We further predict that the so-called hybrid improper ferroelectricity [5] could be manipulated by pressure through indirectly controlling the amplitude of the octahedral rotations.

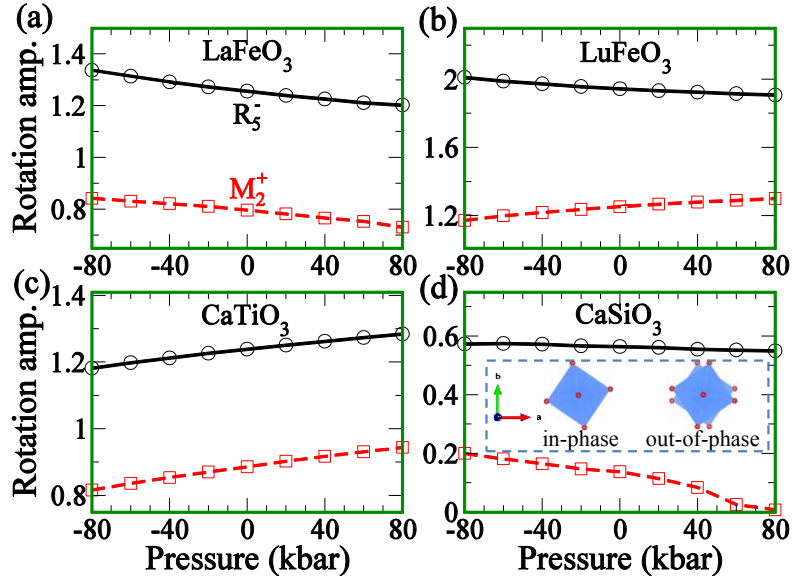


Fig. 1. Pressure effect on octahedral tiltings in Pnma (a) LaFeO₃, (b) LuFeO₃, (c) CaTiO₃, and (d) CaSiO₃. The behaviors of both R_5^- mode (out-of-plane tilt along the [110] axis) and M_2^+ mode (in-plane tilt along the [001] axis) are shown. The “in-phase” and “out-of-phase” tilts are schematized in the inset of (d).

Acknowledgement

Work at UARK is supported by the Office of Basic Energy Sciences, under contract ER-46612 and the DARPA grant HR0011-15-2-0038 (MATRIX program). We also acknowledge the FNR Luxembourg Grants P12/4853155 (M.G, J.I. and J.K.) and INTER/MOBILITY/15/9890527 GREENOX (L.B. and J.I.).

References

- [1] J. Zhao, N.L. Ross, R.J. Angel, Phys. Chem. Miner. **31**, 299 (2004).
- [2] M. Guennou *et al.*, Phys. Rev. B **82**, 134101 (2010).
- [3] P. Bouvier and J. Kreisel, J. Phys.: Condens. Matter **14**, 3981 (2002).
- [4] N.L. Ross, J. Zhao, R.J. Angel, J. Solid State Chem. **177**, 3768 (2004).
- [5] E. Bousquet *et al.*, Nature **452**, 732 (2008); N. A. Benedek and C. J. Fennie, Phys. Rev. Lett. **106**, 107204 (2011); J. M. Rondinelli and C. J. Fennie, Adv. Mater. **24**, 1961 (2012); Hong Jian Zhao, Jorge Íñiguez, Wei Ren, Xiang Ming Chen, and L. Bellaiche, Phys. Rev. B **89**, 174101 (2014).

Origin of Defect Dipole Enhanced Electromechanical Coupling

Shi Liu¹ and R. E. Cohen^{1,2}

1. Extreme Materials Initiative, Geophysical Laboratory, Carnegie Institution for Science, Washington DC
2. Department of Earth- and Environmental Sciences, LMU Munich 80333, Germany

The properties of functional materials are often decisively controlled by structural defects of various dimensionalities (e.g., vacancies and impurities as point defects and dislocations as linear defects).[1] The role of defects in solids of mixed ionic-covalent bonds[2] such as ferroelectric oxides is complex and not well understood.[3] The dipolar defects formed by the association of oxygen vacancies and metal impurities[4] couple strongly with the bulk ferroelectric polarization. The lack of a general first-principle-based atomistic model to understand defect-mediated polarization switching makes it a challenge to control defect functionality that is critical for the development and optimization of nanoscale ferroelectric devices.

Here, using the classic prototypical ferroelectric BaTiO₃ as an example, we simulate the polarization-electric field (P - E) and strain-electric field (ϵ - E) hysteresis loops in the presence of generic defect dipoles (FIG. 1) with large-scale molecular dynamics and provide a quantitative, detailed atomistic picture for the defect-mediated ferroelectric switching. We reveal that the collective orientation of dipolar defects is the key microscopic structure feature that determines the defect type (random bond vs. random field, FIG.2). The macroscopic behavior of ferroelectrics, such as the aging effect[5] and reversible giant electromechanical coupling (RGEM),[6] can be understood by the interplay between the effective electric field from the defect dipoles and the orientation of external driving field. With quantum mechanically derived defect dipole moment, we demonstrate that a small concentration (!0.5%) of acceptor doping can dramatically improve the electromechanical response. This offers the opportunity to improve the performance of cost-competitive polycrystalline ferroelectric ceramics through defect dipole engineering for a range of applications including piezoelectric sensors, actuators, and transducers.

REFERENCE

1. Tilley, R. J. *Defects in Solids*. Vol. 4 (John Wiley & Sons, 2008).
2. Cohen, R. E. Origin of Ferroelectricity in Perovskite Oxides. *Nature* **358**, 136-138, (1992).
3. Kalinin, S. V. *et al.* Defect-Mediated Polarization Switching in Ferroelectrics and Related Materials: From Mesoscopic Mechanisms to Atomistic Control. *Adv. Mater.* **22**, 314-322, (2010).

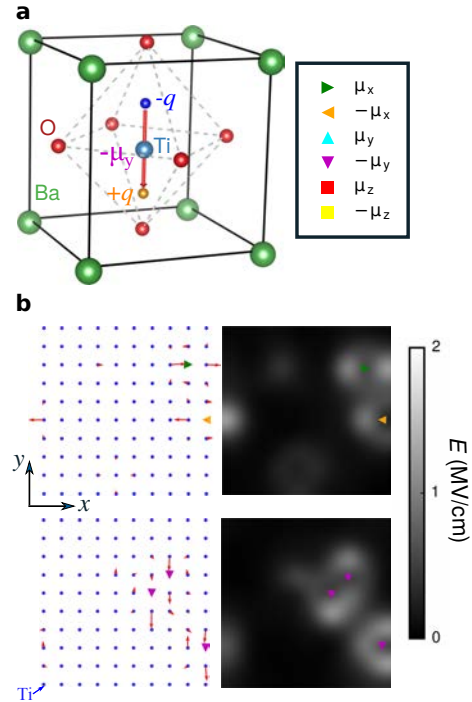


FIG 1. Generic defect dipole model for molecular dynamics. **a**, Schematic of an explicit defect dipole consisted of a pair of oppositely charged dummy atoms in BaTiO₃ unit cell. **b**, Local electric fields experienced by Ti atoms in vector form (left) and intensity map form (right) due to defect dipoles ($q = 0.1e$).

- 4 Poykko, S. & Chadi, D. J. Dipolar Defect Model for Fatigue in Ferroelectric Perovskites. *Phys. Rev. Lett.* **83**, 1231-1234, (1999).
- 5 Jonker, G. H. Nature of Aging in Ferroelectric Ceramics. *J. Am. Ceram. Soc* **55**, 57-&, (1972).
- 6 Ren, X. B. Large Electric-Field-Induced Strain in Ferroelectric Crystals by Point-Defect-Mediated Reversible Domain Switching. *Nat. Mater.* **3**, 91-94, (2004).

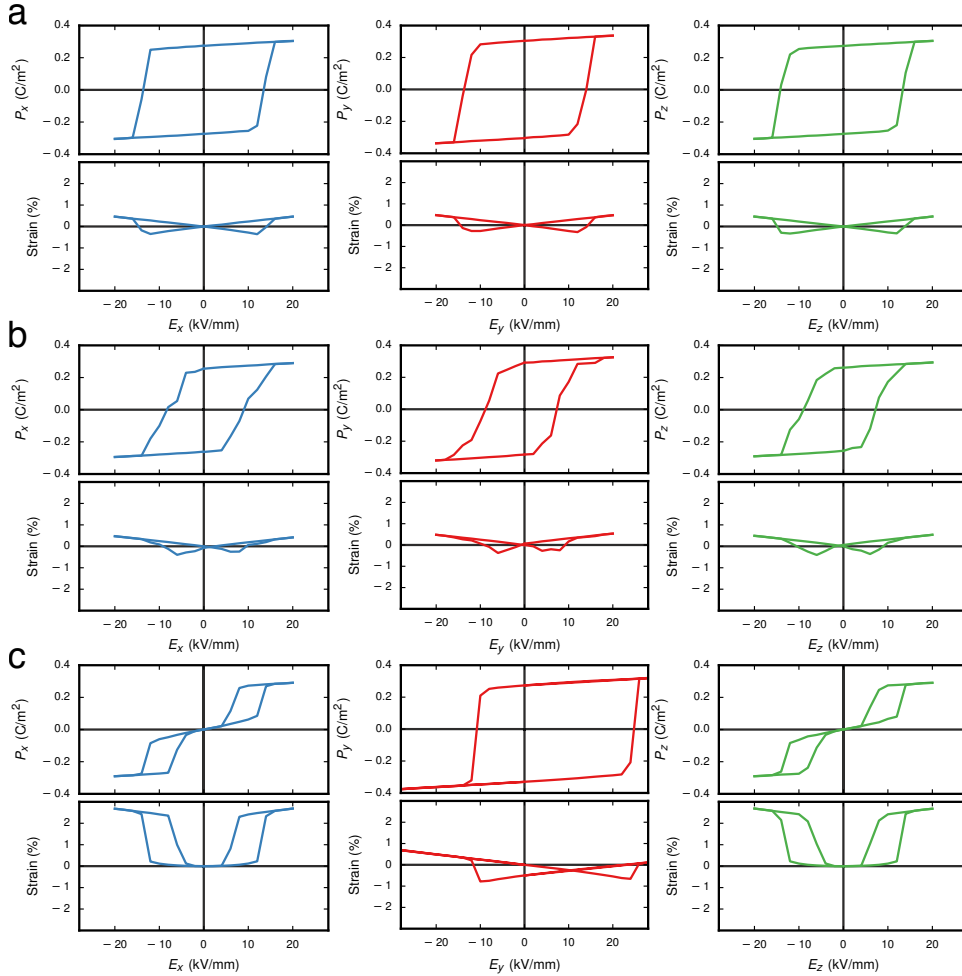


FIG. 2 Molecular dynamics simulations of polarization-electric field ($P-E$) and strain-electric field ($\varepsilon-E$) hysteresis loops in BaTiO_3 with generic defect dipoles. Electric fields are applied along x (blue), y (red), and z (green) axis, respectively. For a given defect concentration, the simulated hysteresis loop is averaged over multiple cycles and multiple configurations. **a**, Isotropic and symmetric hysteresis loops for $n = 1.2\%$, $q = 0.0 e$. The loops are essentially the same as those in pure BaTiO_3 . **b**, Symmetric hysteresis loops for $n = 1.2\%$, $q = 0.1 e$ with defect dipoles randomly oriented. **c**, Double-loops along x and z and horizontally-shifted loops along y for $n = 1.2\%$, $q = 0.1 e$ with defect dipoles aligned along $-y$.

The effect of time-dependent magnetic field on polarization in multiferroics

S. Omid Sayedaghaee^{1,2}, Sergey Prosandeev^{2,4}, Bin Xu^{2,3}, Laurent Bellaiche^{1,2,3}

¹Microelectronics-Photonics Program, University of Arkansas, Fayetteville, AR 72701, USA

²Physics Department, University of Arkansas, Fayetteville, AR 72701, USA

³Institute for Nano Science and Engineering, University of Arkansas, Fayetteville, AR, 702701, USA

⁴Research Institute of Physics and Physical Faculty, Southern Federal University, Stachki Ave. 194, 344090 Rostov-on-Don, Russia

Multiferroics are intensively investigated [1], as it is intriguing to understand couplings between different order parameters, and it is of technological importance to control one ferroic order by varying the other. For example, polarization can be affected by an external magnetic field H_j , which can be expressed as

$$P_i = P_i^s + \alpha_{ij}H_j + \frac{1}{2}\beta_{ijk}H_jH_k \quad (1)$$

where P_i^s is the spontaneous polarization [2]. α_{ij} and β_{ijk} are known as linear and quadratic magnetoelectric (ME) coefficients, respectively. Although α_{ij} and β_{ijk} have been studied in the framework of some static approaches [[3-4] and references therein], the behavior of polarization under ac (i.e, time-dependent) magnetic field has not been studied from atomistic approaches, to the best of our knowledge. The purpose of this study is to investigate the behavior of polarization under application of an *ac* magnetic field h_{ac} superimposed on a *dc* field H_{dc} (that is, $H = H_{dc} + h_{ac}\sin(\omega t)$) by atomistic simulations. For this purpose, we employed an effective Hamiltonian recently developed for BiFeO₃ (BFO) [5], and a Molecular Dynamics (MD) approach [6], based on this Hamiltonian. More specifically we are interested to investigate the dependence of the nonlinear ME coefficient on the frequency of the applied magnetic field. The dependency of polarization on time for (bulk) BFO can be theoretically expressed as [6] (since the linear ME coefficient is small in BFO),

$$P = P_0 + \beta H_{dc}h_{ac}\sin(\omega t) + \frac{1}{2}\beta h_{ac}^2\sin^2(\omega t) \quad (2)$$

The quadratic coefficient β is numerically obtained by fitting the time dependent polarization obtained from MD simulations to Eq. (2). When the frequency of applied magnetic field, ω , is within few GHz, the extracted value for β is in the order of 10^{-8} C/m²T², which is in agreement with measurement reported in Ref. [7]. Figure 1 shows the time behavior of the polarization obtained at the magnetic fields of $h_{ac} = 61.2$ T and $H_{dc} = 245$ T applied along the [1 1 -2] pseudo-cubic direction, at $\omega = 1$ GHz. This simulation resulted in $\beta = 2.71 \times 10^{-8}$ C/m²T² when we considered the coefficient in front of $\sin(\omega t)$ in Eq. (2) and $\beta = 3.13 \times 10^{-8}$ C/m²T² when we considered the coefficient in front of $\sin^2(\omega t)$.

More MD simulations were performed at different frequencies of the applied magnetic field from 1 GHz to hundreds of GHz to explore the dependency of β on frequency.

Address correspondence to E-mail: omids@uark.edu; laurent@uark.edu

Amazingly, we observed that the behavior of β changes significantly when the frequency of the applied magnetic field is around 90 GHz (See Figure 2). This strong effect on polarization oscillations is mostly due to the fact that this specific frequency corresponds to the low-frequency magnon found in Ref. [8].

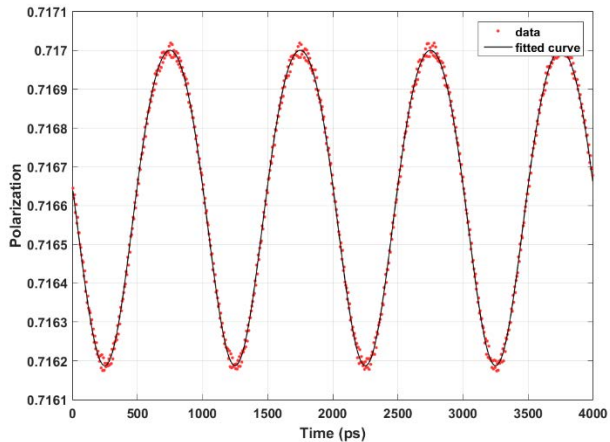


Figure 1 – Polarization vs. time at $\omega = 1\text{GHz}$

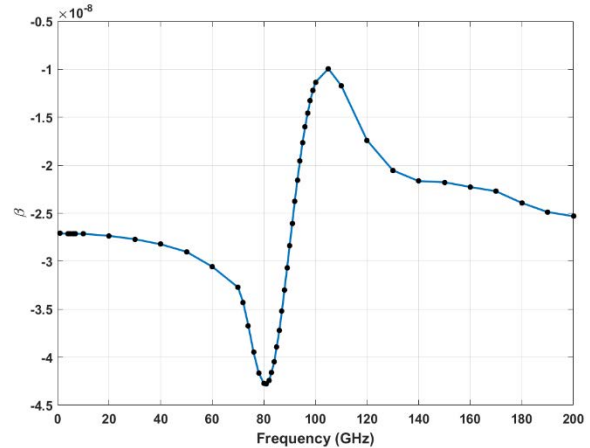


Figure 2 – β vs. frequency of applied magnetic field

We will also present results for higher frequencies than those shown in Fig. 2, and demonstrate there that the polarization has an unusual time-dependence behavior as a result of the influence of the resonant phonon frequency in addition to the frequency of the applied magnetic field. Thus, the dynamical coupling of different order parameters in multiferroics can lead to new effects.

Acknowledgements

This work is financially supported by DARPA Grant HR0011-15-2-0038 (MATRIX program) and the Air Force Office of Scientific Research under Grant No. FA9550-16-1-0065 (B. X. and L.B.). S. P. appreciates support of ONR Grant No. N00014-12-1-1034.

References

- [1] W. Eerenstein, N. D. Mathur, and J. F. Scott, “Multiferroic and magnetoelectric materials,” *Nature*, vol. 442, no. 7104, pp. 759–765, Aug. 2006.
- [2] M. Fiebig, “Revival of the magnetoelectric effect,” *J. Phys. Appl. Phys.*, vol. 38, no. 8, pp. R123–R152, Apr. 2005.
- [3] D. Albrecht, S. Lisenkov, W. Ren, D. Rahmedov, I. A. Kornev, and L. Bellaiche, “Ferromagnetism in multiferroic BiFeO₃ films: A first-principles-based study,” *Phys. Rev. B*, vol. 81, no. 14, Apr. 2010.
- [4] S. Prosandeev, I. A. Kornev, and L. Bellaiche, “Magnetoelectricity in BiFeO₃ films: First-principles-based computations and phenomenology,” *Phys. Rev. B*, vol. 83, no. 2, Jan. 2011.
- [5] S. Prosandeev, D. Wang, W. Ren, J. Íñiguez, and L. Bellaiche, “Novel Nanoscale Twinned Phases in Perovskite Oxides,” *Adv. Funct. Mater.*, vol. 23, no. 2, pp. 234–240, Jan. 2013.
- [6] V. V. Laguta *et al.*, “Room-temperature paramagnetoelectric effect in magnetoelectric multiferroics Pb(Fe_{1/2}Nb_{1/2})O₃ and its solid solution with PbTiO₃,” *J. Mater. Sci.*, vol. 51, no. 11, pp. 5330–5342, Jun. 2016.
- [7] C. Tabares-Muñoz, J.-P. Rivera, A. Bezinges, A. Monnier, and H. Schmid, “Measurement of the quadratic magnetoelectric effect on single crystalline BiFeO₃,” *Jpn. J. Appl. Phys.*, vol. 24, no. S2, p. 1051, 1985.
- [8] D. Wang, J. Weerasinghe, and L. Bellaiche, “Atomistic Molecular Dynamic Simulations of Multiferroics,” *Phys. Rev. Lett.*, vol. 109, no. 6, Aug. 2012.

An Automated Ab Initio Framework for Identifying New Ferroelectrics

Tess Smidt^(1,2), Sebastian E. Reyes-Lillo^(1,2), Anubhav Jain⁽³⁾ and Jeffrey B. Neaton^(1,2,4)

(1) *Molecular Foundry, Lawrence Berkeley National Laboratory, Berkeley, California 94720, USA*

(2) *Department of Physics, University of California, Berkeley, California 94720 USA*

(3) *Material Science Division, Lawrence Berkeley National Laboratory, Berkeley, California 94720, USA*

(4) *Kavli Energy NanoSciences Institute at Berkeley, Berkeley, California, 94720 USA*

(Dated: December 2, 2016)

High-throughput screening of material databases integrated with first principles calculations has been increasingly successful in the discovery and design of new functional materials. Recently, new (anti)ferroelectric and multiferroic materials have been proposed with a wide range of technological properties and physical phenomena [1–5]. In this work, we perform an automated high-throughput search of new ferroelectric materials using the Materials Project database. Our approach goes beyond previous studies by aiming to build a library of known and candidate ferroelectric materials.

In order to identify new ferroelectrics among known compounds, we screen thousands of candidates in the Materials Project, identifying compounds possessing symmetry-related non-polar and polar phase pairs. Among these, we further down-select promising candidates with criteria involving the magnitude of the distortions and energy differences between non-polar and polar structures. Our approach leads to new ferroelectrics, with non-polar and polar structures related by symmetry; and new antiferroelectrics, with non-polar and polar structures related by symmetry but separated by an energy barrier along the distortion path due to coupling to additional structural modes [6]. Table I and Fig. 1 show a selection of new ferroelectric materials found in this work. Additional calculations are performed to compute macroscopic polarizations and electronic band gaps.

We benchmark our results against known ferroelectric materials and available experimental data. Our workflow integrates symmetry tools and is fully parallelized, and results are automatically parsed and stored in a database library. The database is accessible via a web interface and includes distortion animations, and plots of polarization and total energy as a function of distortion. We discuss possible future directions to expand this search methodology to other material classes such as multiferroics.

TABLE I. Selection of promising ferroelectric candidates found through our automatized high-throughput search in the Materials Project. For each compound, we report the non-polar and polar space group number, the energy difference ΔE (meV per formula unit) between non-polar and polar structures, the macroscopic polarization P ($\mu\text{C}/\text{cm}^2$), and electronic band gap E_g (eV) computed using the generalized gradient approximation.

| Compound | Non-polar | Polar | ΔE | P | E_g |
|--|-----------|-------|------------|-----|-------|
| KLaSiS ₄ | 11 | 4 | 21 | 9.7 | 2.85 |
| Cs ₂ PbO ₃ | 63 | 36 | 5 | 7.1 | 1.39 |
| Ca ₅ P ₃ ClO ₁₂ | 176 | 173 | 15 | 2.2 | 5.35 |

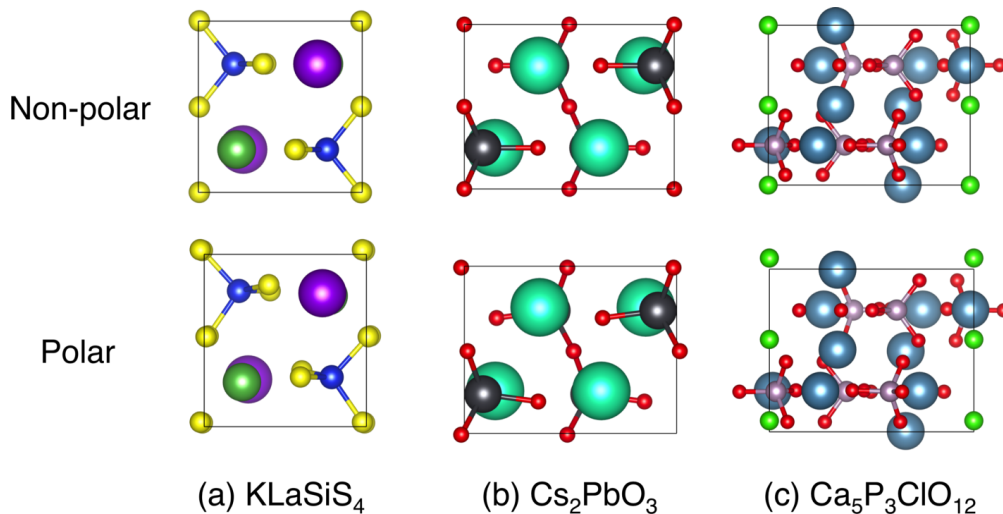


FIG. 1. Non-polar and polar structures for (a) KLaSiS₄ (K: purple, La: green, Si: blue, S: yellow), (b) Cs₂PbO₃ (Cs: emerald green, Pb: grey, O: red) and (c) Ca₅P₃ClO₁₂ (Ca: steel-blue, P: plum, Cl: light green, O: red).

Presenting author electronic address: sreyes@berkeley.edu

-
- [1] J. W. Bennett, K. F. Garrity, K. M. Rabe, and D. Vanderbilt, Phys. Rev. Lett. **109**, 167602 (2012).
 - [2] J. W. Bennett, K. F. Garrity, K. M. Rabe, and D. Vanderbilt, Phys. Rev. Lett. **110**, 017603 (2013).
 - [3] K. F. Garrity, K. M. Rabe, and D. Vanderbilt, Phys. Rev. Lett. **112**, 127601 (2014).
 - [4] K. F. Garrity, arXiv:1610.04279 (2016).
 - [5] J. W. Bennett and K. M. Rabe, J. of Solid State Chem. 195 **21** (2012).
 - [6] S. E. Reyes-Lillo, K. F. Garrity and K. M. Rabe, Phys. Rev. B **90**, 140103(R) (2014).

Effects of biaxial strain on the improper multiferroicity in h-LuFeO₃ films

Kishan Sinha¹, Yubo Zhang², Xuanyuan Jiang¹, Xiao Wang³, Xiaozhe Zhang^{1,4}, Philip J. Ryan⁵, Jong-Woo Kim⁵, John Bowlan⁶, Dmitry A Yarotski⁶, Yuelin Li⁵, Anthony D. DiChiara⁵, Xuemei Cheng³, Xifan Wu², Xiaoshan Xu^{1*}

¹Department of Physics and Astronomy, Nebraska Center for Materials and Nanoscience, University of Nebraska, Lincoln, Nebraska 68588, USA,

²Department of Physics, Temple University, Philadelphia, Pennsylvania 19122, USA

³Department of Physics, Bryn Mawr College, Bryn Mawr, Pennsylvania 19010, USA

⁴Department of Physics, Xi'an Jiaotong University, Xi'an 710049, China

⁵Advanced Photon Source, Argonne National Laboratory, Argonne, Illinois 60439, USA

⁶Center for Integrated Nanotechnologies, Los Alamos National Laboratory, Los Alamos, New Mexico 87545, USA

*Email: xiaoshan.xu@unl.edu

In materials that are both improperly ferroelectric and weakly ferromagnetic, the structural distortions can play a critical role both in originating the ferroic orders and in coupling them. As a prototypical improper ferroelectric material, hexagonal LuFeO₃ (h-LuFeO₃) exhibits ferroelectricity below 1050 K and weak ferromagnetism below 130 K. [1–3] The ferroelectricity is induced by a ferrodistortion [K_3 structural distortion, Fig. 1(a)]. [3–6] The ferromagnetic order, which is parasitic to the antiferromagnetic order, is induced by the K_3 ferrodistortion both in terms of the creation of the local magnetic moments by the Dzyaloshinskii-Moriya (DM) interactions and in terms of the non-zero inter-layer exchange interactions due to the reduction of symmetry. [3,4,7] First principle calculations predict a possible reversal of magnetization by an electric field along the c axis [4], and anomalously large magnetoelectric effects in the a - b plane in h-LuFeO₃ [8], both of which are mediated by the lattice.

Experimentally, detailed roles of the ferrodistortion can be studied by varying the distortion, often by applying an elastic strain. This is unfortunately difficult for h-LuFeO₃, which is unstable in bulk but can be stabilized in epitaxial thin films: The lack of structurally compatible substrates makes the growth of defect-free films impossible and makes the epitaxial strain difficult to control [2,3,9] and there are no bulk counterparts to compare with since the stand-alone hexagonal phase of LuFeO₃ is unstable. As a result, investigation on the strain effect in h-LuFeO₃ has been rare.

In this work, we employed a method of restrained thermal expansion to study the strain effect in h-LuFeO₃. In general, thermal strain may be generated in a material in all crystalline dimensions in an isobaric thermal expansion. However, in an epitaxial thin film, if the film is selectively heated, the out-of-plane dimension is free to expand while the in-plane dimensions of the film is restrained by the substrate (restrained thermal expansion). By comparing the material properties in the isobaric and restrained thermal expansions, the

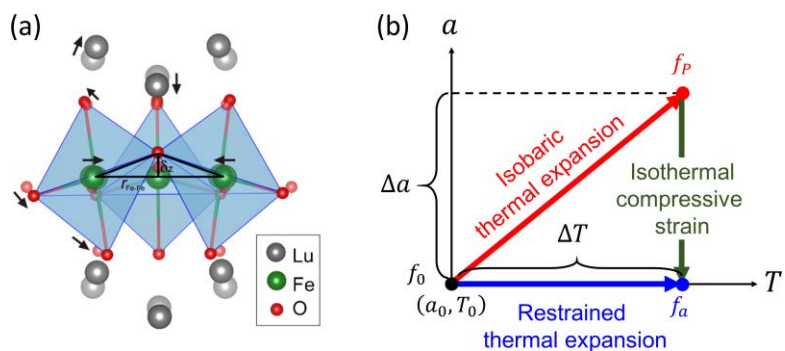


Figure 1. (a) Trimer model of the K_3 ferrodistortion in h-LuFeO₃, which corresponds to the rotation of FeO₅ trigonal bipyramids, the buckling of the Lu layers, and the trimerization. The arrows indicate the atomic displacements when K_3 is enhanced under the compressive biaxial strain. (b) Illustration of the restrained thermal expansion and isobaric thermal expansion in the (a, T) space, where a is the in-plane lattice constants, T is temperature, f is a general physical property.

effect of isothermal compressive strain at a higher temperature can be obtained [Fig. 1(b)]. Using the method of restrained thermal expansion, we studied the strain effect on the K_3 ferrodistortion in h-LuFeO₃. Experimentally, we observed that the biaxial strain in the basal plane of h-LuFeO₃ does significantly couple to the K_3 ferrodistortive, which agrees with the results of our first principle calculation (Fig. 2). We also found from our first principle calculations that the compressive strain combined with the enhanced ferrodistortion, increases the spontaneous electric polarizations but reduces the weak ferromagnetic moments. The elucidation of the strain effect in h-LuFeO₃ is an important advancement of our understanding on the coupling between the lattice and the improper multiferroicity. The experimental characterization of strain effect in h-LuFeO₃, can potentially be extended to measure the electronic and magnetic properties, when additional probes (e.g. optical or soft X-ray) are included. This could be especially important for studying the epitaxial thin films for which the strain effects haven't been fully investigated due to the imperfection in epitaxy or the lack of bulk counterparts.

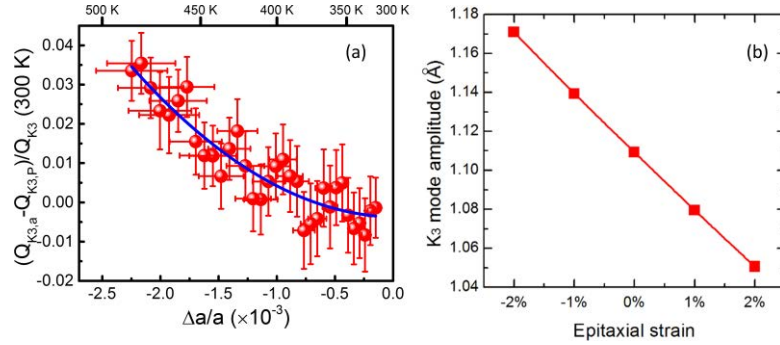


Figure 2. (a) The effect of isothermal biaxial compressive strain on Q_{K_3} . Each data point represents a change of Q_{K_3} caused by a strain $\frac{\Delta a}{a}$ (bottom axis) at the corresponding temperature (top axis). The line is a guide to the eyes. (b) Effect of the biaxial strain $\frac{\Delta a}{a}$ on the K_3 distortion, calculated using the density functional theory.

Acknowledgement

The experimental effort in this work was mainly supported by the National Science Foundation (NSF), DMR under Award DMR-1454618. The theoretical effort was supported by the Air Force Office of Scientific Research under FA9550-13-1-0124. This research used resources of the Advanced Photon Source, a U.S. Department of Energy (DOE) Office of Science User Facility operated for the DOE Office of Science by Argonne National Laboratory under Contract No. DE-AC02-06CH11357. Use of BioCARS was also supported by the National Institute of General Medical Sciences of the National Institutes of Health under grant number R24GM111072. The content is solely the responsibility of the authors and does not necessarily represent the official views of the National Institutes of Health. Time-resolved set-up at Sector 14 was funded in part through a collaboration with Philip Anfinrud (NIH/NIDDK).

References

- [1] Y. K. Jeong, J. Lee, S. Ahn, S.-W. Song, H. M. Jang, H. Choi, and J. F. Scott, *J. Am. Chem. Soc.* **134**, 1450 (2012).
- [2] W. Wang, J. Zhao, W. Wang, Z. Gai, N. Balke, M. Chi, H. N. Lee, W. Tian, L. Zhu, X. Cheng, D. J. Keavney, J. Yi, T. Z. Ward, P. C. Snijders, H. M. Christen, W. Wu, J. Shen, and X. Xu, *Phys. Rev. Lett.* **110**, 237601 (2013).
- [3] X. Xu and W. Wang, *Mod. Phys. Lett. B* **28**, 1430008 (2014).
- [4] H. Das, A. L. Wysocki, Y. Geng, W. Wu, and C. J. Fennie, *Nat Commun* **5**, 2998 (2014).
- [5] C. Xu, Y. Yang, S. Wang, W. Duan, B. Gu, and L. Bellaiche, *Phys. Rev. B* **89**, 205122 (2014).
- [6] C. J. Fennie and K. M. Rabe, *Phys. Rev. B* **72**, 100103 (2005).
- [7] S. Cao, X. Zhang, T. R. Paudel, K. Sinha, X. Wang, X. Jiang, W. Wang, S. Brutsche, J. Wang, P. J. Ryan, J.-W. Kim, X. Cheng, E. Y. Tsymlal, P. A. Dowben, and X. Xu, *J. Phys. Condens. Matter* **28**, 156001 (2016).
- [8] M. Ye and D. Vanderbilt, *Phys. Rev. B* **92**, 35107 (2015).
- [9] E. Magome, C. Moriyoshi, Y. Kuroiwa, A. Masuno, and H. Inoue, *Jpn. J. Appl. Phys.* **49**, 09ME06 (2010).

First-principles and neutron diffraction investigation of polarization in tetragonal BiCoO₃

Santosh KC^{1*}, Keith M. Taddei², Alexei A. Belik³, Clarina De La Cruz² and Valentino R. Cooper¹

¹*Materials Science and Technology Division, Oak Ridge National Laboratory, Oak Ridge, Tennessee 37831, USA.*

²*Quantum Condensed Matter Division, Oak Ridge National Laboratory Oak Ridge, Tennessee 37831, USA.*

³*Research Center for Functional Materials, National Institute for Materials Science, Namiki 1-1, Tsukuba, Ibaraki 305-0044, Japan*

*E-mail: kcs1@ornl.gov

Spin-driven ferroelectric polarization has emerged as an important research field for multiferroic systems [1]. Here, a ferroelectric (FE) polarization can be induced from the breaking of space inversion symmetry due to magnetic ordering in the crystal. The ability to control magnetism using an electric field has potential in novel functional devices such as magnetic data storage, spintronics, logic, and memory devices [2, 3]. Bismuth ferrite (BiFeO₃), which exhibits coupling between ferroelectricity and (anti) ferromagnetism is regarded as one of the most promising multiferroics [4]. BiFeO₃ stabilizes in a perovskite type rhombohedral crystal structure (space group *R3c*) at room temperature. Recently, it was reported to possess a huge spin-driven polarization ($\sim 3.0 \mu\text{C}/\text{cm}^2$) [5]. The ferroelectricity induced by spin ordering may have significant consequences for creating novel magento-electric phenomena in these materials. Fundamental to this response is the strong coupling between changes in octahedral distortions (resulting from magnetic ordering) and the off-centering of Bi cations which define the large polarization in these materials. These results, therefore, suggest that Bi-based perovskites may be a fruitful playground for discovering large spin-driven polarizations.

We have investigated the spin driven polarization in other Bi based 3d transition metal oxides using density functional theory (DFT) calculations. Figure 1 (a) depicts the DFT optimized atomic structure of BiCoO₃ with C-type antiferromagnetic (C-AFM) ordering and the corresponding density of states (DOS) are displayed in Fig.1 (b). Unlike BiFeO₃, BiCoO₃ stabilizes in the *P4mm*, tetragonal, crystal structure. BiCoO₃ has a super-tetragonal structure with a *c/a* ~ 1.27 , which is much larger than that of PbTiO₃ (*c/a*=1.06), suggesting that it should have a large spontaneous ferroelectric polarization (FE) along the [001] direction. Indeed, our DFT results predict that BiCoO₃ is insulating with a calculated total ferroelectric polarization of $\sim 158 \mu\text{C}/\text{cm}^2$ (close to the experimental value of $166.38 \mu\text{C}/\text{cm}^2$ at 300K). The computed atomic distortions for Bi and Co in C-AFM BiCoO₃ are 0.91590 Å and 0.61954 Å, respectively. The orbital hybridization between Bi-O and Co-O (resulting in anomalously large Born effective charges), and a Co³⁺ local magnetic moment play an important role in defining the ferroelectricity and the magnetism of anti-ferromagnetism, respectively. Surprisingly, we estimate that the

spin driven polarization in BiCoO₃ to be $\sim 2.59 \mu\text{C}/\text{cm}^2$, comparable to that of BiFeO₃, despite the absence of large octahedral tilts.

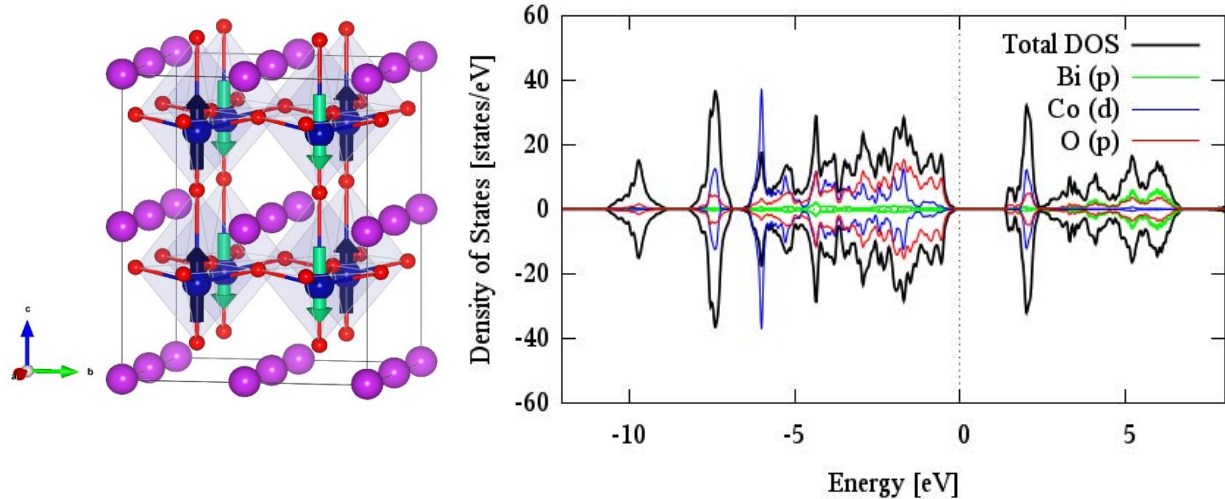


Figure 1 a) DFT optimized atomic structure of C-AFM BiCoO₃. The black and green arrows indicate up and down spin states, respectively. The purple, blue and red spheres represent Bi, Co and O atoms, respectively. (b) Spin resolved density of states (DOS) for C- AFM BiCoO₃ in the tetragonal ($P4mm$) crystal structure. The zero of the energy axis refers to Fermi-level.

To confirm the theoretical predictions, we have characterized BiCoO₃ using neutron diffraction between 600K and 300K. Preliminary neutron data confirms that BiCoO₃ has long range C-type antiferromagnetic ordering below the magnetic transition temperature ($T_N \sim 470$ K). Simultaneously, we observe a significant decrease in the atomic off-center displacements of the Bi and Co cations below the transition temperature. These results indicate a strong coupling between magnetic ordering and polarization and are consistent with our theoretical predictions.

Together, experiment and theory give us significant insights into the magneto-electric coupling in Bi-based perovskite materials which may lead to the design of novel materials in which magnetic and electric field control of polarization and magnetization may be achieved.

- [1] T. Kimura et. al; *Nature* 426, 55 (2003).
- [2] D. Sando et. al.; *Nature materials* 12, 641-646 (2013).
- [3] S. Neusser and D. Grundler; *Advanced Materials* 21, 2927-2932 (2009).
- [4] C. Weingart, N. Spaldin; E. Bousquet; *Physical Review B* 86, 094413 (2012).
- [5] J. H. Lee, and R. S. Fishman; *Physical Review Letters* 115 (20), 207203 (2015).

This research was supported by the US Department of Energy, Office of Science, Basic Energy Sciences, Materials Sciences and Engineering Division and the Office of Science Early Career Research Program and used computational resources at NERSC.

Complex magnetic incommensurability and electronic charge transfer through the ferroelectric transition in multiferroic Co_3TeO_6

Jeffrey W. Lynn,¹ Chi-Hung Lee,² Chin-Wei Wang,³ Yang Zhao,^{1,4} Wen-Hsien Li,^{2,*} A. Brooks Harris,⁵ Kirrily Rule,⁶ Hung-Duen Yang,⁷ and Helmuth Berger⁸

¹*NIST Center for Neutron Research, National Institute of Standards and Technology, Gaithersburg, Maryland 20899, USA*

²*Department of Physics, National Central University, Jhongli 32001, Taiwan*

³*Neutron Group, National Synchrotron Radiation Research Center, Hsinchu 30076, Taiwan*

⁴*Department of Materials Science and Engineering, University of Maryland, College Park, MD 20742 USA*

⁵*Department of Physics and Astronomy, University of Pennsylvania, Philadelphia, PA 19104 USA*

⁶*Bragg Institute, Australian Nuclear Science and Technology Organisation, Lucas Heights, NSW 2234, Australia*

⁷*Department of Physics and Center for Nanoscience and Nanotechnology, National Sun Yat-Sen University, Kaohsiung 80424, Taiwan*

⁸*Institute of Physics of Complex Matter, EPFL, Lausanne, Switzerland*

Many novel physical behaviors have recently been identified in the $M_3\text{TeO}_6$ -class of metal tellurates, where M is a first-row transition metal. Simple commensurate magnetic structures as well as complex incommensurate spin structures, and spontaneous and magnetic-field-driven electrical polarizations, have all been detected. In particular, the monoclinic cobalt tellurate Co_3TeO_6 has been characterized as a type-II multiferroic, where the order parameters of electrical polarization and spontaneous magnetization are closely coupled.[1-4, and references therein] We have carried out polarized and unpolarized neutron diffraction measurements to investigate the nature of the magnetic structures and transitions in monoclinic Co_3TeO_6 . [5] As the temperature is lowered below $T_{M1} = 26$ K long range magnetic order develops, which is fully incommensurate in all three crystallographic directions in the crystal. In particular, no commensurate magnetic order is observed. Below $T_{M2} = 19.5$ K additional, commensurate, magnetic peaks develop, consistent with the Γ_4 irreducible representation. In addition, a splitting of the incommensurate peaks along the h direction develops, which indicates that there are two separate sets of magnetic modulation vectors. Below $T_{M3} = 18$ K, this small additional magnetic incommensurability disappears, ferroelectricity develops with is strongly magnetic field dependent, an additional commensurate Γ_3 irreducible representation appears, and the k component of the incommensurate wave vector

disappears. Synchrotron x-ray diffraction measurements demonstrate that there is a significant shift of the electronic charge distribution from the Te ions at the crystallographic $8f$ sites to the neighboring Co and O ions in this temperature regime. These results, together with the unusually small electric polarization, its strong magnetic field dependence, and the negative thermal expansion in all three lattice parameters, suggest this material is basically an antiferroelectric. Below $T_{M4} = 15$ K the k component of the incommensurate structure reappears, along with second-order incommensurate Bragg peaks. Polarized neutron diffraction data demonstrate that both the first-order and second-order peaks are magnetic in origin. The existence of these new second-order peaks indicates that a small canting of the magnetic structure has occurred that allows a net magnetization to develop. This observation is consistent with the data of Toledano, *et al.*[6] and Singh, *et al.*,[7] and appears similar to what has been found in $\text{ErNi}_2\text{B}_2\text{C}$,[8] for example. Finally, searches were performed for commensurate peaks of the form $(0, 1/2, 1/4)$ as was inferred from powder diffraction data of Ivanov, *et al.* No evidence of such peaks was found, indicating that these peaks are not present in Co_3TeO_6 .

- [1] J. L. Her, C.-C. Chou, Y. H. Matsuda, K. Kindo, H. Berger, K. F. Tseng, C.-W. Wang, W.-H. Li, and H.-D. Yang, *Phys. Rev. B.* **84** 235123 (2011).
- [2] W.-H. Li, C.-W. Wang, D. Hsu, C.-H. Lee, C.-M. Wu, C.-C. Chou, H.-D. Yang, Y. Zhao, S. Chang, J. W. Lynn, and H. Berger, *Phys. Rev. B.* **85** 094431(2012).
- [3] A. B. Harris, *Phys. Rev. B.* **85** 100403(R) (2011).
- [4] C.-W. Wang, C.-H. Lee, C.-Y. Li, C.-M. Wu, W.-H. Li, C.-C. Chou, H.-D. Yang, J. W. Lynn, Q. Huang, A. B. Harris, and H. Berger, *Phys. Rev. B* **88**, 184427 (2013).
- [5] Chi-Hung Lee, Chin-Wei Wang, Yang Zhao, Wen-Hsien Li, Jeffrey W. Lynn, A. Brooks Harris, Kirrily Rule, Hung-Duen Yang, and Helmuth Berger (submitted for publication).
- [6] P. Tolédano, V. Carolus, M. Hudl, T. Lottermoser, D. D. Khalyavin, S. A. Ivanov, and M. Fiebig, *Phys. Rev. B* **85**, 214439 (2012).
- [7] H. Singh, H. Ghosh, T. V. C. Rao, G. Sharma, J. Saha, and S. Patnaik, *J. Appl. Phys.* **119**, 044104 (2016).
- [8] S.-M. Choi, J. W. Lynn, D. Lopez, P. L. Gammel, P. C. Canfield, and S. L. Bud'ko, *Phys. Rev. Lett.* **87**, 107001 (2001).

Atomic Scale Engineering of Multiferroicity in $\text{LuFeO}_3/\text{LuFe}_2\text{O}_4$ Superlattices

Julia A. Mundy¹, Charles M. Brooks², Megan E. Holtz¹, Jarrett A. Moyer³, Hena Das¹, Alejandro F. Rébola¹, John T. Heron^{2,4}, James D. Clarkson⁵, **Steven M. Disseler**⁶, Zhiqi Liu⁵, Alan Farhan⁷, Rainer Held², Robert Hovden¹, Elliot Padgett¹, Qingyun Mao¹, Hanjong Paik², Rajiv Misra⁸, Lena F. Kourkoutis^{1,9}, Elke Arenholz⁷, Andreas Scholl⁷, Julie A. Borchers⁶, William D. Ratcliff⁶, Ramamoorthy Ramesh^{5,10,11}, Craig J. Fennie¹, Peter Schiffer³, David A. Muller^{1,9} & Darrell G. Schlom^{2,9}

1. School of Applied and Engineering Physics, Cornell University, Ithaca, New York 14853, USA.
2. Department of Materials Science and Engineering, Cornell University, Ithaca, New York 14853, USA.
3. Department of Physics and Frederick Seitz Materials Research Laboratory, University of Illinois at Urbana-Champaign, Urbana, Illinois 61801, USA.
4. Department of Materials Science and Engineering, University of Michigan, Ann Arbor, Michigan 48103, USA.
5. Department of Materials Science and Engineering, University of California, Berkeley, California 94720, USA.
6. NIST Center for Neutron Research, National Institute of Standards and Technology, Gaithersburg, Maryland 20899, USA.
7. Advanced Light Source, Lawrence Berkeley National Laboratory, Berkeley, California 94720, USA.
8. Department of Physics, Pennsylvania State University, University Park, Pennsylvania 16802, USA.
9. Kavli Institute at Cornell for Nanoscale Science, Ithaca, New York 14853, USA.
10. Department of Physics, University of California, Berkeley, California 94720, USA.
11. Materials Sciences Division, Lawrence Berkeley National Laboratory, California 94720, USA.

The end goal of almost any multiferroic system is the simultaneous control of both ferromagnetic and ferroelectric moments by their respective conjugate field. However, despite years of investigations, nature has demonstrated few opportunities for these two effects to coexist in the same material, thus engineering artificial multiferroics using heterostructuring at the atomic scale is rapidly becoming an attractive alternative. In this work, we have combined two crystallographically similar but poor multiferroic materials on their own to engineer new family of ferromagnetic multiferroic heterostructure [1].

These heterostructures are based on the family of hexagonal compounds RMO_3 which have been known multiferroics since their discovery in early 1960's. In these materials, the ferroelectric moment results from a structural transition, typically above 700 K, in which the R and O ions displace along the c -axis by disproportionate amounts leading to a net charge displacement. The magnetic transition metal M sites form a triangular lattice in the plane, with superexchange interactions leading to antiferromagnetic ordering only below 150 K [2]. Thus, despite exhibiting both magnetism and ferroelectricity at low temperatures, the two orders are only weakly linked and this material is not expected to be a useful multiferroic near room temperature [3].

On the other hand, LuFe_2O_4 is a hexagonal material with similar lattice constants to the high temperatures phase of the RMO_3 compounds, but ferrimagnetically orders below 240 K and does not undergo any inversion-symmetry breaking structural transitions. In fact, both LuFe_2O_4 and LuFeO_3 structures may be envisioned as simply alternating planes of Fe-O (A) and Lu-O (B) layers, with LuFeO_3 defined by the pattern ABAB..., LuFe_2O_4

and AABAABAAB. Thus, using epitaxial or syntactic growth of individual Fe-O and Lu-O layers we can effectively interpolate between the two compounds. To do so, we have used oxide molecular beam epitaxy which allows precise control of atomically sharp interfaces over large scales, as shown in Figure 1.

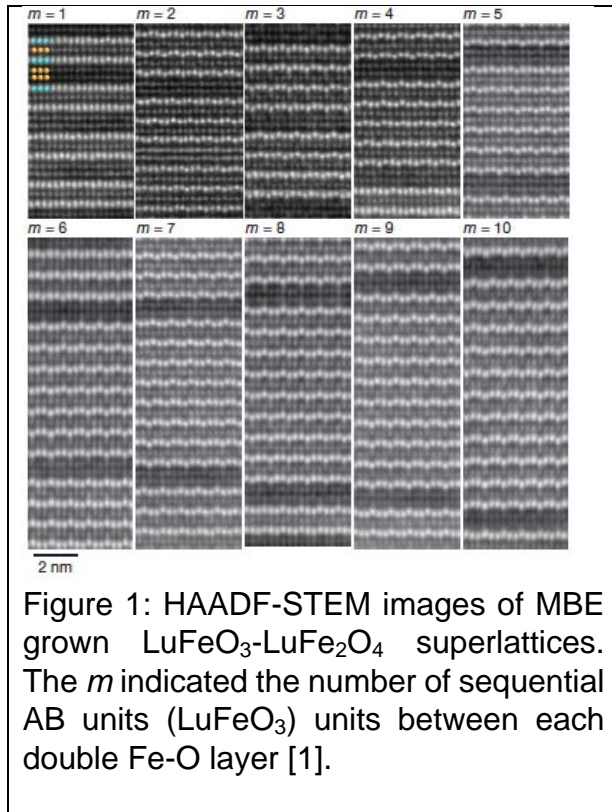


Figure 1: HAADF-STEM images of MBE grown LuFeO_3 - LuFe_2O_4 superlattices. The m indicated the number of sequential AB units (LuFeO_3) units between each double Fe-O layer [1].

Interestingly, we find that introducing more LuFeO_3 lead to an increase in the ferromagnetic ordering temperature of the LuFe_2O_4 -like layers, from 220 K to nearly room temperature uniformly as a function of m . Furthermore, we find that by maximizing T_c , both the robustness of the ferroelectric state and magnetoelectric coupling of the ferromagnetic and ferroelectric moments are also dramatically enhanced.

In this talk I will discuss the development of these superlattice materials, the detailed investigation and discovery of this unexpected result, and the underlying mechanism by which this ferromagnetic enhancement and magnetoelectric coupling occurs. Lastly, I will discuss how this same tuning mechanism be used in other systems to explore new avenues of artificial materials and multiferroics in particular.

[1] J. Mundy, et. al., “Atomically engineered ferroic layers yield a roomtemperature magnetoelectric multiferroic”, *Nature* 537 523 (2016)

[2] S. Disseler, et. al.,” Magnetic Structure and Ordering of Multiferroic Hexagonal LuFeO_3 ”, *Phys. Rev. Lett.* 114, 217602 (2015)

[3] S. Disseler, et. al., “Multiferroicity in doped hexagonal LuFeO_3 ”, *Phys. Rev. B* 92, 054435 (2015).

Intrinsic polarization switching mechanisms in BiFeO₃

Bin Xu¹, Vincent Garcia², Stéphane Fusil², Manuel Bibes², and L. Bellaïche¹

¹Physics Department and Institute for Nanoscience and Engineering, University of Arkansas, Fayetteville, Arkansas 72701, USA

²Unité Mixte de Physique, CNRS, Thales, Univ. Paris-Sud, Université Paris-Saclay, 91767, Palaiseau, France

Polarization switching under an applied electric field in ferroelectric (FE) materials has been intensively studied over many decades, and generates continuous interests for both fundamental understanding and emerging technological devices [1–3]. Different types of switching mechanisms have been observed in experiments, which resulted in the development of several models to explain them. For instance, the classic Kolmogorov-Avrami-Ishibashi (KAI) model [4–6] was proposed to explain the switching occurring in some ferroelectrics through the process of nucleation of reversed domains and domain-wall motion with constant speed – that is schematized in Fig. 1a. However, inhomogeneous switching behavior with limited propagation of domains was also found in Pb(Zr,Ti)O₃ (PZT) [7–11] and BiFeO₃ (BFO) [12] thin films, which is represented in Fig. 1b. Such behavior is well described by the nucleation-limited-switching (NLS) model that is based on independent switching dynamics in different areas of the film with limited propagation. Moreover, homogeneous switching (which is schematized in Fig. 1c), i.e., continuous switching without nucleation of domains, was also realized in ferroelectric films being ultrathin (7 nm or less), where extremely large electric field can be achieved [13–16].

To the best of our knowledge, only a few atomistic simulations have been performed to investigate polarization dynamics in ferroelectrics [17–20]; as a result, several questions remain elusive. For instance, does nucleation-based switching naturally involve extrinsic effects (e.g., defects, pre-existing domains, interfaces with electrodes, etc.) or rather can it also intrinsically occur in defect-free materials? In case they do occur in compounds with no defects, are the KAI and NLS models still applicable to describe them? One may also wonder if the same system can exhibit the three different kinds of switching shown in Fig. 1, depending on the magnitude of the applied electric field, and what physical quantity governs this hypothetical field-induced change of switching mechanism. It is also of interest to determine if different structural phases of the same compound can exhibit different switching mechanisms, and, if it is the case, why it is so.

Here we aim to shed light on these open questions by using a first-principle-based atomistic technique to study defect-free systems made of the most well-known room-temperature multiferroic compound, that is BiFeO₃. Two phases are investigated, that are the rhombohedral *R3c* (R) and the super-tetragonal *P4mm* (T) phases. Remarkably, without defects or pre-existing domains, the switching mechanism in the T phase

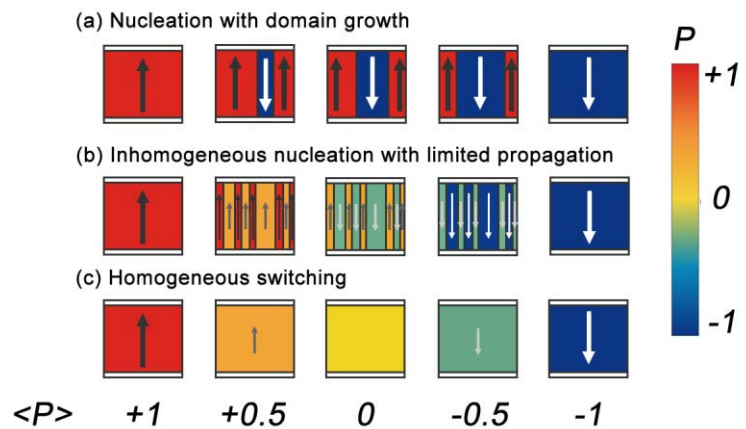


Figure 1. Schematic illustration of three different switching mechanisms: (a) nucleation followed by domain growth (NDG); (b) nucleation limited switching (NLS); and (c) homogeneous switching (HS). The arrows of different sizes and directions indicate the magnitude and direction of the polarization during switching. Domains of different polarization are illustrated by different colors. The numbers at the bottom denote the average (normalized) polarization.

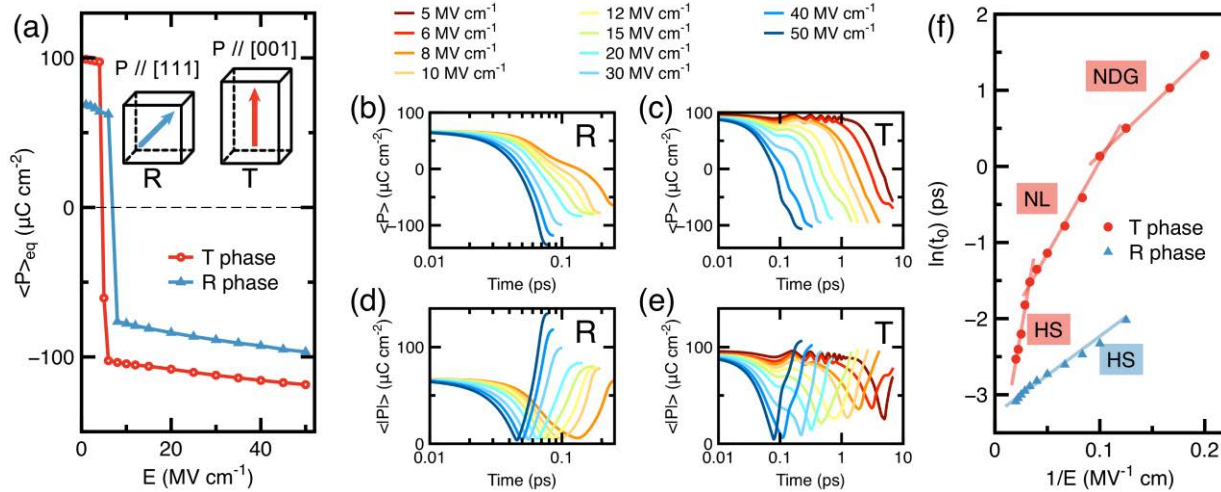


Figure 2. Properties related to the switching of the polarization. (a) Polarization as a function of electric field after equilibrium is reached. (b-e) Time dependence of properties related to electric dipoles during switching under various electric fields. (b,c) Polarization projected along the direction of the applied E-field. (d,e) Supercell average of the magnitude of the local electric dipoles. (f) Logarithm of the zero-crossing characteristic time as a function of the inverse of the electric field magnitude. Discrete points are calculated MD data, and lines are linear fits to the Merz's Law. For the R phase, the initial polarization is along the [111] direction and E is applied along the [-1-1-1] direction. For the T phase, the initial polarization is along the [001] direction and E is applied along the [00 -1] direction.

is found to change with increasing the applied electric field, starting from the nucleation and growth of domains, followed by nucleation-limited switching, to end with homogeneous switching, with the first two steps being well described by the KAI and NLS models, respectively. The reason for the existence of these three different mechanisms within the T phase of BFO, depending on the magnitude of the electric field, is also revealed. Moreover and in contrast to the T phase, the R phase of BFO is found to exhibit a single switching mechanism, that is of homogeneous type. The microscopic origin of such difference between the R and T phases is also provided.

Acknowledgements This work is financially supported by the Department of Energy, Office of Basic Energy Sciences, under contract ER-46612, and Air Force Office of Scientific Research under Grant FA9550-16-1-0065. Financial support from the French Agence Nationale de la Recherche (ANR) through project FERROMON is acknowledged.

References

- [1] J. Scott, *Ferroelectric memories* Vol. 3 (Springer, 2000)
- [2] M. Dawber, *et al. Rev. Mod. Phys.* **77**, 1083 (2005)
- [3] V. Garcia, *et al. Nature* **460**, 81 (2009)
- [4] A. Kolmogorov, *Izv. Akad. Nauk* **1**, 355 (1937)
- [5] M. Avrami, *J. Chem. Phys.* **8**, 212 (1940)
- [6] Y. Ishibashi, *et al. J. Phys. Soc. Jpn.* **31**, 506 (1971)
- [7] O. Lohse, *et al. J. Appl. Phys.* **89**, 2332 (2001)
- [8] A. Tagantsev, *et al. Phys. Rev. B* **66**, 214109 (2002)
- [9] A. Gruverman, *et al. Appl. Phys. Lett.* **87**, 082902 (2005)
- [10] J. Jo, *et al. Phys. Rev. Lett.* **99**, 267602 (2007)
- [11] D. Kim, *et al. Appl. Phys. Lett.* **91**, 132903 (2007)
- [12] S. Boyn, *et al.* (submitted)
- [13] S. Ducharme, *et al. Phys. Rev. Lett.* **84**, 175 (2000)
- [14] J. Jo, *et al. Phys. Rev. Lett.* **97**, 247602 (2006)
- [15] M. Highland, *et al. Phys. Rev. Lett.* **105**, 167601 (2010)
- [16] R. Gaynutdinov, *et al. Physica B* **424**, 8 (2013)
- [17] Y. Shin, *et al. Nature* **449**, 881 (2007)
- [18] S. Liu, *et al. Appl. Phys. Lett.* **103**, 232907 (2013)
- [19] R. Xu, *et al. Nat. Mater.* **14**, 79 (2015)
- [20] S. Liu, *et al. Nature* **534**, 360 (2016)

**Emergence of coupled surface electrochemistry-bulk ferroelectricity state on the nanoscale
--- a combined study of thermodynamics, phase-field and experimental demonstration**

Ye Cao¹, Anna N. Morozovska², Sang Mo Yang³ and Sergei V. Kalinin¹

¹Center for Nanophase Materials Sciences, Oak Ridge National Laboratory,
Oak Ridge, TN 37831, USA

²Institute of Physics, National Academy of Sciences of Ukraine,
46, pr. Nauky, 03028 Kyiv, Ukraine

³Department of Physics, Sookmyung Women's University,
Seoul 04310, Korea

Email: caoy@ornl.gov

Ferroelectricity on the nanoscale has remained a subject of much fascination in physics, chemistry and materials sciences for over half a century. From the applied perspective, this interest is driven by devices ranging from ferroelectric random access memories and ferroelectric gate transistors to ferroelectric tunnel junctions. From fundamental science perspective, this area is linked to basic science of polar and structural distortions driven by depolarization fields, and also overlaps with more general field of polar oxide surfaces. It has been well accepted that polarization discontinuities at surfaces and interfaces create depolarization fields that destabilize ferroelectric polarization and thus necessitate efficient polarization screening. Therefore screening mechanism and screening charge dynamics become strongly coupled to ferroelectric phase stability and domain behavior. Realization of this fact stimulated extensive studies on the screening mechanisms including metal electrodes, band bending (i.e., screening by internal carriers) and external ionic charges.

However, ferroelectric surface still remains largely unknown. From theoretical perspective, the electrostatic and polarization boundary conditions are ill-defined, necessitating *ad hoc* use of fully-screened (fixed potential) or fully-open boundary conditions. For example, while phase-field simulation has been successfully applied to study the domain structure and switching behavior in ferroelectric thin film under physical boundary conditions (BCs) of fixed potential or charge, these BCs are generally not applicable to free ferroelectric surfaces. From experimental viewpoint, more uncertainty exists. The emergence of piezoresponse force microscopy (PFM) has offered a powerful tool for exploring local piezo- and ferroelectric phenomena via detection of electromechanical responses at surfaces. In the last decade a large amount of work claiming ferroelectricity in ultrathin film were made based on the observation of long-lived polar state, remnant polarization, local hysteresis loops and pressure induced mechanical switching. However, similar phenomena were reported for traditionally non-ferroelectric materials, creating significant level of uncertainty in the field.

Here I show that on the nanoscale the bulk ferroelectric state is fundamentally inseparable from the surface electrochemical state, resulting in the emergence of a mixed electrochemical-ferroelectric state. I will first present the theoretical framework and approaches to this emergent

mixed states based on fundamental thermodynamics theory and phase-field simulation with chemical boundary conditions. I will then discuss the temperature, thickness and oxygen partial pressure dependence of this mixed state from thermodynamic calculation, and illustrate the oxygen partial pressure induced switching process in single domain case and polarization rotation behaviors in multi-domain structure via phase-field approaches. Finally I will demonstrate the experimental pathway to establish the presence of this mixed state based on spectroscopic version of piezoresponse force microscopy and contact Kelvin probe force microscopy (cKPFM). This analysis reconciles multiple prior studies, and set forward the predictive pathways for new generations of ferroelectric devices and applications.

This research was sponsored by the Division of Materials Sciences and Engineering, BES, DOE, and was conducted at the Center for Nanophase Materials Sciences, sponsored at Oak Ridge National Laboratory by the Scientific User Facilities Division.

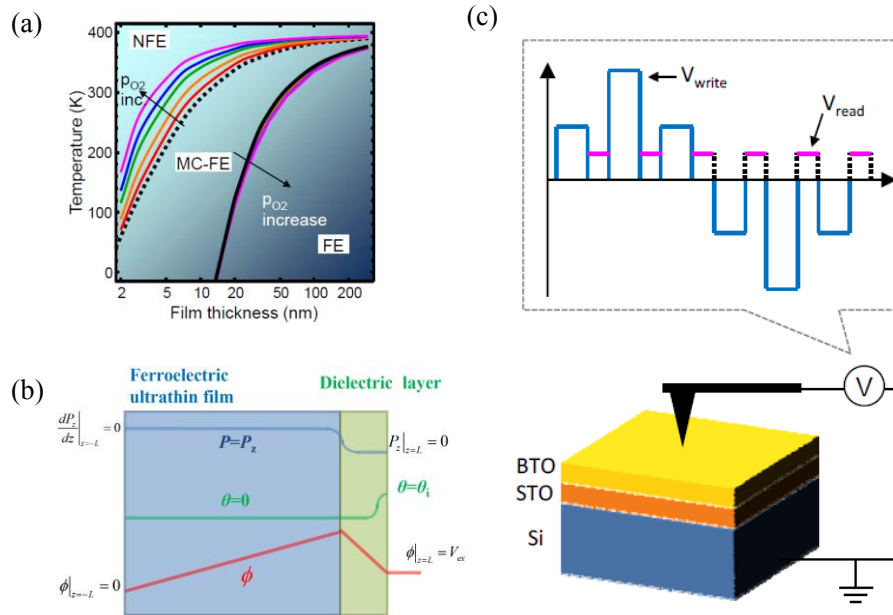


Figure 1, Study of mixed electrochemical-ferroelectric state (MC-FE) based on combined thermodynamics, phase-field and experimental demonstration. (a) Temperature-thickness phase diagram of different ferroelectric states from thermodynamic calculation, (b) Phase-field model of a (001) ferroelectric ultrathin film topped with surface dielectric layer with chemical boundary conditions, (c) A schematic of cKPFM measurements of BaTiO₃ (BTO) thin film.

References:

- [1] Sang Mo Yang, Anna N. Morozovska, Rajeev Kumar, Eugene A. Eliseev, Ye Cao, Lucie Mazet, Nina Balke, Stephen Jesse, Rama K. Vasudevan, Catherine Dubourdieu, Sergei V. Kalinin. "Mixed electrochemical-ferroelectric states in nanoscale ferroelectrics" (unpublished)
- [2] Ye Cao and Sergei V. Kalinin "Phase-field modeling of chemical control of polarization stability and switching dynamics in ferroelectric thin film", accepted by Physical Review B

Persistence of strong and switchable ferroelectricity despite vacancies

Aldo Raeliarijaona and Huaxiang Fu

Department of Physics, University of Arkansas, Fayetteville, Arkansas 72701, USA

Vacancies in ferroelectrics (FE), one key class of native defects, are of considerable importance both fundamentally and technologically.¹⁻³ Fundamentally, vacancies disrupt the interaction among atoms on the microscopic scale, and break the delicate balance^{4,5} between long-range and short-range interactions in FEs. Therefore, vacancies can profoundly affect the superior properties that have been found in FEs such as high electromechanical response,⁶⁻⁸ polarization enhancement in superlattices,⁹ large dielectric coefficient,^{10,11} strong improper ferroelectricity,¹²⁻¹⁵ and unusual phase transition.¹⁶⁻¹⁸ Technologically, vacancies in FEs have been linked to fatigue;¹⁹⁻²¹ they also lead to pinning of polarization near domain wall,²² reduction of polarization magnitude, and increase of coercive field^{3,23}. Consequently, vacancies hamper the vital applications of FEs in ferroelectric memories and piezoelectric devices.²⁴⁻²⁶

On the other hand, vacancies can be beneficial. In fact, vacancies are pivotal in polarization switching by acting as the nucleation centers of antiphase domains,^{27,28} as described in the Kolomogorov-Avrami model^{29,30} of polarization reversal. In ferroelectric tunnel junctions, the control of polarization switching in terms of nucleation and domain growth is instrumental in the realization of FE memristors.³¹ A $V_{\text{Pb}}-V_{\text{O}}$ di-vacancy complex was shown to enhance the local dipole moment in PbTiO_3 .³² Vacancies were also demonstrated to induce a large electromechanical response in aged BaTiO_3 crystals³³ and broaden the dielectric peaks in disordered FEs³⁴.

There are reasons that vacancies are detrimental to the polarization in FEs. It is known that Ti $3d$ and O $2p$ hybridization is important for ferroelectric instability.^{4,5,35} The Ti-O chains (or the B-O chains in general) are critical in the formation of ferroelectricity. Creation of Ti or O vacancies disrupts the Ti-O chains, thereby affecting the polarization properties. Furthermore, since polarization switching depends on the local structure and local interaction near defects, existence of vacancies drastically alters the chemical bonding in the neighborhood of the vacancy sites and is thus expected to impact the polarization switching.

However, the profound effects of vacancies (and broken Ti-O chains) on polarization have not been confirmed, and a different conclusion may utterly alter the current knowledge on defect physics in FEs. The lack of confirmation is due to the fact that there are outstanding problems that prevent us from obtaining a microscopic understanding on how vacancies *quantitatively* change the polarization and polarization-related properties. First, the stable state of a vacancy is often charged, and indeed, the most stable O vacancy in PbTiO_3 is the positively charged V_{O}^{2+} . Here we use the notation V_{X}^q to denote

a vacancy of species X carrying an amount of charge q . For charged vacancies in a periodic solid, a fundamental question arises, that is, whether polarization is well-defined and physically meaningful. Second, when vacancy is present, there is a possibility that the system could be metallic due to defect states, in which conducting electrons may screen the polarization if there is any. It thus remains unclear whether it is possible to quantitatively determine the magnitude of polarization when vacancies occur in FEs. As a consequence of these standing problems, an accurate understanding of the influence of vacancies, which goes beyond the qualitative argument based on the Ti-O chains, is lacking. This hampers the important effort toward the design of FEs by controlling vacancies.

Another subject of equal importance is the mechanism of polarization switching. Among various models²⁷⁻³⁰ that describe polarization switching in FEs, a consensus is that the switching is initiated by nucleation of an antiphase domain. However, little is understood on how the antiphase domain forms in the first place. In other words, the knowledge—of how the polarization is reversed *in the neighborhood of the defects* to form an antiphase domain at the key stage of nucleation—is microscopically unknown. In studies of ideal FEs without defects, polarization reversal is realized¹ by shifting the atoms from one of the degenerate potential wells, say the state with $\mathbf{P} > 0$, going through the centrosymmetric configuration, and ending at the enantiomorphic state with $\mathbf{P} < 0$. This, to our knowledge, is the only approach employed in studying the energetics of polarization switching. However, when vacancies emerge, the approach may not apply since it does not take vacancies into consideration. Because nucleation often occurs near vacancies, we thus need to account for the presence of vacancies in the process of polarization switching. Specifically we must consider how polarization is switched in the immediate neighborhood of the vacancies, which is in fact the important mechanism for nucleation. Nevertheless, with charged vacancies, it is unclear whether polarization is well defined, and it is even less clear by what mechanism the polarization is switched.

Here we perform first-principles studies to investigate the influence of vacancies on ferroelectric polarization and polarization switching in prototypical BaTiO_3 of tetragonal symmetry. We demonstrate using the modern theory of polarization^{36,37} that, in contrast to common wisdom, defective BaTiO_3 with a large concentration of vacancies V_{O}^{2+} (or V_{Ti}^{4-} , or V_{Ba}^{2-}) possesses a strong nonzero electric polarization. Breaking of Ti-O bonds is found to have relatively little effect on the magnitude of polarization, which is rather striking. Furthermore, a

previously unrecognized microscopic mechanism, which is particularly important when vacancies are present, is proposed for polarization switching. The mechanism immediately reveals that (i) the switching barrier in the presence of V_O^{2+} is small with $\Delta E=8.3$ meV per bulk formula cell, and the polarization is thus switchable even when vacancies exist; (ii) The local environment of vacancy is surprisingly insignificant in polarization switch-

ing. These results provide new knowledge and will stimulate more theoretical and experimental interest on defect physics in FEs. Concurrently, these studies suggest that there are rich and interesting physics to be learnt when vacancy and ferroelectricity coexist.

This work was supported by the Office of Naval Research.

-
- ¹ Lines, M. E. & Glass, A. M. *Principles and applications of ferroelectrics and related materials* (Clarendon Press, Oxford, 1977).
- ² Dawber, M., Rabe, K. M. & Scott, J. F. Physics of thin-film ferroelectric oxides. *Rev. Mod. Phys.* **77**, 1083-1130 (2005).
- ³ Scott, J. F. & Dawber, M. *Appl. Phys. Lett.* **76**, 3801-3803 (2000).
- ⁴ Cohen, R. E. *Nature (London)* **358**, 136-138 (1992).
- ⁵ Cohen, R. E. & Krakauer, H. *Phys. Rev. B* **42**, 6416-6423 (1990).
- ⁶ Park, S.-E. & Shrout, T. R. *J. Appl. Phys.* **82**, 1804-1811 (1997).
- ⁷ Fu, H. & Cohen, R. E. *Nature (London)* **403**, 281-283 (2000).
- ⁸ Iniguez, J. & Bellaiche, L. *Phys. Rev. Lett.* **87**, 095503 (2001).
- ⁹ Neaton, J. B. & Rabe, K. M. *Appl. Phys. Lett.* **82**, 1586 (2003).
- ¹⁰ George, A. M., Iniguez, J. & Bellaiche, L. *Nature (London)* **413**, 54-57 (2001).
- ¹¹ Choi, Y.-K., Hoshina, T., Takeda, H., Teranishi, T. & Tsurumi, T. *Appl. Phys. Lett.* **97**, 212907 (2010).
- ¹² Fennie, C. J. & Rabe, K. M. *Phys. Rev. B* **72**, 100103(R) (2005).
- ¹³ Bousquet, E. *et al. Nature (London)* **452**, 732-736 (2008).
- ¹⁴ Benedek, N.A. & Fennie, C.J. *Phys. Rev. Lett.* **106**, 107204 (2011).
- ¹⁵ Benedek, N. A. *Inorg. Chem.* **53**, 3769-3777 (2014).
- ¹⁶ Naumov, I. I., Bellaiche, L. & Fu, H. *Nature (London)* **432**, 737-740 (2004);
- ¹⁷ Naumov, I. & Fu, H. *Phys. Rev. Lett.* **98**, 077603 (2007);
- ¹⁸ Fu, X., Naumov, I. I. & Fu, H. *Nano. Lett.* **13**, 491-496 (2013).
- ¹⁹ Brazier, M., Mansour, S. & McElfresh, M. *Appl. Phys. Lett.* **74**, 4032-4034 (1999).
- ²⁰ Pöykkö, S. & Chadi, D. J. *Phys. Rev. Lett.* **83**, 1231-1234 (1999).
- ²¹ Yang, F. *et al. Appl. Phys. Lett.* **92**, 022908 (2008).
- ²² He, L. & Vanderbilt, D. *Phys. Rev. B* **68**, 134103 (2003).
- ²³ Zhang, Y., Li, J. & Fang, D. *Phys. Rev. B* **82**, 064103 (2010).
- ²⁴ Scott, J. F. *Ferroelectric memories* (Springer, Berlin, 2000).
- ²⁵ Uchino, K. *Piezoelectric Actuators and Ultrasonic Motors* (Kluwer Academic, Boston, 1996).
- ²⁶ Scott, J. F. *Science* **315**, 954-959 (2007).
- ²⁷ S. Jesse *et al. Nat. Mater.* **7**, 209-215 (2008).
- ²⁸ S. V. Kalinin *et al. Phys. Rev. Lett.* **100**, 155703 (2008).
- ²⁹ Avrami, M. *J. Chem. Phys.* **8**, 212-224 (1940).
- ³⁰ Orihara, H., Hashimoto, S. & Ishibashi, Y. *J. Phys. Soc. Jpn.* **63**, 1031-1035 (1994).
- ³¹ Chanthbouala, A. *et al. Nat. Mater.* **11**, 860-864 (2012).
- ³² Cockayne, E. & Burton, B. P. *Phys. Rev. B* **69**, 144116 (2004).
- ³³ Ren, X. *Nat. Mater.* **3**, 91-94 (2004).
- ³⁴ Bellaiche, L., Iniguez, J., Cockayne, E. & Burton, B. *Phys. Rev. B* **75**, 014111 (2007).
- ³⁵ Ghosez, P., Gonze, X. & Michenaud, J.-P. *Ferroelectrics* **206**, 205-217 (1998).
- ³⁶ King-Smith, R.D. and Vanderbilt, D. *Phys. Rev. B* **47**, 1651-1654 (1993).
- ³⁷ Resta, R. *Rev. Mod. Phys.* **66**, 899-915 (1994).

Structural and Magnetic Depth Profiles of Magneto-Ionic Heterostructures Beyond the Interface Limit

Dustin A. Gilbert,^{1*} Alexander J. Grutter,^{1*} Elke Arenholz,² Kai Liu,³ B. J. Kirby,¹

Julie A. Borchers,¹ Brian B. Maranville¹

¹NIST Center for Neutron Research, National Institute of Standards and Technology, Gaithersburg, MD 20899

²Advanced Light Source, Lawrence Berkeley National Laboratory, Berkeley, CA 94720, USA

³Physics Department, University of California, Davis, CA 95616, USA

*These authors contributed equally to this work

email: dustin.gilbert@nist.gov

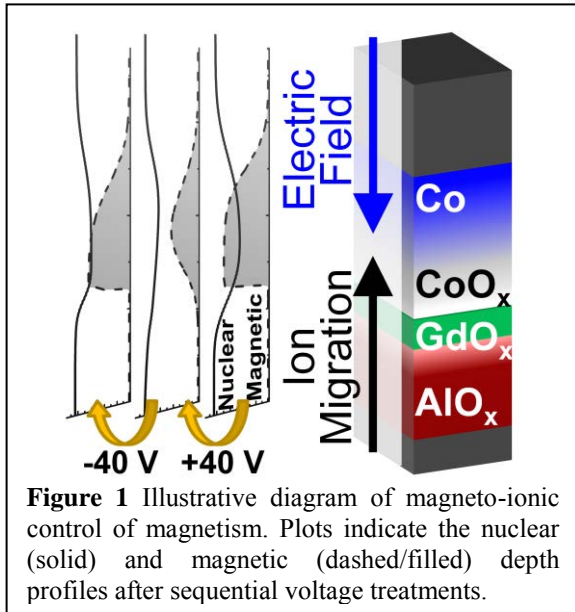
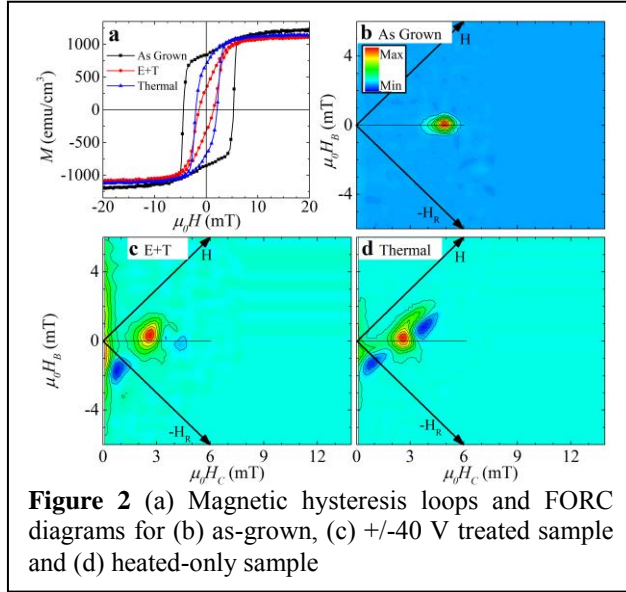


Figure 1 Illustrative diagram of magneto-ionic control of magnetism. Plots indicate the nuclear (solid) and magnetic (dashed/filled) depth profiles after sequential voltage treatments.

Electric-field control of magnetism provides a promising route towards ultralow power information storage and sensor technologies. The foundational works on magneto-ionics [1,2] have demonstrated control of perpendicular magnetic anisotropy in bilayer films for potential non-volatile data storage technologies. In these works, a bilayer film is prepared with an ultra-thin Co (9 Å) layer which is on the cusp of having a perpendicular easy axis, adjacent to an oxide film (GdO_x). Using an electric field, oxygen is migrated from the oxide into the Co/GdO_x interface. This modifies the perpendicular magnetic anisotropy, changing the preferred magnetic orientation, and allowing data to be stored in the magnetic configuration controlled by electric fields.

Building on these works, we investigate voltage-driven oxygen migration beyond the interface in relatively thick AlO_x/GdO_x/Co(15 nm) films.[3] Unlike the ultra-thin films discussed above, these films show predominantly bulk-like properties, including a traditional in-plane magnetic easy axis, reflective optical surfaces, and are expected to have bulk-like electrical and thermal properties. However, these bulk films present new challenges to magneto-ionic control, including enhanced Faraday screening and longer-range ion migration.

Using polarized neutron reflectometry (PNR) the magnetic and structural depth profiles were directly mapped (Fig. 1). PNR has the unique and powerful ability to non-destructively map the ionic migration (observed in the nuclear scattering), and its non-monotonic impact on the magnetism inside of the material. The fitted profiles show that after an initial voltage treatment at +40 V at 230° C for 15 minutes, there is a broadening of the nuclear interface and enhancement of the nuclear scattering within the Co film. Commensurate with this enhancement is a suppression of the magnetic scattering, especially at the interface. Overall, we observe a 60% reduction in the magnetism within the film, located predominantly at the GdO_x/Co interface. Reversing the voltage polarity partly recovered the nuclear profile, and the magnetism recovered to 90% of its initial value.

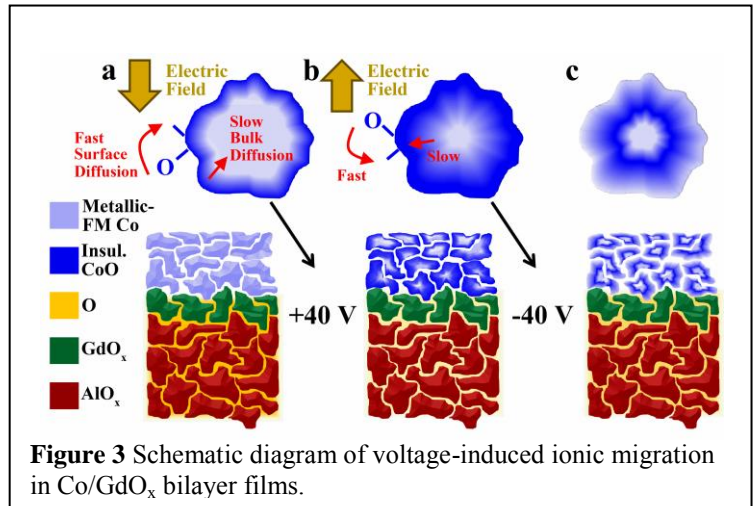


Magnetic hysteresis loops confirm a partial recovery of the saturation magnetization, but interestingly the other magnetic qualities remain significantly impacted (Fig. 2). In-particular, the magnetic remanence and major-loop coercivity is suppressed by 70% and 55%, respectively. This implies a change in the reversal mechanism, which is investigated using the first order reversal curve (FORC) technique.[4] The FORC diagrams show that after the sequential +/-40V treatment the sample consists of two magnetic phases, while the as-grown sample has only a single phase.[5] This suggests that, while the migration is largely reversible, the remaining oxygen is distributed in such a way as to

disrupt long-range correlation.

Element specific x-ray absorption spectroscopy and circular dichroism (XAS, XMCD) measurements confirm oxidation of the Co, and suppression of its magnetization. Interestingly, XAS showed that the Gd did not change its oxidation state, indicating the heating and electric field treatment is not inducing oxide breakdown.

Considering these results together, we develop a model which explains our observations, Figure 3. In this model, oxygen originates from off-stoichiometry grain surfaces and boundaries. Upon application of an electric field, the oxygen migrates into the Co layer, moving quickly along the grain surfaces, and diffusing slowly into the bulk. Reversing the electric field quickly de-populates the grain surfaces, recovering its metallic properties. Once the surface is metallic it screens the electric field, leaving the remaining oxygen trapped within the grain, resulting in the observed two phases. This work provides the first insight into control of bulk-like magnetic properties with an electric field, and presents new opportunities for ultra-low power, magnetic devices and technologies



References

- [1] U. Bauer, L. Yao, A. J. Tan *et al.*, Nature Mater. **14**, 174 (2015).
- [2] C. Bi, Y. Liu, T. Newhouse-Illige *et al.*, Phys. Rev. Lett. **113**, 267202 (2014).
- [3] D. A. Gilbert, A. J. Grutter, E. Arenholz *et al.*, Nature Commun. **7**, 12264 (2016).
- [4] D. A. Gilbert, G. T. Zimanyi, R. K. Dumas *et al.*, Sci. Rep. **4**, 4204 (2014).
- [5] D. A. Gilbert, J.-W. Liao, L.-W. Wang *et al.*, APL Mater. **2**, 086106 (2014).

Switching Dynamics and Mechanisms in Morphotropic $\text{PbZr}_x\text{Ti}_{1-x}\text{O}_3$ from Atomistic Modelling

Jacob B. J. Chapman^{1,2}, Oliver. T. Gindele^{1,2}, Anna V. Kimmel^{1,2} & Dorothy M. Duffy¹

Jacob.chapman.13@ucl.ac.uk

1. Department of Physics and Astronomy, University College London, Gower Street, London, WC1E 6BT, UK

2. Materials Division, National Physical Laboratory, Hampton Road, Teddington, TW11 0LW, UK

Switchable polarisation of functional ferroelectric ceramics such as lead zirconate titanate $\text{PbZr}_{1-x}\text{Ti}_x\text{O}_3$ (PZT), a solid solution of PbTiO_3 and PbZrO_3 , makes it a critical component in many technologies, including non-volatile memories, transducers and waveguides. PZT exhibits its greatest piezoelectric properties and electromechanical response at the morphotropic phase boundary (MPB) around $x=0.5$ and this composition has been widely utilised in applications ranging from actuators to inkjet printers. Switching of Ti-rich PZT has been shown to be characterised by creep-depinning due to a nucleation and growth mechanism, reverse switching or successive ferroelastic transitions depending on the driving field orientation [1,2]. However, the dynamic properties of the switching dynamics at low temperatures, vital for applications in aeronautical and space applications, for the MPB regime remain poorly characterised [3].

In this work, we use large scale molecular dynamics using the shell model forcefield of Gindele *et al* [4], to model the dynamic switching behaviour of PZT in the vicinity of the MPB-composition. We show that, in the absence of domain walls, which precludes creep-depinning, the local B-cation disorder is responsible for temperature dependent, competitive switching mechanisms. We model switching of $x=0.5$ PZT at 100 K and 300 K, by pre-poling the simulated sample into a [001] tetragonal phased monodomain and then applying a reverse field to facilitate picosecond switching. At 100 K we show that, in the absence of pre-existing domain walls, diamond-shaped orthorhombic domains, approximately faceted by (101) surfaces, nucleate in the material. These are the 3-dimensional analogues to the bevelled nuclei shown as the growth mechanism on 2-dimensional 180° domain walls [5]. For nuclei exceeding a critical radius, fast growth of the facets forming charged domain walls with the [001] bulk occurs to minimise the electrostatic energy cost (Figure 2a). This growth is followed by conventional domain growth via domain wall motion (Figure 2b). Reverse domains then nucleate in the orthorhombic domain which grow until the sample has switched. A switching process via nucleation of orthorhombic domains provides an explanation for experimental studies on $\text{PbZr}_{0.414}\text{Ti}_{0.585}\text{O}_3$ ceramics, where the double peaks in the switching current were proposed to occur due to non- 180° domain switching resulting from the residual stresses developed during forward poling [6]. This scenario is supported by the results of small scale MD that suggest bulk-reorientation via an intermediate orthorhombic state in PbTiO_3 [7].

Further, we identify that the nucleation and switching are facilitated by Zr-site centred unit cells and by extension, Ti within Zr-rich environment. Since PbZrO_3 has an orthorhombic

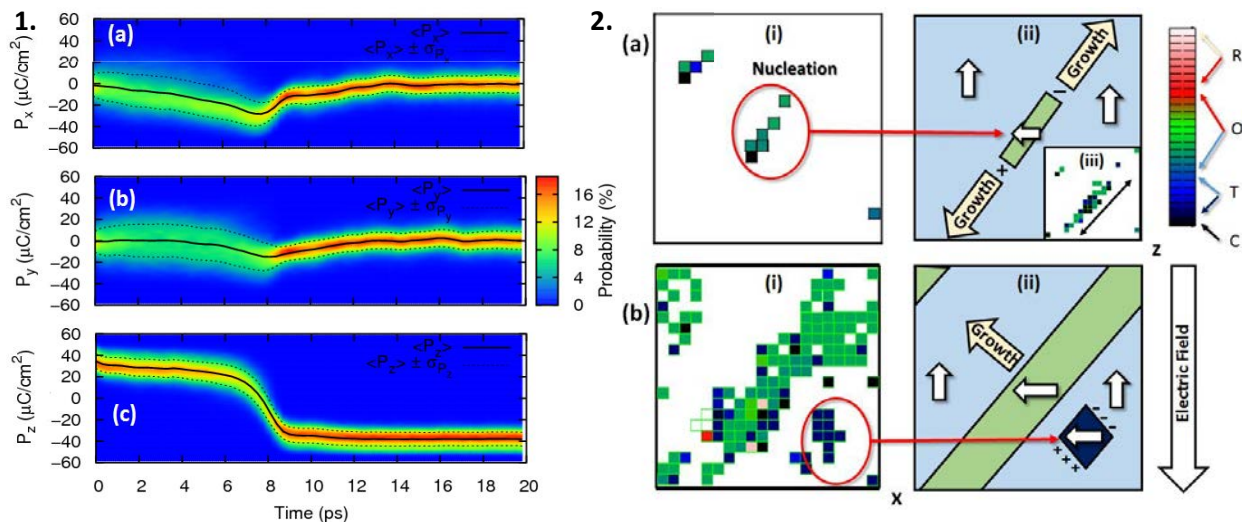


Figure 1. Density of Probability of each component of the order parameter during switching of $\text{PbZr}_{0.5}\text{Ti}_{0.5}\text{O}_3$ at 100 K. **Figure 2.** (i) Cross-sectional xz snapshots of the growth and formation of intermittent domains with an orthorhombic local structure to facilitate low temperature switching via low energy domain walls. Each square represents a unit cell with $P_z < 0$ and a colour representing its local structure. (ii) Cartoons of each snapshot.

(AFE) groundstate, these clusters allow for the nucleation of locally orthorhombic domains to facilitate growth via lower energy 71° and 109° domain walls without a large elastic energy penalty [1]. We find Ti in Zr-rich environments have suppressed ferroelectric displacements which may incorrectly be perceived as dead-regions. However, we show these Ti-centred unit cells remain ferroelectrically active due to the oxygen-octahedral displacement in the MPB-composition. At higher temperatures (300 K), the critical nucleus and barriers for reversal become negligible compared to the thermal fluctuation of dipoles [8] enabling the depinning-like process of fast nucleation of switched nanodomains through a paraelectric state (ie tracing the soft Γ -mode as in PbTiO_3).

This work highlights the subtle complex features of the low temperature atomistic switching mechanisms of PZT at the MPB-composition and proves atomistic level insight that is crucial for the development of functional nanoscale control of switching in ferroelectrics.

- [1] R. Xu et al, *Nature Materials* **14**,79 (2015)
- [2] S. Liu, I. Grinberg & A. M. Rappe, *Nature* **534**, 360 (2016)
- [3] O. Gindele, J. B. J. Chapman, C. Vecchini, P. Thompson, M. G. Cain, D. M. Duffy & A. V. Kimmel, in *preparation for submission* (2016)
- [4] O. Gindele, A. Kimmel, M. G. Cain & D. Duffy, *J. Phys. Chem. C* **119**, 17784 (2015)
- [5] Y.H. Shin, I. Grinberg, I.W. Chen & A. M. Rappe, *Nature* **449**, 881 (2007)
- [6] T.M.Kamel & G. de With, *J. Appl. Phys.* **102**, 044118 (2007)
- [7] X. Zeng & R. E. Cohen, *Appl. Phys. Lett.* **99**, 142902 (2011)
- [8] M. Vopsariou, J. Blackburn, M.G.Cain & P.M.Weaver, *Phys. Rev. B* **82**, 024109 (2010)

This work is supported by the EPSRC (EP/G036675/1) via the Centre for Doctoral Training in Molecular Modelling and Materials Science at University College London and the National Measurement Office of the UK Department of Business Innovation and Skills.

Antiferroelectric switching pathways and the relation between nonpolar and polar states in PbZrO_3 from first principles

Brian M. Abbett,¹ Karin M. Rabe,² and Craig J. Fennie¹

¹*School of Applied & Engineering Physics, Cornell University, Ithaca, New York 14853*

²*Department of Physics and Astronomy, Rutgers University, Piscataway, New Jersey 08854*

The macroscopic and atomistic properties of ferroelectrics are relatively well understood compared with antiferroelectrics. On an atomistic scale, switching between two polar states can proceed via motion of domain walls¹ and is often mediated by a rotation of the polarization as in BiFeO_3 ² or $\text{Ca}_3\text{Ti}_2\text{O}_7$ ³. Group theoretic and first principles work^{2,3} have helped elucidate these atomistic mechanisms in detail. While the macroscopic definition of antiferroelectricity is clearly defined as a characteristic double P - E hysteresis loop and dielectric response⁴, an atomistic understanding of antiferroelectricity has proved elusive. Rabe recently proposed antiferroelectrics are materials with a nonpolar ground state with a polar state nearby in free energy which can be reached by application of an external electric field⁴. Symmetry arguments can be used to constrain what structures can be involved in the paraelectric to antiferroelectric phase transition⁵. Both of these theories make it clear that antiferroelectricity is not a property of a single ground state structure - there must be other structures involved.

We used first principles calculations and group theory to investigate the relation between the $Pbam$ ground state of PbZrO_3 and its electric field induced $R3c$ polar state with the goal of understanding why PbZrO_3 is antiferroelectric. As a first step towards relating the two structures we found that the metastable $Ima2$ structure is effectively dynamically unstable to $R3c$. This instability passes through space group Cc , which is a common subgroup of $Ima2$ and $R3c$. A group-subgroup tree showing the relation between relevant space groups is given in Fig. 1(a). The dynamic instability of $Ima2$ to $R3c$ proceeds as a rotation of the polarization and octahedral rotation axis and is shown schematically in Fig 1(b). This relation between $Ima2$ and $R3c$ allows us to investigate the relation between $Pbam$ and $Ima2$ rather than a direct relation to $R3c$.

The main difference between the $Pbam$ and $Ima2$ structures is the displacement pattern of Pb ions - both have the same octahedral rotation pattern and similar amplitude displacements of the Pb ions. In $Pbam$ the Pb ions displace along the $[110]$ direction in a nonpolar pattern, while in $Ima2$ all the Pb ions displace along $[110]$ in the same direction. As both of these structures are low in energy, we hypothesized that other patterns of Pb displacements

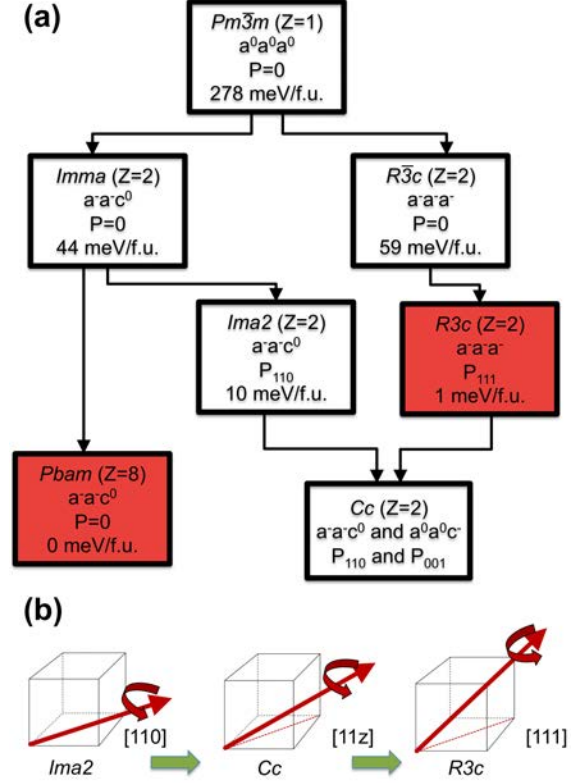


FIG. 1. (a) Group-subgroup relations are indicated by solid lines for several relevant structures. Octahedral rotation pattern, polarization direction, and energy relative to the $Pbam$ structure are shown for each space group. No energy is given for Cc as this structure relaxes into $R3c$. Dynamically stable space groups are shaded red. (b) The relaxation pathway from $Ima2$ to $R3c$ through their common subgroup Cc is shown schematically as a rotation of the octahedral rotation axis (curved red arrows) and polarization axis (solid red arrows) from $[110]$ to $[111]$.

along the $[110]$ direction would be comparably low in energy. In general such displacement patterns cannot be uniquely labeled with space group names. We thus label each displacement pattern using a string of integers with each integer representing the number of consecutive aligned Pb displacements along the $[1\bar{1}0]$ axis. Several examples are given in Fig. 2.

We performed a full structural relaxation for ev-

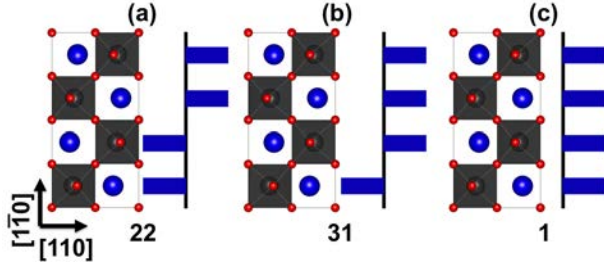


FIG. 2. Examples of several Pb/O displacement patterns. Blue/red spheres are Pb/oxygen. Shaded gray indicates ZrO_6 octahedra. Blue bars highlight the displacement direction each plane of Pb ions. (a) The 22 pattern, as in the experimental *Pbam* structure, (b) the 31 pattern, (c) the 1 pattern of *Ima2*.

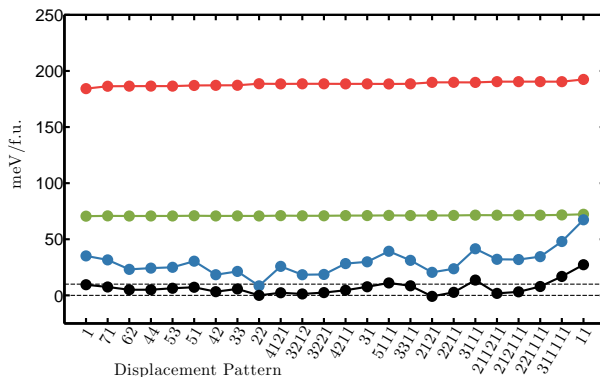


FIG. 3. Calculated energies relative to the *Pbam* ground state structure. Black points show the energy of fully relaxed structures. Green and red points show the energy of Pb displacing against oxygen in each displacement with and without octahedral rotations. Blue points show energy of structures generated using our structural model before any relaxation. Dashed lines show the energy of the relaxed experimental structure and 10 meV/f.u. above it.

ery unique displacement pattern commensurate with a unit cell with 80 or fewer atoms combined with $a^-a^-c^0$ octahedral rotations. Nearly every struc-

ture considered was within 10 meV/f.u. of the relaxed ground state, as shown in Fig. 3. We also note that the energy of structures with only Pb ions displacing against oxygen with or without octahedral rotations is nearly independent of the Pb displacement pattern.

The combination of Pb displacements and $a^-a^-c^0$ octahedral rotations allows other distortions through an allowed trilinear coupling term between phonon branches, which has been noted previously^{6,7}. We developed a structural model based on this coupling to predict the crystal structure for an arbitrary displacement pattern in PbZrO_3 . The energies of crystal structures predicted by this model are shown in Fig. 3. This model can be used to justify the existence of an infinite set of low energy structures in PbZrO_3 corresponding to arbitrary displacement of the Pb ions. Our findings are consistent with the entire Pb ion displacement phonon branch being soft in PbZrO_3 ⁶.

This set of low energy structures includes the *Pbam* ground state and *Ima2*, which we have shown is dynamically unstable to *R3c*. The existence of these low energy structures demonstrates the relation between *Pbam* and *R3c* and explains why they are close in energy. It further suggests there are many switching pathways between *Pbam* and *R3c* in which the Pb ions individually switch their displacements. We have calculated a number of switching barriers between from *Pbam* to *R3c* and have found a switching barrier as low as 8 meV/f.u. in a 120 atom unit cell. Larger unit cells can only reduce this energy barrier further.

The energy landscape we found helps explain why PbZrO_3 is an antiferroelectric: it has a non-polar *Pbam* ground state and a large number of low energy switching barriers leading to a metastable polar *R3c* state. This explains why PbZrO_3 can be readily switched into the polar *R3c* state with an electric field. It is not clear if this type of energy landscape is a defining feature of antiferroelectrics, though any material which has a similar energy landscape should be antiferroelectric.

¹ G. Catalan, J. Seidel, R. Ramesh, and J. F. Scott, *Rev. Mod. Phys.* **84**, 119 (2012).
² J. T. Heron, J. L. Bosse, Q. He, Y. Gao, M. Trassin, L. Ye, J. D. Clarkson, C. Wang, J. Liu, S. Salahuddin, D. C. Ralph, D. G. Schlom, J. Iniguez, B. D. Huey, and R. Ramesh, *Nature* **516**, 370 (2014).
³ E. A. Nowadnick and C. J. Fennie, *Phys. Rev. B* **94**, 104105 (2016).
⁴ K. M. Rabe, “Antiferroelectricity in oxides: A reexamination,” in *Functional Metal Oxides* (Wiley-VCH

Verlag GmbH & Co. KGaA, 2013) pp. 221–244.
⁵ P. Tolédano and M. Guennou, *Phys. Rev. B* **94**, 014107 (2016).
⁶ J. Hlinka, T. Ostapchuk, E. Buixaderas, C. Kadlec, P. Kuzel, I. Gregora, J. Kroupa, M. Savinov, A. Klic, J. Drahokoupil, I. Etxebarria, and J. Dec, *Phys. Rev. Lett.* **112**, 197601 (2014).
⁷ J. Iniguez, M. Stengel, S. Prosandeev, and L. Bellaiche, *Phys. Rev. B* **90**, 220103 (2014).

Deterministic Domain Switching in Ferroelectric Thin Films by Mechanical Probe: Synergy of Piezoelectricity and Flexoelectricity

Bo Wang¹, S. M. Park^{2,3}, T. W. Noh^{2,3}, L. Q. Chen¹

¹ Department of Materials Science and Engineering, Pennsylvania State University, University Park, Pennsylvania 16802, United States

² Center for Functional Interfaces of Correlated Electron Systems, Institute for Basic Science (IBS), Seoul 151-742, Korea

³ Department of Physics and Astronomy, Seoul National University, Seoul 151-742, Korea

The existence of spontaneous polarization and the controllable switching of it by external fields underlie the potential applications of ferroelectric materials as non-destructive readout memories, photovoltaic solar cells and next-generation transistors [1]. While conventionally controlled by the electrical bias of a scanning probe, the polarization domain in ferroelectric thin films can also be reoriented by mechanical force through the tip by virtue of the electromechanical couplings including both piezoelectric and flexoelectric effects [2]. Utilizing this method, arbitrary-shaped nanodomains can be mechanically written and tuned in thin-film ferroelectric capacitors [3], a promising step towards functional devices based on domain and domain wall topology.

Although the mechanical approach for polarization switching has been demonstrated in a number of ferroelectric materials, most investigations concern only the 180° reversal of the out-of-plane polarization, highlighting the dominant role of flexoelectricity over piezoelectricity [2]. However, a systematic study is still lacking for the domain switching in more complex situations where both non-180° ferroelastic and 180° ferroelectric switching coexist and the piezoelectric and flexoelectric effects compete with each other. Moreover, for mechanically loaded scanning probe, the frictional shear strains give rise to considerable lateral flexoelectric fields, which is usually ignored but can be tuned to achieve deterministic domain switching as presented in this work.

In this work, we performed phase-field simulations and piezoelectric force microscope (PFM) to study the mechanical-induced switching behaviors in two prototype ferroelectric thin films, e.g., the tetragonal BaTiO₃ (BTO) and rhombohedral BiFeO₃ (BFO) thin films. The phase-field model incorporates both the piezoelectric and the flexoelectric effects to single out their respective roles in the mechanical switching process in ferroelectric thin films. The simulation results show 180° ferroelectric switching in BTO regardless of the friction force but both non-180° ferroelastic switching and 180° ferroelectric switching are obtained in BFO depending on the direction of friction force. Moreover, a synergetic contribution of piezoelectricity and flexoelectricity is suggested in the ferroelectric switching in both materials whereas the flexoelectricity may either aid or counteract the piezoelectricity in ferroelastic switching.

We test our prediction by applying force through scanning probe onto the BTO and BFO thin films and study the direction dependence of polarization switching path. The domain structures given by in-plane and out-of-plane PFM images corroborate the simulations results: while the polarization can be flipped by mechanical tip in BTO, it shows an insensitivity of tip scanning direction. On the other hand, both 71° and 180° domain switching are observed in BFO and can

be selectively controlled by the tip motion, which is not applicable through the electric-biased scanning probe. Our work will provide a novel approach for domains engineering in BiFeO_3 and should also deepen the understanding of piezoelectricity and flexoelectricity in mechanical-induced polarization switching in ferroelectric thin films.

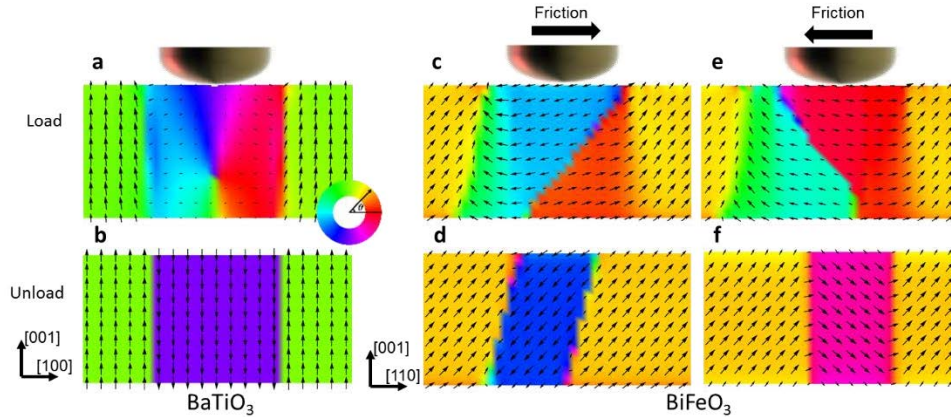


Figure 1 Phase-field simulation of polarization distribution in 5 nm BTO (a,b) and BFO (c-f) thin films under tip load (a,c,e) and after unload (b,d,f). 180° polarization switching is observed in BTO regardless of the existence of friction force while in BFO, either 180° or 71° switching path depends on the friction directions. Inset in (a) shows the color ring of polarization orientation.

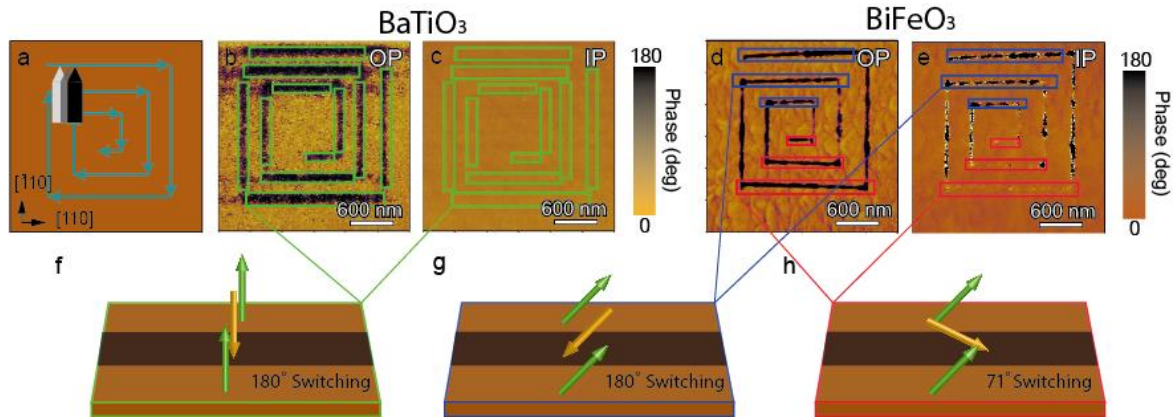


Figure 2 Ferroelectric polarization switching by mechanical line scan. (a) Schematic of the mechanical line scan path where arrow indicates the direction of tip movement. (b,c) The out-of-plane and in-plane PFM phase images after mechanical scan performed on the BTO and BFO (d,e) thin film. (f,g,h) Schematic display of polarization configuration after mechanical scan.

References

- [1] Martin, L. W., & Rappe, A. M. (2016). Thin-film ferroelectric materials and their applications. *Nature Reviews Materials*, 2, 16087.
- [2] Lu, H., Bark, C. W., et al. (2012). Mechanical writing of ferroelectric polarization. *Science*, 336 (6077), 59-61.
- [3] Lu, H., Wang, B., Li, T., et al. (2016). Nanodomain Engineering in Ferroelectric Capacitors with Graphene Electrodes. *Nano Letters*, 16(10): 6460-6466.

Tuesday's Abstracts

Palladium-based Ferroelectrics and Multiferroics

Shalini Kumari¹, Dhiren K. Pradhan¹, Nora Ortega¹, Kallol Pradhan¹, Christopher DeVreugd², Gopalan Srinivasan², Ashok Kumar³, Tula R. Paudel,⁴ Evgeny Y. Tsymlal,⁴ Alice M. Bumstead,⁵ Maadhav Kotari,⁵ John T. S. Irvine,⁵ J. F. Scott⁵, and Ram S. Katiyar¹

¹Department of Physics and Institute for Functional Nanomaterials, Univ. Puerto Rico, San Juan, PR 00931, USA.

²Physics Department, Oakland University, Rochester, Michigan 48309-4401, USA.

³CSIR-National Physical Laboratory, Dr. K. S. Krishnan Marg, New Delhi 110012, India.

⁴Department of Physics, University of Nebraska, Lincoln, NE 68588-0299 USA.

⁵Department of Chemistry and Department of Physics, University of St. Andrews, St. Andrews KY16 ST, U. K.

Palladium normally does not easily substitute for Ti or Zr in perovskite oxides. Moreover, Pd is not normally magnetic (but becomes ferromagnetic under applied uniaxial stress or electric fields). Despite these two great obstacles, we have succeeded in fabricating lead zirconate titanate with 30% Pd substitution. The resulting material is multiferroic (ferroelectric-ferromagnet) at room temperature. The processing is slightly unusual, and the density functional theory provided shows that it occurs because of Pd⁺⁴ in the oversized Pb⁺² site; if all Pd⁺⁴ were to go into the Ti⁺⁴ perovskite B-site, no magnetism would result.

Large room-temperature magnetoelectric effects in single-phase material is one of the aims of scientists working worldwide in the area of multiferroics, similar to the desire for room-temperature superconductors. These systems require the presence of simultaneous ferroic order parameters with strong ME coupling for an increased number of logic states. During the last fifteen years the multiferroic (MF) research communities have been searching for an alternative room temperature MF material with large magnetoelectric (ME) coupling for possible applications in high density electronic components, and low heat dissipation memory and logic devices. In the past few years, we have investigated several multi-component systems such as Pb(Zr,Ti)O₃(PZT) - Pb(Fe,Ta/Nb/W)O₃, and related family members, which have shown better ME effects compared to bismuth ferrite. In continuation to our search for larger ME effect, we have studied Pb(Zr_{0.20}Ti_{0.80})_{0.70}Pd_{0.30}O_{3-δ} (PZTP30) system with an unusually large (30%) palladium occupancy in B site of PZT. This material exhibited a giant ME coupling coefficient ~0.36 mV/cm.Oe. Our new system is a simple tetragonal crystal structure with space group *P4mn* as probed by X-ray diffraction (XRD), and Raman studies. A neutral Pd atom (Kr 4d¹⁰) has square planar complex, which gives zero magnetic moment ($\mu=0$) and diamagnetism, but when it is in Pd⁺² or Pd⁺⁴ ionic states, it provides large magnetic moment with outer cell configuration 4d⁸5s⁰ or 4d⁶5s⁰ with unpaired electrons in its d-shell. It has also been proven that electric control can change diamagnetic Pd to ferromagnetic, magnetism in clusters of Pd atoms,

and large magnetization in multilayer structures with Pt and Fe. The presence of Pd in PZTP30 has been confirmed by XPS and XRF studies and assigned with related binding energies of Pd⁺² and Pd⁺⁴ ions as 336.37 eV, 342.9 eV, and 337.53 eV, 343.43 eV, respectively, which may be the origin of room temperature magnetism in Pd substituted PZT ceramics. A sharp first order ferroelectric phase transition was observed at ~569 K (+/-5 K) that is confirmed from dielectric, Raman, and thermal analysis. Both ferromagnetic and ferroelectric orderings with large ME are measured. Fig.1a-c show nonmagnetic results for Pd at Ti sites; but (d) shows ferromagnetism for Pd+4 at Pb+2 sites.

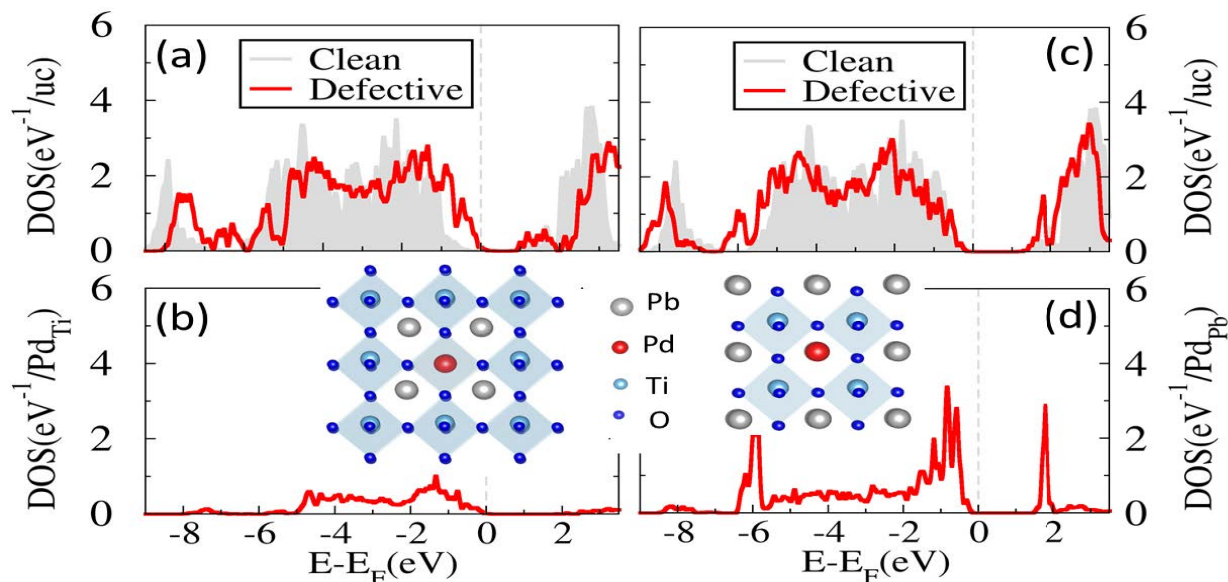


Figure 1. DFT of Pd in PZT: (a-c) at Ti sites; (d) Pd+4 at Pb+2 sites.

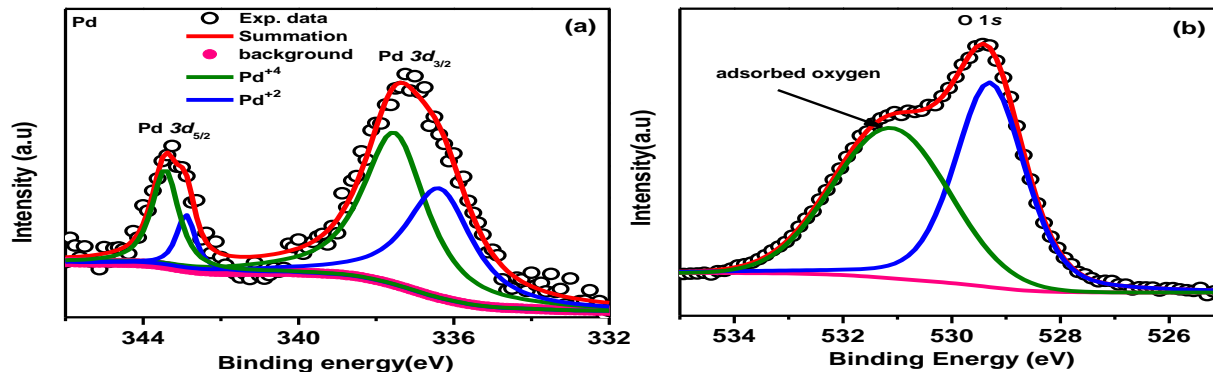


Figure 2. Kumari et al.

XPS of Pd in PZT:Pd.

Effective control of magnetization rotation as a function of applied electric field in FeGa/NiFe multilayers on PMN-PT

M.E. Jamer¹, C.R. Rementer², T. Barra³, Q. Xu⁴, P. Nordeen³, G. Carman³, Y. Wang⁴, D.B. Gopman⁵, A.J. Grutter¹, J. Borchers¹, B.J. Kirby¹, and J.P. Chang²

¹ Center for Neutron Research, National Institute of Standards and Technology, Gaithersburg, MD

² Chemical and Biomolecular Engineering, University of Los Angeles, Los Angeles, CA

³ Mechanical and Aerospace Engineering, University of Los Angeles, Los Angeles, CA

⁴ Electrical Engineering, University of Los Angeles, Los Angeles, CA

⁵ Materials Science & Engineering Division, National Institute of Standards and Technology, Gaithersburg, MD

There is a growing interest in developing magnetostrictive compounds for micro actuators and novel microwave magnetic devices to replace Terfenol-D, as it is difficult to fabricate and contains rare earth materials. Galfenol, Fe_xGa ($x = 75-85$), is the most prominent possible alternative due to its large magnetostriction (>200 ppm), high piezomagnetic coefficient (3 ppm/Oe), and high stiffness (70 GPa).¹ In previous research, Fe_xGa and NiFe were deposited in a multilayer heterostructure in order to exchange couple the two layers, thereby improving the properties of the galfenol layer while maintaining the magnetostrictive integrity.²

In this work, multilayer laminates were fabricated with $\text{Fe}_{86}\text{Ga}_{14}$ and $\text{Ni}_{81}\text{Fe}_{19}$ on piezoelectric PMN-PT [011] in order to explore voltage control of the magnetization. Using SQUID magnetometry with *in situ* poling, we find that straining the substrate with 400 V in remnant magnetic field strains the multilayer enough to induce a significant change in anisotropy. To understand how this effect varies with proximity to the piezoelectric substrate, we have used polarized neutron reflectometry to determine the depth profiles of the structure and in-plane vector magnetization as functions of applied magnetic field and voltage. We find that we are insensitive to any structural changes with voltage, but we do observe pronounced magnetic changes. Figure 1 shows the voltage-dependent spin-flip scattering in 1 mT following saturation

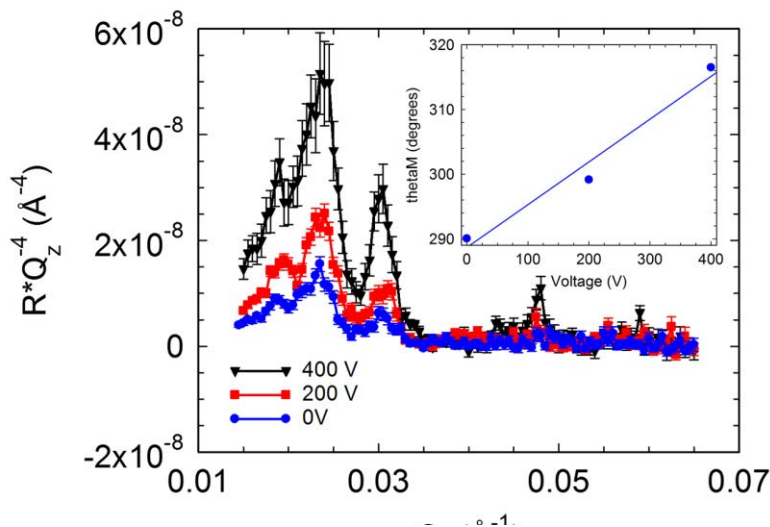


Figure 1 The spin flip component of the polarized neutron reflectometry data. The inset shows the angle of rotation as a function of voltage.

along the [011] direction for a $[20 \text{ nm } \text{Fe}_{86}\text{Ga}_{14} / 7 \text{ nm } \text{Ni}_{81}\text{Fe}_{19}]_3 / 20 \text{ nm } \text{Fe}_{86}\text{Ga}_{14}$ multilayer on a PNM-PT substrate. Application of 400 V results in an enormous increase in spin-flip scattering, unambiguously demonstrating a substantial rotation of the magnetization perpendicular to the applied magnetic field direction. Model fitting of the data suggests that the $\text{Fe}_{86}\text{Ga}_{14}$ and $\text{Ni}_{81}\text{Fe}_{19}$ layers rotated coherently. The magnetic rotation versus voltage plot is seen in the inset of Figure 1.

The plot indicates that the magnetic moment rotates by 45 degrees between the 0 V and 400 V state.

Results for a series of multilayers with different layer thicknesses will be discussed. These measurements thus provide direct evidence of a voltage-induced rotation of the both the NiFe and FeGa magnetization as well as a means to separate the response of the magnetostrictive and soft layer components. Magneto-optic imaging film (MOIF) apparatus will be used to explore the domain formation and field dependence.

¹ Ueno, T., et al. (2008). "Micro-magnetostrictive vibrator using iron-gallium alloy." *Sensors and Actuators a-Physical* 148(1): 280-284.

² Lupu, N., et al. (2008). "Electrochemical deposition of FeGa/NiFe magnetic multilayered films and nanowire arrays." *Journal of Applied Physics* 103(7).

Effects of atomic short-range order on properties of the $\text{PbMg}_{1/3}\text{Nb}_{2/3}\text{O}_3$ relaxor ferroelectric

Sergey Prosandeev and L. Bellaiche

Physics Department and Institute for Nanoscience and Engineering, University of Arkansas, Fayetteville, Arkansas 72701, USA

The effect of atomic *short-range* order on the macroscopic and microscopic properties of the prototype of relaxor ferroelectrics, that is, lead magnesium niobate $\text{Pb}(\text{Mg}_{1/3}\text{Nb}_{2/3})\text{O}_3$ (PMN), is studied via the combination of an annealing technique and a large-scale effective Hamiltonian method [1]. The investigated short-range order gradually varies from the case of fully disordered solid solutions to the situation for which the first three nearest-neighbor shells of the B lattice of PMN adopt a rocksalt ordering between a sublattice made of pure Nb ions and a randomly distributed sublattice consisting of 2/3 of Mg and 1/3 of Nb. The characteristic temperatures of relaxor ferroelectrics (namely, the Burns, so-called T^* , and depolarizing temperatures) significantly increase when strengthening this short-range chemical order, which is accompanied by an overall enhancement of the size of the polar nanoregions as well as of some antiferroelectric interactions. These results can be understood by the fact that chemical short-range order strongly modifies the internal electric fields felt by the Pb ions (see Figure 1).

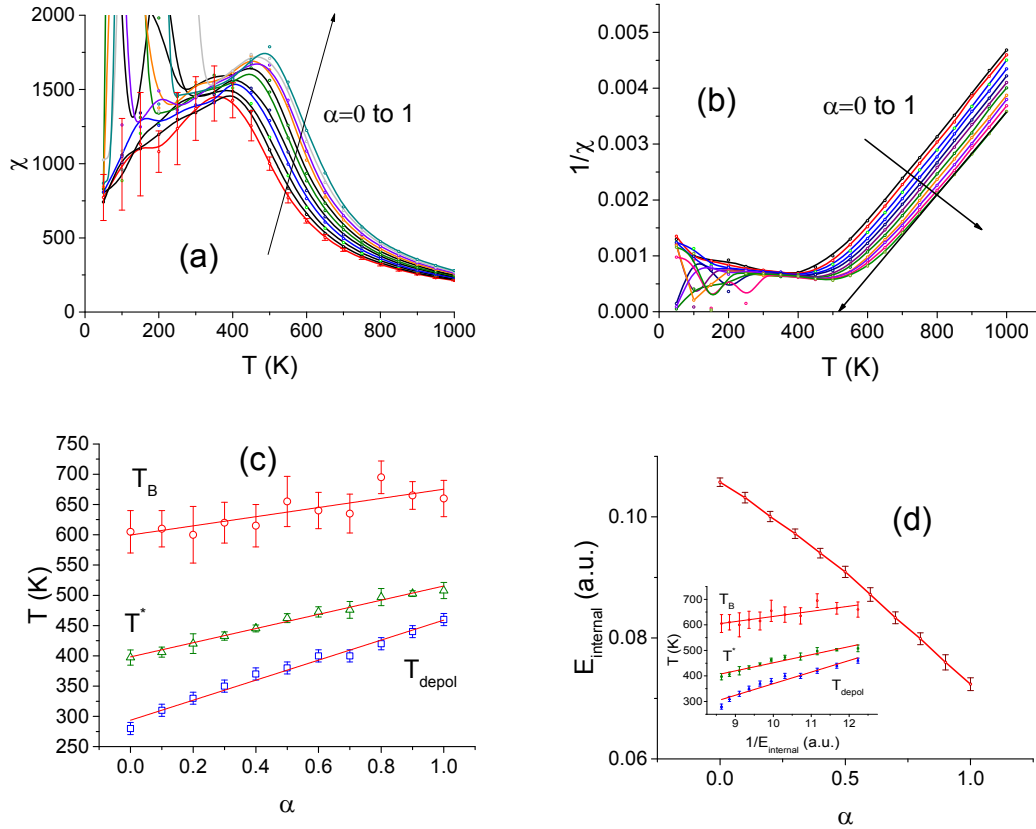


FIG. 1. Predicted properties of PMN as a function of the chemical short-range order parameter α : (a) dielectric permittivity; (b) inverse of the dielectric permittivity; (c) the T_B , T^* , and T_{depol}

characteristic temperatures; and (d) the averaged magnitude of the internal electric field E_{internal} acting on Pb ions. The inset in (d) presents the dependence of T_B , T^* , and T_{depol} on the inverse of E_{internal} . The solid lines are guides for the eye, and error bars result from the summation over 30 different configurations for each α .

This work is financially supported by ONR Grant No. N00014-12-1-1034 and ARO Grant No. W911NF-16-1-0227.

The computations were made possible thanks to the MRI Grant 0722625 from NSF, the ONR Grant No. N00014-15-1-2881 (DURIP) and a Challenge grant from the Department of Defense.

REFERENCES

1. S. Prosandeev and L. Bellaiche, *Phys. Rev. B* **94**, 180102(R) (2016).

The Origin of Ultrahigh Piezoelectricity in Relaxor-Ferroelectric Solid Solution Crystals

Fei Li,¹ Shujun Zhang,² Long-Qing Chen,¹ Thomas R. Shroud¹

¹Materials Research Institute, Pennsylvania State University, University Park, PA 16802, USA

²Institute for Superconducting and Electronic Materials, Australia Institute of Innovative Materials, University of Wollongong, NSW 2500, Australia

Perovskite ferroelectrics (general formula, ABO_3) exhibit the highest electromechanical activity among all known piezoelectrics. One of the most remarkable breakthroughs in perovskite ferroelectrics is the discovery of ultrahigh piezoelectricity ($d_{33}^* = 1500 \sim 2500 \text{ pC N}^{-1}$) and electromechanical coupling factors ($k_{33}^* > 0.9$) in domain-engineered relaxor-ferroelectric solid solution crystals with MPB compositions, e.g., $Pb(Mg_{1/3}Nb_{2/3})O_3$ - $PbTiO_3$ (PMN-PT) and $Pb(Zn_{1/3}Nb_{2/3})O_3$ - $PbTiO_3$ (PZN-PT) crystals.

Compared to normal ferroelectrics, a key signature of relaxor-ferroelectric solid solutions is the existence of polar nanoregions (PNRs), a nano-scale inhomogeneity, that coexist with normal ferroelectric domains. Despite two decades of extensive studies, the contribution of polar nanoregions to the underlying piezoelectric properties of relaxor-ferroelectrics has yet to be established. Here, we quantitatively characterize the contribution of polar nanoregions to the dielectric/piezoelectric responses of relaxor-ferroelectric crystals using a combination of cryogenic experiments and phase-field simulations. The contribution of polar nanoregions to the room-temperature dielectric and piezoelectric properties is in the range of 50-80%. A mesoscale mechanism is proposed to reveal the origin of the high piezoelectricity in relaxor-ferroelectrics, where the polar nanoregions aligned in a ferroelectric matrix can facilitate polarization rotation.

This mechanism emphasizes the critical role of local structure on the macroscopic properties of ferroelectric materials, where a modest amount of nanoscale inhomogeneity can lead to dramatically enhanced ferroic properties.

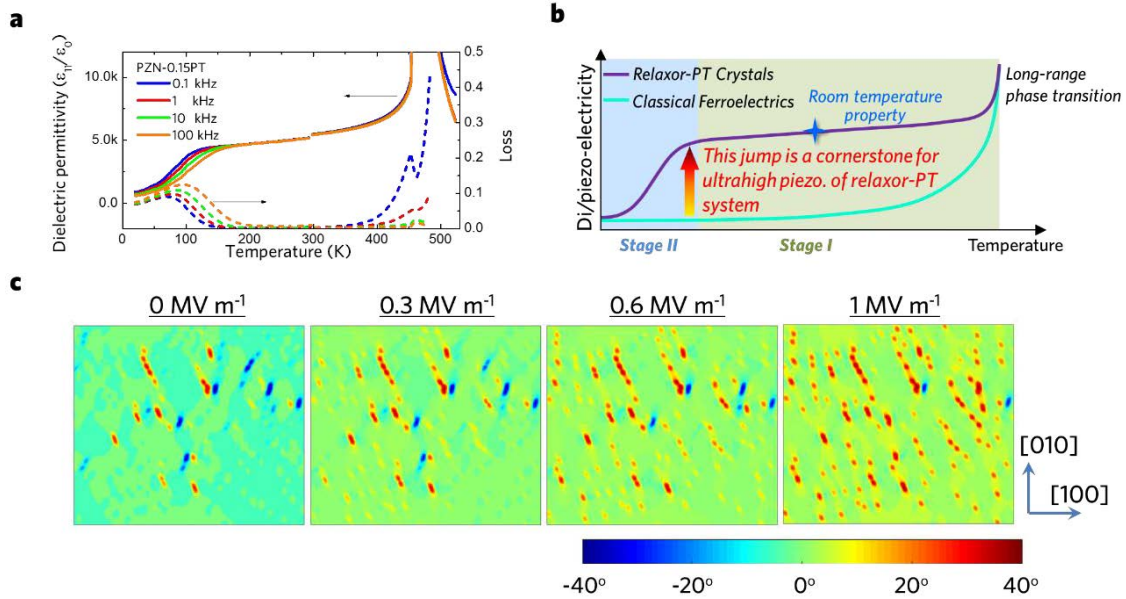


Figure a shows the measured temperature dependence of transverse dielectric response for single-domain PZN-0.15PT crystals. Figure b gives a schematic plot showing the major difference of dielectric/piezoelectric properties between relaxor-PT crystals and normal ferroelectric crystals. Figure c shows phase-simulation results for the microstructural evolution of [100]-poled PZN-0.15PT crystals under a transverse [010] E-field from 0 to 1 MV m⁻¹, where the color bar denotes the angle between the polar vector and [100] direction. As shown in Figure c, PNRs play an important role in enhancing the susceptibility of polarization versus perpendicular electric fields.

Reference:

Fei Li et al, The origin of ultrahigh piezoelectricity in relaxor-ferroelectric solid solution crystals, Nature Communications, 7, 13807 (2016)

The PNR \rightleftharpoons Relaxor Transitions in PSN with nearest neighbor [Pb-O] divacancies [$Pb_{1-X}(Sc_{1/2}Nb_{1/2})O_{3-X}$] and PMN [$Pb(Mg_{1/3}, Nb_{2/3})O_3$]

B. P. Burton, Eric Cockayne, D. B. Gopman, and Gunay Dogan

Materials Measurement Laboratory, National Institute of Standards and Technology Gaithersburg, MD 20899-8520, USA

Sarah Hood

*Materials Measurement Laboratory, National Institute of Standards and Technology Gaithersburg, MD 20899-8520, USA and
Hood College, Frederick, MD 21701, USA*

PACS numbers: 77.80.Bh, 77.84.Dy, 64.70.Kb, 61.46.-w

In previous work, [1] molecular dynamics (MD) simulations based on a first-principles-derived effective Hamiltonian for $Pb_{1-X}(Sc_{1/2}Nb_{1/2})O_{3-X}$ (PSN, with nearest-neighbor Pb-O divacancy pairs) was used to calculate $X_{[Pb-O]}$ vs. T , phase diagrams for PSN with various quenched disorder configurations: ideal rock-salt type chemical order; nanoscale chemical short-range order; and random chemical disorder. We show that the phase diagrams should include an additional region in which a glassy relaxor-phase (or state) is predicted (Fig. 1), and show that the regions previously labeled RFE for relaxor ferroelectric should be divided into a PNR region, in which there are Polar Nano-Regions, and a relaxor region in which there is a glassy phase, or state.

Curves for the Burns temperature, $T_B(X_{[Pb-O]})$, [2] and the FE-transition temperature, $T_{FE}(X_{[Pb-O]})$ are identical to those in [1]. Curves for $T^*(X_{[Pb-O]})$, the PNR \rightleftharpoons Relaxor transition, or crossover, were located by plotting T -dependent $q_{\xi\xi}$ - and $q_{\Delta t}$ -curves where: $q_{\xi\xi}$ is the self-overlap order parameter, [3] Eqn. 1; and $q_{\Delta t}$ Eqn. 2, is an autocorrelation function that compares the displacement of atom ξ_i at time- t with ξ_i at time- $t + \Delta t$ (typically, $\Delta t = 100$ MD-snapshots = 6.0 picoseconds).

The idea behind $q_{\Delta t}$ is that a time-sensitive order parameter may be more sensitive to the sort of PNR-stiffening that Dkhil et.al. [4] associate with T^* :

$$q_{\xi\xi} = \frac{1}{N} \sum_i \langle \vec{\xi}_i \cdot \vec{\xi}_i \rangle \quad (1)$$

and

$$q_{\Delta t} = \frac{1}{N} \sum_i \langle \vec{\xi}_{i,t} \cdot \vec{\xi}_{i,t+100} \rangle \quad (2)$$

where: N is the number of Pb-sites; summations are over the all Pb-displacements; and angle brackets indicate averaging over the last 1000 MD-snapshots in a 5000 snapshot series. Within the precision of these simulations, both order parameters yield the same results for $T^*(X_{[Pb-O]})$.

The general cooling-trends of $q_{\xi\xi}(T)$ - and $q_{\Delta t}(T)$ -curves are similar: there are broad minima at or near T_B ; smooth increases from T_B down to T^* ; a small discontinuity (or rapid change in slope) at T^* ; and erratic variation below T^* . The erratic variations in $q_{\xi\xi}(T)$ - and $q_{\Delta t}(T)$ (Fig. 1a), and their evolution as functions of MD-time (Fig. 1b) are interpreted as reflecting the glassy character of the system. Specifically, in the relaxor region, below T^* , and above the red dotted line, the MD-simulation evolves towards convergence via various local minima as shown by the complex paths of $q_{\xi\xi}(T, t)$ - and $q_{\Delta t}(T, t)$ in Fig. 1b. Such evolutionary paths are strongly suggestive of a glassy system that has many local minima in its configuration space.

A modified version of the PSN-model [1] was used to model $Pb(Mg_{1/3}, Nb_{2/3})O_3$ (PMN) [5] and similar results were obtained Fig. 2. As for PSN: depending on the chemical configuration, the Relaxor \rightleftharpoons PNR transition may be weakly first order; and T^* is a sensitive function of cation configuration but T_B is not.

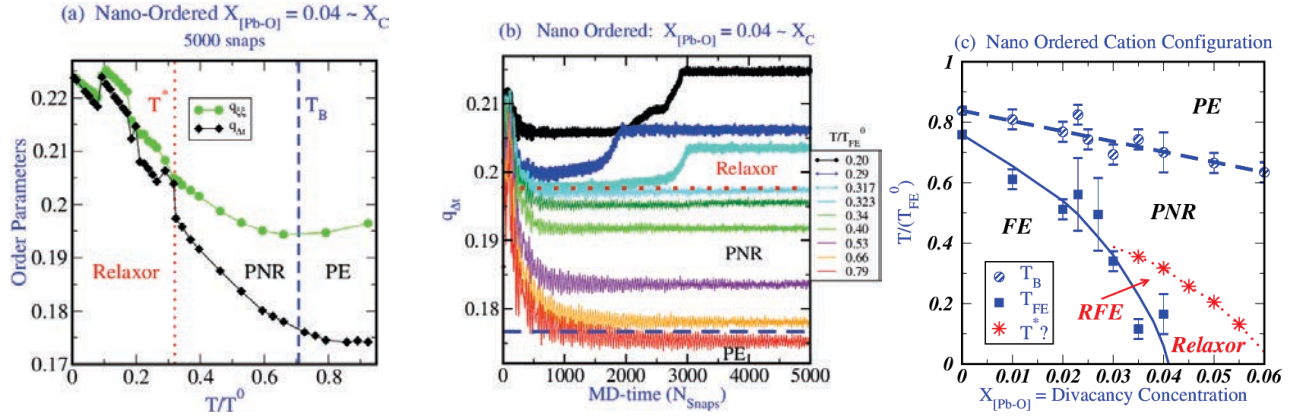


FIG. 1: Order parameters as functions of temperature for a nano-ordered Sc:Nb cation-configuration of $Pb_{1-x}(Sc_{1/2}Nb_{1/2})O_{3-x}$, with 25% ordered regions in a random matrix and $X=0.04$: (a) T^* appears to mark a weakly first-order phase transition (an $\approx 1\%$ discontinuity in $q_{\xi\xi}$ or $\approx 2\%$ in $q_{\Delta t}$); (b) is a plot of $q_{\Delta t}$ as a function of MD-simulation time, where N_{snaps} is the number of snapshots in a 5000 snapshot series. At $T < T^*$, above the horizontal dotted red line, the system traverses local minima before, apparently, converging; (c) calculated $X_{[Pb-O]}$ vs. T phase diagram for the system $Pb_{1-x}(Sc_{1/2}Nb_{1/2})O_{3-x}$, with a nano-ordered Sc:Nb cation-configuration (25% ordered regions in a random matrix). Labels: PE indicates a normal paraelectric; PNR indicates a system in which chemically ordered regions, with few random fields, \vec{h}_i , have higher polarization than the random matrix; FE indicates a ferroelectric ground-state; RFE indicates a relaxor-region above the FE-ground-state. Vertical dashed blue line indicates the Burns temperature (T_B). Solid blue line indicates the $FE \rightleftharpoons PNR$, or $FE \rightleftharpoons RFE$ transition. Red dotted line with large \times -symbols indicates $RFE \rightleftharpoons PNR$ or $Relaxor \rightleftharpoons PNR$ transition, or crossover.

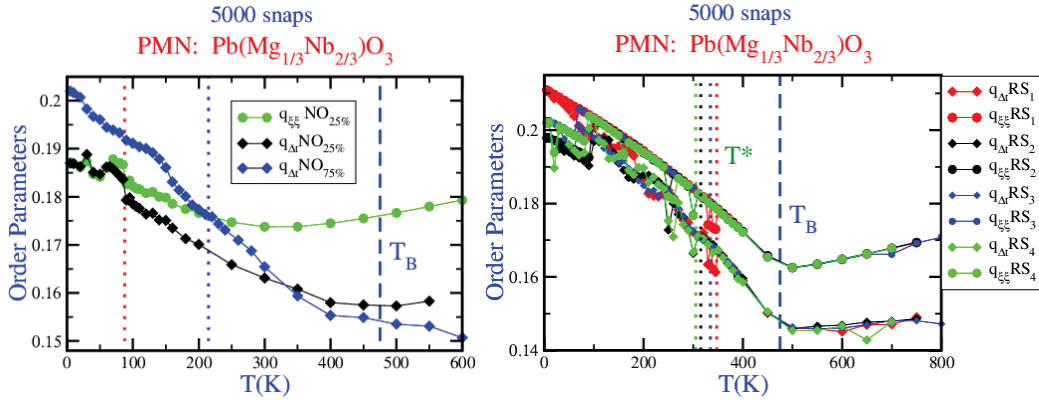


FIG. 2: Order parameter vs. temperature curves that were used to define the relaxor-region in $Pb(Mg_{1/3}, Nb_{2/3})O_3$, with various cation configurations: (left-panel) $NO_{25\%}$ has 25% chemically ordered regions (COR) in a random matrix; $NO_{75\%}$ has 75% COR in a random matrix; RS has "random site" ordering (NaCl order with Nb on one B-site and $Mg_{1/3}Nb_{2/3}$ on the other B-site); (right-panel) results for four replicas in the Random Site configuration [6] with a 40K-range of T^* -values predicted. As cation order increases, from $NO_{25\%}$, to $NO_{75\%}$, to RS, the apparent first-order character of the $PNR \rightleftharpoons relaxor$ transition decreases. Also, T^* is clearly sensitive to changes in cation order.

- [1] B. P. Burton, E. Cockayne, S. Tinte and U. V. Waghmare, Phys. Rev. B **77**, 144114 (2008).
- [2] G. Burns and F. H. Dacol, Solid State Commun. **48**, 853 (1983).
- [3] T. Castellani and A. Cavagna J. Stat. Mecha. P05012 (2005) PII: S1742-5468(05)99356-4
- [4] B. Dkhil, P. Femeiner, A. Al-Barakaty, L. Bellaiche, E. Dul'kin, E. Mojaev, and M. Roth, Phys. Rev. B **80** 064103 (2009).
- [5] B. P. Burton, E. Cockayne, S. Tinte and U. V. Waghmare, Phase Trans. **79**, 91 (2006).
- [6] L. Farber, M. Valant, M. A. Akbas, and P. K. Davies, J. Amer. Ceram. Soc. **85** 2319- (2002).

Observation of Ferroelectric Vortices in Oxide Superlattices

C. T. Nelson^{1*}, A. K. Yadav¹, S. L. Hsu¹, Z. Hong², A. R. Damodaran¹, P. Shafer³, Pablo García-Fernández⁴, Pablo Aguado-Puente⁵, J. D. Clarkson¹, Javier Junquera⁴, E. Arenholz³, L. Q. Chen², L. W. Martin¹ & R. Ramesh¹

¹Department of Materials Science and Engineering, University of California Berkeley, Berkeley, CA 94709

²Department of Materials Science and Engineering, Penn State University, University Park, PA 16802

³Advanced Light Source, Lawrence Berkeley National Laboratory, Berkeley, California 94720, USA.

⁴Departamento de Ciencias de la Tierra y Física de la Materia Condensada, Universidad de Cantabria, Cantabria Campus Internacional, Avenida de los Castros s/n, 39005, Santander, Spain

⁵Centro de Física de Materiales, Universidad del País Vasco, 20018, San Sebastián, Spain

*email: ctnelson@berkeley.edu

Complex spin topologies, such as vortices and skyrmions, have garnered great attention for potential application in high density ferromagnetic solid-state memories. Although topological defects in the electrical analog, ferroelectrics, have demonstrated many useful functional properties such as increased electrical conductivity,⁽¹⁻³⁾ expectations for similar complex topologies are muted by inherent differences in behavior, particularly the high anisotropy and dominant Ising-type domain wall properties of the proper ferroelectrics. Nanoscale characterization by Transmission Electron Microscopy (TEM) has previously found local rotational Néel-type domain wall behavior at polydomain junctions at ferroelectric / dielectric interfaces where rotational flux-closure structures form from depolarizing fields.⁽⁴⁻⁶⁾ In this work I present the observation of a high density array of ferroelectric vortices from confinement of PbTiO₃ in paraelectric SrTiO₃ layers in an oxide superlattice geometry.

(PbTiO₃)_{10unit cell} × (SrTiO₃)_{10u.c.} superlattices epitaxially grown on a DyScO₃ (110)_O substrates by Pulsed Laser Deposition form a polarization distribution in the PbTiO₃ layers consisting of a dense array of smoothly rotating Néel character vortices with ~10nm periodicity. The vortex structure is shown by atomic-resolution Scanning TEM (STEM) in Figure 1. These vortices further exhibit long-range interlayer ordering with a dominant preference to align vortices with matching rotations, i.e. clockwise over clockwise and vice versa (see Figure 2). This vortex structure and ordering is evidenced in macroscale samples by in-plane superlattice reflections in X-ray diffraction corresponding to the vortex periodicity. First-principles calculations indicate a significant non-uniform axial polarization

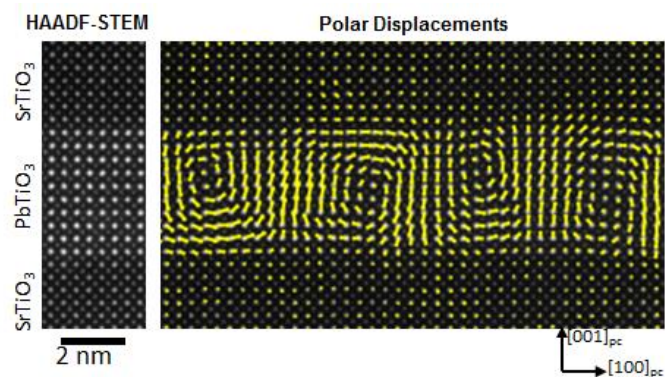


Figure 1: Ferroelectric Vortices in a PbTiO₃ layer by HRSTEM. (left) HAADF image of the PTO/STO superlattice. (right) Polarization distribution with vectors indicating the cation sublattice local non-centrosymmetry (4 – nearest neighbors).

component resulting in a topologically charged axial normal surface. X-ray circular difference (XCD) measurements indicate the ferroelectric vortices are indeed chiral.

The vortex structure is predominantly the result of competition of the elastic, electrostatic, and domain wall (or gradient) energy which exhibits superlattice layer thickness dependence. Phase-field, used to model large volume $\text{PTO}_n \times \text{STO}_n$ superlattices, shows for small n ($< \approx 10$ u.c.) uniform in-plane polarization dominates, for large n ($> \approx 16$ u.c.) discrete flux closure domain patterns dominate, but for intermediate n (see $n=10$ in Figure 2) the vortex configuration is stable, a trend also observed in TEM thickness-dependence studies. Furthermore, a growth regime of bistability of the vortex and uniform in-plane polarization is observed experimentally at both the nanoscale (TEM) as well as macroscale (Piezoresponse Force Microscopy and XRD). This bistable regime is sensitive to the application of external electric-fields demonstrating reversible switching between a uniform state and a high density ferroelectric vortex / modulating ferroelastic structure.

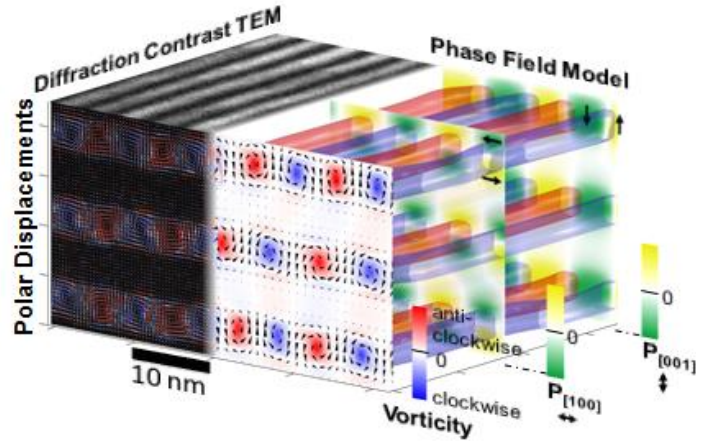


Figure 2: $\text{PTO}_{10}/\text{STO}_{10}$ Vortex Array Structure. (left) experiment: diffraction contrast TEM (top surface) and STEM overlaid with vorticity colorized red/blue polarization vectors (front face). (right) phase field model with cross sections of vorticity, in-plane polarization $P_{[100]pc}$ and out-of-plane polarization $P_{[001]pc}$.

References:

1. J. Seidel *et al.*, Conduction at domain walls in oxide multiferroics. *Nat. Mater.* 8, 229 (2009).
2. T. Sluka, A. K. Tagantsev, P. Bednyakov, N. Setter, Free-electron gas at charged domain walls in insulating BaTiO_3 . *Nat. Commun.* 4, (2013).
3. N. Balke *et al.*, Enhanced electric conductivity at ferroelectric vortex cores in BiFeO_3 . *Nat Phys* 8, 81 (2012).
4. C. L. Jia, K. W. Urban, M. Alexe, D. Hesse, I. Vrejoiu, Direct Observation of Continuous Electric Dipole Rotation in Flux-Closure Domains in Ferroelectric $\text{Pb}(\text{Zr},\text{Ti})\text{O}_3$. *Science* 331, 1420 (2011).
5. C. T. Nelson *et al.*, Spontaneous vortex nanodomain arrays at ferroelectric heterointerfaces. *Nano Lett.* 11, 828 (2011).
6. Y. L. Tang *et al.*, Observation of a periodic array of flux-closure quadrants in strained ferroelectric PbTiO_3 films. *Science* 348, 547 (2015).

Domain walls and ferroelectric reversal in corundum derivatives

Meng Ye

Institute for Molecular Engineering, University of Chicago, Chicago, Illinois 60615, USA and
Department of Physics and Astronomy, Rutgers University, Piscataway, New Jersey 08854-8019, USA*

David Vanderbilt

Department of Physics and Astronomy, Rutgers University, Piscataway, New Jersey 08854-8019, USA

Recently, attention has been drawn to a family of polar materials that can be regarded as derivatives of the corundum A_2O_3 structure but with cation ordering on the A site. The best-known examples are the binary-cation materials $LiNbO_3$ (LNO) and $LiTaO_3$, belonging to the general formula ABO_3 , but ternary-cation materials $A_2BB'O_6$ are also under investigation. Both the LNO-type ABO_3 and the ordered-LNO $A_2BB'O_6$ cation orderings are compatible with ferroelectricity along the rhombohedral axis [1], and their structures are illustrated in Fig. 1. Each cation is in a distorted oxygen octahedron; these only fill two thirds of the octahedral sites, leaving cation-vacant positions that we denote by “–”. The ferroelectric (FE) reversal is driven by migration of each A cation from its own oxygen octahedron to the cation-vacant octahedron above or beneath it [2, 3]. The reversal path can be qualitatively described by two variables ξ_1 and ξ_2 defined in Fig. 1(a).

Domain walls (DWs) are the topological defects that mediate polarization reversal in FEs, and they may exhibit quite different geometric and electronic structures compared to the bulk. Unfortunately, many of the newly

proposed ABO_3 and $A_2BB'O_6$ corundum derivatives are the result of high-pressure syntheses and are only available as powder samples, so that it remains unclear whether they can form FE domains that can be reversed by an electric field. Thus, until the experimental growth of single crystals and subsequent observation of DW motion can be achieved, theory can play an important role in understanding the static and dynamic properties of DWs in corundum derivatives.

In this work, we use first-principles methods to study the formation and motion of FE DWs in corundum derivatives at the atomic scale in order to characterize their intrinsic properties and their role in the FE reversal process. The FE candidates that we consider are $LiNbO_3$, $LiTaO_3$, $ZnSnO_3$, $FeTiO_3$, $MnTiO_3$, Li_2ZrTeO_6 , Li_2HfTeO_6 , and Mn_3WO_6 .

We construct a supercell with a polarization-up domain and a polarization-down domain that are related by inversion through a center located in the FE DW separating them. In addition, we assume that the B/B' and O sublattices are preserved throughout the supercell, so that the DW only results from the interchange of A and – sublattices (that is, migration of A cations into vacancies) on one side of the DW. This is motivated by the greater mobility of the A cation species. In addition, only the 180° charge-neutral DW is considered, in which the polarization direction is parallel to the DW plane but antiparallel between domains.

Different orientations of DWs are considered in our calculations. Since corundum derivatives have three-fold symmetry, there are two types of 180° DWs depending on the orientation of the DW plane. We refer to a DW in the x - z or $(01\bar{1}0)$ plane as an X-wall and one in the y - z or $(2\bar{1}\bar{1}0)$ plane as a Y-wall. Directions of the two planes are shown in Fig. 1(b). Our calculations reveal that the

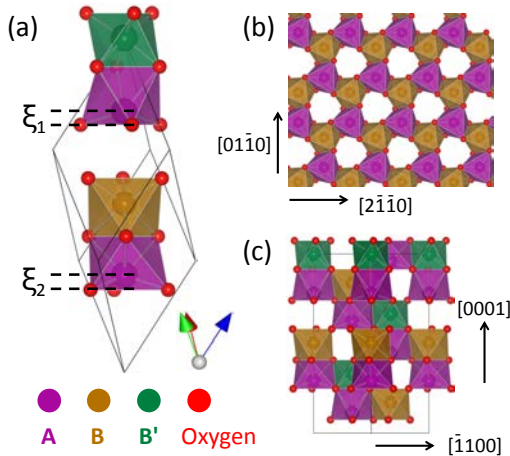


FIG. 1. Structure of ordered-LNO corundum derivatives $A_2BB'O_6$, and of LNO-type ABO_3 corundum derivatives if $B' = B$. (a) Side view of the rhombohedral unit cell. ξ_1 (or ξ_2) is the vertical distance between an A cation and the oxygen plane that it penetrates during the polarization reversal. (b) Top view of the AB layer and (c) side view in the enlarged hexagonal-setting cell.

TABLE I. Formation energies of X-walls and Y-walls, in units of mJ/m^2 . The magnetic orderings are shown in the column labeled “Mag.”.

| LNO-type | Mag. | X | Y | Ordered-LNO | Mag. | X | Y |
|-----------|--------------|-----|-----|---------------|----------------|----|----|
| $LiTaO_3$ | | 71 | 63 | Li_2ZrTeO_6 | | 29 | 20 |
| $LiNbO_3$ | | 160 | 138 | Li_2HfTeO_6 | | 30 | 21 |
| $ZnSnO_3$ | | 106 | 81 | Mn_3WO_6 | <i>uud-ud</i> | 68 | 42 |
| $MnTiO_3$ | <i>ud-ud</i> | 171 | 153 | Mn_3WO_6 | <i>udu-dud</i> | 67 | 41 |
| $FeTiO_3$ | <i>ud-ud</i> | 183 | 108 | Mn_3WO_6 | <i>udu-udu</i> | 75 | 45 |

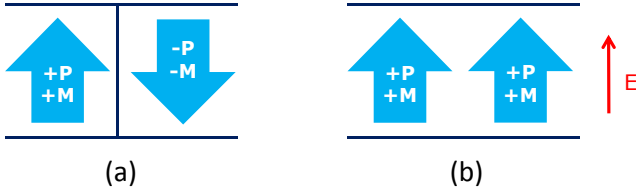


FIG. 2. Illustration of magnetolectric coupling at FE DWs when $udu-dud$ is favored. (a) Magnetization direction is coupled to the polarization direction in different FE domains. (b) When the polarization is reversed by an electric field, the magnetization reverses as well.

Y-wall is energetically favored in all the cases that we have studied, as shown by the converged DW formation energies in Table I.

We also consider the effect of FE DWs on the magnetic ordering in a prototype material Mn_3WO_6 . The magnetic ground state of Mn_3WO_6 that preserves the rhombohedral unit cell is the ferrimagnetic udu state, in which “ u ” and “ d ” represent spin-up and spin-down states on magnetic cations A_1 , A_2 and B in that order (A_1 and A_2 are face-sharing with B' and B cations). Because of the time-reversal symmetry, udu and dud have exactly the same energy in the bulk Mn_3WO_6 . However, there are two possibilities for the magnetic order across a FE DW: the magnetization may be the same on both sides of the DW, denoted by $udu-udu$, or it may reverse, denoted by $udu-dud$. Our computed formation energies for both the $udu-udu$ and $udu-dud$ DWs, summarized in Table I, suggest that the magnetization-reversing $udu-dud$ DW is energetically favored. Such an interlocking of FE and magnetic domains implies that the magnetization can be reversed by an electric field through the domain wall motion, as illustrated in Fig. 2. This provides an extrinsic

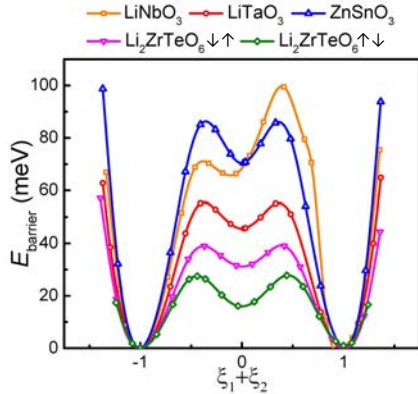


FIG. 3. Energy profiles of the DW reversal for selected corundum derivatives. Energy units are meV per unit cell.

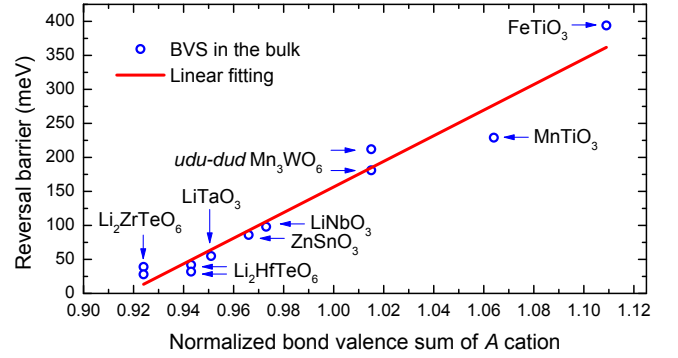


FIG. 4. Scatterplot of DW-mediated reversal barrier *versus* normalized A-cation bond valence sum (i.e., divided by valence charge).

reversal at the DW is achieved by using the reaction coordinate $\xi_1 + \xi_2$ as a structural constraint [1] and applying it only to the unit cell at the DW. The energy profiles of DW reversal for selected corundum derivatives are shown in Fig. 3.

In Fig. 4, we plot the DW reversal barrier *versus* the normalized bond valence sum (BVS) V_{BVS} defined through the equation [4]

$$V_{BVS} = \sum_i \exp[(R_0 - R_i)/b]. \quad (1)$$

V_{BVS} estimates the number of electrons that are associated with the local bonds. Here R_i is the bond length between A cations and the i th nearest neighboring oxygen anions, R_0 is a tabulated parameter and b is an empirical constant 0.37 \AA . A roughly linear relationship is observed between the normalized V_{BVS} of the A cations and the DW-mediated reversal barriers, which implies the dominance of short-range interactions in the corundum derivatives. This linear relationship can provide a useful rule of thumb in predicting the DW-mediated reversal barrier of potential new FE materials of the class of corundum derivatives.

* mengy@uchicago.edu

- [1] M. Ye and D. Vanderbilt, Phys. Rev. B **93**, 134303 (2016).
- [2] I. Inbar and R. E. Cohen, Phys. Rev. B **53**, 1193 (1996).
- [3] M. Veithen and Ph. Ghosez, Phys. Rev. B **65**, 214302 (2002).
- [4] I. D. Brown and D. Altermatt, Acta Crystallographica Section B **41**, 244 (1985).

Direct visualization of magnetoelectric domains

Yanan Geng¹, Hena Das², Aleksander L. Wysocki², Xueyun Wang¹, S-W. Cheong¹, M. Mostovoy³, Craig J. Fennie², and Weida Wu¹

¹Department of Physics and Astronomy and Rutgers Center for emergent materials, Rutgers University, Piscataway, NJ 08854 USA

²School of Applied and Engineering Physics, Cornell University, Ithaca, NY, 14853, USA

³Zernike Institute for Advanced Materials, University of Groningen, Nijenborgh 4, 9747 AG, Groningen, Netherlands

Multiferroics are materials with coexisting magnetic and ferroelectric orders. The cross-coupling between two ferroic orders can result in strong magnetoelectric (ME) coupling. Therefore, it is of both fundamental and technological interest to visualize topological defects of cross-coupled orders in multiferroics. Recently, topological defects with six interlocked structural antiphase and ferroelectric domains merging into a vortex core were revealed in multiferroic hexagonal manganites [1,2]. Numerous Z_6 -vortices were found to form an intriguing self-organized network, and were used to test Kibble-Zurek model of early universe [3,4]. Many emergent phenomena, such as enhanced conduction and unusual piezoelectric response, were observed in charged ferroelectric domain walls protected by these topological defects [5,6]. Using cryogenic magnetic force microscopy (MFM), we discovered alternating uncompensated magnetic moments at vortex domain walls in hexagonal manganites [7], which demonstrates the coupling between ferroelectric and magnetic orders.

In this talk, I will present the demonstration of a new microscopy technique called magnetoelectric force microscopy (MeFM), which is a combination of MFM and *in-situ* modulated electric fields (\mathbf{E}) to detect the \mathbf{E} -induced magnetization (\mathbf{M}_E), as illustrated in Figure 1. Using MeFM, we directly observed the local, intrinsic, i.e. bulk ME response of each multiferroic domain in the hexagonal (*h*-) ErMnO_3 , in excellent agreement with a symmetry analysis, a microscopic model and first-principles calculations [8]. Furthermore, a giant enhancement of the ME response was observed in the proximity of a critical point below 2 K, suggesting that critical fluctuations of competing orders may be harnessed for colossal \mathbf{E} -induced magnetic responses. The direct visualization of ME domains at mesoscopic scales opens up explorations of emergent phenomena in multifunctional materials with multiple coupled orders.

The FE domain pattern (Fig. 2a) on the (001) surface of *h*- ErMnO_3 was visualized with PFM at RT. Using topographic features as alignment marks, MeFM images were taken at the *same* location [7]. In zero magnetic field, the Mn^{3+} spins order in a 120° pattern with magnetic symmetry $P\bar{6}_3cm$ (B_2), which forbids any linear magnetoelectric effect [9]. Consistently, no MeFM contrast was observed in 0 T at 4 K (Fig. 2b) with $E=10$ kV/cm. In a large field, an A_2 ($P6_3cm$) phase, which allows diagonal components of α , emerges from the B_2 ground state [9,11]. In the A_2 phase, the in-plane Mn^{3+} spins rotate through 90° from that of the B_2 phase, resulting in a net magnetic moment (M_z) along the z -axis due to canting of spins

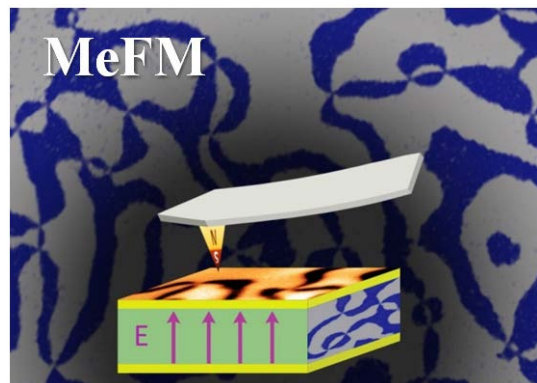


Figure 1 | Cartoon of MeFM. MeFM is a combination of MFM and *in-situ* electric field. Background: PFM image of Z_6 vortex domains of *h*- ErMnO_3 . A MeFM image of *h*- ErMnO_3 is shown on top of sample.

of Mn^{3+} ions. Indeed, a sharp MeFM contrast was observed in 8 T at 4 K (Fig. 2d). The sign of the MeFM signal changes at ferroelectric domain walls, i.e. the ME domain pattern is identical to the ferroelectric one (Fig. 2c), suggesting $\alpha_{zz} \propto M_z P_z$. In the A_2 phase, M_z originates from anisotropic Dzyaloshinskii-Moriya interactions between neighboring Mn^{3+} spins [8]. A symmetry analysis shows that $M_z \propto \mathbf{L}_{A_2} \cdot \mathbf{Q}_{K_3}$, where \mathbf{L}_{A_2} is the magnetic order parameter describing the symmetry of the A_2 phase. Because $P_z \propto Q_{K_3} \cos 3\Phi$ at $T \ll T_c$ [12], the trimer mode (\mathbf{Q}_{K_3}) mediates an effective cross-coupling between P_z and M_z (\mathbf{L}_{A_2}), i.e. a linear magnetolectric effect (Fig. 2e). This effect can also be understood in terms of a simple phenomenological free energy expansion $f^{\text{ME}} \propto \cos(3\Phi) L_{A_2} E_z H_z$ derived from a symmetry analysis, giving $\alpha_{zz} \propto \cos(3\Phi) L_{A_2} \propto M_z P_z$, which is in excellent agreement with our experimental observation and the recent microscopic model [8]. Qualitatively, the \mathbf{E} -field induces changes of \mathbf{Q}_{K_3} through \mathbf{P} , leading to changes of \mathbf{M}_z (Fig. 2f). The excellent agreement between our MeFM results and the microscopic model provides compelling evidence for the fundamental mechanism of lattice mediated ME couplings, which may be generalized to other materials [8,13].

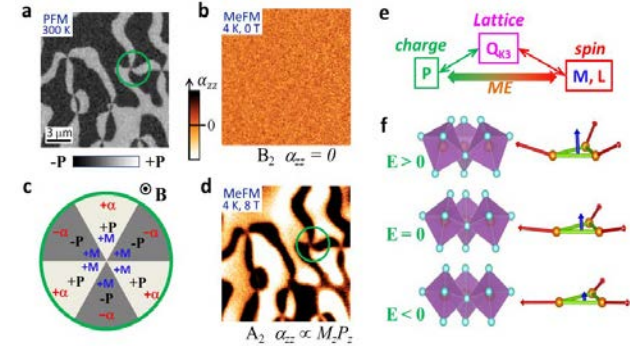


Figure 2 | MeFM results of $h\text{-ErMnO}_3$. a, b and d, RT-PFM image, 4 K MeFM images at 0 and 8.0 T, were taken at the *same* location on the (001) surface of a $h\text{-ErMnO}_3$ single crystal, respectively. The white (dark) color in PFM image represents up (down) ferroelectric domain. c, a cartoon of the ME coefficient (α_{zz}) of the A_2 phase in different ferroelectric domains in $h\text{-ErMnO}_3$. e, a cartoon illustration of the effective ME coupling via structural instability. f, cartoon illustrations of the mechanism of lattice-mediated ME response.

Reference

- [1] T. Choi, Y. Horibe, H. T. Yi, Y. J. Choi, W. Wu, and C. S-W., Nat. Mater. **9**, 253 (2010).
- [2] T. Jungk, Á. Hoffmann, M. Fiebig, and E. Soergel, Appl. Phys. Lett. **97**, 012904 (2010).
- [3] S. M. Griffin, M. Lilienblum, K. T. Delaney, Y. Kumagai, M. Fiebig, and N. A. Spaldin, Phys. Rev. X **2**, 041022 (2012).
- [4] S.-Z. Lin *et al.*, Nature Physics **10**, 970 (2014).
- [5] E. B. Lochocki, S. Park, N. Lee, S.-W. Cheong, and W. Wu, Appl. Phys. Lett. **99**, 232901 (2011).
- [6] W. Wu, Y. Horibe, N. Lee, S.-W. Cheong, and J. R. Guest, Phys. Rev. Lett. **108**, 077203 (2012).
- [7] Y. Geng, N. Lee, Y. J. Choi, S. W. Cheong, and W. Wu, Nano Letters **12**, 6055–6059 (2012).
- [8] H. Das, A. L. Wysocki, Y. Geng, W. Wu, and C. J. Fennie, arXiv:1302.1099 (2013).
- [9] T. H. O'Dell, *The electrodynamics of magneto-electric media* (North-Holland, Amsterdam, 1970), Seires of monographs on selected topics in solid state physics.
- [10] F. Yen, C. dela Cruz, B. Lorenz, E. Galstyan, Y. Y. Sun, M. Gospodinov, and C. W. Chu, J. Mater. Res. **22**, 2163 (2007).
- [11] T. Lottermoser, T. Lonkai, U. Amann, D. Hohlwein, J. Ihringer, and M. Fiebig, Nature **430**, 541 (2004).
- [12] C. J. Fennie and K. M. Rabe, Phys. Rev. B **72**, 100103(R) (2005).
- [13] W. Wang *et al.*, Phys. Rev. Lett. **110**, 237601 (2013).

Surface potential imaging of polar ferroelastic domain walls

N. Barrett,¹ G. Nataf,^{1,2} M. Guennou,² J. Kreisel,² P. Hicher,²
R. Haumont,³ L. Tortech,¹ D. Martinotti,¹ and C. Mathieu¹

¹*SPEC, CEA, CNRS, Université Paris Saclay, CEA-Saclay, 91191 Gif sur Yvette cedex, France**

²*Materials Research and Technology Department,*

Luxemburg Institute of Science and Technology, 41 rue du Brill, 4422 Belvaux, Luxembourg

³*ICMMO, UMR CNRS 8182, Bt 410 Université Paris Sud. 91405 Orsay Cedex, France*

Ferroic domain walls may play an important role in post-CMOS electronics, given their small size and distinct functional properties. We demonstrate that the polarization in domain walls of CaTiO_3 locally modifies the surface potential. We use low energy electron microscopy to measure surface potential variations and show that it can be controlled by electron injection. This may enable devices based on a non-destructive information readout of domain wall polarity.

PACS numbers: 68.37.Xy, 71.15.Mb, 73.20.At, 77.80.Dj

Ultra-high storage densities combined with low power consumption is a major challenge for post-CMOS electronics in order to enable downscaling [1]. Domain wall (DW) engineering in ferroic materials is one possible route where the DW rather than the bulk material becomes the active element. Compared with domains, DWs are much smaller, inhomogeneous, and may have lower symmetry and completely different static or dynamic physical properties. The challenge then is to predict and control the nanoscale DW functionality [2]. DW conductivity in ferroelectrics is one functionality that is now well established and has been intensely studied [3]. Charged DWs can show conductivity many orders of magnitude higher than in bulk domains or in neutral DWs [4], providing a potential route for nanometric metallic sheets in a dielectric matrix. Proofs of concept for device applications have already been given [5].

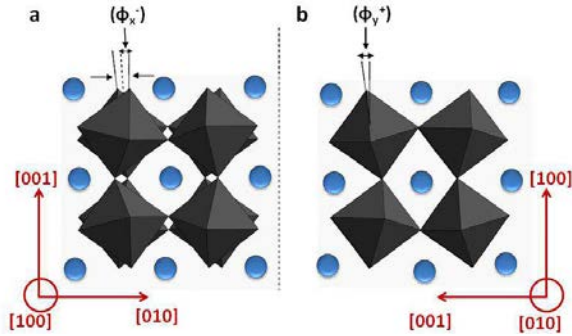


FIG. 1. Projections of the crystal structure viewing tilt angles along (a) the $[100]$ and (b) $[001]$ directions.

Ferroelastic materials can contain a very high density of functional twin boundaries or ferroelastic DWs. Twins can be polar [6] with dipole moments in the wall aligned parallel or antiparallel [7] to the apex and therefore serve as robust, nanoscale functional devices such as memory

cells.

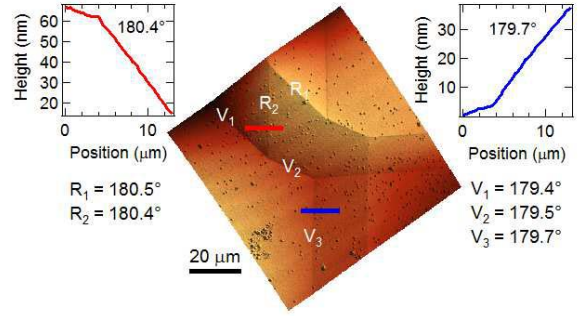


FIG. 2. AFM topography of the sample surface. The valleys and ridges of the domain walls are labeled V and R, respectively. The insets show the height profile perpendicular to a ridge (red) and to a valley (blue).

In ferroelastic walls quite remarkable phenomena are observed, e.g., twin walls that can support superconducting currents within an otherwise insulating material [8]. The mineral perovskite, CaTiO_3 (CTO) consists of corner linked TiO_6 octahedra with Ca atoms distributed between the octahedra. Its distortion from the ideal cubic structure is explained by the tilting of deformable TiO_6 octahedra around their three symmetry axes. Under ambient conditions, CTO has $Pbnm$ symmetry and a Glazer octahedral tilt system of $a^-a^-c^+$. The symmetry reduction from cubic to orthorhombic allows for twinning, i.e. domains with slightly different orientations separated by twin walls. The primary order parameter, the octahedral tilt, dominates in the bulk of the uniform solid and disappears inside the wall. Competing secondary order parameters such as polarity show the inverse behavior, appearing inside twin walls while being suppressed in the bulk [9].

We have used low energy electron microscopy (LEEM) and Atomic Force Microscopy (AFM) to probe the polarity of twin boundaries or DWs in the non-polar dielectric single-crystal oxide CaTiO_3 . Five DWs are labelled in the 3D AFM map of Fig 2 (center): two ridges R1 and R2; three valleys V1, V2 and V3. These twins create a factory roof-like surface topography, although as shown in the insets the tilt angles are very small.

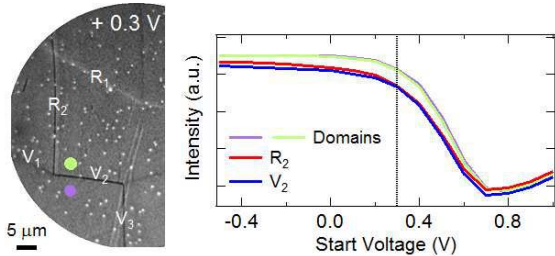


FIG. 3. Electron image at SV 0.3 V and reflectivity as a function of SV showing a 100 mV shift in the MEM-LEEM transition to lower SV at the DWs.

Figure 3(left) shows the electron image of the surface. Adjacent domains present the same intensity because the material is non-polar and therefore the work function is not expected to change from one domain to another. This is similar to the case of in-plane polarized ferroelectric domains in, for example, BaTiO_3 [10]. R1 is bright, corresponding to negative polarity whereas R2, V2 and V3 are dark suggesting a positive or outwards pointing polarity. Furthermore, on electron injection, the latter are screened and the contrast disappears.

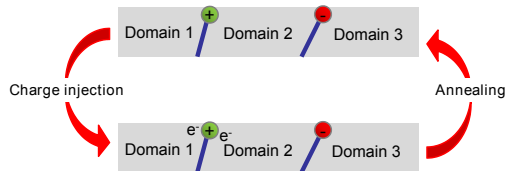


FIG. 4. Cartoon showing the reversible screening of positive (upward pointing) DW by electron injection.

The screening is reversible under annealing at 300°C whereas the positions of the DW do not change. This is strong evidence of the polar nature of ferroelastic twins in CaTiO_3 and both valleys and ridges can have inwards or outwards pointing polarity, as predicted by theory [7]. The polarity results from biquadratic coupling between the antiferrodistortive tilts of the oxygen octahedral and the polarization. Flexoelectricity can also polarize walls due to the strong local strain gradients [11].

We gratefully acknowledge funding from the Agence Nationale de la Recherche project CHEM-SWITCH and HREELM.

* Correspondence should be addressed to nick.barrett@cea.fr

- [1] A. Srivastava, ed., *Nano-CMOS and Post-CMOS Electronics: Devices and Modelling*, Materials, Circuits & Devices (Institution of Engineering and Technology, 2016).
- [2] G. Catalan, J. Seidel, R. Ramesh, and J. F. Scott, *Reviews of Modern Physics* **84**, 119 (2012).
- [3] J. Seidel, L. W. Martin, Q. He, Q. Zhan, Y.-H. Chu, a. Rother, M. E. Hawkrige, P. Maksymovych, P. Yu, M. Gajek, N. Balke, S. V. Kalinin, S. Gemming, F. Wang, G. Catalan, J. F. Scott, N. a. Spaldin, J. Orenstein, and R. Ramesh, *Nature materials* **8**, 229 (2009).
- [4] T. Sluka, A. K. Tagantsev, P. Bednyakov, and N. Setter, *Nature Communications* **4** (2013), 10.1038/ncomms2839.
- [5] J. R. Whyte and J. M. Gregg, *Nature communications* **6**, 7361 (2015).
- [6] D. D. Viehland and E. K. Salje, *Advances in Physics* **63**, 267 (2014).
- [7] T. Zykova-Timan and E. K. H. Salje, *Applied Physics Letters* **104**, 2012 (2014).
- [8] A. Aird and E. Salje, *J. Phys.: Condens. Matter* **377** (1998).
- [9] L. Goncalves-Ferreira, S. A. T. Redfern, E. Artacho, E. Salje, and W. T. Lee, *Physical Review B - Condensed Matter and Materials Physics* **81**, 1 (2010).
- [10] J. E. Rault, T. O. Mente, a. Locatelli, and N. Barrett, *Scientific reports* **4**, 6792 (2014).
- [11] E. K. H. Salje, S. Li, M. Stengel, P. Gumbsch, and X. Ding, *Physical Review B - Condensed Matter and Materials Physics* **94**, 1 (2016).

Polar Metals by Geometric Design

T. H. Kim¹, D. Puggioni², Y. Yuan³, L. Xie^{4,5}, H. Zhou⁶, N. Campbell⁷, P. J. Ryan⁶, Y. Choi⁶, J.-W. Kim⁶, J. R. Patzner¹, S. Ryu¹, J. P. Podkaminer¹, J. Irwin⁷, Y. Ma, C. J. Fennie⁸, M. S. Rzchowski⁷, X. Pan⁴, V. Gopalan³, J. M. Rondinelli², C. B. Eom^{1*}

¹Department of Materials Science and Engineering, University of Wisconsin-Madison, Madison, Wisconsin 53706, USA

²Department of Materials Science and Engineering, Northwestern University, Evanston, Illinois 60208

³Department of Materials Science and Engineering and Materials Research Institute, Pennsylvania State University, University Park, Pennsylvania 16802, USA.

⁴Department of Chemical Engineering and Materials Science and Department of Physics and Astronomy, University of California-Irvine, Irvine, California 92697, USA.

⁵National Laboratory of Solid State Microstructures and College of Engineering and Applied Sciences, Nanjing University, Nanjing, Jiangsu 210093, China.

⁶Advanced Photon Source, Argonne National Laboratory, Argonne, Illinois 60439, USA

⁷Department of Physics, University of Wisconsin-Madison, Madison, Wisconsin 53706, USA.

⁸School of Applied and Engineering Physics, Cornell University, Ithaca, New York 14853, USA.

*Correspondence and requests for materials should be addressed to ceom@wisc.edu

Gauss's law dictates that the net electric field inside a conductor in electrostatic equilibrium is zero by effective charge screening; free carriers within a metal eliminate internal dipoles that may arise owing to asymmetric charge distributions. Quantum physics supports this view, demonstrating that delocalized electrons make a static macroscopic polarization, an ill-defined quantity in metals—it is exceedingly unusual to find a polar metal that exhibits long-range ordered dipoles owing to cooperative atomic displacements aligned from dipolar interactions as in insulating phases. Here we describe the quantum mechanical design and experimental realization of room-temperature polar metals in thinfilm $ANiO_3$ perovskite nickelates using a strategy based on atomicscale control of inversion-preserving (centric) displacements. We predict with *ab initio* calculations that cooperative polar A cation displacements are geometrically stabilized with a nonequilibrium amplitude and tilt pattern of the corner-connected NiO_6 octahedra—the structural signatures of perovskites—owing to geometric constraints imposed by the underlying substrate. Heteroepitaxial thin-films grown on $LaAlO_3$ (111) substrates. Heteroepitaxial thin-films grown on $LaAlO_3$ (111) substrates fulfil the design principles. We achieve both a conducting polar monoclinic oxide that is inaccessible in compositionally identical films grown on (001) substrates, and observe a hidden, previously unreported, non-equilibrium structure in thin-film geometries [1]. We expect that the geometric stabilization approach will provide novel avenues for realizing new multifunctional materials with unusual coexisting properties.

References

1. “Polar Metals by Geometric Design”, T. H. Kim, D. Puggioni, Y. Yuan, L. Xie, H. Zhou, N. Campbell, P. J. Ryan, Y. Choi, J.-W. Kim, J. R. Patzner, S. Ryu, J. P. Podkaminer, J. Irwin, Y. Ma, C. J. Fennie, M. S. Rzchowski, X. Q. Pan, V. Gopalan, J. M. Rondinelli, and C. B. Eom, *Nature* **533**, 68 (2016)

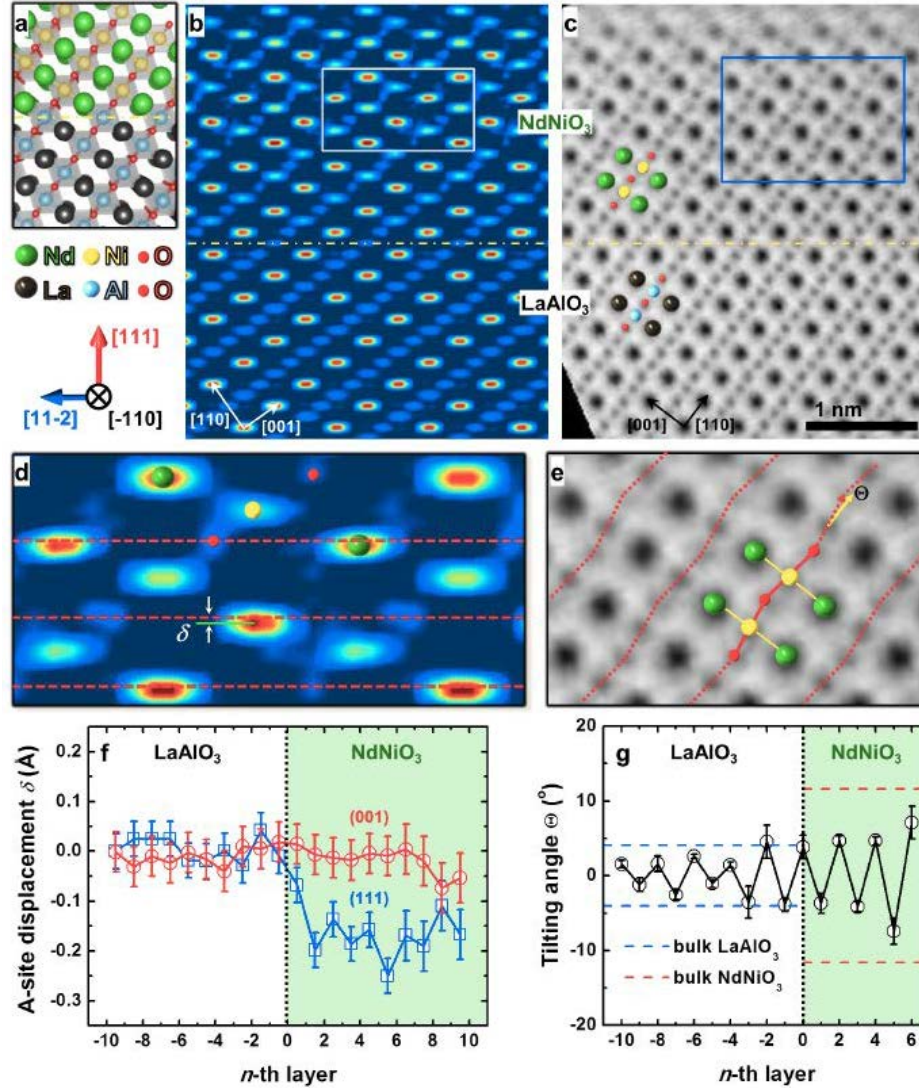


Figure. Non-centrosymmetric NdNiO₃ thin films on LaAlO₃ (111) substrates. **a**, Schematic illustration of the atomic-scale thin-film heterostructure, **b**, **c**, Two-dimensional electron density maps sliced through the pseudocubic (110) plane reconstructed through synchrotron CTR measurements and subsequent COBRA analyses (**b**) and STEM-ABF images captured along the pseudocubic [110] zone axis in cross-sectional view (**c**). In **a**–**c**, the interface is marked by the yellow dash–dotted lines. **d**, **e**, Magnified images of electron density maps (**d**) and ABF images (**e**) for the regions indicated by open rectangles in **b** and **c**, respectively. In **d**, red broken lines represent the positions of oxygen atoms (marked with red colors), which are taken as references to measure relative off-center displacements (δ) of Nd atoms (marked with green colors). In **e**, red broken lines are used as guidelines to show tilting of the NiO₆ octahedra in the NdNiO₃ layer with an angle of Θ , obtained by calculating the angle formed between a line (O–O, red dotted arrow) connecting two nearest oxygen atoms and another line (B–B, yellow solid arrow) connecting two nearest B-site atoms. **f**, **g**, Layer-dependent evolution of the A-site relative polar displacements (**f**) and BO₆ octahedra tilt angles (**g**) across the interface in NdNiO₃/LaAlO₃ (111) thin films. The 0th layer represents the NdNiO₃/LaAlO₃ interface. In the two-dimensional electron density map of **b**, the A-site acentric displacements shown in **f** are measured with respect to oxygen atoms as displayed in **d**. Error bars are statistical, based on measurements of the A-site displacement (**f**) or tilting angle (**g**). Details of the statistical analyses used are described in Methods. In **g**, the blue and red broken lines represent the tilting angles of bulk LaAlO₃ ($\sim -4.0^\circ$) and NdNiO₃ ($\sim 11.6^\circ$), respectively.

Ab-initio Design of Two-Dimensional Electron Gas in Nonpolar/Nonpolar Oxide Interface via Polarization Discontinuity

Kesong Yang*

Department of NanoEngineering, University of California San Diego, CA 92093, USA

Email: kesong@ucsd.edu, web site: <http://www.nano.ucsd.edu/~kesong/>

All-oxide electronics represents one of the most promising technologies for next-generation nanoelectronic devices beyond the traditional silicon technology, and producing two-dimensional electron gas (2DEG) at the interface of heterostructures (HS) is one of the most attractive technologies for nanoelectronics application. Recent discovery of 2DEG induced by the polar catastrophe (discontinuity) at the polar/nonpolar $(\text{LaO})^{1+}/(\text{TiO}_2)^0$ interface between LaAlO_3 (LAO) and SrTiO_3 (STO) perovskite insulators opens a new avenue to prepare highly conductive oxides.[1]

In addition to the polar catastrophe, another possible approach to produce 2DEG is via polarization discontinuity, see **Figure 1**. Compared to the success of producing 2DEG via polar catastrophe, few efforts have been made to explore possibility of producing 2DEG in the perovskite-oxide HS through polarization discontinuity. In particular, the two perovskite oxides forming the oxide heterostructure could be both nonpolar. Compared to the success of producing 2DEG in the polar/nonpolar LAO/STO system, the 2DEG at the nonpolar/nonpolar perovskites interface remains rarely explored. Moreover, the polarization-discontinuity-induced 2DEG has a great advantage as compared to that induced by polar catastrophe, that is, the polarization can be controlled by an external electrical field, and thus the interfacial conductivity can be tuned more efficiently, and the heterostructure is readily implemented in practical devices. Since many perovskite oxides are equipped with ferroelectric/piezoelectric property, to study perovskite-based 2DEG systems via polarization discontinuity is of great fundamental and practical interests.

Interestingly, very recently, Chen and co-workers have reported an insulator-to-metal transition in the nonpolar/nonpolar $\text{CaZrO}_3/\text{SrTiO}_3$ HS, and found that the system shows a metallic behavior at t (CaZrO_3 film thickness) > 6 uc, but has insulating behavior at $t \leq 6$ uc.[2] By combining scanning transmission electron microscopy (STEM) and electron energy-loss spectroscopy (EELS) characterization, they found that the Ca^{2+} and Zr^{4+} cations in the CaZrO_3 film move toward the SrTiO_3 substrate, which is caused by the lattice-mismatch-induced compressive strain on the CaZrO_3 film. This indicates that the relative displacement between the cations and anions in the CaZrO_3 film produces a piezoelectric polarization, which plays a crucial role in forming the 2DEG in the $\text{CaZrO}_3/\text{SrTiO}_3$ HS system. In spite of the encouraging

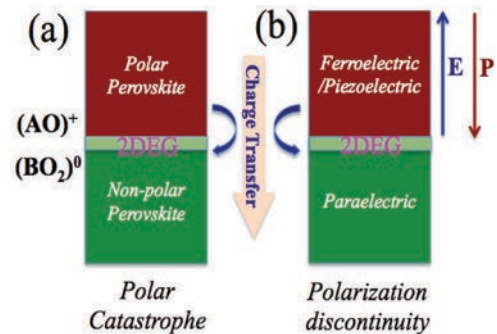


Figure 1: Scheme of the formation mechanism of the 2DEG via (a) polar catastrophe and (b) polarization discontinuity. The former drives the charge transfer from the $(\text{AO})^+$ layer to the $(\text{BO}_2)^0$ layer, forming 2DEG. The latter refers to that the internal electrostatic field (E) drives the charge transfer from the polarized domain to the non-polarized paraelectric domain, forming the 2DEG.

experimental finding, several open fundamental questions naturally arise, such as the influence of the surface termination on the interfacial electronic properties and the dependence of the electron transport property on the thickness of the CaZrO₃ film.

To reveal the origin of interfacial conductivity in the CaZrO₃/SrTiO₃ HS, we have studied the structural and electronic properties of nonpolar/nonpolar CaZrO₃/SrTiO₃ using first-principles electronic structure calculations.[3] In this system, four types of HS-based slab models were studied, i.e., TiO₂/CaO and SrO/ZrO₂ interface models with CaO and ZrO₂ surface terminations in each model. We investigated the strain-induced polarization and resulting electronic properties in these models and found that there exists an insulator-to-metal transition as the CaZrO₃ film thickness increases, which is well consistent with the experimental findings. To further verify the hypothesis to produce the 2DEG via polarization discontinuity in the perovskite-oxide HS, we have also explored the possibility of producing a 2DEG at nonpolar/nonpolar AHfO₃/SrTiO₃ (A=Sr, Ca, and Ba) interface via modeling HS-based slab systems.[4] We found that there also exists a critical film thickness to produce a strong enough polarization toward the interface and resulting insulator-to-metal transition in the AHfO₃/SrTiO₃ system. In these two types of HS systems, the polarization magnitude as a function of the film thickness, charge transfer mechanism, interfacial electronic states, and charge carrier density were discussed in detail. This work reveals a clear picture for the strain-induced polarization and consequent formation of the 2DEG at the perovskite interfaces, and provides a possible approach to create 2DEG via strain-induced polarization discontinuity in the nonpolar/nonpolar perovskite oxide heterostructures.

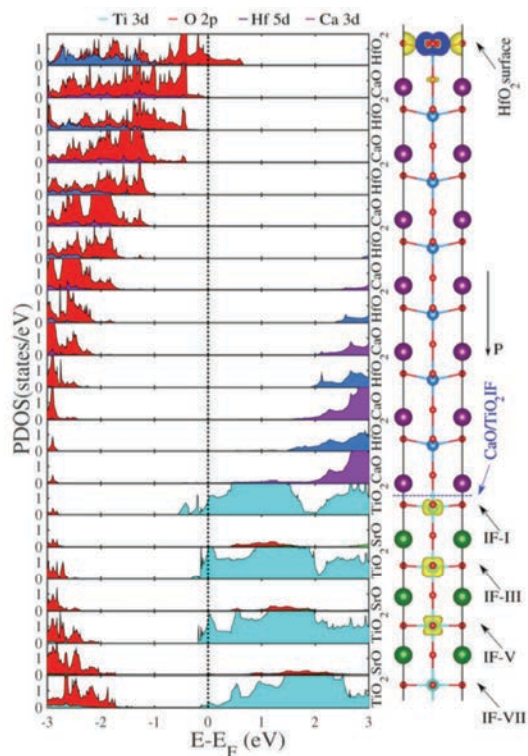


Figure 2: Calculated layer-resolved partial DOS for the (CaO)⁰/(TiO₂)⁰ interface model with HfO₂ surface termination in the (CaHfO₃)₇/SrTiO₃ HS, along with its charge density plot projected on the bands forming the metallic states.

7886: , -\$1 \$;< +6 ? 2%&; 6 @+66,4&A1 \$B4C5) -3%62#6-6, " 62<5 E0F3G4 E6 "-3\$4%" 32)" +;6
 I 2-(3"6JKL;6)KEAJKM67KNNJ96

7166O, "%6@=#6626O3"2-4%66H 4, 61 \$B4C6? \$A41 "%#\$%255") -3%62#6#P26#-324%6*() "*"6
 .523Q-4%6-62%\$-,"3 ? 4"6%\$%.536 \$1 .5"R6R4"64%"312"); 6 2%"6D"-6S;6TJU8TSJ;6KN8S96

7E6I 2Q43F2H23+6O, "%&;6/+6O%&;6V6O3"2-4%66G? \$A41 "%#\$%26/5) -3%62#6#6\$%.523I \$%.5236
 : R4"6["312)"6P26 \$523Q-4%66#) \$%4%(40643#A 34%4.5#6<?2564#6\$H6D'3 E0F3G4: E6
 >-"3\$#-3) -(3"; 6<OF6<.5 6_2-" 31%" 32)" #6;6EUNEUU67KN8M66

7J6O,"%&;6/+6 2Q43F2H23+6O%&;6V6O 4#A 34%4.5#6\3' * 4)-4\$6\$H6D\$A41 "%#\$%26/5) -3%62#6
 X3P"%66 \$523Q-4%66#) \$%4%(40646\$%.523I \$%.5236<>H E0F3G4 E6< O2;6F362%"6296
 >-"3\$#-3) -(3"#6<OF6<.5+62-"3-6%"312)"# 6;6E8USU6E8UML67KN8M66

Electron Doping and Charge Ordering of SmNiO_3 from First Principles

Michele Kotiuga and Karin M. Rabe

Department of Physics and Astronomy

Rutgers, The State University of New Jersey, Piscataway, NJ, USA

mkotiuga@physics.rutgers.edu

Rare earth nickelates (ReNiO_3) have rich phase diagrams involving charge, orbital and magnetic order. Most notably, all of these materials, with the exception of $\text{Re}=\text{La}$, undergo a metal-insulator transition, which is accompanied by a Ni-O bond disproportionation [1, 2]. The structural change takes the metallic $Pbnm$ structure, with all Ni sites equivalent, to a monoclinic $P2_1/n$ with two inequivalent Ni sites [3, 4] (see Fig. 1(a) and (b)). In recent experimental work, doping SmNiO_3 (SNO) with interstitial hydrogen at room temperature has resulted in a new insulating state, characterized by a large change in the resistivity [5]. In this work we begin with a study of electron doping of SNO and the subsequent change in the gap. Then we turn our attention to the bond disproportionation of SNO with a variety of charge orderings (for example Fig. 1(c) and (d)) and the potential to generate polar phases in a superlattice with other rare earth nickelates.

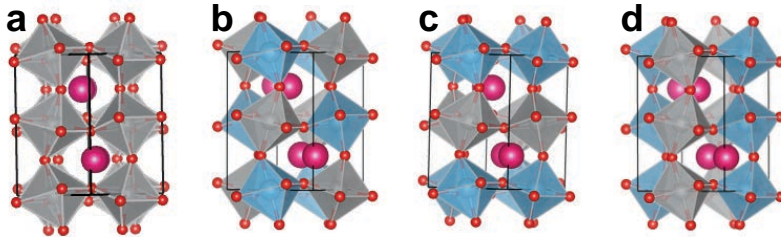


FIG. 1. (a) $Pbnm$ structure of SNO; (b) $P2_1/n$ structure of SNO with checkerboard charge ordering; (c) $P2_1/a$ structure of SNO with layering charge ordering; (d) $P2_1/m$ structure of SNO with columnar charge ordering

At room temperature, SNO contains nominally Ni^{3+} and is a small gap insulator. Upon doping, the added hydrogen splits into a proton and an electron. The electron localizes on a Ni site resulting in a half filled e_g band and a large splitting between the occupied and unoccupied e_g states. Here we use density functional theory (DFT) + U method within the generalized gradient approximation (using the PBE functional) to study the effect of added electrons on the crystal and electronic structure of SNO. We consider added electron concentrations of $\frac{1}{4}$, $\frac{1}{2}$, $\frac{3}{4}$ and 1 electron per Ni (see Fig. 2). We focus on the change in electronic structure between the undoped and fully doped (1 electron per Ni) cases. We analyze the changes in the local crystal and electronic structure and magnetic ordering, and relate the changes to the changes in optical and transport properties observed experimentally. We find that the fully doped SNO has a gap of ~ 3 eV, much larger than the ~ 0.5 eV gap of undoped SNO, and that the gap is relatively independent of octahedral distortions and magnetic ordering.

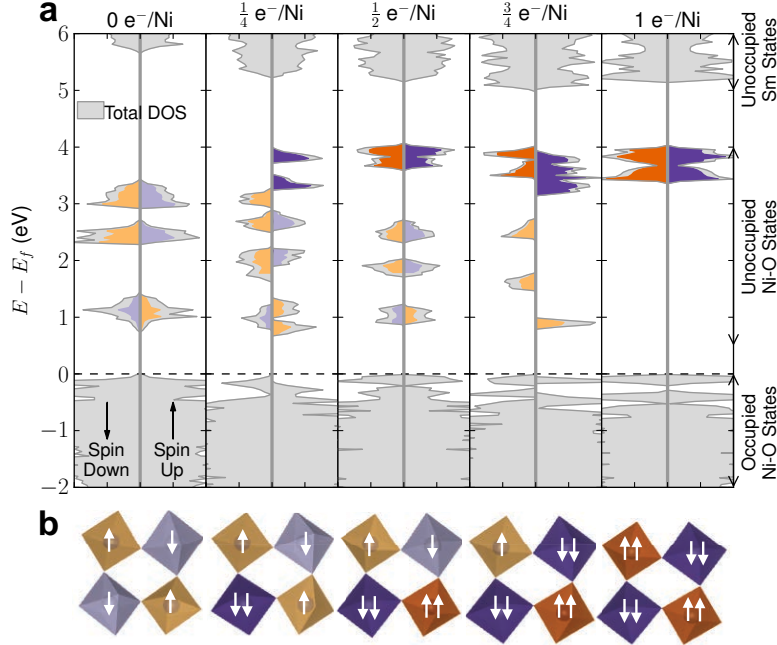


FIG. 2. (a) The total density of states (DOS), shown in gray, of SNO at doping concentrations of 0, $\frac{1}{4}$, $\frac{1}{2}$, $\frac{3}{4}$ and 1 electron per Ni. The unoccupied Ni projected density of states (PDOS) is shown in color, orange and purple corresponding to the appropriate Ni sublattice. The lighter colors indicate Ni³⁺ and the darker, Ni²⁺. The difference between the total DOS and PDOS illustrates the covalent nature of the NiO₆ octahedron. (b) The occupied e_g levels of each Ni for the corresponding doping levels. The direction of the arrows indicated spin up and down. The same color scheme is used as above.

Even though the gap is not very sensitive to the crystal and magnetic structure, the character of the occupied bands is affected. We investigate the variation of the electronic structure due to various charge ordering patterns, such as rock salt and other layered and columnar patterns (see Fig. 1). Finally, we construct a superlattices with EuNiO₃, including polar phases [6], and study their preferred charge orderings and electronic structure.

-
- [1] S. Middey, J. Chakhalian, P. Mahadevan, J. Freeland, A. Millis, and D. Sarma, Annual Review of Materials Research **46** (2016).
 - [2] R. J. Green, M. W. Haverkort, and G. A. Sawatzky, Physical Review B **94**, 195127 (2016).
 - [3] H. Park, A. J. Millis, and C. A. Marianetti, Physical Review B **89** (2014).
 - [4] J. Varignon, M. N. Grisolia, J. Íñiguez, A. Barthélémy, and M. Bibes, arXiv:1603.05480 (2016).
 - [5] J. Shi, Y. Zhou, and S. Ramanathan, Nature Cosmmunications **5**, 4860 (2014).
 - [6] S. Y. Park, A. Kumar, and K. M. Rabe, arXiv:1606.07835 (2016).

Engineering a ferroelectric superlattice from metallic components

Saurabh Ghosh^{1,2}, Rohan Mishra^{1,2,3}, Albina Y. Borisevich^{1,2} and Sokrates T. Pantelides^{1,2}

¹Department of Physics and Astronomy, Vanderbilt University, Nashville, Tennessee 37235, USA

²Materials Science and Technology Division, Oak Ridge National Laboratory, Oak Ridge, Tennessee 37831, USA

³Department of Mechanical Engineering and Materials Science, Washington University in St. Louis, St. Louis, Missouri 63130, USA

Email: saurabh.ghosh@vanderbilt.edu; ghoshs@ornl.gov

Ferroelectrics are insulating materials with spontaneous microscopic polarization, which can be reversed by the application of an electric field [1]. Interestingly, in 1965, Anderson and Blount first suggested that polar displacements, which drive a material from a high-symmetry paraelectric phase to a low-symmetry ferroelectric phase, can exist in a metal [2]. However, successful coupling between an external electric field and polarization demands that the system must be an insulator because a nonzero electric field cannot be sustained in a metal. The question then arises if it is possible to design a material that undergoes a transition from a ferroelectric-like metallic (FEL/M) phase to a true ferroelectric insulating (FE/I) phase. To achieve such transition, two conditions need to be satisfied: First, the polar displacements need to be present in both phases and second; the system has to go through a metal-insulator transition. Transition metal oxides (TMO) heterostructures offer many adjustable parameters to engineer functional properties including metal-insulator transitions and ferroelectricity [3, 4] and could therefore be a logical choice to find such a system.

Here, we use first-principles density-functional-theory (DFT) and DFT+U (static $d-d$ Coulomb interaction) calculations to consider superlattices (SLs) constructed from metallic components and propose a mechanism to functionalize FEL/M-to-FE/I transition. We have considered $(\text{La}_{0.75}\text{Sr}_{0.25}\text{MnO}_3)_m / (\text{LaNiO}_3)_n$ superlattices (SLs) as both $\text{La}_{0.75}\text{Sr}_{0.25}\text{MnO}_3$ and LaNiO_3 are metallic oxides [5, 6]. We found that within short-period SLs of the form $(\text{La}_{0.75}\text{Sr}_{0.25}\text{MnO}_3)_m / (\text{LaNiO}_3)_n$ (where $m/n = 1/1, 2/2, 3/1$), 2/2 SL can have a FEL/M phase that can undergo a metal-insulator transition. Further, we predict that insulating SL 2/2 is ferroelectric with large spontaneous polarization (i.e., FE/I phase). The high symmetry structure of 2/2 SL is $P4/mmm$. The dominant distortions present in $P4/mmm$ superlattice are mainly octahedral rotations. However, careful analysis of phonon modes reveals a hidden ‘ferroelectric like (FEL)’ mode as shown in Figure 1(a), which transforms like the irreducible representation Γ_5 of $P4/mmm$. The lowest symmetry phase is found to be Pm , which is a non-centrosymmetric space group and thus can be polar. The high symmetry $P4/mmm$ and low symmetry Pm phase are related to each other as, $P4/mmm \rightarrow a^0 a^0 c^+ + (a^- a^- c^0 + \text{FEL}) \rightarrow Pm$, where $a^0 a^0 c^+$ and $a^- a^- c^0$ are octahedral rotation and tilt distortions, respectively.

The lowest energy magnetic state for both the structures are found to be antiferromagnetic with zero net magnetic moment. Furthermore, the lowest energy Pm phase is found to be metallic. The important question is how to open the gap? It has been reported that double perovskite $\text{La}_2\text{MnNiO}_6$, both in orthorhombic and monoclinic structure, is insulating [7]. Informed by this finding, we can rephrase the original question: (a) Can Mn/Ni intermixing opens the gap? and if it opens the gap then, (b) can the ferroelectric mode persist and ferroelectric polarization be measured in an intermixed structure? To investigate this we have considered different patterns of Mn/Ni

intermixing and found that changing the degree of intermixing can cause the system to transition from FEL/M phase to a true ferroelectric insulating FE/I phase. Moreover, the degree of intermixing can tune the band gap. Structural analysis reveals that the ‘ferroelectric like’ mode also persists after opening the gap. The calculated polarization in Pm phase is found to be $9.31 \mu\text{C}/\text{cm}^2$.

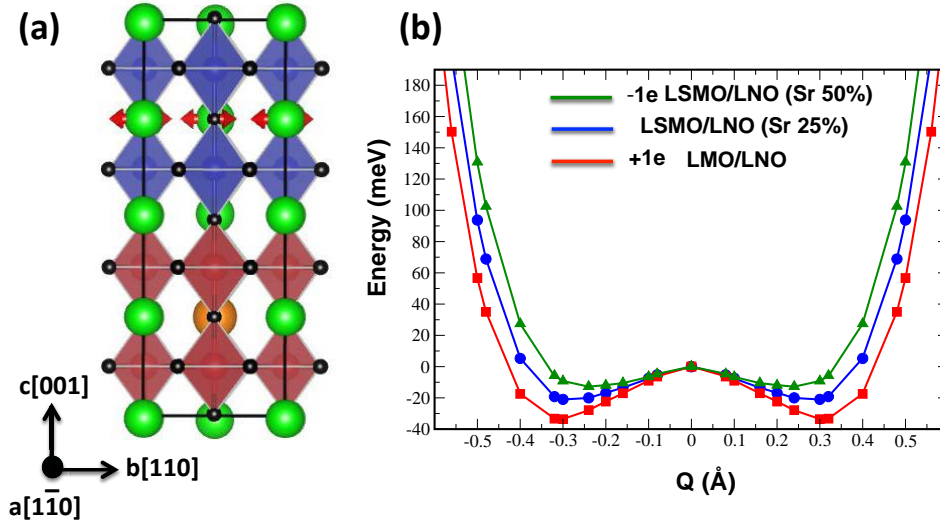


Figure 1: (a) The “ferroelectric like (FEL)” mode in 2/2 SL. Due to $(a\bar{a}c^0)$ mode both La^{3+} and apical O^{2-} ions are displaced from their respective centrosymmetric positions. In case of 2/2 SL the magnitude of displacements of La^{3+} and apical O^{2-} sandwiched between two Ni-Ni bilayers are significantly larger when compared to other layers (not shown). (b) The carrier concentration dependence of the FEL mode, where ‘Q’ represents mode amplitude. Here, La, Sr, Mn, Ni and O atoms are represented by Green, Orange, Red, Blue and Black color, respectively.

Our analysis shows that in Pm phase Ni cations now have two distinct sites, Ni_1 and Ni_2 . In case of Ni_1 sites, NiO_6 octahedron is slightly contracted, while in case of Ni_2 sites, the respective octahedron is slightly elongated in the crystallographic ab -plane. Presence of two different types of Ni sites also has been confirmed from local magnetic moment data. These results point towards disproportionation of Ni sites (into oxidation states $+2-x$ and $+2-y$, where $x-y$ is the difference in the oxidation state of Ni_1 and Ni_2), which leads to the metal-insulator transition. Further, we found that the FEL distortion strongly depends on the carrier concentration as shown in Figure 1(b), which can lead to design of ‘polar metals’ with tunable band gap and polarization.

To summarize, we have found that intermixed 2/2 SL can be ferroelectric with a large spontaneous polarization. The ferroelectric distortion persists even when the system is metallic, which leads to the possibility of designing of ‘polar metals’. Disproportionation of the Ni sites is found to be the origin of metal-insulator transition from ferroelectric-like metallic phase to ferroelectric insulating phase in these superlattices.

References: [1] W. Känzig (1957), ‘Ferroelectrics and Antiferroelectrics’. Solid State Physics 4, Academic Press. p. 5. ISBN 0-12-607704-5. [2] P. W. Anderson et. al. Phys. Rev. Lett. 14, 217 (1965). [3] M. Imada et.al. Rev. Mod. Phys. 70, 1039 (1998). [4] H. W. Jang et. al. Science 309, 391 (2005). [5] M. Salamon et.al. Rev. Mod. Phys. 73, 584 (2001). [6] P. Lacorre et. al. J. Solid State Chem. 91, 225 (1991). [7] H. Das et. al. Phys. Rev. Lett. 100, 18 (2008).

Acknowledgement: This work is supported by DOE Grant number DE-FG02-09ER46554 (SG, STP) and by DMSE of the DOE BES (RM, AYB)

‘Ferroelectric’ metals reexamined: Fundamental mechanisms and design considerations for new materials

Nicole A. Benedek*

Department of Materials Science and Engineering, Cornell University, Ithaca, NY 14853 USA

The recent observation[1] of a ferroelectric-like structural transition in metallic LiOsO_3 has generated a flurry of interest in materials that simultaneously exhibit another pair of supposedly contra-indicated properties: polarity and metallicity. Polar metals are thought to be rare because free electrons screen out the long-range electrostatic forces that favor a polar structure with a dipole moment in every unit cell. However, such materials are of interest, particularly because in many cases they have the potential to exhibit and provide opportunities to explore exotic quantum phenomena.[2] For example, antisymmetric spin-orbit interactions in polar and non-centrosymmetric superconductors are thought to give rise to non-standard pairing mechanisms and a host of unusual and fascinating properties: extremely large and highly anisotropic upper critical fields, topologically protected spin currents, and complex phase diagrams involving superconductivity and magnetism. Polar metals may facilitate the design of materials with controllable metal-insulator transitions and, paradoxically, *insulating* multiferroics, as shown by recent theoretical predictions on $\text{LiOsO}_3/\text{LiNbO}_3$ superlattices.[3] Highly conductive ferroelectric oxides – those with carrier concentrations close to a metal-insulator transition – are of interest for oxide-based thermoelectrics.[4] The practical applications of polar metals and highly conductive ferroelectrics are largely unexplored but promising avenues for further research.

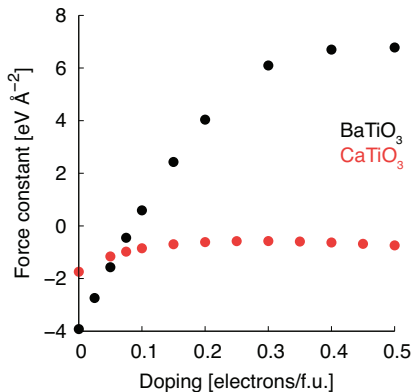


FIG. 1: Variation in the force constant of the ferroelectric mode of BaTiO_3 and CaTiO_3 as a function of electron doping.

In this talk, I will explore the question of whether ‘ferroelectricity’ and metallicity are really contra-indicated and use the insights gained to suggest design principles for new polar metals.[5] I will use the terms polar metal and ‘ferroelectric’ metal interchangeably to describe materials that belong to one of the 10 polar crystal classes and have a non-zero density of states at the Fermi level. The usual driving force for polar distortions is assumed to be long-range electrostatic forces. Is this picture correct? This is the question I will investigate in this talk. I will first use crystal chemical models and first-principles density functional theory calculations to investigate the mechanism of inversion symmetry-breaking in the recently synthesized polar metal LiOsO_3 . I will then consider the behavior of the polar instability in electron-doped BaTiO_3 , SrTiO_3 and CaTiO_3 from the perspective of lattice dynamics. Our results show (see Figure 1) that although the ferroelectric instability of BaTiO_3 is eventually suppressed under doping (in agreement with previous work[6]), the ferroelectric instability of CaTiO_3 weakens but persists under the same conditions. Our work has illustrated a connection between the compatibility of metallicity and polar distortions and the mechanism through which the polar phase emerges (a connection that was also noticed by Ref. 7). Namely, the polar phase of the materials resistant to doping or metallicity (CaTiO_3 and LiOsO_3) emerges through a geometric mechanism, rather than one involving charge transfer or hybridization. Hence, the most promising class of materials to search for new polar metals would appear to be metallic compounds with a tendency towards a polar distortion *that emerges through a geometric mechanism*. However, although it is tempting to conclude that polar or non-centrosymmetric metals must be geometric ‘ferroelectrics’, there exist several (and quite probably more) counter-examples, such as members of the hexagonal LiGaGe -type intermetallic family, recently explored by Bennett and co-workers[8, 9]. Extensive investigations by different groups over the past several years have resulted in the discovery of new ferroelectric mechanisms, however as far as we are aware, much of this effort has focused on a select few families of materials, particularly complex oxides. There is likely much still to learn about mechanisms of polar distortion in other classes of materials, particularly the intermetallics, and the manner in which charge carriers may modify, compete with or suppress these distortions will probably differ compared to the oxides. Hence, the design process for new polar

*email: nab83@cornell.edu

metals should start with an understanding of ferroelectric mechanisms in the materials family of interest and it is hoped that this work stimulates further research in this direction.

-
- [1] Y. Shi, Y. Guo, X. Wang, A. J. Princep, D. Khalyavin, P. Manuel, Y. Michiue, A. Sato, K. Tsuda, S. Yu, et al., *Nature Materials* **12**, 1024 (2013).
- [2] E. Bauer and M. Sigrist, eds., *Non-Centrosymmetric Superconductors: Introduction and Overview* (Springer, 2012).
- [3] D. Puggioni, G. Giovannetti, M. Capone, and J. M. Rondinelli, *Physical Review Letters* **115**, 087202 (2015).
- [4] S. Lee, J. A. Bock, S. Trolrier-McKinstry, and C. A. Randall, *Journal of the European Ceramic Society* **32**, 3971 (2012).
- [5] N. A. Benedek and T. Birol, *Journal of Materials Chemistry C* **4**, 4000 (2016).
- [6] Y. Wang, X. Liu, J. Burton, S. S. Jaswal, and E. Y. Tsymbal, *Physical review letters* **109**, 247601 (2012).
- [7] D. Puggioni and J. M. Rondinelli, *Nature Communications* **5**, 3432 (2014).
- [8] J. W. Bennett, K. F. Garrity, K. M. Rabe, and D. Vanderbilt, *Phys. Rev. Lett.* **109**, 167602 (2012).
- [9] J. W. Bennett, K. F. Garrity, K. M. Rabe, and D. Vanderbilt, *Phys. Rev. Lett.* **110**, 017603 (2013).

Electronic origin of spin-phonon coupling effect in transition-metal perovskites

Hongwei Wang^{1, 2}, Lixin He¹, Hong Jiang³, Cameron C. Steele², and Xifan Wu²

1. Key Laboratory of Quantum Information, University of Science and Technology of China, Hefei, Anhui 230026, China
2. Department of Physics, Temple University, 1925 N 12th Street, Philadelphia, Pennsylvania 19122, USA
3. Beijing National Laboratory for Molecular Sciences, College of Chemistry and Molecular Engineering, Peking University, 100871 Beijing, China

Spin-phonon coupling effect in transition metal perovskites has been identified by the fact that the low-lying phonon modes, as well as the polar ones, are significantly softened when the spin coupling is changed from being antiferromagnetic to ferromagnetic. We study the electronic origins of spin-phonon coupling effect by using SrMnO₃ and BiFeO₃ as examples. In particular, we compute the superexchange interactions via the virtual electronic hopping processes by a recently developed extended Kugel-Khomskii model based on maximally localized Wannier functions, in which the electronic screening is considered by constrained random phase approximation. The spin-phonon coupling effect can be understood as the tendency towards the suppressed superexchange interaction under the structural distortion along the phonon mode. However, the electronic structure plays a crucial role in the above. On one hand, phonon modes that effectively change the hybridization between Mn-3*d* and O-2*p* are found to have strong spin-phonon coupling effect. On the other hand, the rather different details in the virtual hopping processes originating from the distinct electronic configurations in Mn⁴⁺ and Fe³⁺ ions explain the much weaker spin-phonon coupling effect in BiFeO₃ than that of SrMnO₃. Our results bridge the gap between the Goodenough-Kanamori-Anderson phenomenological rule based on metal-oxygen-metal angle only and the electronic structure calculation of materials. Furthermore, it also provides useful guidance to the search for new spin-phonon coupling materials.

Domains and ferroelectric switching pathways in $\text{Ca}_3\text{Ti}_2\text{O}_7$ from first principles

Elizabeth A. Nowadnick* and Craig J. Fennie

School of Applied and Engineering Physics, Cornell University, Ithaca, NY 14853, USA

There is a great deal of interest in ferroelectrics that allow a coupling between the polarization and another order parameter (OP), making electric field control of non-polar OPs possible. For example, the search for strategies to directly couple magnetization and polarization provided an impetus to understand new mechanisms for ferroelectricity, such as spin-induced ferroelectricity,^{1,2} and more recently, octahedral rotation-induced ferroelectricity.³⁻⁵ This latter type of ferroelectricity, termed “hybrid improper ferroelectricity,” is a mechanism where a polarization can be induced via a trilinear coupling to two octahedral rotations (or other structural distortions⁶) of different symmetry. Hybrid improper ferroelectricity was predicted theoretically in $\text{ABO}_3/\text{A}'\text{BO}_3$ superlattices^{3,5,6} and in $n=2$ Ruddlesden-Popper (RP) materials.⁴ Recently, it was experimentally demonstrated in the $n=2$ RP compounds $\text{Ca}_3\text{Ti}_2\text{O}_7$ ⁷ and $\text{Sr}_3\text{Sn}_2\text{O}_7$ ⁸ and a complex domain structure was observed.^{9,10} The observation of an unexpectedly low switching barrier and abundant structural domains suggests that these domains may be critical to ferroelectric switching, but the precise pathway by which the polarization reverses remains an open question.

In this talk we will present our steps to address this question.¹¹ We use a combination of group theory and first-principles calculations to survey the energetics of $\text{Ca}_3\text{Ti}_2\text{O}_7$ in a space of low-energy metastable structures, and enumerate the possible ferroelectric switching pathways within this space. While here we focus on $\text{Ca}_3\text{Ti}_2\text{O}_7$, the approach we introduce is generic to all $\text{A}_3\text{B}_2\text{O}_7$ RP materials.

At room temperature $\text{Ca}_3\text{Ti}_2\text{O}_7$ crystallizes in the orthorhombic polar space group $A2_1am$ as shown in Fig. 1(a). This distorted structure can be decomposed into three distinct structural distortions that transform like irreducible representations (irreps) of $I4/mmm$:⁴ two octahedral rotation-like distortions that transform like X_3^- and X_2^+ , respectively, and a polar distortion that transforms like Γ_5^- . The polar distortion is induced by a trilinear coupling to the two octahedral rotation distortions:⁴

$$\mathcal{F}_{\text{tri}} = \alpha Q_{X_3^-} Q_{X_2^+} Q_P. \quad (1)$$

It is clear from Eq. 1 that reversing the polarization direction ($Q_P \rightarrow -Q_P$) requires reversing one but not both of the octahedral rotation OPs.

To make progress towards elucidating the switching pathways, we notice that in Fig. 1(a) the polar distortion primarily consists of a 2-against-1 displacement of the Ca ions in each $n = 2$ perovskite slab.^{12,13} The atomic

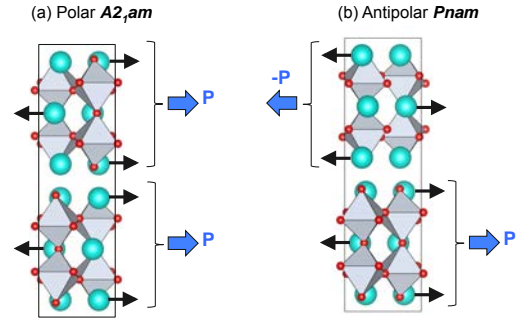


FIG. 1. (a) Polar structure $A2_1am$ and (b) antipolar structure $Pnam$.

displacements in adjacent perovskite slabs are in the same direction, leading to a net polarization. One may wonder, what would happen if each slab still has the same 2-against-1 displacement of Ca ions, but now in opposite directions, which would lead to an antipolar structure (space group $Pnam$), shown in Fig. 1(b)? This antipolar structure is energetically close to the polar one, because the perovskite slabs are weakly connected across the rocksalt layer. The same combination of irreps ($X_3^- \oplus X_2^+$) that induces the polar distortion in $A2_1am$ also can induce this antipolar distortion, when the irreps are taken along different directions in OP space. The key to describing these polar and antipolar structures on an equal footing is to use the full two-dimensional OPs¹⁴ to describe the structural distortions in $\text{Ca}_3\text{Ti}_2\text{O}_7$.

We use these two-dimensional OPs to first describe the polar and antipolar structures, and their orthorhombic twin domains, and then systematically identify the possible switching scenarios. In particular, we predict an additional type of domain wall (besides ferroelastic, ferroelectric, and antiphase boundaries), which we call a “stacking domain wall.” This stacking domain wall is an interface between a polar domain with polarization \mathbf{P} stacked on top of (along [001]) a polar domain with polarization $-\mathbf{P}$. At this stacking domain wall, which lies parallel to the ab plane, the structure locally is antipolar (as in Fig. 1(b)). We suggest atomic scale imaging of the local Ca displacements to observe these stacking domain walls experimentally.

We find multiple types of switching paths that have similar low energy barriers, suggesting that ferroelectric switching may proceed via more than one mechanism in $\text{Ca}_3\text{Ti}_2\text{O}_7$, a result that has implications for potential applications. In addition, the multiple “barrier structures” that we identify in our ferroelectric switching study may also describe the local structures at

domain walls in the sample. This lays the groundwork for understanding the unexpectedly complex domain

structure of $\text{Ca}_3\text{Ti}_2\text{O}_7$, consisting of a network of multiple types of domain walls and topological defects.

* E-mail: nowadnick@cornell.edu

¹ T. Kimura, T. Goto, H. Shintani, K. Ishizaka, T. Arima, and Y. Tokura, *Nature* **426**, 55 (2003).

² Y. Tokura, S. Seki, and N. Nagaosa, *Reports on Progress in Physics* **77**, 076501 (2014).

³ E. Bousquet, M. Dawber, N. Stucki, C. Lichtensteiger, P. Hermet, S. Gariglio, J. M. Triscone, and P. Ghosez, *Nature* **452**, 732 (2008).

⁴ N. A. Benedek and C. J. Fennie, *Phys. Rev. Lett.* **106**, 107204 (2011).

⁵ J. M. Rondinelli and C. J. Fennie, *Advanced Materials* **24**, 1961 (2012).

⁶ J. Varignon, N. C. Bristowe, E. Bousquet, and P. Ghosez, *Scientific Reports* **5** (2015).

⁷ Y. S. Oh, X. Luo, F.-T. Huang, Y. Wang, and S.-W. Cheong, *Nature Materials* **14**, 407 (2015).

⁸ Y. Wang, F.-T. Huang, X. Luo, B. Gao, and S.-W. Cheong, *Advanced Materials* (2017).

⁹ F.-T. Huang, F. Xue, B. Gao, L. Wang, X. Luo, W. Cai, X.-Z. Lu, J. Rondinelli, L. Chen, and S.-W. Cheong, *Nature communications* **7** (2016).

¹⁰ F.-T. Huang, B. Gao, J.-W. Kim, X. Luo, Y. Wang, M.-W. Chu, C.-K. Chang, H.-S. Sheu, and S.-W. Cheong, *arXiv:1606.01203* (2016).

¹¹ E. A. Nowadnick and C. J. Fennie, *Phys. Rev. B* **94**, 104105 (2016).

¹² N. A. Benedek, A. T. Mulder, and C. J. Fennie, *Journal of Solid State Chemistry* **195**, 11 (2012).

¹³ A. T. Mulder, N. A. Benedek, J. M. Rondinelli, and C. J. Fennie, *Advanced Functional Materials* **23**, 4810 (2013).

¹⁴ A. B. Harris, *Phys. Rev. B* **84**, 064116 (2011).

Optimizing the electrocaloric effect by *ab initio* simulations

Anna Grünebohm¹, Takeshi Nishimatsu², Madhura Marathe³, and Claude Ederer³

¹ *Department of Physics and CENIDE, University of Duisburg-Essen, 47048 Duisburg, Germany*

² *Institute for Materials Research, Tohoku University, Japan*

³ *Materials Theory, ETH Zürich, 8093 Zürich, Switzerland*

The electrocaloric effect (ECE) is the adiabatic temperature change of a material in a varying external electrical field which is promising for novel cooling devices [1]. We report on different ways to optimize the electrocaloric properties of BaTiO₃ by means of *ab initio*-based molecular dynamics simulations [2]. First of all, the highest ECE can be found at the ferroelectric transitions. Therefore, the Sr-concentration in solid solutions of (Ba,Sr)TiO₃ [5], see Fig. 1 (a), or strain applied to BaTiO₃ films [4], see Fig. 1 (b), can be used to tune the optimal operation temperature. Furthermore, the operation range can be broadened, e.g. by polar defects [3], see Fig. 1 (c), or the coupling between the external field and domain walls found under tensile strain [4]. In all cases, also the relative orientation between external field and polarization direction of the ferroelectric phase has a high impact on the ECE: If the external field stabilizes a phase with higher entropy, e.g. if a field along [001] is applied to the orthorhombic phase with polarization along [011], the transition entropy superimposed to the conventional ECE even turns the sign of the ECE, i.e. the sample heats up if the field is removed. The same inverse ECE can be found in clamped films, see Fig. 1 (b). Still more striking, a giant inverse caloric effect has been observed in a broad temperature range for the defect doped material, if the defect dipoles and the external field are not parallel to each other, see Fig. 1 (d). We present a systematic comparison of the different routes of optimization and the impact of the relative field direction.

References

- [1] X. Moya, *et al.*, Nature Mater. **13**,439 (2014).
- [2] T. Nishimatsu *et al.*, Phys. Rev. B **78**, 104104 (2008).
- [3] A. Grünebohm and T. Nishimatsu, Phys. Rev. B **93**, 134101, (2016),
Y.-B. Ma *et al.*, Phys. Rev. B **94**, 094113, (2016).
- [4] M. Marathe and C. Ederer, Appl. Phys. Lett. **104**, 212902 (2014),
A. Grünebohm, M. Marathe, and C. Ederer, Euro. Phys. Lett. **115**, 47002 (2015).
- [5] T. Nishimatsu *et al.*, J. Phys. Soc. Japn. **85**, 114714 (2016).

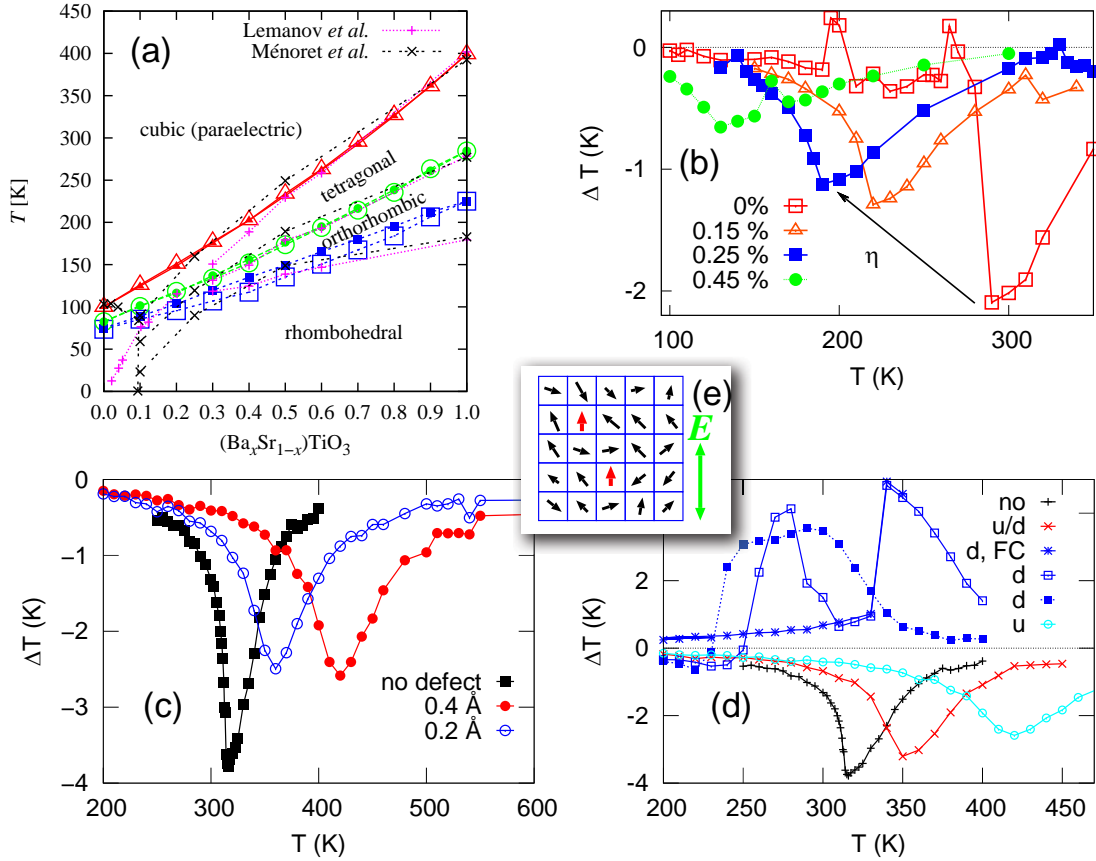


Figure 1: (a) Ferroelectric transition temperatures of $\text{Ba}_x\text{Sr}_{1-x}\text{TiO}_3$ found in the simulations (black) compared to experimental values taken from literature (adopted from [5]). (b)-(d) Caloric response of BaTiO_3 if an external field of 100 kV/cm along (001) is removed. (b) Influence of tensile strain on the ECE of clamped BaTiO_3 (adopted from [4]). (c)-(d) Influence of 1% polar defects on the ECE of BaTiO_3 . (c) Influence of the defect strength (d) Influence of the defect dipole orientation relative to the external field: parallel (u), antiparallel (d), and randomly along both directions (u/d). (e) Model for defects with slow relaxation: the local dipole moments of randomly chosen lattice sites are frozen during the field ramping.

Ballistic Photovoltaic Effect in Ferroelectric Barium Titanate

Jonathan E. Spanier¹, and Vladimir M. Fridkin^{1,2}

1. Department of Physics, Drexel University, Philadelphia, PA 19104, USA

2. Federal Center for Crystallography and Photonics, Shubnikov Institute of Crystallography, Moscow 119333, Russia

The ballistic bulk photovoltaic effect in crystals without center of symmetry is caused by asymmetric distribution of non-thermalized carrier momentum, a consequence of the violation of Boltzmann principle of detailed balance. Finite-size scaling of bulk photovoltaic effect-generated electric field in epitaxial BaTiO₃ (001) films and photo-Hall effect response involving the bulk photovoltaic current reveal ballistic transport of bulk photovoltaic effect-generated electrons in BaTiO₃. The obtained data permit determination of mobility, lifetime and free path of non-thermalized carriers. Optically-generated high-mobility conduction in a ferroelectric insulator at room temperature opens a new paradigm for facile control of ballistic transport distinct from existing low-dimensional semiconductor interfaces, surfaces, layers or other structures

1. S. M. Young and A. M. Rappe, Phys Rev. Lett. 109, 116601 (2012)

2. B. I. Sturman and V. M. Fridkin, The Photovoltaic and Photorefractive Effects in Noncentrosymmetric Materials (Gordon and Breach, Philadelphia, 1992)

3. J. E. Spanier, V. M. Fridkin, A. M. Rappe et al, Nature Photonics AOP (2016)

Transparent EuTiO₃ films: a possible two-dimensional magneto-optical device

Annette Bussmann-Holder^{1*}, Krystian Roleder², Benjamin Stuhlhofer¹, Gennady Logvenov¹, Arndt Simon¹, Jürgen Köhler¹

¹Max-Planck-Institut für Festkörperforschung, Heisenbergstr. 1, D-70569 Stuttgart, Germany

²Institute of Physics, University of Silesia, ul. Uniwersytecka 4, 40-007 Katowice, Poland

ETO has the cubic perovskite structure at room temperature [1] and undergoes a structural phase transition to tetragonal at $T_S=282\text{K}$ [2]. Below $T_N=5.7\text{K}$ the Eu $4f^7$ spins order G-type antiferromagnetic [3], and large magneto-electric coupling takes place as evidenced by the magnetic field dependence of the dielectric constant [4]. Very unusual magnetic field dependent properties are observed in the paramagnetic phase at high temperature as demonstrated by the field dependence of T_S [5] and anomalies in the magnetic susceptibility at T_S [6]. These results indicate some kind of *hidden magnetism* in the paramagnetic phase which is supported by muon spin rotation (μSR) data where a strong field dependence of the μSR relaxation rate is observed [7]. Similarly, resonant ultrasound spectroscopy

(RUS) experiments [8] reveal a pronounced influence of a magnetic field on the acoustic properties of ETO.

In order to identify the magnetism at high temperature thin films of outstanding quality of ETO have been fabricated. The magneto-optical activity of these high quality transparent thin films of insulating ETO deposited on a thin SrTiO₃ (STO) substrate with both being *non-magnetic* materials are demonstrated to be a versatile tool for light modulation. The operating temperature is close to room temperature and admits multiple device engineering. By using small magnetic fields birefringence of the samples can be switched off and on. Similarly, rotation of the sample in the field can modify its birefringence Δn . In addition, Δn can be increased by a factor of 4 in very modest fields with simultaneously enhancing the operating temperature by almost 100K (Figure 1). Besides of these amazing results two more structural phase transitions have been identified, namely one from tetragonal to monoclinic at $T^*=190\text{K}$ and a second one from monoclinic to triclinic around $T'\approx 100\text{K}$. Both phase transitions are susceptible to magnetic fields and evidence spin activity in ETO far above its Néel temperature.

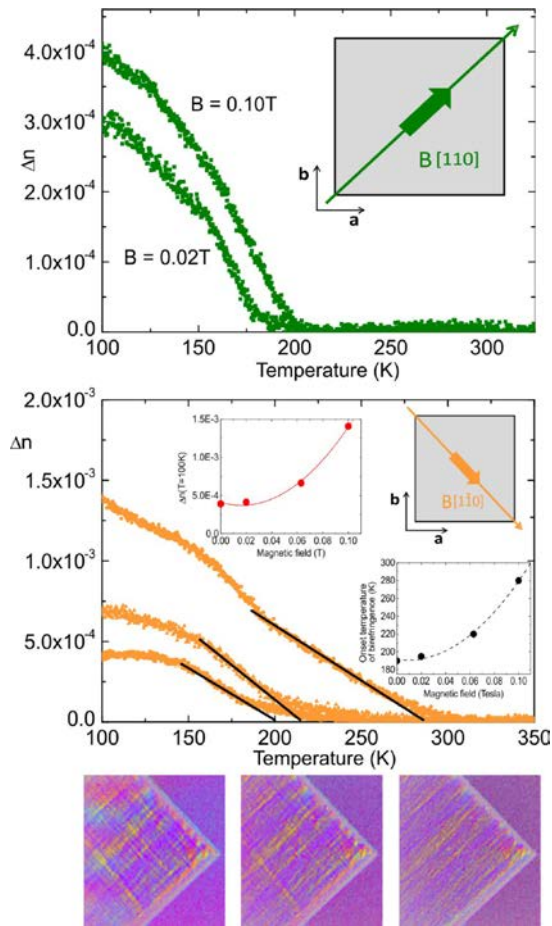


Figure 1 (top) Birefringence of the ETO film in a field of $H=0.02\text{T}$ and $H=0.1\text{T}$ with the field direction along $[110]$. **(middle)** Birefringence measured with the field along $[1\bar{1}0]$, and field strengths $H=0.02\text{T}$ (the lowest curve), 0.063T (middle curve) and $H=0.1\text{T}$ (the highest curve). The straight lines refer to the extrapolated onset temperatures of Δn as shown in the inset (right) to this figure. The insets show the onset temperature of Δn versus magnetic field (right) and $\Delta n(T=100\text{K})$ versus H (left). **(bottom)** $\Delta\Phi$ images in a magnetic field of $H=0.1\text{T}$ taken along $[1\bar{1}0]$ for temperatures $T = 85, 170, 240\text{K}$ (from left to right).

References

1. Brous, J., Fankuchen, I., & Banks, E. *Acta Crystallogr.* **6**, 67-69 (1953),.
2. Bussmann-Holder, A., Köhler, J., Kremer, R. K., & Law, J. M. *Phys. Rev. B* **83**, 212102 1-4 (2011),
3. McGuire, M. T. R., Shafer, M. W., Joenk, R. J., Halperin, H. A., & Pickart, S. J. *J. Appl. Phys.* **37**, 981-985 (1966).
4. Katsufuji, T., & Takagi, H. *Phys. Rev. B* **64** 054415 (2001).
5. Guguchia, Z., Keller, H., Köhler, J., & Bussmann-Holder, A. *J. Phys.: Condens. Matter* **24**, 492201 1-4 (2012) doi:10.1088/0953-8984/24/49/492201
6. Caslin, K., Kremer, R. K., Guguchia, Z., Keller, H., Köhler, J., & Bussmann-Holder, A. *J. Phys.: Condens. Matter* **26**, 022202 (2014).
7. Guguchia, Z. et al., *Phys. Rev. B* **90** 064413 1-5 (2014).
8. Schiemer, Jason et al., , *Phys. Rev. B* **93**, 054108 1-18 (2016).

The insulating phases of VO₂ are Mott-Hubbard insulators

Christopher Hendriks, Eric J. Walter, Tyler J. Huffman,
M. Mumtaz Qazilbash, and Henry Krakauer*

Department of Physics, College of William and Mary, Williamsburg, VA 23187, USA

Vanadium dioxide (VO₂) typically transforms from an insulating monoclinic (M₁) to a metallic rutile (R) phase upon heating. However, intermediate insulating triclinic (T) and magnetic (M₂) phases can be stabilized for some temperature, doping, and strain conditions. Broadband optical spectroscopy data have been obtained [1] on the T and M₂ phases in the *same* sample. While only half the V atoms are dimerized in M₂ compared to M₁ and T, the measured optical gap is essentially unaltered by the first-order structural phase transition between them. Moreover, the optical interband features in the T and M₂ phases are remarkably similar to those previously observed in the well-studied M₁ phase. This shows that the electronic structure is insensitive to the lattice structure. This is also seen in our first-principles hybrid density functional theory (DFT) calculations, using the Heyd-Scuseria-Ernzerhof (HSE) [2, 3] screened exchange functional. As seen in Fig. 1, the calculated spectra are in excellent agreement with the experimental measurements.

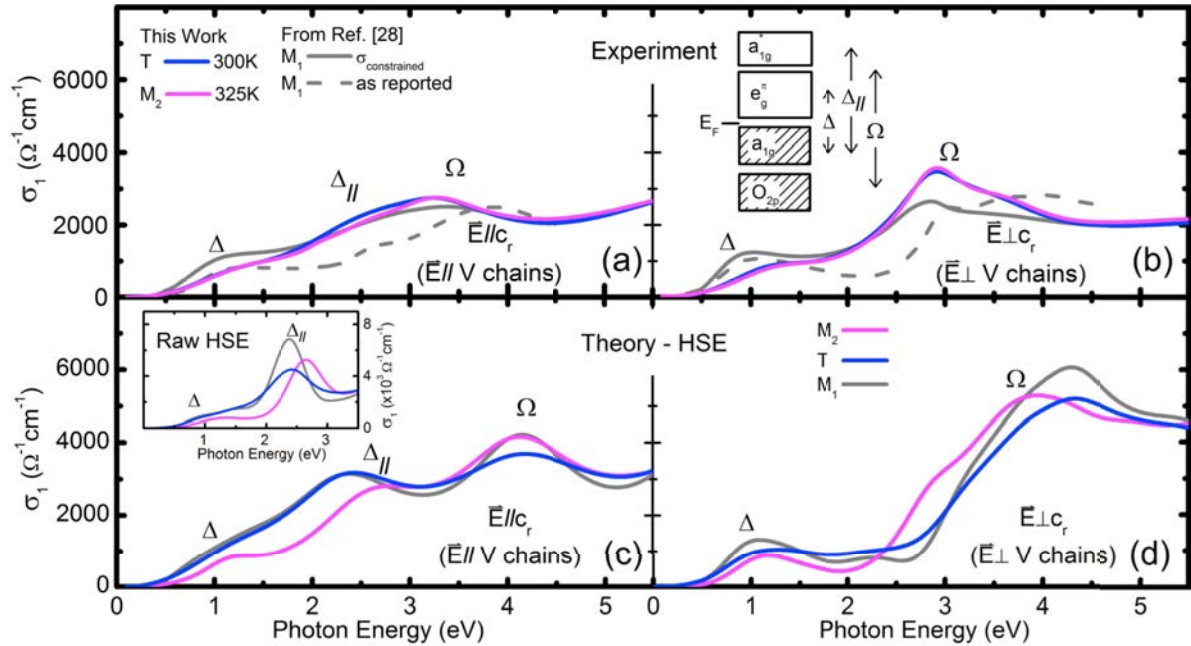


FIG. 1: Experimental optical conductivity σ_1 of the M₂ and triclinic T phases: (a) parallel to the vanadium (V) chains (c_r direction); (b) perpendicular to the vanadium (V) chains. For comparison, accurate optical conductivity of the M₁ phase is extracted from the reflectance spectrum reported in [4] by using the complex conductivity of the T phase measured in this work as a constraint above 4 eV [1]. The inset in panel (b) shows an effective energy level diagram along with optical interband transitions that appear in the conductivity spectra. First-principles HSE calculated optical conductivities are presented in (c) and (d). The calculated raw conductivities are broadened by 0.3 eV. The calculated conductivity for $E||c_r$ contains a very sharp $\Delta||$ feature [see inset of panel (c)]. To account for lifetime effects not handled in the static HSE treatment, the $\Delta||$ feature, which is assigned to transitions between the lower and upper Hubbard bands in the Mott picture, is further broadened to a FWHM of 1.5 eV in the main panel of (c), which better models the experiment.

The Vienna Ab-initio Simulation Package (VASP) [5] was used to perform first-principles HSE optical conductivity calculations on the insulating phases of VO₂. With suitably chosen α , the

fraction of exact exchange, HSE has been shown to often provide a good description of electronic properties ranging from band to Mott-Hubbard insulators [6, 7]. We will discuss the choice of α used in our HSE calculations and its relation to intra-atomic electron-electron repulsion U , as in DFT+ U calculations.

As the energy gap is insensitive to the different lattice structures and the vanadium-vanadium dimerization of the three insulating phases, we rule out Peierls effects as the dominant contributor to the opening of the gap. Instead, the energy gap arises from intra-atomic Coulomb correlations. Knight shift measurements [8] are indicative of localized electrons on the equally spaced vanadium atoms in the M_2 chains; its absence in the dimerized chains of all three insulating phases has long complicated the elucidation of the metal-insulator transition. In contrast to a more conventional Mott insulator, where valence electrons are localized on individual ions, the dimerized vanadium chains contain bonded spin singlets which are localized on the vanadium dimers. This fact has made it difficult to conclusively distinguish between the Peierls and Mott-Hubbard pictures in the exhaustively studied M_1 phase. The present study of the M_2 and T phases, with their non-equal V chains, was essential to decouple, for the first time, the effects of dimerization and electronic correlations.

*Presenter email: hxkrak@wm.edu

Acknowledgments: Theoretical work was supported by ONR grant N00014-12-1-1042; experimental work was supported by NSF DMR (grant # 1255156). All calculations were performed on the High Performance Computing cluster at the College of William and Mary.

-
- [1] T. J. Huffman, C. Hendriks, E. J. Walter, J. Yoon, H. Ju, R. Smith, G. L. Carr, H. Krakauer, and M. M. Qazilbash. *ArXiv e-prints:1608.08227*, 2016.
 - [2] Jochen Heyd, Gustavo E. Scuseria, and Matthias Ernzerhof. *The Journal of Chemical Physics*, 118(18):8207, 2003.
 - [3] Jochen Heyd, Gustavo E. Scuseria, and Matthias Ernzerhof. *The Journal of Chemical Physics*, 124(21):219906, 2006.
 - [4] Hans Verleur, A. Barker, and C. Berglund. *Physical Review*, 172(3):788–798, 1968.
 - [5] Jürgen Hafner. *Journal of computational chemistry*, 29(13):2044–78, 2008. See also references therein.
 - [6] Cesare Franchini. *Journal of physics. Condensed matter*, 26(25):253202, 2014.
 - [7] Jiangang He and Cesare Franchini. *Physical Review B*, 86(23):235117, 2012.
 - [8] J. Pouget, H. Launois, T. Rice, P. Dernier, A. Gossard, G. Villeneuve, and P. Hagenmuller. *Physical Review B*, 10(5):1801–1815, 1974.

Ferroelectricity in PbTiO_3 at high pressures?

R. E. Cohen,^{1,2} Muhtar Ahart,¹ and Russell J. Hemley³

¹Extreme Materials Initiative, Geophysical Laboratory, Carnegie Institution for Science, Washington, D.C., ²LMU Munich, Department of Earth and Environmental Sciences, ³Department of Civil and Environment Engineering, The George Washington University, Washington DC 20052 USA; and Lawrence Livermore National Laboratory, Livermore CA 94550 USA

The classic ferroelectric PbTiO_3 continues to surprise. For many years it was believed that ferroelectrics such as PbTiO_3 would become paraelectric under pressure, and this was observed clearly in Raman experiments in the 1980s. [1] We however predicted a morphotropic phase transition under pressure [2] that we verified experimentally. [3] At higher pressures it seemed to become paraelectric, but DFT computations [4, 5] predicted higher pressure ferroelectricity, and this seemed to be confirmed by experiments. [6] However, we performed Second Harmonic Generation

(SHG) measurements on PbTiO_3 to 100 GPa and down to 10 K and find no evidence for a polar ground state or ferroelectricity above 20 GPa (Fig. 1). A previous search of structures found ferroelectric R3c from 12-38 GPa with R-3c possibly at higher pressures, [7] but further study [8] showed that the ferroelectric R3c was more stable than R-3c up to 100 GPa. We were unable to determine from analysis of first-principles molecular dynamics simulations a definitive centrosymmetric structure consistent with the experiments.

Finally we have found consistency from DFT computations that show from 20-90 GPa that the centrosymmetric I4mcm structure is most stable, with no soft modes; I4mcm is the same structure as the ground state of SrTiO_3 , and it quenches the polar instability. We used ABINIT with the WC exchange-correlation functional, 6x6x6 k-point grids in 10 atom cells with PAWs developed using opium and tested against LAPW with WIEN2K. We do predict a polar I4cm structure above 90 GPa, but the double well depth is very small.

We have computed phonons at Γ using quantum espresso [9] with GRBV ultrasoft pseudopotentials [10] using density functional perturbation theory (DFPT). The results show stable modes up to 90 GPa, at which point a polar slightly soft-mode appears, consistent with the total energy computations showing I4cm at these highest pressures. The soft

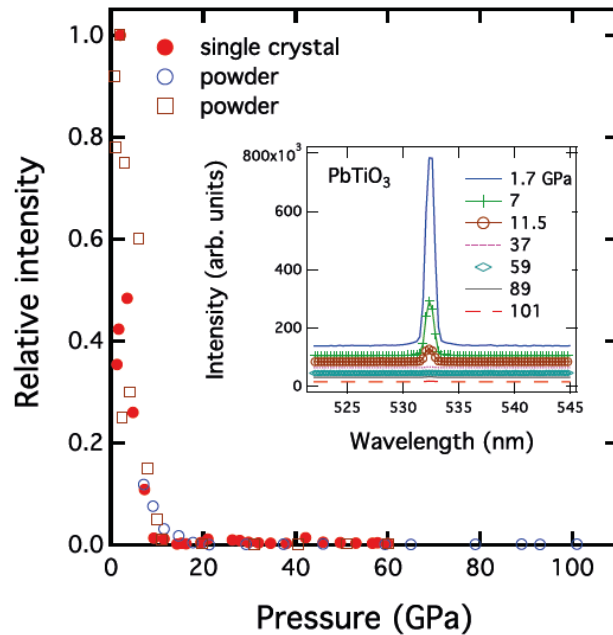


Figure 1. Pressure dependence of the integrated intensity of our in situ nano-Second Harmonic Generation (SHG) measurements. We normalize the integrated intensity with the intensity obtained at ambient pressure. We performed three experimental runs: first run, solid circle (red) marks, neon pressure medium; second run, open circle (blue), single crystal, neon pressure medium; third run, solid square (green) marks, neon pressure medium. The SHG spectrum of the PbTiO_3 single crystal at selected pressures. The wavelength of the incident light is 1064 nm, so the SHG signals appear at 532 nm. The temperature was about 10 K.

mode only appears when the irregular part of the dynamical matrix is omitted, or for the $q00$ direction, but not for $00q$ (Fig. 3).

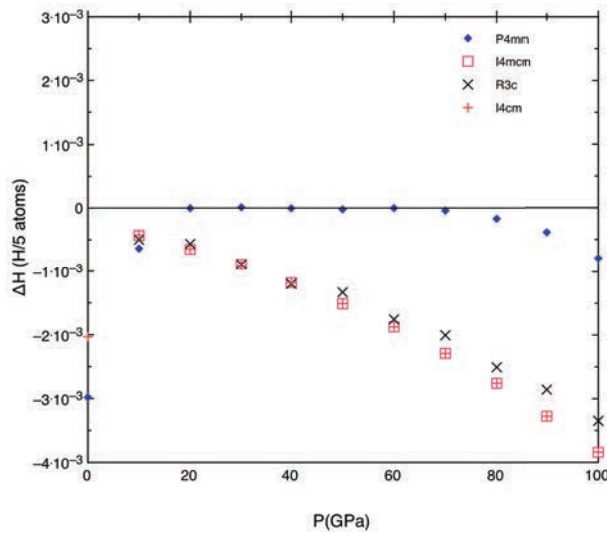


Figure 2. Enthalpies relative to cubic Pm3m perovskite versus pressure computed using ABINIT with the WC exchange-correlation functional. The centrosymmetric I4mcm phase is most stable above 20 GPa. Between 90-100 GPa polar I4cm is most stable

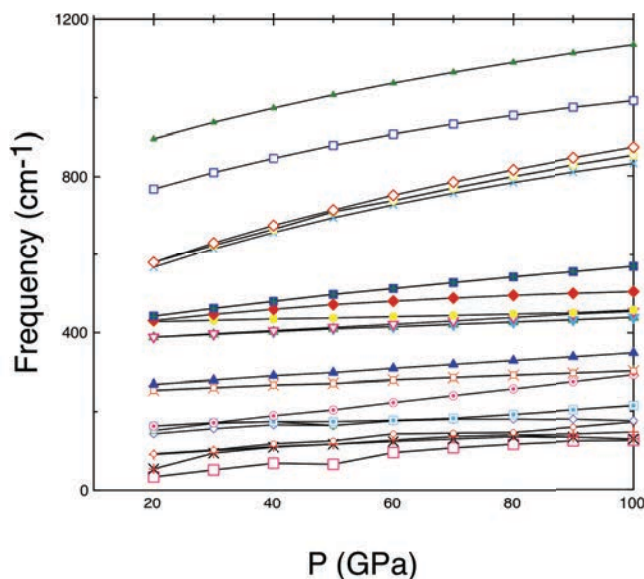


Figure 3. Mode frequencies at Γ for the $00q$ direction versus pressure computed using DFPT for the I4mcm structure.

Lorenzo, S. Carlo, S. Sandro, S. Gabriele, P. S. Ari, S. Alexander, U. Paolo, and M. W. Renata, *J.Phys.: Condens.Matter* **21**, 395502 (2009).

[10] K. F. Garrity, J. W. Bennett, K. M. Rabe, and D. Vanderbilt, *Computational Materials Science* **81**, 446 (2014).

The origin of the ultrahigh pressure ferroelectricity will be discussed. This work has been supported by the US ONR, ERC Advanced grant ToMcaT, NSF, CDAC, EFREE, and the Carnegie Institution for Science.

References

[1] J. Sanjurjo, E. López-Cruz, and G. Burns, *Phys.Rev.B* **28**, 7260 (1983).

[2] Z. Wu and R. Cohen, *Phys. Rev. Lett.* **95**, 037601 (2005).

[3] M. Ahart, M. Somayazulu, R. E. Cohen, P. Ganesh, P. Dera, H.-k. Mao, R. J. Hemley, Y. Ren, P. Liermann, and Z. Wu, *Nature* **451**, 545 (2008).

[4] I. A. Kornev and L. Bellaiche, *Phase Transitions* **80**, 385 (2007).

[5] I. Kornev, L. Bellaiche, P. Bouvier, P. E. Janolin, B. Dkhil, and J. Kreisel, *Phys. Rev. Lett.* **95** (2005).

[6] P. E. Janolin, P. Bouvier, J. Kreisel, P. Thomas, I. Kornev, L. Bellaiche, W. Crichton, M. Hanfland, and B. Dkhil, *Phys. Rev. Lett.* **101** (2008).

[7] P. Ganesh and R. E. Cohen, *J.Phys.: Condens.Matter*, 064225 (2009).

[8] R. E. Cohen, M. Ahart, S. Mandal, J. Nossa, P. Ganesh, I. Naumov, A. F. Goncharov, Stanislav V. Sinogeikin, and R. J. Hemley, in *Fundamental Physics of Ferroelectrics 2015* (Oak Ridge, 2015).

[9] G. Paolo, B. Stefano, B. Nicola, C. Matteo, C. Roberto, C. Carlo, C. Davide, L. C. Guido, C. Matteo, D. Ismaila, C. Andrea Dal, G. Stefano de, F. Stefano, F. Guido, G. Ralph, G. Uwe, G. Christos, K. Anton, L. Michele, M.-S. Layla, M. Nicola, M. Francesco, M. Riccardo, P. Stefano, P. Alfredo, P.

Wednesday's Abstracts

Brillouin Scattering Spectroscopy on Crossover from Strong to Weak Relaxor Behaviors of Uniaxial Tungsten Bronze Ferroelectrics

S. Kojima¹, M. Aftabuzzaman¹, K. Matsumoto¹, J. Dec², and W. Kleemann³

¹*Division of Materials Science, University of Tsukuba, Tsukuba, Ibaraki 305-8573, Japan*

²*Institute of Materials Science, University of Silesia, PL 40-007 Katowice, Poland*

³*Applied Physics, Duisburg-Essen University, D 47048 Duisburg, Germany*

kojima@bk.tsukuba.ac.jp

Relaxor ferroelectrics (REFs) have attracted much attention owing to their colossal piezoelectric effect and their wide variety of applications to piezoelectric devices. Pb-based multidimensional REFs with the perovskite structure have been extensively studied, whereas the understanding of uniaxial relaxors is still insufficient. Strontium barium niobate, $\text{Sr}_x\text{Ba}_{1-x}\text{Nb}_2\text{O}_6$ (SBN100x), is one of the technologically important uniaxial REFs owing to its very large electrooptic and pyroelectric coefficients, making it useful for applications such as sensors and data storage. The ab-plane of uniaxial tetragonal tungsten bronze (TTB) structure is shown in Fig. 1. In SBN, the largest A2 sites are occupied by the larger divalent Ba and Sr ions, while the A1 sites are occupied only by the smaller Sr ions. One-sixth of all the A sites (A1+A2 sites) are vacancies, which are the main origin of random fields (RFs). The relaxor behaviors of SBN have been discussed on the basis of the random field Ising Model [1]. With increasing Sr/Ba ratio, SBN shows the crossover from a normal ferroelectric to a relaxor ferroelectric with an increase in charge disorder at the A sites. Recently $\text{Ca}_x\text{Ba}_{1-x}\text{Nb}_2\text{O}_6$ (CBN100x) has also attracted attention by its similar relaxor nature to SBN and the relatively high Curie temperature, which is useful for the application.

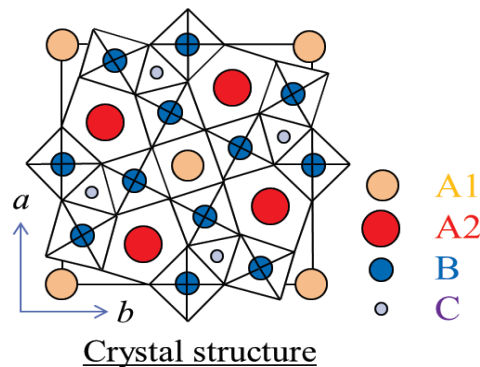


Figure 1 Tetragonal tungsten bronze structure (ab-plane).

Relaxor ferroelectric SBN61 with a strong charge disorder, undergoes a diffuse phase transition on cooling from a prototypic tetragonal $4/mmm$ phase to a ferroelectric tetragonal $4mm$ phase with a spontaneous polarization along the c-axis [2,3]. In contrast, SBN26 with weak charge disorder undergoes a sharp ferroelectric phase transition. In the present work, Brillouin scattering of the solid solutions of $\text{Sr}_x\text{Ba}_{1-x}\text{Nb}_2\text{O}_6$ (SBN100x), $\text{Ca}_x\text{Ba}_{1-x}\text{Nb}_2\text{O}_6$ (CBN100x), and mixed solid solutions of SBN61 and CBN28 was studied using a tandem Fabry-Perot interferometer [4,5].

The temperature dependence of the sound velocity of a longitudinal acoustic (LA) mode along the c-axis of SBN26 and SBN70 on zero field cooling (ZFC) is shown in Fig. 1(a). The LA velocity of SBN26 with weak charge disorder shows the a sharp anomaly in the vicinity of the Curie temperature, T_C , while that of SBN70 with strong charge disorder shows the broad diffusive anomaly in the vicinity of T_C and the remarkable decrease of the LA velocity below T_C caused by the existence of a nanodomain state.

The temperature dependence of the LA velocity of SBN61 on field cooling (FC) and ZFC is shown in Fig. 2(b). Field cooled SBN61 with no nonodomain state shows a sharp elastic anomaly and the hardening of the LA velocity below T_C being similar to that of SBN26, while ZFC of SBN61 with a nanodomain state gives rise to a broad diffusive anomaly and the decrease of the LA velocity similar to SBN70 as shown in Fig. 2(b) [6]. Critical slowing down towards T_C was clearly observed for the central peaks in both SBN26 and CBN28 [3], while it becomes diffusive as the Sr/Ca content increases [6,7]. In SBN61 and SBN70, the diffusive stretched critical slowing down was observed in the vicinity of T_C .

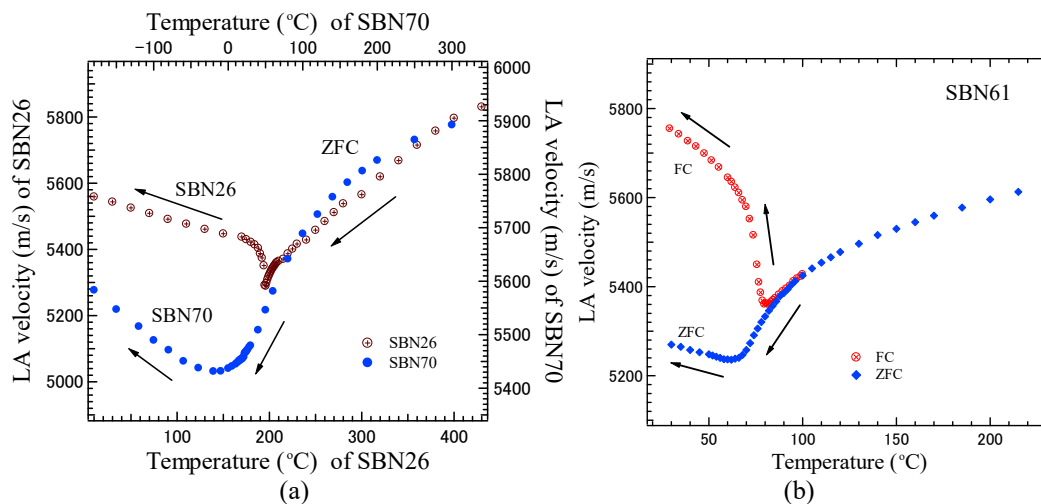


Figure 2. Temperature dependence of LA velocity, (a) ZFC of SBN26 and SBN70, (b) ZFC and FC of SBN61.

References

- [1] W. Kleemann, J. Dec, P. Lehnen, R. Blinc, B. Zalar, and R. Pankrath, *Europhys. Lett.* **57**, 14 (2002).
- [2] V. V. Shvartsman, J. Dec, S. Miga, T. Łukasiewicz, and W. Kleemann, *Ferroelectrics* **376**, 1 (2008).
- [3] F. Jiang and S. Kojima, *Phys. Rev. B* **66**, 184301 (2002).
- [4] K. Suzuki, K. Matsumoto, J. Dec, T. Łukasiewicz, W. Kleemann, and S. Kojima, *Phys. Rev. B* **90**, 064110 (2014).
- [5] S. Kojima, *Jpn. J. Appl. Phys.* **49**, 07HA01 (2010).
- [6] K. Matsumoto and S. Kojima, *Jpn. J. Appl. Phys.* **54**, 10NC04 (2015).
- [7] Md. Aftabuzzaman, J. Dec, W. Kleemann, and S. Kojima, *Jpn. J. Appl. Phys.* **55**, 10TC01 (2016).

Ab initio study of doping and strain in ferroelectric HfO₂

Mehmet Dogan,* Nanbo Gong, Tso-Ping Ma, and Sohrab Ismail-Beigi
*Center for Research on Interfaces Structures and Phenomena,
Yale University, New Haven, CT*

Achieving ferroelectricity in thin films is the subject of decades long research endeavor because of potential technological applications such as ferroelectric field effect transistors (FeFET) and memory (FeRAM). HfO₂ is widely used as a gate oxide in transistor devices today, and the recent discovery of ferroelectricity in HfO₂-based thin films has sparked great research [1, 2]. It has been shown by various experimental studies that ferroelectricity in HfO₂-based films arises from the polar orthorhombic phase (space group: Pca2₁) that is created during the rapid annealing process with the presence of a capping electrode (typically TiN). It has also been demonstrated that the ferroelectric properties of these films strongly depend on factors such as the doping species, doping concentration, annealing temperature and film thickness [3]. Even though devices based on these films are already being designed and developed, a microscopic understanding of the effects of the aforementioned factors is presently lacking. This is, in part due to the polycrystalline and complex nature of the HfO₂ films that have been grown, and in part due to the relative newness of this field.

To our knowledge hafnia-based thin films have been polycrystalline with differently oriented grains of monoclinic (P2₁/s), tetragonal (P4₂/nmc) and orthorhombic (Pca2₁) phases in various ratios (see Figure 1). The monoclinic and the tetragonal phases are non-polar and they are the observed bulk phases of HfO₂ at room temperature and at high temperature, respectively. The experiments demonstrate that the orthorhombic phase arises during the rapid annealing with a capping electrode. In addition, the amount of doping is crucial in determining the ferroelectric properties. Because the relative ratio of the orthorhombic phase over the other phases is what decides the robustness of ferroelectricity in the HfO₂ films, a structural understanding of the favorable conditions for this phase is crucial in optimizing the growth procedure. To this end, in this *ab initio* study, we investigate the energetics of different bulk phases of HfO₂ with varying amounts of Si and Zr doping and different epitaxial strain states. We have found that at certain doping levels the transformation of the high temperature tetragonal phase to the out-of-plane polarized orthorhombic phase is favored (see Figure 2). These results, together with additional analysis, help explain the common experimental observations as well as some of the underlying causes from an atomic structure viewpoint. We also describe preliminary results on simulated HfO₂ thin films including the interface with the electrode to get a more comprehensive understanding of the energetics in thin films.

* mehmet.dogan@yale.edu

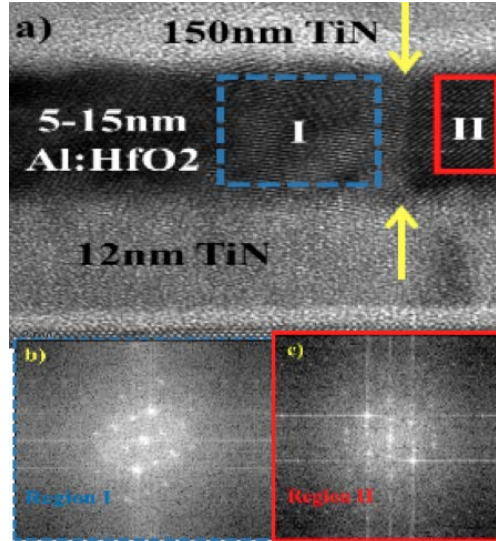


FIG. 1. a) A TEM image of TiN - Al:HfO₂ - TiN MFM structure. A grain boundary is seen between two yellow arrows. b) & c) FFT of two grains in (a) respectively. Reproduced with permission from Ref. [4].

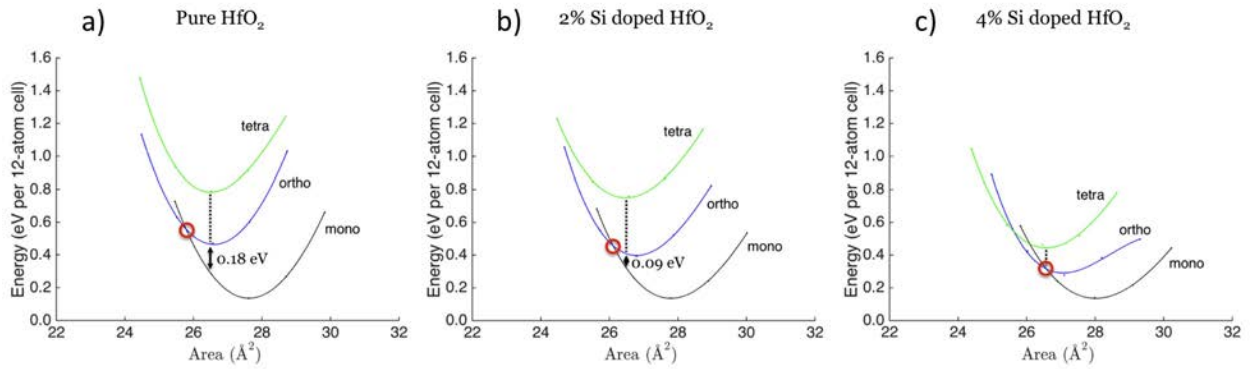


FIG. 2. Energy vs cell base area for the three phases of a) undoped, b) 2% Si doped, c) 4% Si doped HfO₂ for a plane matching that allows out-of-plane polarization in the orthorhombic phase.

-
- [1] T. S. Böscke, J. Müller, D. Bräuhäus, U. Schröder, and U. Böttger, Applied Physics Letters **99**, 102903 (2011).
 - [2] J. Müller, T. S. Böscke, U. Schröder, S. Mueller, D. Bräuhäus, U. Böttger, L. Frey, and T. Mikolajick, Nano Letters **12**, 4318 (2012).
 - [3] M. H. Park, Y. H. Lee, H. J. Kim, Y. J. Kim, T. Moon, K. D. Kim, J. Müller, A. Kersch, U. Schroeder, T. Mikolajick, and C. S. Hwang, Advanced Materials **27**, 1811 (2015).
 - [4] N. Gong, X. Sun, H. Jiang, Q. Xia, and T. P. Ma, 46th IEEE Semiconductor Interface Specialists Conference (SISC'15) (2015).

Polarization-Controlled Modulation Doping in Ferroelectric/Semiconductor Heterostructures

Xiaohui Liu and Karin M. Rabe

*Department of Physics and Astronomy, Rutgers University, Piscataway,
New Jersey 08854-8019, USA*

In most ferroelectric field-effect transistor (FFET) configurations, the modulation of the conductivity by switching of the ferroelectric gate is dominated by the electrostatically-induced change in carrier concentration in the channel. However, recent work on PZT/LaNiO₃ has shown that the conductivity of the on state can be dramatically increased by opening of conducting channels in the ferroelectric itself. [1] In this work, we present first-principles calculations for ferroelectric BaTiO₃ on n-type SrTiO₃, showing an even larger effect of this type. We show that for polarization pointing into the semiconductor, additional conducting channels are created in BaTiO₃ near the interface due to the metallization of several layers of BaTiO₃. We present a simple model that shows that conduction in the ferroelectric is largely controlled by the work function step between the ferroelectric and the channel material.

We performed first-principles density functional theory calculations with the QuantumESPRESSO package on BaTiO₃/n-SrTiO₃ and PbTiO₃/n-SrTiO₃ systems, where the electron doping in n-SrTiO₃ is simulated using virtual crystal approximation for the oxygens, extending a previous study of BaTiO₃/n-SrTiO₃ [2]. The supercell is constructed by stacking unit cells along the [001] direction and the in-plane lattice constant of the supercell is constrained to the calculated LDA lattice constant of SrTiO₃, $a = 3.871$ Å, which corresponds to an in-plane strain of about -2.1% on BaTiO₃; this constrains the phases to be tetragonal. The system has 8 unit cells of BaTiO₃ or PbTiO₃ sandwiched between 10 unit cells of SrRuO₃ and 16 unit cells of n-SrTiO₃ doped at a level of 0.09 electrons per functional unit cell. The BaTiO₃/n-SrTiO₃ and BaTiO₃/SrRuO₃ interfaces are terminated with TiO₂. The atomic structure of the supercell is relaxed until forces are converged to less than 20 meV/Å on each atom.

For the BaTiO₃/n-SrTiO₃ interface, Figure 1 shows the local electron density of states near the Fermi energy for the ground-state structures of each polarization state. When polarization is pointing away from n-SrTiO₃, we can see depletion of electrons in n-SrTiO₃ near the interface; the conduction bands of n-SrTiO₃ bend up in this case. However, when polarization is pointing into n-SrTiO₃, the electrons accumulate in a few layers of BaTiO₃ and screen the bound charge “in situ”. [3] We can see that more than two unit cells of BaTiO₃ are occupied by free electrons and metallized. The metallization of BaTiO₃ opens up additional channels for conduction in the on state. Further, the added electrons in BaTiO₃ do not see disorder from donor species and therefore feel less scattering than in bulk n-BaTiO₃. Therefore, we expect that the additional conducting channels in BaTiO₃ will have relatively high mobility and electrons in these channels will dramatically increase the conductivity of the on state. This ferroelectric-polarization-control of conducting channels improves the functionality of ferroelectric field-effect transistors.

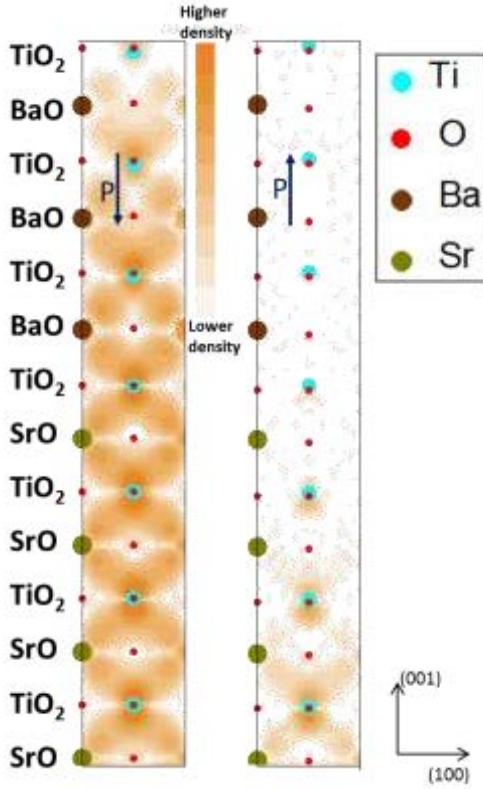


FIG. 1. A 2D projection of the local density of electronic states derived from first-principles calculations integrated within $\pm k_B T$ eV of the Fermi level with $T=300\text{K}$ near the interface $\text{BaTiO}_3/\text{n-SrTiO}_3$.

In this system, the work function step between BaTiO_3 and SrTiO_3 plays a key role in the accumulation of electrons in BaTiO_3 . The sensitivity to the direction of polarization is large since the conduction bands of BaTiO_3 and SrTiO_3 are aligned (the electron affinities of BaTiO_3 and SrTiO_3 are both around 4.0eV). When polarization is pointing away from n-SrTiO_3 , the negative bound charge bends the conduction band of n-SrTiO_3 up above the Fermi level and empties the conduction band near the interface. When polarization is pointing into n-SrTiO_3 , the positive bound charge bends the conduction

band of BaTiO_3 below the Fermi level, leading to the transfer of electrons into the conduction band of BaTiO_3 near the interface.

Our studies on $\text{PbTiO}_3/\text{n-SrTiO}_3$ systems show similar results. Metallization of several layers of PbTiO_3 near the interface is found for polarization pointing into the n-SrTiO_3 . The larger work function difference between PbTiO_3 and SrTiO_3 is thus balanced by the larger bending of bands on switching resulting from the larger polarization of PbTiO_3 .

-
- [1] M. S. J. Marshall, A. Malashevich, A. S. Disa, M.-G. Han, H. Chen, Y. Zhu, S. Ismail-Beigi, F. J. Walker, and C. H. Ahn, *Phys. Rev. Appl.* 2, 051001 (2014).
 - [2] X. H. Liu, J. D. Burton, and E. Y. Tsybal, *Phys. Rev. Lett.* 116, 197602 (2016).
 - [3] G. Gerra, A. K. Tagantsev, N. Setter, and K. Parlinski, *Phys. Rev. Lett.* 96, 107603 (2006).

Mechanism of polarization switching in wurtzite-structured zinc oxide thin films

Hiroki MORIWAKE¹, Ayako KONISHI¹, Takafumi OGAWA¹, Craig A. J. FISHER¹,
Akihide KUWABARA¹, Takao SHIMIZU², Shintaro YASUI², Mitsuru ITOH²

¹ Nanostructures Research Laboratory, Japan Fine Ceramics Center, Nagoya, Aichi, JAPAN

² Materials and Structures Laboratory, Tokyo Institute Technology, Yokohama, Japan

The properties of a potentially new class of ferroelectric materials based on wurtzite-structured ZnO thin films are examined using first-principles calculations. Theoretical P - E hysteresis loops were calculated using the fixed- D method for both unstrained and (biaxially) strained single crystals. Ferroelectric polarization switching in ZnO (S.G. $P6_3mc$) is shown to occur via an intermediate non-polar structure with centrosymmetric $P6_3/mmc$ symmetry by displacement of cations relative to anions in the long-axis direction. The calculated coercive electric field (E_c) for polarization switching was estimated to be 7.2 MV/cm for defect-free monocrystalline ZnO. (Fig.1) During switching, the short- and long-axis lattice parameters expand and contract, respectively. The large structural distortion required for switching may explain why ferroelectricity in this compound has not been reported experimentally for pure ZnO. Applying an epitaxial tensile strain parallel to the basal plane is shown to be effective in lowering E_c during polarization, with a 5% biaxial expansion resulting in a decrease of E_c to 3.5 MV/cm. (Fig.2) Comparison with calculated values for conventional ferroelectric materials suggests that ferroelectric polarization switching of wurtzite-structured ZnO may be achievable by preparing high-quality ZnO thin films with suitable strain levels and low defect concentrations.

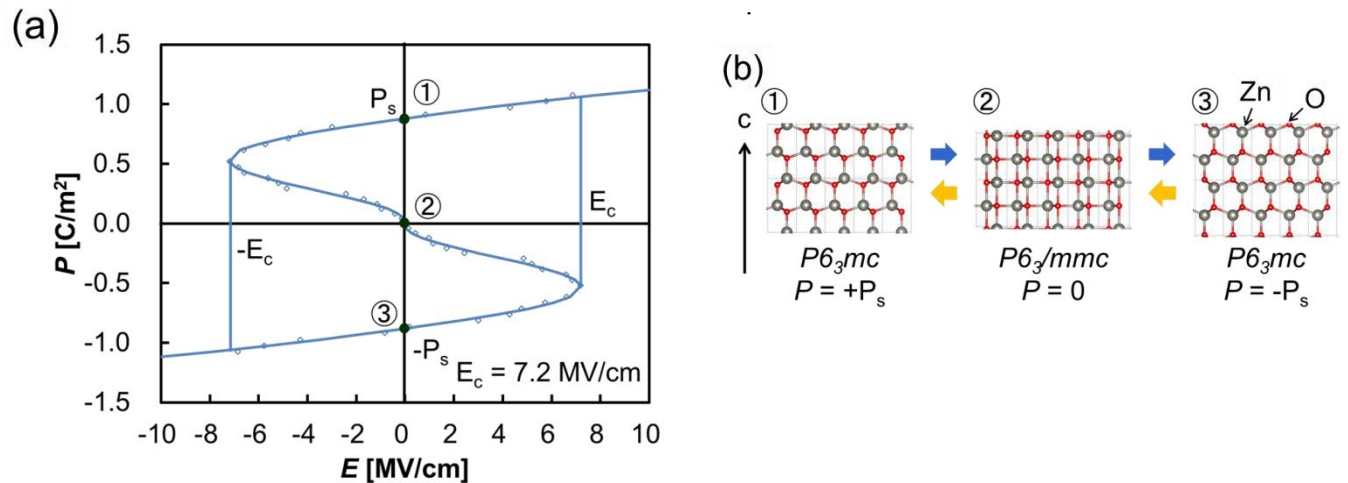


Fig. 1 (a) Theoretical P - E hysteresis loop for a wurtzite-structured ZnO single crystal calculated using the fixed- D method. Lines connecting data points are guides for the eye only. (b) Changes in crystal structure of ZnO during polarization switching from $+P_s$ to $-P_s$. In ① and ③, ZnO is in a polar state, with crystal symmetry $P6_3mc$, while in ② ZnO is in an intermediate non-polar state with crystal symmetry $P6_3/mmc$. Gray lines are unit cell edges.

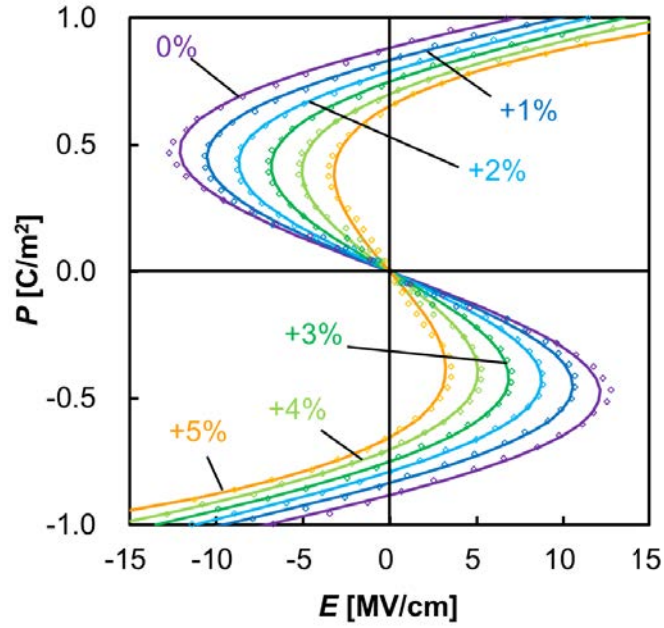


Fig. 2 Theoretical P - E hysteresis loops for wurtzite-structured ZnO single crystals with (0001) in-plane (biaxial) strains of 0 to +5% (tensile).

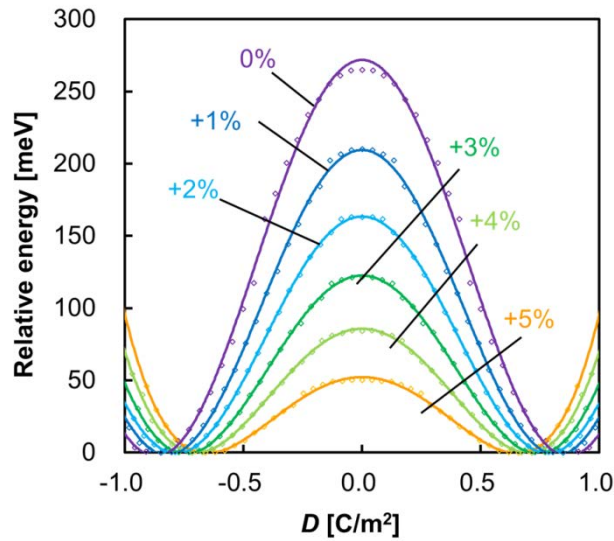


Fig. 3 Energy barriers of polarization switching under lateral strains of 0 to 5%. As strain increases, the energy barrier decreases significantly, from around 260 meV in the bulk crystal to 51 meV in the 5% strained system.

References

- [1] Ayako Konishi, Takafumi Ogawa, Craig A. J. Fisher, Akihide Kuwabara, Takao Shimizu, Shintaro Yasui, Mitsuru Itoh, and Hiroki Moriwake, *Appl. Phys. Lett.*, **109**, 102903 (2016).

212 species of macroscopic symmetry breaking revisited

J. Hlinka, V. Janovec, and P. Ondrejko

Institute of Physics, Academy of Sciences of the Czech Republic, Prague, Czech Republic

e-mail of the corresponding author: hlinka@fzu.cz

Keywords: ferroaxial, species, structural phase transitions, symmetry-breaking

Ferroelectric phase transitions are a special case of structural symmetry-breaking phase transitions on the one side and analogues to ferromagnetic phase transitions on the other side. The comparison of ferroelectric phase transitions with other phase transitions associated with macroscopic symmetry breaking are of interest that can yield interesting insights in conventional and non-conventional ferroelectricity in various modern multiferroic systems [1].

As an interesting example, one can deal with the so-called ferroaxial [2] phase transitions, phase transitions in which the order parameter is a macroscopic structural distortion with an axial vector symmetry.

As a side work, we have actually inspected all 212 species [3,4] of structural phase transitions with the macroscopic symmetry-breaking from the point of view of symmetry-imposed limitations on the morphic changes of the associated tensorial crystal properties [1]. An interactive lookup tool allowing one to access the (13×13) -sized property matrices of all 212 species is also available at <http://palata.fzu.cz/species/13x13axial>. The aim of this presentation is to clarify the notation for the macroscopic symmetry breaking species based on the classes of group-subgroup relations, and the content of our website look-up tool [1].

| Crystal family | Crystal classes |
|----------------|---|
| Triclinic | $1^\dagger, \bar{1}^\dagger$ |
| Monoclinic | $2^\dagger, m^\dagger, 2/m^\dagger$ |
| Orthorhombic | $222, mm2, mmm$ |
| Tetragonal | $4^\dagger, \bar{4}^\dagger, 4/m^\dagger, 422, 4mm, \bar{4}2m, 4/mmm$ |
| Hexagonal | $3^\dagger, \bar{3}^\dagger, 32, 3m, \bar{3}m, 6^\dagger, \bar{6}^\dagger, 6/m^\dagger, 622, 6mm, \bar{6}m2, 6/mmm$ |
| Cubic | $23, m\bar{3}, 432, \bar{4}3m, m\bar{3}m$ |

Table I. List of 32 crystal classes and distribution of pyroaxial classes (marked by the dagger sign) within the 6 crystal families(from Ref. [1]).

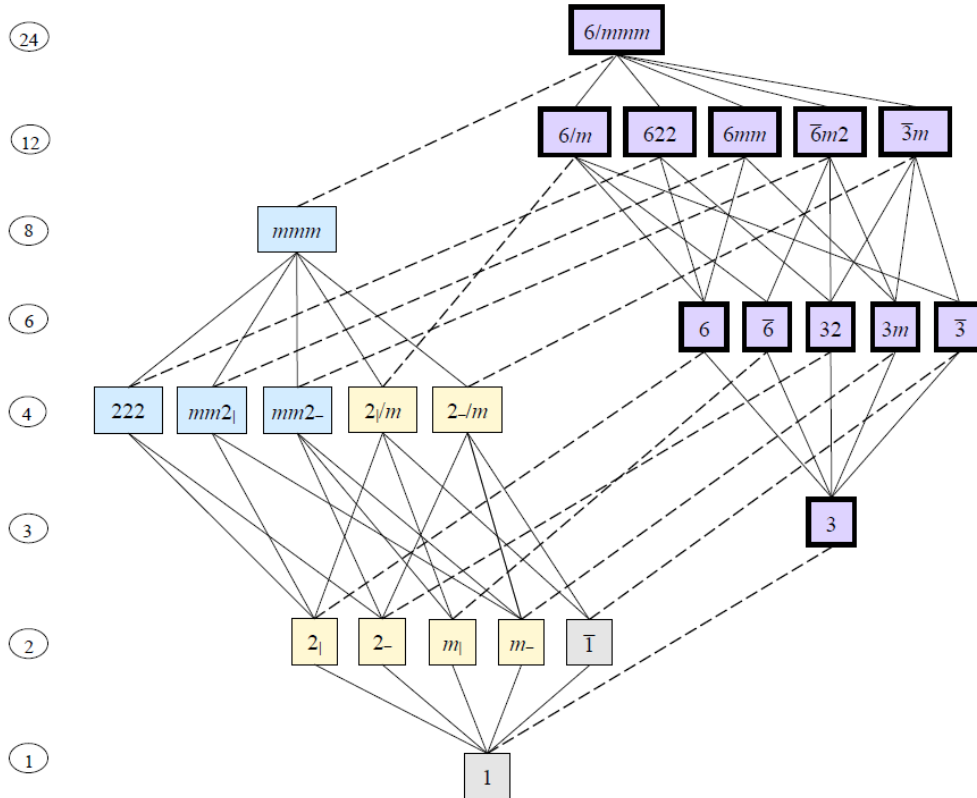


Figure 1. Subordination of hexagonal species. Each top-down connected path starting in one of the bold-frame vertices corresponds to one of the hexagonal species. Note that several paths may give the same species. Full, dashed, and dotted lines indicate group-subgroup relations of index 2, 3, and 4, respectively. Numbers in ovals give the order of the point group [1].

This work has been supported by Czech Science Foundation (project 15-04121S).

References:

- [1] J. Hlinka, J. Privratska, P. Ondrejko, and V. Janovec, *Symmetry Guide to Ferroaxial Transitions*, Phys. Ref. Lett. **116**, 177602 (2016).
- [2] R. D. Johnson, L. C. Chapon, D. D. Khalyavin, P. Manuel, P. G. Radaelli, and C. Martin, *Giant Improper Ferroelectricity in the Ferroaxial Magnet $\text{CaMn}_7\text{O}_{12}$* , Phys. Rev. Lett. **108**, 067201 (2012).
- [3] K. Aizu, *Possible species of "ferroelastic" crystals and of simultaneously ferroelectric and ferroelastic crystals*, J. Phys. Soc. Jpn. **27**, 387 (1969).
- [4] V. Kopsky, *Tensor parameters of ferroic phase transitions*, Phase Transitions **73**, 1 (2001).

Inelastic light scattering studies on relaxor ferroelectric $0.83\text{Pb}(\text{Mg}_{1/3}\text{Nb}_{2/3})\text{O}_3\text{-}0.17\text{PbTiO}_3$ single crystals

M. A. Helal¹, M. Aftabuzzaman¹, S. Tsukada², Šarūnas Svirskas³, Maksim Ivanov³, Jūras Banys³, and S. Kojima¹

¹Graduate School of Pure and Applied Sciences, University of Tsukuba, Tsukuba, Ibaraki 305-8573, Japan.

²Faculty of Education, Shimane University, Matsue, Shimane 690-8504, Japan.

³Faculty of Physics, Vilnius University, Sauletekio av. 9, Vilnius, LT-10222, Lithuania

E-mail address of corresponding author: helalphy82@gmail.com

Introduction

One of the most interesting group of disordered materials in condensed matter physics undergoing structural phase transition is the relaxor ferroelectrics (RFs) which are characterized by their nanometric local region so called polar nanoregions (PNRs) [1,2]. The compositional disorder, i.e., the disorder in the arrangement of different ions at a crystallographic equivalent site, is a common structural property of RFEs. Differences in the atomic radii and valences of the two B-site cations can lead to the formation of the chemically order nanosized regions (CORs) with a $Fm\bar{3}m$ symmetry dispersed in a disordered matrix with an average $Pm\bar{3}m$ symmetry [3,4]. Despite of many theoretical and experimental results, $(1-x)\text{PbMg}_{1/3}\text{Nb}_{2/3}\text{O}_3\text{-}x\text{PbTiO}_3$ (PMN- x PT) requires additional studies since the physical properties of both PNRs and CORs are still remain unclear. In the present study, the temperature and angular dependence of Raman scattering has been performed to investigate the local phenomena in PMN-17PT single crystals. In addition, the slowing down mechanism of PNRs towards the Curie temperature has been studied by the Brillouin scattering.

Results

Figure 1 shows the Raman spectra of PMN-17PT single crystals measured at some selected temperatures. Here we have mainly focused on the two characteristic modes denoted by A and B.

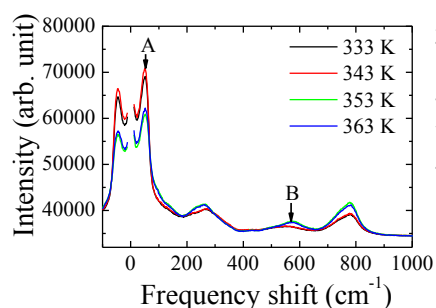


Fig. 1. Raman spectra of PMN-17PT at some selected temperatures.

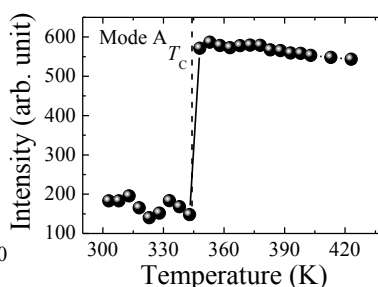


Fig. 2. Temperature dependences of intensity of mode A.

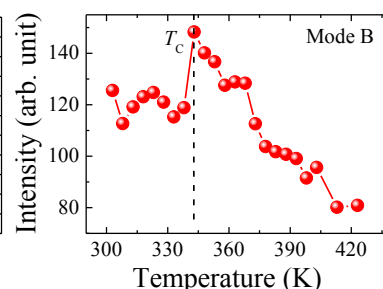


Fig. 3. Temperature dependences of intensity of mode B.

It is clear that the mode A shows almost temperature independent behavior in a paraelectric phase which is the characteristic of CORs. In contrast, the intensity of the mode B decreases with increasing temperature above the Curie temperature, T_C (~ 348 K), which is consistent with the behavior of PNRs. In order to confirm the origin of these two modes, we also analyze the angular dependences of Raman spectra in a paraelectric cubic phase at 423 K. Our calculated results for the F_{2g} mode of $Fm\bar{3}m$ symmetry shows very good agreement with the observed A mode. In addition, the observed intensity variations for

the B mode shows good agreement with the calculated results for the rhombohedral $E(x,y)$ -mode of PNRs.

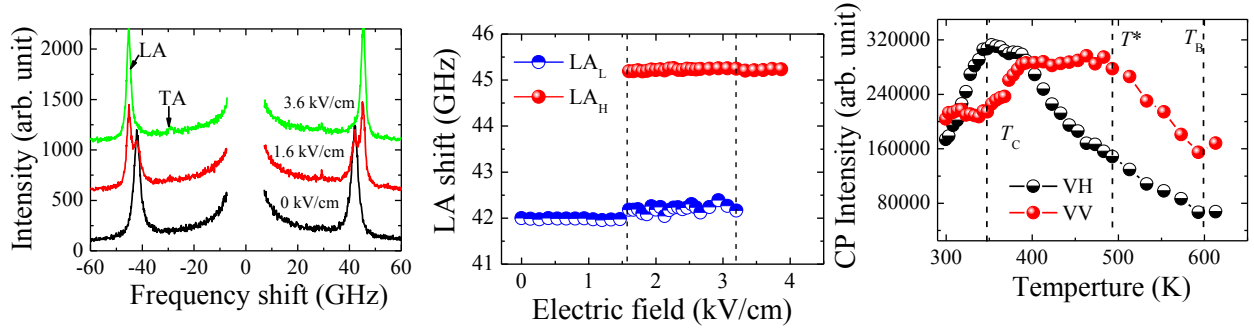


Fig. 4. Brillouin spectra measured at some selected electric fields at 303 K.

Fig. 5. Field dependence of LA shift at 303 K.

Fig. 6. Temperature dependence of broad CP intensity.

Figure 4 represents the Brillouin spectra at some selected electric fields at 303 K. By applying electric field along the [100] direction, the longitudinal acoustic mode (LA) begins to split at 1.6 kV/cm and exist up to 3.2 kV/cm, indicating the coexistence of ferroelectric macro- and nano-domains state caused by the random fields. However just above 3.2 kV/cm, two LA modes merge into single LA mode which reflect the field induced phase transition from rhombohedral to tetragonal phase.

In order to observe the relaxation dynamics of PNRs, we have also measured the temperature dependence of broad depolarized (VH) and polarized (VV) central peaks (CPs) by Brillouin scattering. At higher temperature, the VV-CP intensity is stronger than VH-CP as shown in Fig. 6. This result indicates that, at high temperature range, where the correlations among the PNRs is weak, rapid 180° reorientations of the off-center ions causes the dominance of the VV component of CP over the VH component. In addition, on cooling, the correlations among the PNRs become stronger, therefore their motion will be more restricted in fewer orientations, gradually losing the symmetric 180° -reorientations. As a result, below the intermediate temperature, T^* , the intensity of the VV-CP decreases while VH-CP increases. The relaxation time determined from the width of the CPs shows stretched critical slowing down due to the strong random fields. These results are discussed in comparison with those of the broadband dielectric spectroscopy, which relate to CORs and PNRs.

Conclusions

The ferroelectric phase transition and origin of the first order Raman modes in a paraelectric cubic phase of PMN-17PT single crystals were investigated. From our analysis, it is shown that the presence of CORs and PNRs with $Fm\bar{3}m$ and $R3m$ symmetry, respectively, in a cubic phase are responsible for the high temperature Raman spectrum. Under the sufficient electric field, the LA mode splitting was observed due to the mixed state of macro- and nano- domains caused by the random fields. The field induced rhombohedral to tetragonal phase transition was determined from the appearance of the TA mode in Brillouin scattering. The relaxation time of CP exhibits stretched critical slowing down towards the cubic to rhombohedral phase transition suggesting the order-disorder nature of the phase transition.

References

- [1] A. A. Bokov and Z. -G. Ye, J. Mater. Sci. **41**, 31 (2006).
- [2] K. Hirota, S. Wakimoto, and D. E. Cox, J. Phys. Soc. Jpn. **75**, 111006 (2006).
- [3] I. W. Chen, P. Li, and Y. Wang, J. Phys. Chem. Solids **57**, 1525 (1996).
- [4] P. K. Davies and M. A. Akbas, J. Phys. Chem. Solids **61**, 159 (2000).

Pressure-induced multiferroics via pseudo Jahn-Teller effects and novel couplings

Changsong Xu, Yang Li, Bin Xu, Jorge Íñiguez, Wenhui Duan*, and Laurent Bellaiche*

Dr. Changsong Xu, Yang Li, Prof. Wenhui Duan
State Key Laboratory of Low-Dimensional Quantum Physics and Collaborative Innovation
Center of Quantum Matter, Department of Physics, Tsinghua University, Beijing 100084, China
E-mail: dwh@phys.tsinghua.edu.cn

Dr. Changsong Xu, Dr. Bin Xu, Prof. L. Bellaiche
Physics Department and Institute for Nanoscience and Engineering, University of
Arkansas, Fayetteville, Arkansas 72701, USA
E-mail: laurent@uark.edu

Prof. Jorge Íñiguez
Materials Research and Technology Department, Luxembourg Institute of Science and
Technology, Avenue des Hauts-Fourneaux 5, L-4362 Esch/Alzette, Luxembourg

The NH_4CdCl_3 -type crystal structure was discovered in the said compound by H. Brasseur et al. in 1938.^[1] It was then experimentally and theoretically found in many AB_2S_3 sulfides,^[2,3] and also in iodate compounds, such as $\text{CH}_3\text{NH}_3\text{PbI}_3$.^[4] Xu *et al* further predicted, by using a first-principles-based genetic algorithm, that the NH_4CdCl_3 -type structure can also become the ground state of many ABO_3 oxides and ABF_3 fluorites, when under high enough pressure.^[5] Considering its generality and its occurrence after the perovskite (Pv) and post-perovskite (ppPv) structures when gradually increasing the hydrostatic pressure in various ABO_3 and ABF_3 compounds, the NH_4CdCl_3 -type structure was named as post-post-perovskite (ppPv) in Ref.^[5] – which is the convention we will also adopt here.

Interestingly, as far as we can tell, the ppPv structure has never been found (or predicted) to display an electrical polarization or the so-called Jahn-Teller (JT) distortions – intimately related to magnetism and electronic structure – in any material, including ABO_3 and ABF_3 systems. This is in line with the common belief that hydrostatic pressure suppresses structural distortions of the type that is typically related to electric polarization and Jahn-Teller effects.^[6,7]

Here we use first-principles simulations to predict that such beliefs have to be revisited.^[8] More precisely, we discover that applying pressure to many magnetic rare-earth manganites RMnO_3 not only leads to the stabilization of the ppPv structure, but also induces pseudo Jahn-Teller effects that, in turn, yields a spontaneous electrical polarization via a previously unknown coupling. Interestingly, the latter coupling only involves the polarization and the mentioned JT distortion; this feature sets the new coupling apart from other trilinear effects^[9, 10] in which a third structural distortion appears, as it strongly suggests the possibility of an easier control of JT effects and related electronic properties via the application of electric field.

Furthermore, the resulting polar and magnetic phase is found to survive when quenched to ambient pressure. Hence, our calculations reveal a new strategy to design novel tunable multiferroics within the family of ppPv compounds. This discovery should be of high interest given, on one hand, the scarcity of multiferroic materials and, on the other hand, the technological promise of materials with JT distortions and electronic properties tunable by application of electric fields.^[11]

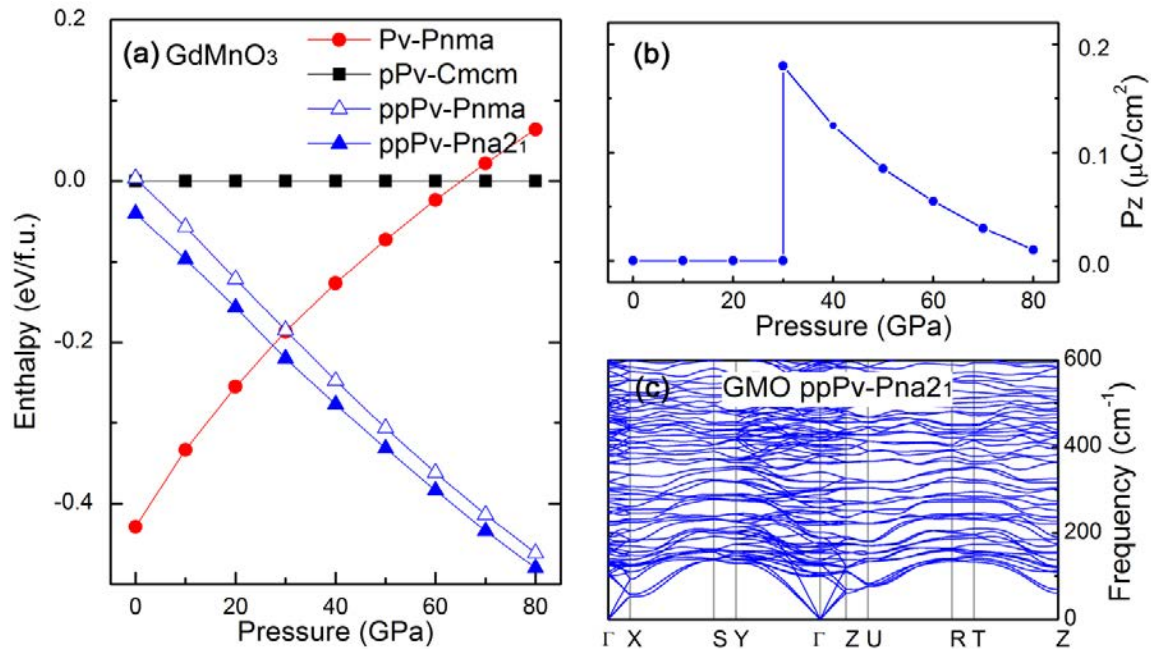


Fig 1. Properties of GdMnO₃. (a) Phase diagram under pressure; (b) polarization along z-axis; (c) phonon spectrum under 40 GPa

- [1] H. Brasseur, L. Pauling, Journal of the American Chemical Society 1938, 60, 2886.
- [2] R. Lelieveld, D. Ijdo, Acta Crystallographica Section B: Structural Crystallography and Crystal Chemistry 1978, 34, 3348.
- [3] J. A. Brehm, J. W. Bennett, M. R. Schoenberg, I. Grinberg, A. M. Rappe, The Journal of Chemical Physics 2014, 140, 224703.
- [4] W.-J. Yin, T. Shi, Y. Yan, Adv. Materials 2014, 26, 4653.
- [5] C. Xu, B. Xu, Y. Yang, H. Dong, A. R. Oganov, S. Wang, W. Duan, B. Gu, L. Bellaiche, Phys. Rev. B 2015, 91, 020101.
- [6] I. A. Kornev, L. Bellaiche, Phase Transitions 2007, 80, 385.
- [7] M. Baldini, V. Struzhkin, A. Goncharov, P. Postorino, W. Mao, Phys. Rev. Lett. 2011, 106, 066402.
- [8] *Pressure-induced multiferroics via pseudo Jahn-Teller effects and novel couplings* Changsong Xu, Yang Li, Jorge Íñiguez, Wenhui Duan and L. Bellaiche Advanced Functional Materials (in press)
- [9] J. Varignon, N. C. Bristowe, P. Ghosez, Phys. Rev. Lett. 2016, 116, 057602.
- [10] J. Varignon, N. C. Bristowe, E. Bousquet, P. Ghosez, Scientific Reports 2015, 5.
- [11] N. A. Spaldin, S.-W. Cheong, R. Ramesh, Phys. Today 2010, 63, 38.

Antiferroelectric topological insulators in ABC compounds

Bartomeu Monserrat,^{1,2,*} Joseph W. Bennett,¹ Karin M. Rabe,¹ and David Vanderbilt¹

¹*Department of Physics and Astronomy, Rutgers University, Piscataway, New Jersey 08854-8019, USA*

²*TCM Group, Cavendish Laboratory, University of Cambridge, J. J. Thomson Avenue, Cambridge CB3 0HE, United Kingdom*

(Dated: December 2, 2016)

Topological insulators and related materials [1] exhibit interesting properties such as robust edge currents or spin-momentum locking that make them promising candidates for technological applications. In this context, the control of topological order by means of electric fields is an interesting route to applications of these materials in electronics and spintronics.

Recent work has explored the use of electric fields to control topological order in ferroelectric materials, as shown schematically in Fig. 1a. These ferroelectric topological insulators exhibit two polarization states that can be used to, for example, control the spin texture around the Dirac cones of the surface states [2]. Several materials have been proposed to exhibit these properties: Tomiņaga and co-workers have proposed that superlattices of the ferroelectric material GeTe and the topological insulator Sb₂Te₃ exhibit electric field control of topological order [3]; Liu and co-workers have recently proposed that strained CsPbI₃ is a ferroelectric topological insulator [4]; and Di Sante and co-workers have shown that ferroelectricity and topological order coexist in the family of ABC hyperferroelectrics, which could be candidates for thin-film applications [2].

In this work we explore the possibility of controlling topological order in antiferroelectric materials. Ferroelectric materials exhibit two states of opposite polarity, but antiferroelectrics are more flexible as they exhibit two states of opposite polarity, and a third antipolar state. If all three states in an antiferroelectric correspond to a topological insulator, then the two polar states would be similar to those of the ferroelectric topological insulator, and the third state would be one without polarization. Perhaps more interestingly, if the two polar states and the antipolar state had distinct topological orders, then such an antiferroelectric topological insulator could be used to induce topological phase transitions using electric fields, as shown schematically in Fig. 1b.

We study potential antiferroelectric topological insulators in the recently proposed orthorhombic ABC family of materials [5]. These materials have a nonpolar reference structure of hexagonal $P6_3/mmc$ space group, which has energy-lowering distortions to a polar hexagonal $P6_3mc$ structure, and to an antipolar orthorhombic $Pnma$ structure. We use a convention in which the B and C atoms form hexagonal layers, and the A atoms are arranged in the stuffing sites in between. Bennett and co-workers have proposed a range of compounds in which the

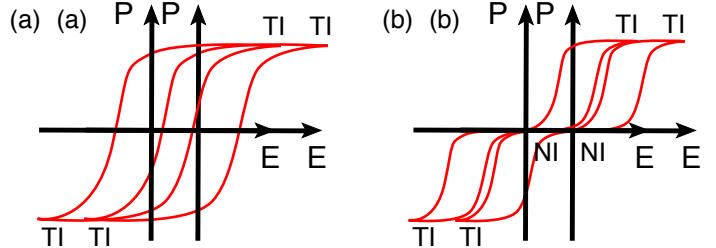


FIG. 1. Schematic representation of (a) a ferroelectric topological insulator and (b) an antiferroelectric topological insulator with an antipolar normal insulator (NI) state and two polar topological insulator (TI) states.

$Pnma$ antipolar structure has the lowest energy, with a small energy barrier to the $P6_3mc$ polar structure, which suggests the possibility of using these materials as antiferroelectrics [5]. The large number of possible ABC compounds with these characteristics make them an excellent platform to search for the coexistence of antiferroelectricity and other types of order. In particular, we find that the energy of the $P6_3/mmc$ structure is significantly higher than that of the $P6_3mc$ and $Pnma$ structures at the in-plane lattice constant of 4.7 Å.

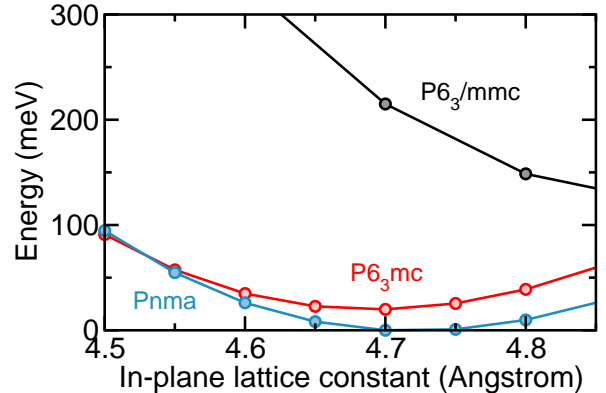


FIG. 2. Energy of the LiMgBi compounds of nonpolar $P6_3/mmc$, polar $P6_3mc$, and antipolar $Pnma$ structures as a function of in-plane lattice constant.

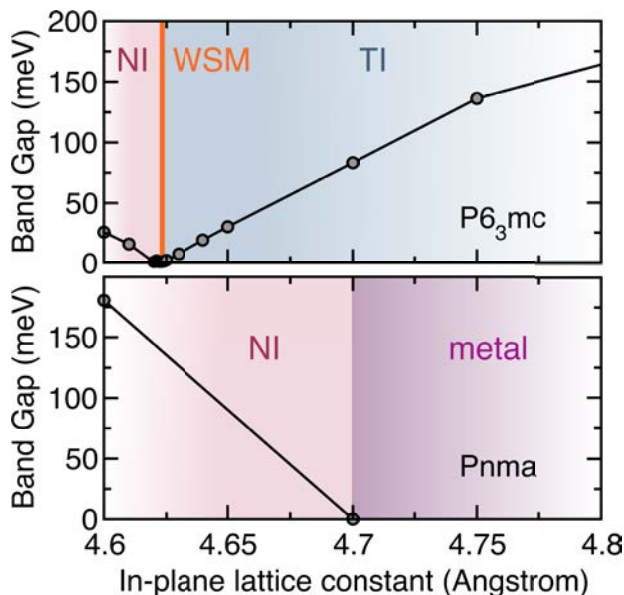


FIG. 3. Band gap of the LiMgBi compounds of polar $P6_3mc$ and antipolar $Pnma$ structures as a function of in-plane lattice constant, together with their topological character. The $P6_3mc$ structure exhibits regions in which it is a topological insulator (TI), a Weyl semimetal (WSM), and a normal insulator (NI), whereas the $Pnma$ structure exhibits metallic and normal insulator phases.

$P6_3mc$, and the antipolar $Pnma$ structures as a function of in-plane lattice constant (epitaxial strain) is shown in Fig. 2. The lowest energy structure is the antipolar $Pnma$ structure, which is 20 meV lower in energy than the polar $P6_3mc$ structure at an in-plane lattice constant of 4.70 Å. With decreasing lattice constant the energy difference between the two structures also decreases, facilitating phase transitions between the two. The small energy difference is suggestive of the potential antiferroelectric behaviour of this material, which could be tuned by means of epitaxial strain.

To investigate the topological properties of the LiMgBi compounds, we show the band gap of the antipolar $Pnma$ and the polar $P6_3mc$ structures as a function of in-plane lattice constant in Fig. 3. We further calculate the topological Z_2 index for the insulating phases, by following the adiabatic pumping of the Wannier charge centers over the Brillouin zone [6]. The antipolar $Pnma$ structure is a normal insulator for in-plane lattice constants smaller than 4.70 Å, and a metal for larger values of the lattice constant. The polar $P6_3mc$ structure is a topological insulator for in-plane lattice constants above 4.623 Å, and a normal insulator for in-plane lattice constant below 4.621 Å. These two phases are connected by a Weyl semimetal phase as required for a topological phase transition in a system without inversion symmetry [7]. The

Weyl semimetal phase only exists in a small range of 0.002 Å. Combining the results for the polar and antipolar structures, the LiMgBi compound is a candidate antiferroelectric topological insulator for in-plane lattice constants between 4.623 Å and 4.700 Å. Furthermore, it is an antiferroelectric topological insulator of the type shown in Fig. 1b, in which the polar structures are topological insulators, and the antipolar structure is a normal insulator.

In conclusion, ABC compounds are a rich playground in which to explore the existence of antiferroelectric topological insulators. The family of compounds $AMgBi$ ($A = \text{Li, Na, K}$) exhibits an interesting interplay between antiferroelectric and topological properties as a function of both pressure and strain, of which LiMgBi under strain is only a representative case. As another example, we also find regions of the phase diagram in which there are antiferroelectric topological insulators with the three states being topological insulators. Superlattices made of these three compounds expand the possibilities even further, holding promise for the experimental realization of some of these compounds.

This work was funded by NSF grant DMR-1408838. B.M. thanks Robinson College, Cambridge, and the Cambridge Philosophical Society for a Henslow Research Fellowship.

* monserrat@physics.rutgers.edu

- [1] C. L. Kane and E. J. Mele, “ Z_2 topological order and the quantum spin Hall effect,” *Phys. Rev. Lett.* **95**, 146802 (2005).
- [2] Domenico Di Sante, Paolo Barone, Alessandro Stroppa, Kevin F. Garrity, David Vanderbilt, and Silvia Picozzi, “Intertwined Rashba, Dirac, and Weyl fermions in hexagonal hyperferroelectrics,” *Phys. Rev. Lett.* **117**, 076401 (2016).
- [3] J. Tominaga, A. V. Kolobov, P. Fons, T. Nakano, and S. Murakami, “Ferroelectric order control of the Dirac-semimetal phase in $\text{GeTe-Sb}_2\text{Te}_3$ superlattices,” *Adv. Mater. Interfaces* **1**, 1300027 (2014).
- [4] Shi Liu, Youngkuk Kim, Liang Z. Tan, and Andrew M. Rappe, “Strain-induced ferroelectric topological insulator,” *Nano Lett.* **16**, 1663 (2016).
- [5] Joseph W. Bennett, Kevin F. Garrity, Karin M. Rabe, and David Vanderbilt, “Orthorhombic ABC semiconductors as antiferroelectrics,” *Phys. Rev. Lett.* **110**, 017603 (2013).
- [6] Alexey A. Soluyanov and David Vanderbilt, “Computing topological invariants without inversion symmetry,” *Phys. Rev. B* **83**, 235401 (2011).
- [7] Shuichi Murakami and Shun-ichi Kuga, “Universal phase diagrams for the quantum spin Hall systems,” *Phys. Rev. B* **78**, 165313 (2008).

Poster Session Abstracts

Photostriction in bismuth ferrite from first principles

Charles Paillard^{1,2}, Bin Xu¹, Brahim Dkhil², Gregory Geneste³ & Laurent Bellaiche¹

¹ Physics Department and Institute for Nanoscience and Engineering, University of Arkansas, Fayetteville, Arkansas 72701, USA

² Laboratoire SPMS, CentraleSupélec/CNRS, UMR 8580, Grande Voie des Vignes, 92 295 Châtenay-Malabry, France

³ CEA, DAM, DIF, F-91297 Arpajon, France

E-mail address : cha.paillard@gmail.com

Since 2009, the investigation of the coupling of multiferroic materials with light has experienced a renewed interest, as above-bandgap photovoltages were found to occur in BiFeO₃ (BFO) thin films¹. The so-called bulk photovoltaic effect (BPVE) (B') (²), occurring in any material lacking inversion symmetry³, has therefore attracted interest for the design of new efficient and cheap solar cells⁴. Therefore, the lack of inversion symmetry of ferroelectrics makes them natural candidates to the design of new kinds of solar cells, and also provides them with interesting piezoelectric properties⁵. The lack of inversion symmetry of ferroelectrics is also fundamental to their so-called piezoelectric properties, i.e. the coupling of their electric polarization to strain. Therefore, ferroelectrics offer a natural route towards the realization of light-induced actuators among the so-called class of photostrictive materials. Experimental evidences towards this goal have appeared in the last five years, with intense studies of the so-called photostriction in bismuth ferrite^{6,7}. Besides this steady state response of ferroelectrics to excitation by light, a giant shear strain induced by femtosecond laser pulses has been detected in bismuth ferrite, and attributed to the conjunction of the B') (and the piezoelectric effect in BFO^{8,9}. In addition, time-resolved synchrotron diffraction showed that shifting of Bragg peaks on a picosecond time scale occurs in both bismuth ferrite⁹ and a more conventional ferroelectric, lead titanate¹⁰. However, until now, theory has not investigated the coupling of light with electromechanical properties of ferroelectrics on a microscopic scale. To tackle this problem, we employ a 4-SF scheme¹¹ in which the occupation numbers of the 6 d-orbitals are constrained. We apply this method to various prototypical ferroelectric and multiferroic materials, such as bismuth ferrite¹². This scheme yields a photostriction effect of the same order of magnitude than the ones recently observed. It also predicts a strong dependence of photostrictive response on both the reached conduction state and the crystallographic direction (along which this effect is determined). In particular, according to our results, BFO should shrink along its pseudo-cubic and polarization axes, with the pseudo-cubic angle getting closer to 90°, while the directions perpendicular to the polarization, such as [100]_{pc}, stretches under excitation of electrons in the conduction band (see Figure 1); another of our main results is that photostriction is found to originate from the combination of screening of the polarization at the unit cell scale by the photoexcited carriers, and converse piezoelectric effect¹².

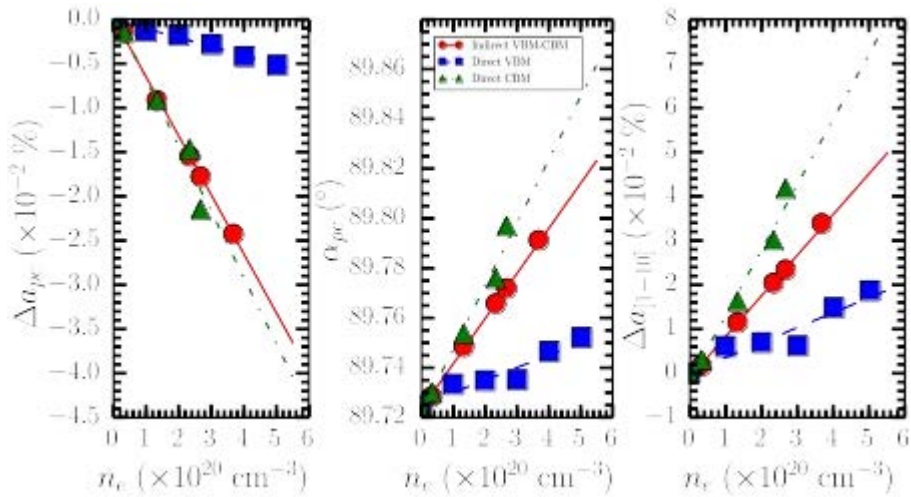


Figure 1: Left Panel: Lengths shorten in the pseudo-cubic directions for photo-excited electrons generated by different optical transitions; Middle panel: the pseudo-cubic angle increases; Right panel: lengths in the directions $\langle 1-10 \rangle$, perpendicular to P, increase. Red circles, blue squares and green triangles correspond to Indirect VBM-CBM, direct VBM and direct CBM transitions resp.

5 \$' \$acknowledges support from a public grant overseen by the French <ational =esearch Agenc* !; <=" as part of the >Investissements d'Avenir" program (referenceAA<=-10-L; BC-0035, Babex <anoSaclay"\$ B\$C. and L\$B\$ thank the support from the ; ir Force Office of Scientific =esearch Dnder Grant F; 9550-16-1-0065 and the D; = ' ; grant H=00###-15-2-0038 (M; %=2C program"\$

References

- ¹ S. Y. Yang, J. Seidel, S. J. Byrnes, P. Shafer, C.-H. Yang, M. D. Rossell, P. Yu, Y.-H. Chu, J. F. Scott, J. W. Ager, L. W. Martin, and R. Ramesh, *Nature Nanotechnology* **5**, 143 (2010).
- ² B. I. Sturman and V. M. Fridkin, *The Photovoltaic and Photorefractive Effects in Noncentrosymmetric Materials*, Gordon and Breach Science Publishers (1992).
- ³ V. M. Fridkin, *Crystallography Reports* **46**, 654 (2001).
- ⁴ B. Kundys, *Applied Physics Review* **2**, 011301 (2015).
- ⁵ B. Kundys, M. Viret, D. Colson, and D. O. Kundys, *Nature Materials* **9**, 803 (2010).
- ⁶ B. Kundys, M. Viret, C. Meny, V. Da Costa, D. Colson, and B. Doudin, *Physical Review B* **85**, 092301 (2012).
- ⁷ P. Ruello, T. Pezeril, S. Avanesyan, G. Vaudel, V. Gusev, I. C. Infante, and B. Dkhil, *Applied Physics Letters* **100**, 212906 (2012).
- ⁸ M. Lejman, G. Vaudel, I. C. Infante, P. Gemeiner, V. E. Gusev, B. Dkhil, and P. Ruello, *Nature Communications* **5**, 4301 (2014).
- ⁹ D. Schick, M. Herzog, H. Wen, P. Chen, C. Adamo, P. Gaal, D. G. Schlom, P. G. Evans, Y. Li, and M. Bargheer, *Physical Review Letters* **112**, 097602 (2014).
- ¹⁰ D. Daranciang, M. J. Highland, H. Wen, S. M. Young, N. C. Brandt, H. Y. Hwang, M. Vattilana, M. Nicoul, F. Quirin, J. Goodfellow, T. Qi, I. Grinberg, D. M. Fritz, M. Cammarata, D. Zhu, H. T. Lemke, D. Walko, E. M. Dufresne, Y. Li, J. Larsson, D. A. Reis, K. Sokolowski-Tinten, K. A. Nelson, A. M. Rappe, P. H. Fuoss, G. B. Stephenson, and A. M. Lindenberg, *Physical Review Letters* **108**, 087601 (2012).
- ¹¹ R. M. Martin, *Electronic Structure: Basic Theory and Practical Methods*, Cambridge University Press (2008).
- ¹² C. Paillard, B. Xu, B. Dkhil, G. Geneste and L. Bellaiche, *Physical Review Letters* **116**, 247401 (2016).

Electrocaloric effect in relaxor Ba(Zr,Ti)O₃ from atomistic simulations

Zhijun Jiang,^{1,2} Sergei Prokhorenko,² D. Wang,¹ Sergey Prosandeev,² Y. Nahas,² J. Íñiguez,³ and L. Bellaiche^{2,*}

¹*School of Electronic and Information Engineering & State Key Laboratory for Mechanical Behavior of Materials, Xi'an Jiaotong University, Xi'an 710049, China*

²*Physics Department and Institute for Nanoscience and Engineering, University of Arkansas, Fayetteville, Arkansas 72701, USA*

³*Materials Research and Technology Department, Luxembourg Institute of Science and Technology, 5 avenue des Hauts-Fourneaux, L-4362 Esch/Alzette, Luxembourg*

The electrocaloric effect (ECE) is the change in temperature and dipolar entropy induced by a change in electric field [1, 2]. The ECE has the potential to lead to an efficient solid-state refrigeration for a broad range of applications [3, 4]. Moreover, relaxor ferroelectrics are characterized by the existence of polar nanoregions, for which the long-range ferroelectric ordering is disrupted by structural disorder, leading to polar-glass states that can be easily switched by the electric field to ordered states with high polarization. Relaxor ferroelectrics might be the best candidates for cooling devices with a high ECE [5, 6]. Here we study the mechanisms of ECE in Ba(Zr_{0.5}Ti_{0.5})O₃ (BZT) relaxor ferroelectrics. We use first-principles-based effective Hamiltonian approach combined with Monte Carlo (MC) and Molecular Dynamics (MD) simulations that have been recently developed for BZT solid solutions [7, 8] to investigate the ECE in disordered BZT.

The electrocaloric coefficient α can be computed from MC (indirect) and MD (direct) simulations using the following relation:

$$\alpha = \frac{\Delta T}{\Delta E} \quad (1)$$

where ΔT and ΔE are the change in temperature and the change in the electric field. Here, we want to determine and understand the ECE coefficient using two indirect and two direct methods. For the indirect methods, one is based on the Maxwell thermodynamical relationship $(\partial S/\partial E)_T = (\partial P/\partial T)_E$, leading to the adiabatic temperature change $\Delta T = -\int_{E_1}^{E_2} \frac{T(E)}{C_E(T)} (\frac{\partial P}{\partial T})_E dE$, where T is the temperature, P is the polarization, C_E is the heat capacity per unit volume under constant dc electric field. This method will be called MC-1 here. The second MC scheme computes ECE coefficient using the cumulant formula given in Ref. [9], that is: $\alpha = -1.945 Z^* a_{lat} N T \left(\frac{\langle |u|E \rangle - \langle |u| \rangle \langle E \rangle}{\langle E^2 \rangle - \langle E \rangle^2} \right)$, where Z^* is the Born effective charge, a_{lat} is the five-atom lattice constant, N is the number of sites in the supercell, T is the initial temperature, u is the local mode, E is the internal energy, and $\langle \rangle$ denotes the average over all the supercell sites. This method will be called MC-2 here. For the direct methods, one determination of the electrocaloric effect is accomplished like in Ref. [10] and will be called MD-1. It uses dc and ac electric fields. The other one is based on the ramping method of Ref. [11] and will be called MD-2.

The polarization as a function of temperature obtained from

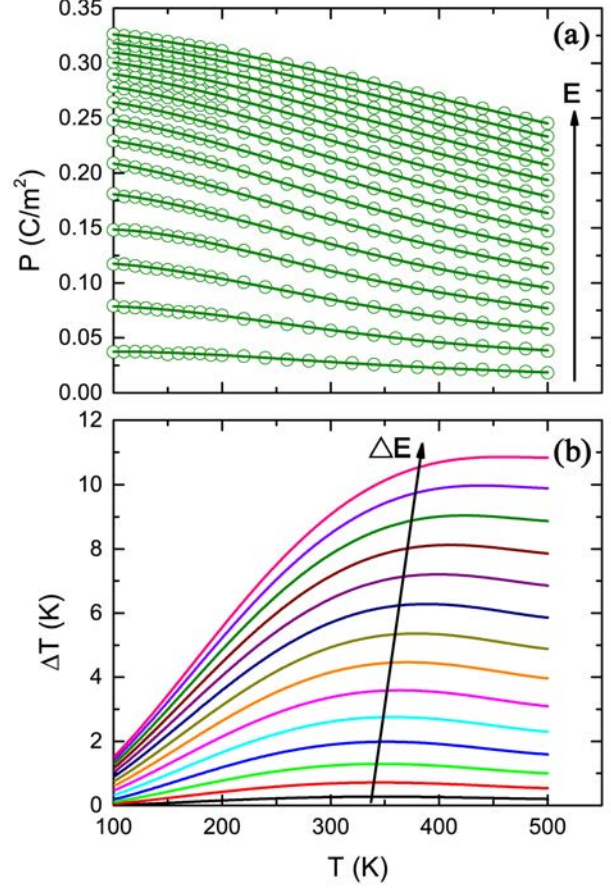


Figure 1: (a) The dependencies $P(T)$ at selected dc electric field in the range $2.0 \times 10^7 - 3.0 \times 10^8$ V/m. (b) The electrocaloric temperature change ΔT as a function of temperature in response to different electric field changes $\Delta E = E_2 - E_1$ ($E_1 = 2 \times 10^7$ V/m) applied along the [001] direction.

MC-1 simulations for Ba(Zr_{0.5}Ti_{0.5})O₃ at the dc electric field range of $2.0 \times 10^7 - 3.0 \times 10^8$ V/m is presented in Fig. 1(a). Values of $(\partial P/\partial T)$ were obtained from fourth-order polynomial fits to $P(T)$ curves. The electrocaloric temperature changes for temperature range 100-500 K are given in Fig. 1(b) for MC-1.

Figure 2 shows the electrocaloric coefficient α as a function of electric field E_0 at 300 K for the different indirect and direct methods. Here, $E_0 = \frac{E_1 + E_2}{2}$ for MC-1 and $E_0 = dc$ field for MD-1, MC-2 and MD-2. The results show a similar

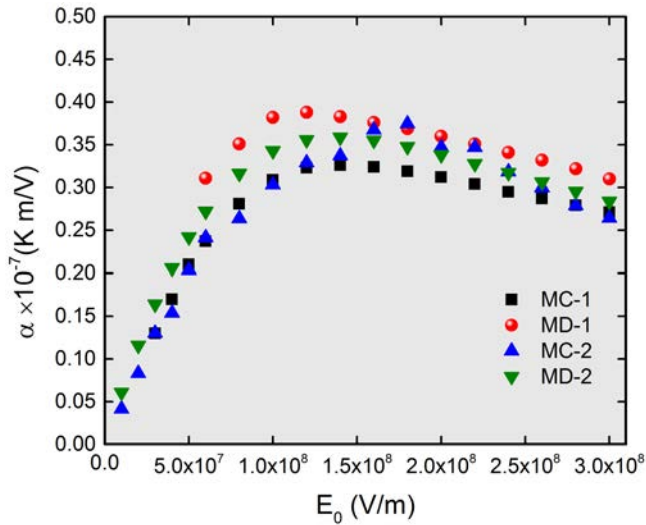


Figure 2: Electrocaloric coefficient α as a function of electric field E_0 for the different indirect and direct approaches at 300 K.

trend for the different indirect and direct simulations at 300 K: α is vanishing at small fields, then increases with the field before more-or-less being constant with field. α is thus strongly nonlinear, unlike in typical ferroelectrics. Note that we also calculated the ECE below the freezing temperature T_f ($\simeq 130$ K [7]), which shows that the indirect methods cannot be used to accurately compute the ECE due to non-ergodicity. In order to gain a microscopic understanding of ECE in BZT, we will also investigate the relationship between dipolar configurations and α .

Z.J., Sergei P. and L.B. thank the DARPA grant HR0011-15-2-0038 (MATRIX program). Z.J. also acknowledges support from the National Natural Science Foundation of China (NSFC), Grant No. 51390472, 11574246, U1537210,

National Basic Research Program of China, Grant No. 2015CB654903, and China Scholarship Council. Sergey P. thanks ONR Grant N00014-12-1-1034, and Y.N. thanks ARO grant W911NF-16-1-0227. We also acknowledge funding from the Luxembourg National Research Fund through the inter-mobility (Grant 15/9890527 Greenox, J.I and L.B.) and Pearl (Grant P12/4853155 Cofermat, J.I.) programs. Some computations were also made possible thanks to the MRI grant 0722625 from NSF, the ONR grant N00014-15-1-2881 (DURIP) and a Challenge grant from the Department of Defense.

* Electronic address: laurent@uark.edu

- [1] J. F. Scott, *Annu. Rev. Mater. Sci.* **41**, 229 (2011).
- [2] A. S. Mischenko, Q. Zhang, J. F. Scott, R. W. Whatmore, and N. D. Mathur, *Science* **311**, 1270 (2006).
- [3] Y. Bai, G.-P. Zheng, and S.-Q. Shi, *J. Appl. Phys.* **108**, 104102 (2010).
- [4] X. Moya, S. K.-Narayan, N. D. Mathur, *Nat. Mater.* **13**, 439 (2014).
- [5] S. G. Lu, B. Rožič, Q. M. Zhang, Z. Kutnjak, R. Pirc, M. Lin, X. Li, and L. Gorný, *Appl. Phys. Lett.* **97**, 202901 (2010).
- [6] X.-S. Qian, H.-J. Ye, Y.-T. Zhang, H. Gu, X. Li, C. A. Randall, and Q. M. Zhang, *Adv. Funct. Mater.* **24**, 1300 (2014).
- [7] A. R. Akbarzadeh, S. Prosandeev, E. J. Walter, A. Al-Barakaty, and L. Bellaiche, *Phys. Rev. Lett.* **108**, 257601 (2012).
- [8] D. Wang, J. Hlinka, A. A. Bokov, Z.-G. Ye, P. Ondrejčević, J. Petzelt, and L. Bellaiche, *Nat. Commun.* **5**, 5100 (2014).
- [9] S. Bin-Omran, I. A. Kornev, and L. Bellaiche, *Phys. Rev. B* **93**, 014104 (2016).
- [10] S. Prosandeev, I. Ponomareva, and L. Bellaiche, *Phys. Rev. B* **78**, 052103 (2008).
- [11] M. Marathe, A. Grünebohm, T. Nishimatsu, P. Entel, and C. Ederer, *Phys. Rev. B* **93**, 054110 (2016).

Defect-engineering: the case of $\text{LaBaCo}_2\text{O}_{5+\delta}$ compounds

Yurong Yang,¹ Chunrui Ma,^{2,3} Ming Liu,⁴ Hongjian Zhao,^{1,5} Yuan Lin,⁶ Chonglin Chen³ and Laurent Bellaiche¹

¹Physics Department & Institute for Nanoscience and Engineering, University of Arkansas, AR 72701, USA

²State Key Laboratory for Mechanical behavior of Materials, Xi'an Jiaotong University, Shaanxi 710049, PRC

³Department of Physics and Astronomy, University of Texas at San Antonio, TX 78249, USA

⁴Electronic Materials Research Laboratory, Key Laboratory of the Ministry of Education and International Center for Dielectric Research, Xi'an Jiaotong University, Shaanxi, 710049, PRC

⁵Laboratory of Dielectric Materials, Department of Materials Science and Engineering, Zhejiang University, Zhejiang, 310027, PRC

⁶State Key Laboratory of Electronic Thin films and Integrated Devices, University of Electronic Science & Technology of China, Sichuan 610054, PRC

Email: yyrwater@uark.edu

In the present study, we wonder if defect engineering can lead to novel properties. More precisely, we computationally investigate two types of $\text{LaBaCo}_2\text{O}_{5+\delta}$ (LBCO) compounds: $\text{LaBaCo}_2\text{O}_6$ with no defect (see Fig. 1 a) *versus* $\text{LaBaCo}_2\text{O}_5$ that possesses oxygen vacancies [1] (see Fig. 1 b).

The defect-free $\text{LaBaCo}_2\text{O}_6$ compound is predicted by first-principles calculations to adopt a tetragonal symmetry with a $P4/mmm$ space group and an axial ratio of $c/a=0.965$, that is smaller than 1. Our *ab-initio* calculations also yield that this defect-free system is metallic and is a ferromagnet having a spontaneous total magnetization of $2.5 \mu_B$ per five atoms, as consistent with measurements [2]. On the other hand, our calculations provide dramatically different properties for $\text{LaBaCo}_2\text{O}_5$. For instance, it has a monoclinic symmetry with a space group of Pc and axial ratio of $c/a=1.018$ (and which is thus larger than 1). It is also found to be insulating and to possess a polarization having an out-of-plane component (i.e., along the pseudo-cubic [00-1] axis) of about $1.3 \mu\text{C}/\text{cm}^2$ of magnitude, and an in-plane component of about $6.1 \mu\text{C}/\text{cm}^2$ along the pseudo-cubic [110] direction.

Moreover, the ground state of the defectuous $\text{LaBaCo}_2\text{O}_5$ compound is doubly degenerate, with the resulting two states having the same out-of-plane polarization while having *opposite* in-plane polarizations. Figure 2 shows a top view of the atomic structure of these two degenerate ground states. $\text{LaBaCo}_2\text{O}_5$ system possesses two different types of Co ions: Co ions that are denoted as Co(O) and experiencing an octahedral environment due to their six neighboring oxygen atoms *versus* Co ions that are labeled by Co(T) and that are tetrahedrally coordinated (they are located at the center of a CoO_4 tetrahedron). In Fig. 2, one can clearly see that, comparing to the oxygen in CoO_6 octahedral, the CoO_4 tetrahedra rotate about the [001] direction in clockwise or anticlockwise fashion, which results in the existence of an in-plane polarization, P_{in} . Interestingly, P_{in} is along the pseudo-cubic [110] direction *versus* the pseudo-cubic [-1-10] direction in the left and right panels of Fig. 2, respectively, because the rotation about the [001] direction of the CoO_4 tetrahedra is reversed between these left and right panels.

Experiments we further conducted demonstrate the possibility to grow highly-epitaxial $\text{LaBaCo}_2\text{O}_5$ films with ordered oxygen vacancies, via reduction treatments, and confirmed our predictions. These findings can open a new avenue for the design and synthesis of multiferroics

via defect-engineering.

Figure 1: Atomic structures used to mimic $\text{LaBaCo}_2\text{O}_6$ with no defect (a) and $\text{LaBaCo}_2\text{O}_5$ with oxygen vacancies (b). The Red and blue spheres correspond to O and Co ions, respectively. The light blue and green spheres represent Ba and La ions, respectively.

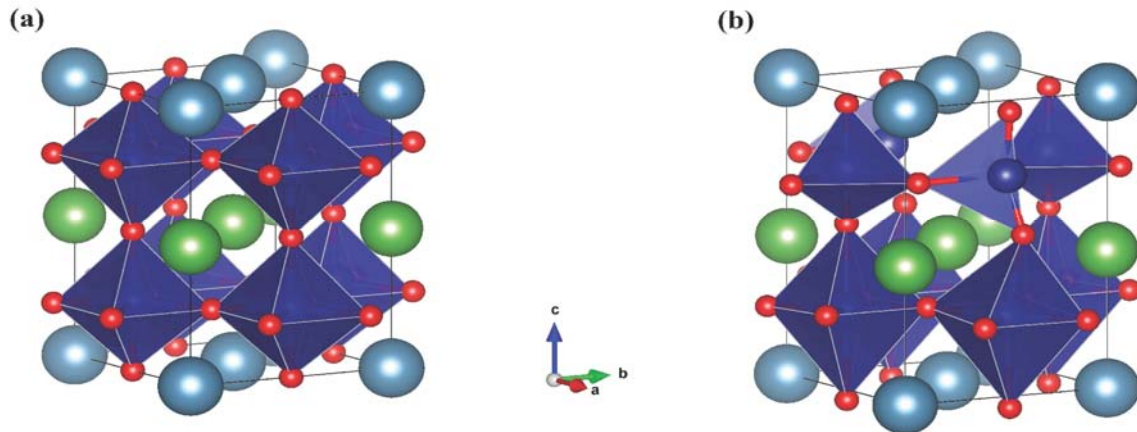
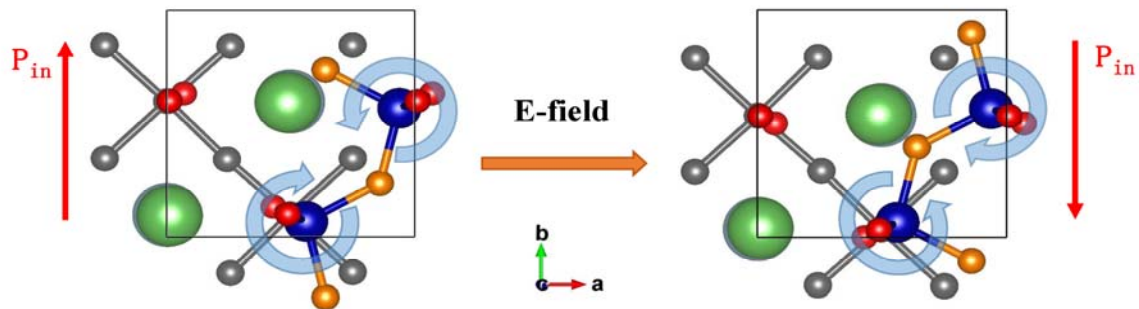


Figure 2: Top view of the atomic structures of the two degenerate ground states of $\text{LaBaCo}_2\text{O}_5$. The left panel and right panel configurations possess in-plane polarization, P_{in} , along the pseudo-cubic $[110]$ direction and $[-1-10]$ direction, respectively. The oxygen atoms in the Co(O)O_2 plane (Co in an octahedral environment) are shown in gray, while those belonging to the Co(T)O plane (Co in a tetrahedral environment) are depicted in orange. The other oxygen atoms are shown in red, while blue spheres correspond to Co ions. The light blue and green spheres represent Ba and La ions, respectively.



In summary, playing with oxygen vacancies in LBCO can transform the system from a ferromagnetic metal of tetragonal symmetry to a predominantly ferroelectric, antiferromagnetic with a weak magnetization, and adopting a low-symmetry monoclinic ground state. Defect-engineering in LBCO is therefore promising to alter and control various properties, and create new multiferroics.

This work is supported by ONR Grant N00014-12-1-1034. We also acknowledge a challenge grant from DoD allowing us the access of supercomputers.

References:

- [1] Y. M. Kim, J. He, M. D. Biegalski, et al., Nat. Mater. **11**, 888 (2012).
- [2] E.-L. Rautama, P. Boullay, A. K. Kundu, V. Caignaert, et al., Chem. Mater. **20**, 2742 (2008).

Increasing energy storage capabilities of space-charge dominated ferroelectric thin films using interlayer coupling

Jun Ouyang^{1,2} (e-mail: ouyangjun@sdu.edu.cn)

1. School of Materials Science and Engineering, Shandong University, Jinan, China, 250061; 2. National Institute of Standards and Technology, Gaithersburg, MD, 20899

Coupling effects between adjacent layers endow ferroelectric bi-layers or multilayers unique physical properties. For example, large dielectric constants may result from interface charge couplings in ferroelectric/ferroelectric or ferroelectric/dielectric bi-layers consisting of materials with different polarizabilities.^[1] In this talk, we will demonstrate that by combining the interlayer electrostatic coupling with the effect of a space charge layer near the electrode interface^[2] in a BaTiO₃/BiFeO₃ (BTO/BFO) ferroelectric bi-layer, the capacitive energy storage characteristics, including the energy density and charge-discharge efficiency, can be significantly improved (as compared with those of the single-layer films) (Fig.1). The bilayer film showed a slim P-E hysteresis loop characterized by a small remnant polarization and a large saturated one ($P_s \gg P_r$, Fig.1), which can be well explained by a competition between the effect of space charges (dominant at low field) and that of the interlayer charge coupling (dominant at high field) (Fig.2). The recoverable electric energy density was increased by about 85% from that of the single layer BaTiO₃ film (from $\sim 28 \text{ J/cm}^3$ to $\sim 51 \text{ J/cm}^3$, Fig. 1b).^[3]

References:

- [1] A.L. Roytburd, S. Zhong, S.P. Alpay, “Dielectric anomaly due to electrostatic coupling in ferroelectric-paraelectric bilayers and multilayers”, *Appl. Phys. Lett.* **87** (2005) 092902.
- [2] W. Zhang, Y. Gao, L. Kang, M. Yuan, Q. Yang, H. Cheng, W. Pan, J. Ouyang*, “Space-charge dominated epitaxial BaTiO₃ heterostructures”, *Acta Materialia*, **85**, 207 (2015).
- [3] H. Zhu, M. Liu, Y. Zhang, Z. Yu, W. Pan and J. Ouyang*, “Increasing energy storage capabilities of space-charge dominated ferroelectric thin films using interlayer coupling”, *Acta Materialia*, **122**, 252 (2017)

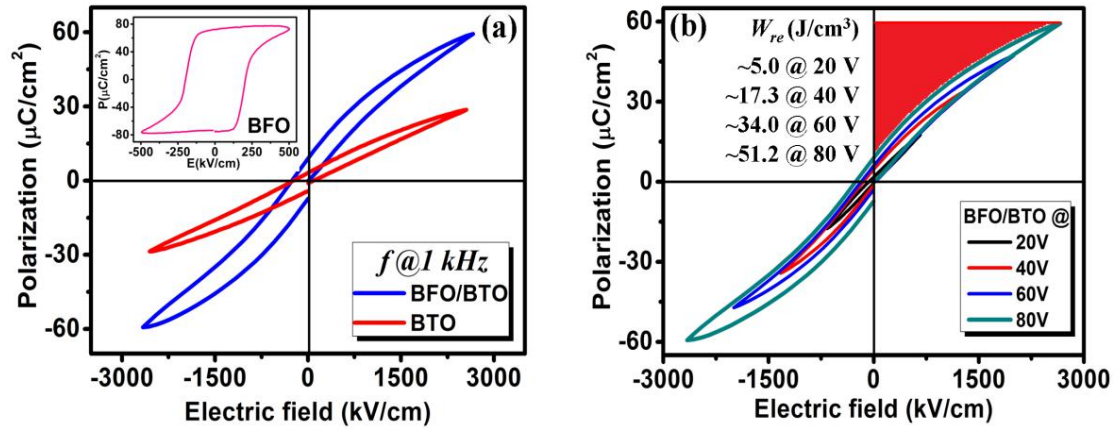


Fig. 1 (a) P-E loops of BTO and BFO/BTO bilayer films, the inset shows P-E loop of a sputtered BFO film with a thickness of ~ 500 nm. (b) P-E loops and recoverable electric energy densities (W_{re}) of the BFO/BTO bilayer measured at different maximum electric fields, the red-shaded area represents W_{re} . [3]

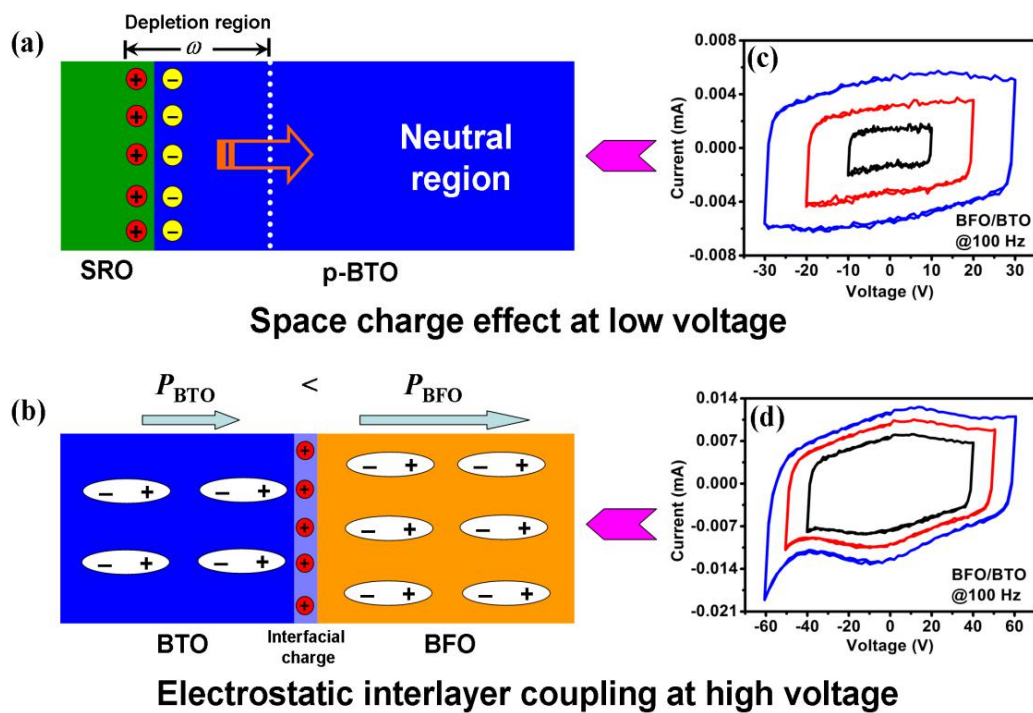


Fig. 2 (a) Illustration of the space charge effect and (c) the corresponding polarization switching currents at low voltages; (b) illustration of the interlayer charge coupling and (d) the corresponding polarization switching currents at high voltages for the BFO/BTO/SRO/STO heterostructure. [3]

Local and Macroscopic Properties of BaTi₂O₅

*[Shinya Tsukada](#)¹⁾, Yasuhiro Yoneda²⁾, Yasuhiro Fujii³⁾ and Yukikuni Akishige¹⁾

¹⁾Shimane University, Matsue, Shimane, Japan

²⁾Japan Atomic Energy Agency, Sayo-cho, Sayo-gun, Hyogo, Japan

³⁾Ritsumeikan University, Kusatsu, Shiga, Japan

*tsukada@edu.shimane-u.ac.jp

Ferroelectric oxides, such as BaTiO₃ and Pb(Mg_{1/3}Nb_{2/3})O₃, show large responses to an external electric field, which makes them attractive in application to electric devices. In these materials, there exists a distinction between local symmetry and the higher average symmetry. It is now common that large responses in ferroelectric perovskites are attributed to not only phonons at $k \sim 0$ but also relaxations of local structure called “polar nanoregions”. Thus, careful investigation of both local and macroscopic properties are essential to understand these materials.

BaTi₂O₅ shows larger dielectric response at $T_C \sim 743$ K than that of BaTiO₃ at $T_C \sim 410$ K [1]. So BaTi₂O₅ can be used as capacitance for high temperature application. Here, the origin of the high dielectric constant at T_C is still in controversy. The present study addresses this issue by using synchrotron X-ray powder diffraction and angle-resolved polarized Raman scattering experiments to investigate the static and dynamic properties of BaTi₂O₅.

Single crystals of BaTi₂O₅ for this Raman scattering experiments were grown from the melt of BaTiO₃ and TiO₂ starting from 1659 K. The crystals were needlelike along the b -axis and hexagonal column shape where a -surfaces (100) were obtained as shown in FIG. 1. Powders of BaTi₂O₅ for synchrotron X-ray diffraction were fabricated by using solid-state-reactions from BaCO₃ and TiO₂.

The long-range crystal structure obtained by Rietveld refinements shows good agreement with the short-range structure (atomic pair-distribution function), indicating that BaTi₂O₅ is homogeneous with the monoclinic point group of C_2 [2]. Surprisingly, no inhomogeneous structure contributes to the large dielectric response. Relationship between the laboratory system of Raman scattering and crystallographic axes of BaTi₂O₅ are shown in FIG. 1 (a). On the basis of the homogeneous monoclinic structure, angle-resolved Raman scattering intensity at the backscattering geometry is calculated as shown in FIG. 1(b). Figure 2 shows the experimental results in the ferroelectric phase at 303 K and in the paraelectric phase at 843 K. By comparing FIG. 1 and FIG. 2, we can easily assign each Raman peaks to A- or B-modes. The temperature dependence of the Raman spectra show marked changes only for quasi-elastic scattering which can be assigned to be A-mode. We consider that the origin of the large dielectric response at T_C is hopping Ti-ions and their correlations. Therefore, BaTi₂O₅ is understood in the framework of order-disorder phase transition picture.

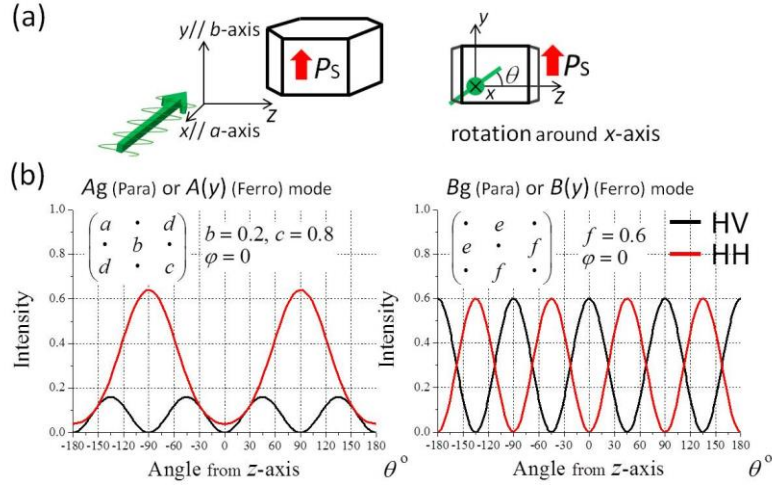


FIG 1. (a) Relationship between the laboratory system and crystallographic axes of BaTi_2O_5 . (b) Calculated polarization angle dependence of Raman intensity in the HH and HV geometries for $C2/m$ (paraelectric) and $C2$ (ferroelectric) structures of BaTi_2O_5 under the values $b=0.2, c=0.8, f=0.6$.

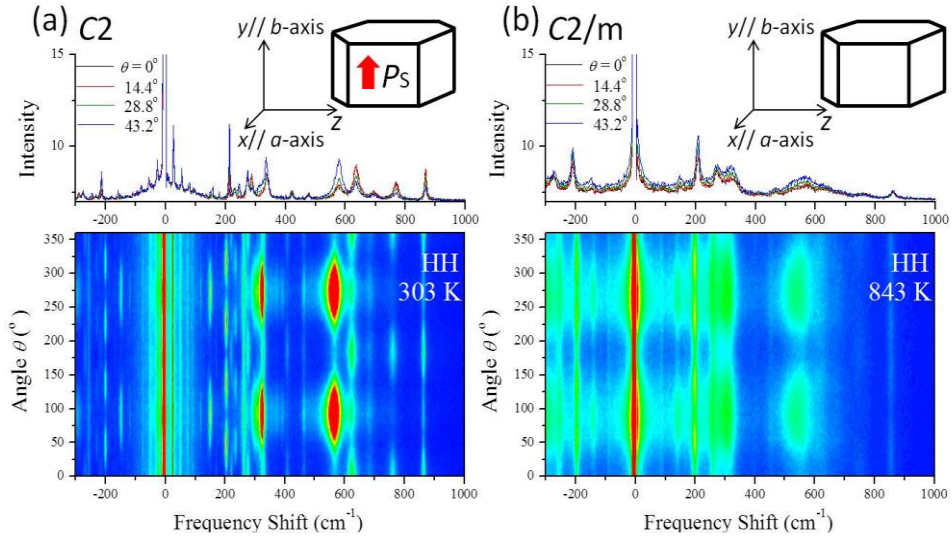


FIG 2. Angle-resolved-polarized Raman spectra from BaTi_2O_5 crystal in ferroelectric phase at 303 K (a) and paraelectric phase at 843 K (b).

REFERENCES

- [1] Y. Akishige, K. Fukano, and H. Shigematsu, *Jpn. J. Appl. Phys.* **42**, L946 (2003).
- [2] M. Yashima, R. Tu, T. Goto, and H. Yamane., *Appl. Phys. Lett.* **87**, 101909 (2005).

**Atomic scale structural complexities in antiferroelectric
Pb(Yb_{0.5}Nb_{0.5})O₃ and its solid solutions with PbTiO₃ revealed using
high resolution electron microscopy**

P. Nukala¹, C. Cochard^{1,2}, O. Guedes³, B. Dkhil¹, P-E. Janolin¹,

¹*CentraleSupélec, Grande voie des Vignes, Chatenay-Malabry, France, 92295*

²*MRT Département, Luxembourg institute of science and technology, 5 Avenue des
Hauts-Fourneaux, 4362 Esch-sur-Alzette, Luxembourg*

³*Etudes et productions Schlumberger, 1 rue Henri Becquerel, 92140 Clamart, France.*

Email of presenting author: pavan.nukala@centralesupelec.fr

The solid solution of double perovskite Pb(Yb_{0.5}Nb_{0.5})O₃ (PYN) with PbTiO₃ (PT) can be considered as a model system for the study of various polar orders which evolve macroscopically from antiferroelectric to ferroelectric through relaxor state with increasing PT concentration [1]. Yet, the structural details that can explain all the observations from various diffraction based studies on these solid solutions remain elusive. For e.g. in the x-ray diffraction studies on pure PYN, the chemical order on the B site and antipolar order are revealed through (1/2, 1/2, 1/2)_{pseudo-cubic (pc)} and (3/8, 3/8, 0)_{pc} modulation vectors respectively, and a monoclinic distortion is observed [1-3]. However, our own x-ray synchrotron and neutron (check if it is true) data reveal that not all reflections and their refinements can be satisfactorily explained through just these modulations.

To dissect the structural complexities and in general understand the general features leading to antiferroelectricity and relaxor behaviors, we systematically investigated this problem via modern tools of electron microscopy. Four different samples, i.e. PYN, PYN_{0.9}-PT_{0.1}, PYN_{0.8}-PT_{0.2}, PYN_{0.7}-PT_{0.3} were prepared via mechanical milling. First, we analyse in detail the structure of PYN to understand the interplay between various structural orders giving rise to antiferroelectric properties. Using high angle annular dark field STEM imaging, we first show the existence of complete B-site chemical ordering along [111]_{pc} direction (Fig. 1), an information hard to obtain using x-ray scattering owing to the non-existence of disordered PYN samples. Then we quantify the antipolar Pb displacements and modulations with $k_{\text{mod}}=(3/8, 3/8, 0)$. The B-cation displacements are also imaged, and with the help of electron diffraction we confirm a long-range existence of these respective modulations. Through annular bright field STEM imaging, sensitive to lighter atoms such as oxygen, we map the positions of oxygen atoms along various zones and deduce the oxygen octahedral tilt patterns and distortions.

On samples, which are doped with Ti, the onset of relaxor behavior can be identified via the disappearance of superstructure corresponding to antipolar displacements upon $\sim 10\%$ PT doping, while B-site chemical order is still retained. The distribution of Ti in these solid solutions, and structure-property correlation corresponding to the evolution of relaxor properties with Ti doping will be discussed.

Keywords: Piezoelectric, antipolar displacements, z-contrast imaging, electron diffraction, annular bright field.

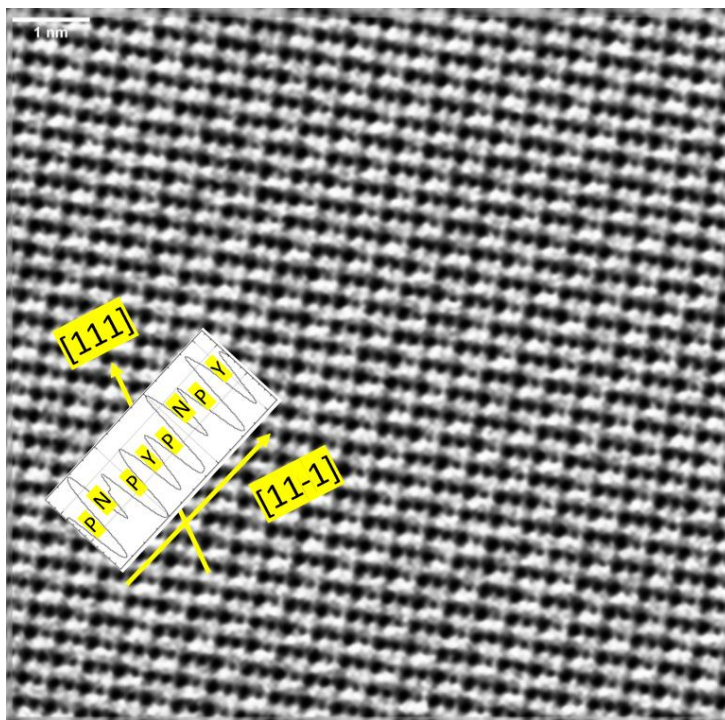


Figure 1: Bright field STEM image along $[-110]_{pc}$ zone axis clearly revealing the complete B-site chemical order along $[11-1]$ direction (corners to body-centers)

References

- [1] Cochard, C., $Pb(Yb_{1/2}Nb_{1/2})O_3-PbTiO_3$: a Model Solid Solution for the Study of the Different Polar Orders, PhD Thesis, CentraleSupélec (2015)
- [2] Kwon, K.R., Choo, W.K., *J.Phys:Cond.Mater.*, **3**, 2147 (1991).
- [3] Demidova, V., Gagarina, E., Ivanova, T., Sakhnenko, V., *Ferroelectrics*, **159**, 191 (2004)

Ferroelectric film dynamics simulated by a second-order time-dependent Landau model

Michael S. Richman,^{1,*} Paul Rulis,¹ and Anthony N. Caruso¹

¹Department of Physics and Astronomy, University of Missouri-Kansas City, Kansas City, Missouri 64110, USA

*E-mail: msrxt4@mail.umkc.edu

Based on the work of B. Wang *et al.* [J. Appl. Phys., **94**, 3384 (2003)], which established a second-order time-dependent Ginzburg–Landau equation and a model for domain switching in ferroelectric films that employs this equation, we simulate the reaction of a ferroelectric film system’s polarization \vec{P} to an applied electric field $\vec{E} = \vec{E}_0 \sin(\tilde{\omega}\tilde{t})$ where \vec{E}_0 , $\tilde{\omega}$, and \tilde{t} represent field amplitude, field frequency, and time, respectively. Departing from the work of Y.-L. Wang *et al.* [J. Mater. Sci., **46**, 2695 (2011)] that established the model produces experimentally expected scaling of \vec{E} – \vec{P} loop area $\langle \vec{A} \rangle$ as a function of $\tilde{\omega}$ for a system reacting to low- $\tilde{\omega}$ fields, we demonstrate that this model also produces experimentally expected scaling of $\langle \vec{A} \rangle$ in the high- $\tilde{\omega}$ regime. Further, we determine that this scaling implies, in agreement with empirical observations, that a characteristic time τ_1 exists for system relaxation and that this time is inversely proportional to \vec{E}_0 when the latter is sufficiently high. It is the value of τ_1 that determines whether or not complete domain reversal occurs at a given $\tilde{\omega}$. We also determine the dependence between field parameters and whether \vec{P} exhibits a symmetry-restoring oscillation (SRO) or a symmetry-breaking oscillation (SBO). Only SROs exhibit a symmetry identical to that of the applied field, i.e., $X(\tilde{t}) = -X(\tilde{t} + T/2)$ where T represents the period of the applied field and X represents \vec{E} or \vec{P} . To our knowledge, no existing work that employs a second-order time-dependent Ginzburg–Landau equation or a second-order time-dependent Landau–Khalatnikov equation demonstrates results of the type we present.

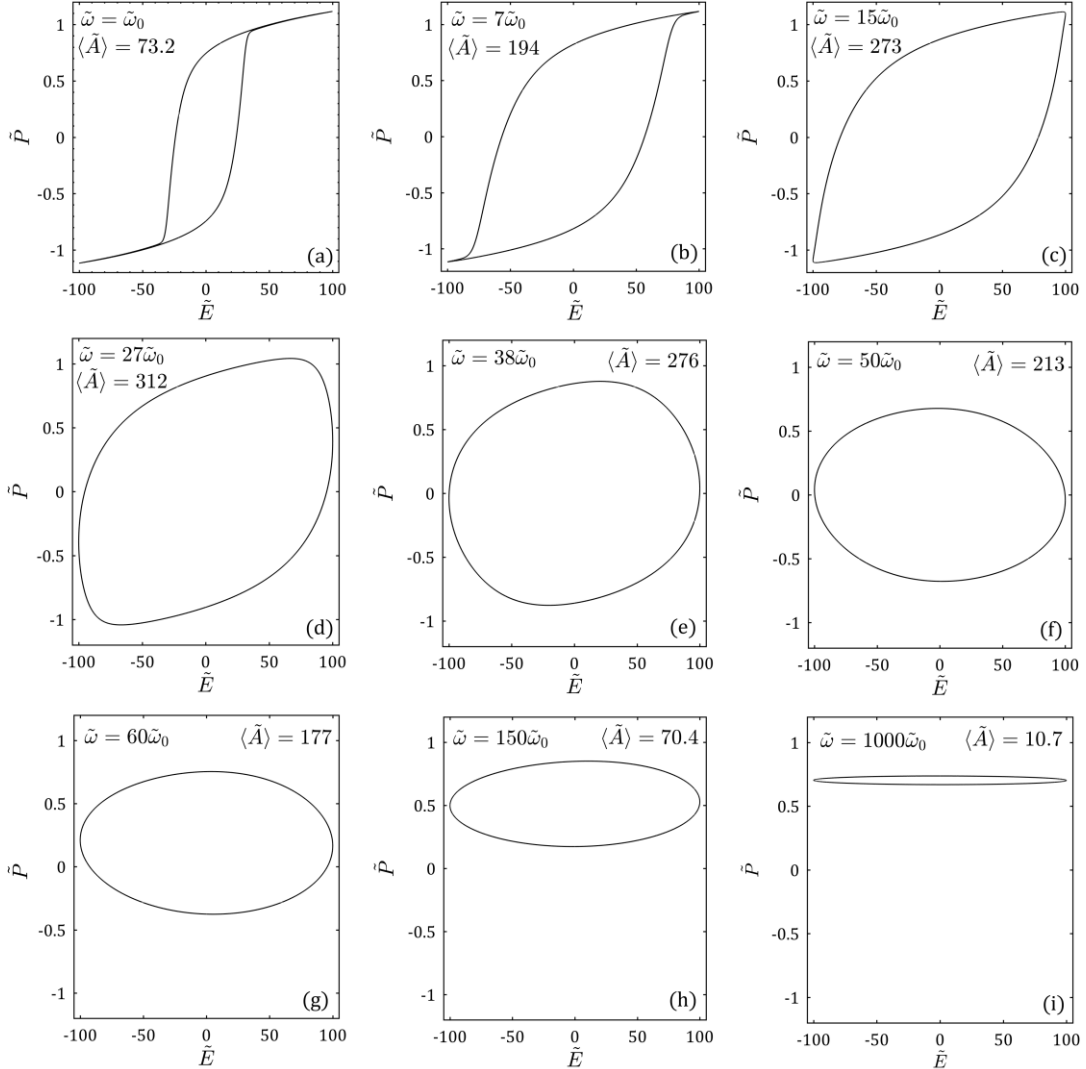


FIG. 1. \vec{E} – \vec{P} loops for $\vec{E}_0 = 100$ and the field frequencies indicated. The loop area for each loop is indicated.

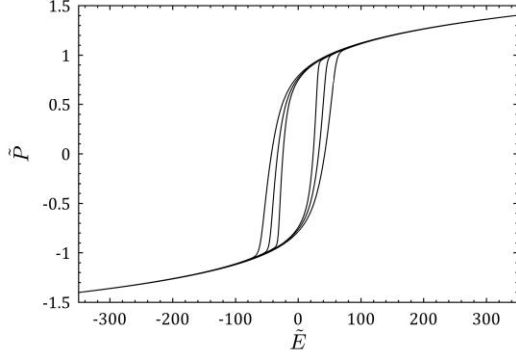


FIG. 2. \tilde{E} - \tilde{P} loops for $\tilde{E}_0 = 100, 200,$ and $350,$ respectively, from the innermost to the outermost loop. For each loop, $\tilde{\omega} = \tilde{\omega}_0.$

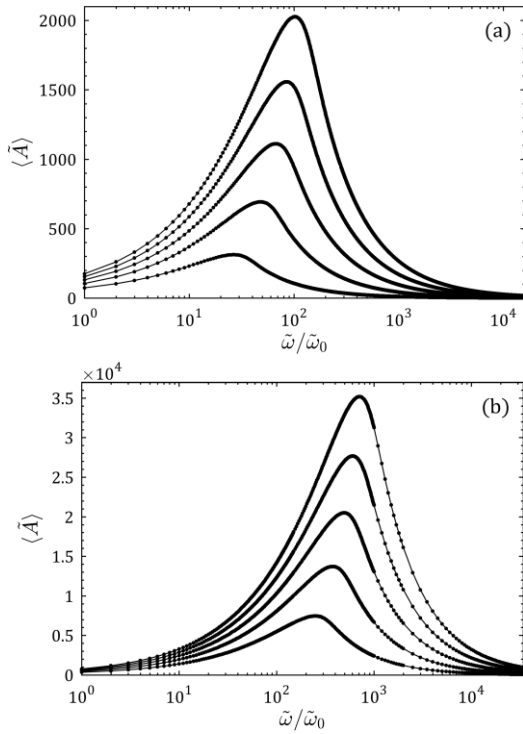


FIG. 3. $\langle \tilde{A} \rangle$ as function of $\tilde{\omega}$ for (a) $\tilde{E}_0 = 100, 200, 300, 400,$ and $500,$ respectively, from the lowermost to the uppermost curve and (b) $\tilde{E}_0 = 1500, 2500, 3500, 4500,$ and $5500,$ respectively, from the lowermost to the uppermost curve. For both (a) and (b) the $\tilde{\omega}$ axis is in a logarithmic scale and the lines connecting the data points serve as guides to the eye.

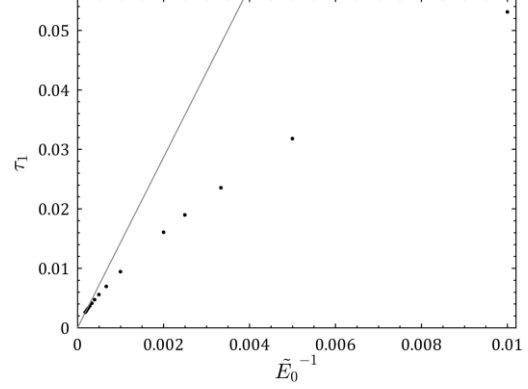


FIG. 4. τ_1 as a function of $\tilde{E}_0^{-1}.$ The solid line represents an inverse linear relationship between τ_1 and $\tilde{E}_0.$

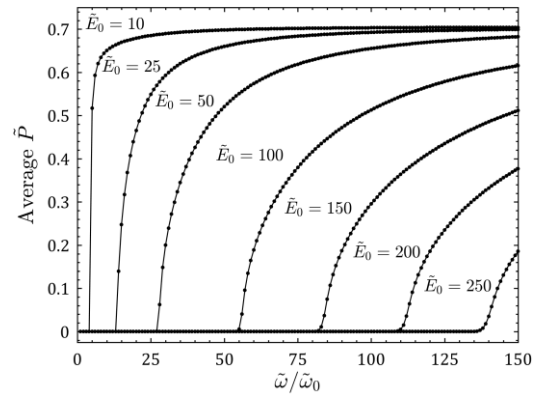


FIG. 5. Averaged \tilde{P} as a function of $\tilde{\omega}$ for the field amplitudes indicated. The lines connecting the data points serve as guides to the eye.

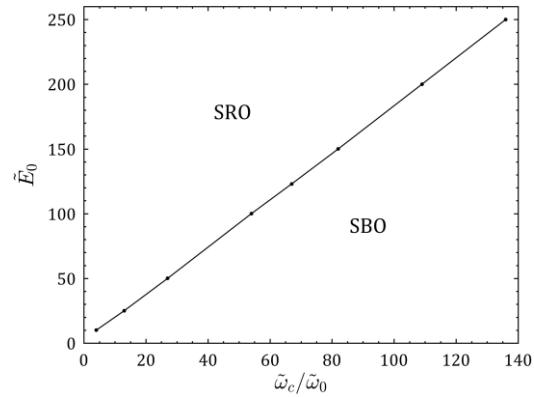


FIG. 6. Bifurcation curve indicating whether a symmetry-restoring oscillation (SRO) or a symmetry-breaking oscillation (SBO) exists for the field parameters indicated. The lines connecting the data points serve as a guide to the eye.

This work was supported by the Office of Naval Research under award N00014-16-1-2067.

Speckle Photography with LiNbO₃ Crystal for the Measurement of In-Plane Displacement Field Distribution of Distant Objects

Nasser A. Moustafa^{1,2} and A. Albarakaty¹

¹ Physics Department, Umm-Al-Qura University, Makkah, SA

² Physics Department, Faculty of Science, Helwan University, Ain Helwan, Cairo, Egypt

E-mail: Nasseramoustafa@gmail.com

Ferroelectric materials are of great interest because of their rich applications. Several techniques have been used to understand their behaviors. In this work, we use Speckle Photography method (SPM) [1-4] to measure the optical properties and surface deformations of bulk LiNbO₃ single crystals. Two beam coupling configuration using LiNbO₃ crystal as a recording medium has been extensively used for real time in-plane displacement of a transparent rough object. Low Power He-Ne laser was used to create the index grating of the speckle pattern inside the crystal and reads the grating to give the Young's fringes. In this technique, for the in-plane displacement measurement, the image of the transmitted object is formed in the crystal. The aim of the present work is to extend the applicability of the two-beam coupling configuration using LiNbO₃ as a recording medium for the evaluation of in-plane displacement of a transparent rough object using speckle photography method [5-10], and exam the validity and the accuracy of SPM method to study the structure and optical properties of perovskite materials.

Theoretical background

A diffused surface is illuminated by a beam from a laser source. The image of the object is formed on the recording plate. The recording plate is assumed have sufficient resolution. Two recordings are made with the object deformed between the two exposures. To delineate the displacement information, the processed plate, called the double-exposure speckle gram, is subjected to either a point-wise or whole-field filtering operation. The amplitude at any point $A_1(\zeta, \eta)$ in the image plane (ζ, η) can be expressed as

$$A_1(\zeta, \eta) = \frac{e^{i2\pi z/\lambda}}{i\lambda z} \iint a(x, y) \exp\left[-i\frac{\pi}{\lambda z}(x^2 + y^2)\right] \times \exp\left[i\frac{\pi}{\lambda z}[(\zeta - x)^2 + (\eta - y)^2]\right] dx dy \quad (1)$$

where $a(x, y)$ is the diffuser function, z is the distance between the diffuser and the plane passing through the point of convergence, and λ is the wavelength of the light used. This expression may be further simplified to

$$A_1(u, v) = C \iint a(x, y) e^{-i2\pi(ux + vy)} dx dy = CFT[a(x, y)] \quad \text{where } C = \exp\left[i\frac{\pi}{\lambda z}[(\zeta - x)^2 + (\eta - y)^2]\right], \quad u = \zeta/\lambda z \quad \text{and} \quad v = \eta/\lambda z \quad (2).$$

During the second exposure, amplitude distribution $A_2(u, v)$ after giving a displacement x_o to the diffuser can be expressed as $A_2(u, v) = C \iint a(x + x_o, y) e^{-i2\pi(ux + vy)} dx dy = C \iint a(x, y) e^{i2\pi ux_o} e^{-i2\pi(ux + vy)} dx dy = CFT[a(x, y)] e^{i2\pi ux_o}$ (3).

Resultant amplitude $A_R(u, v)$ after double exposure is the sum of the amplitude distributions after respectively the first and second exposures, i.e., $A_R(u, v) = A_1(u, v) [1 + \cos(2\pi ux_o)]$ (4)

Thus the intensity as detected by the CCD camera kept at the plane (η, ζ) is $I_R(u, v) = \frac{2}{\lambda^2 z^2} |A_1(u, v)|^2 [1 + \cos(2\pi ux_o)]$

Description of the experimental set-up

Fig.1 shows the experimental set-up of speckle recording in a LiNbO₃ crystal. This crystal is 5 mm x 5 mm x 5 mm in size. The optical configuration is implemented to study the in-plane displacement field distribution in a transparent, rough object, which have grain size 3 μm , and is placed at a distance 19.3 cm from the LiNbO₃ crystal. The object is illuminated with a coherent low power laser beam ($\lambda = 632.8 \text{ nm}$, $P = 10 \text{ mw}$). The laser beam spot at the diffuser plane was kept 1.4 cm in diameter to ensure suitable speckle size. The spot on the object is imaged by the imaging lens ($f = 75 \text{ mm}$). Nearly half portion of the incident beam illuminates the diffuser. Remaining portion of the laser beam enters the crystal directly. The diffuser is mounted on a high resolution X-Y translation stage. The

pump beam derived from the same laser source is added at an angle 38.62° (external) with respect to the object beam. The pump beam interferes with the object beam inside the crystal creating the necessary speckle gram. In the optical arrangement, the image of the region of interest will be extremely small, therefore essentially a highly localized dynamic grating will be formed inside the crystal. If an in-plane displacement given to the object will result in the shift of its image at the crystal plane and this will disturb the two-beam coupling. At this instant of time in the observation plane, we have two diffracted waves, and these two waves on interference, give rise to Young's fringes at the observation plane (CCD plane). The magnitude of the in-plane displacement x_o can be related with fringe width β of the Young's fringes at the CCD plane, the magnitude of the imaging system M and the distance z between the crystal planes and the observation plane using $x_o = \frac{\lambda z}{M\beta}$

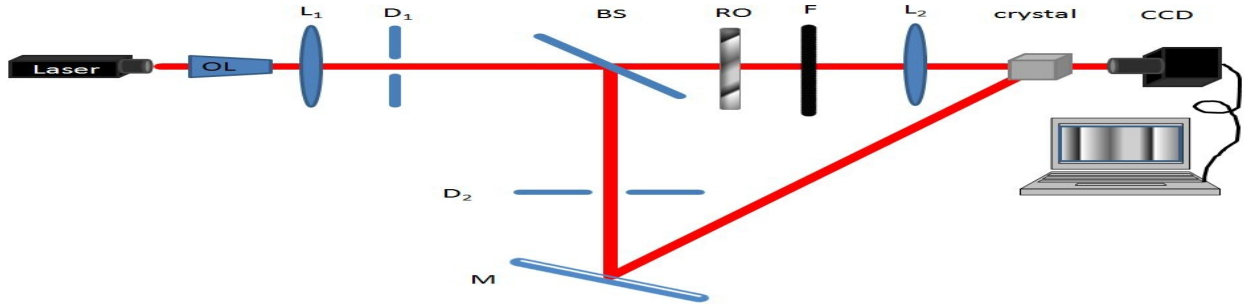


Fig.1: Experimental set-up for speckle photography with photorefractive crystal: OL: objective lens, L_1 : lens, D_1 and D_2 : pupil apertures, BS: beam splitter, RO: rough object, F: filter, L_2 : lens, Crystal LiNbO₃, CCD: fourier plane, M: mirror, I_1 : average intensity of the reference plane wave, I_2 : average intensity of the pump beam.

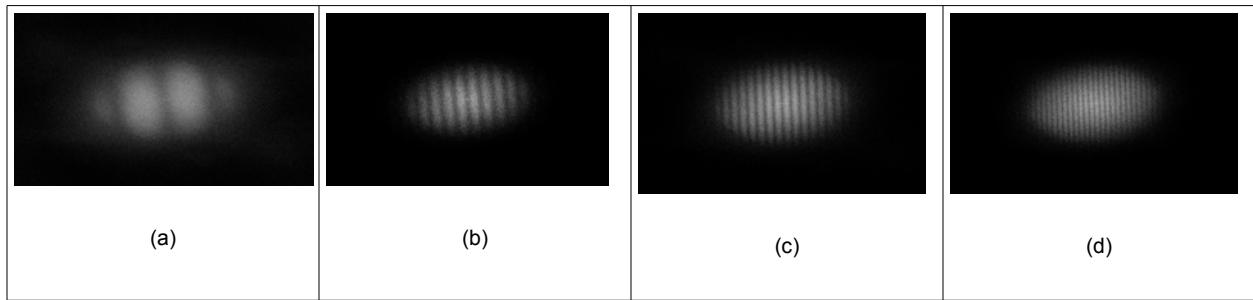


Fig.2: In-plane displacement fringe patterns when the object's shift (a) $x_o = 2\mu\text{m}$, (b) $x_o = 8\mu\text{m}$, (c) $x_o = 12\mu\text{m}$ and (d) $x_o = 20\mu\text{m}$.

Acknowledgment

This work is completely supported by King Abdulaziz City for Science and Technology under grant number 12-NAN2287-10.

References

- [1] B.Pouet, S.Krishnaswamy, Appl. Opt. **35** (1996) 787-794.
- [2] M.H. Majles Ara, C. Vijayan, N.K. Mohan, R.S. Sirohi, Optik **110** (1999) 383-388.
- [3] S.H.Collicott, L.Hesselink, Proc. SPIE **814** (1998) 700-704.
- [4] Myrian Tebaldi, Nestor Bolognini, Luis Arizmendi, Opt. Commu. **234** (2004) 43-51.
- [5] Nasser A. Moustafa, International Journal of Physics and Research (IJPR), Vol. **3**, Issue 3, 61-72, (2013).
- [6] Nasser A. Moustafa, Proc. SPIE 8791, Videometrics, Range Imaging, and Applications XII; and Automated Visual Inspection, Munich, Germany, 87911P (May 24, 2013).
- [7] Spagnolo GS, Paoletti D, and Ambrosini D, Opt. Commun. **169**, 51-57 (1999).
- [8] Yamaguchi I. In Sirohi RS (ED), Speckle Metrology. Marcel Dekker Inc., New York 1993.
- [9] Yamaguchi I, J.Opt.Soc.Am. **A1**, 81-86 (1984).
- [10] Slazar F, and Gascon F, Opt. Commun. **119**, 77-84 (1995).

Structure and properties of $\text{Pb}(\text{Mg}_{1/4}\text{Nb}_{1/2}\text{Ti}_{1/4})\text{O}_3$ Nanodot from first principles based effective Hamiltonian approach

A. Albarakati¹, S. Prosandeev^{2,3}, D. Wang⁴, and L. Bellaiche²

¹ Physics Department, Umm Al-Qura University, Makkah, Saudi Arabia

² Physics Department and Institute for Nanoscience and Engineering, University of Arkansas, Fayetteville, Arkansas 72701, USA

³ Research Institute of Physics, Southern Federal University, 344090 Rostov on Don, Russia

⁴ School of Electronic and Information Engineering and State Key Laboratory for Mechanical Behavior of Materials, Xians Jiaotong University, Xi'an 710049, China
E-mail: a_albrak@yahoo.com

Relaxor ferroelectric systems (bulk/nanostructure) are very important because of their unusual properties and potential applications [1,2]. Atomistic simulations can reveal many interesting features of bulk or nanostructured materials that may lead to new applications. For example, calculations of the dipole pattern in nanodots of BaTiO_3 and $\text{PbZr}_{1-x}\text{Ti}_x\text{O}_3$ [3,4] showed a vortex structure, which is characterized by a toroidal moment. In this study, Monte-Carlo (MC) and Molecular dynamics (MD) methods, within the frame work of Effective Hamiltonian (Heff), are used to simulate $\text{Pb}(\text{Mg}_{1/4}\text{Nb}_{1/2}\text{Ti}_{1/4})\text{O}_3$ nanodots (PMN-25PT NanoDot) for various cases, such as the size of nanodot, the distribution of B-site atoms, and various concentration/distribution of oxygen vacancies (OVs).

We can summarize our work as follows. First, we extend Heff developed in reference [5] to include the influence of surfaces and OVs by adding terms that characterize the interaction of surfaces and OVs with local dipoles and strains. Second, we perform MC and MD simulations under ideal open circuit condition from high to low temperature for various nanodots. During each simulation, the size of dot, the distribution of B-site atoms, the amount and distribution of OVs, and the temperature are kept fixed. The outputs of our simulations are local mode \mathbf{u} (which are directly proportional to polarizations), homogenous strains, and static/dynamic dielectric susceptibility as function of frequency. Third, we compute toroidal and hyper-toroidal moments as well as their susceptibilities, using the methods shown in reference [6].

Results of these MC and MD simulations reflect the importance of the size of nanodot and the distribution of B-site atoms. For example, figures 1-4 display the dielectric susceptibility (real and imaginary parts) versus frequency at 50K for a disordered $10 \times 10 \times 10$ PMN-25PT nanodot, a perfectly ordered $10 \times 10 \times 10$ PMN-25PT nanodot, a disordered $5 \times 5 \times 40$ PMN-25PT nanodot (along x-axis), and a disordered $5 \times 5 \times 40$ PMN-25PT nanodot (along z-axis). These and other results will be discussed in details.

This work is supported by King Abdulaziz City for Science and Technology under grant number 11-NAN1414-10 and ONR Grant N00014-12-1-1034.

References:

- [1] Park S-E. and Shrout T.R., J. Appl. Phys. 82, 1804 (1997).
- [2] Park S-E. and Shrout T.R., Ultrason. Ferroelectr. Freq. Control 44, 1140 (1997).
- [3] H. Fu and L. Bellaiche, Phys. Rev. Lett. 91, 257601 (2003).
- [4] Ivan I. Naumov, L. Bellaiche, and Huaxiang Fu, Nature 432, 737-740 (2004).
- [5] Al-barakaty A., *Finite-temperature properties of complex perovskite from first principles calculations*, Ph.D thesis, University of Arkansas, 2004.
- [6] S. Prosandeev and L. Bellaiche, J. Mater. Sci. 44, 5235-5248 (2009).

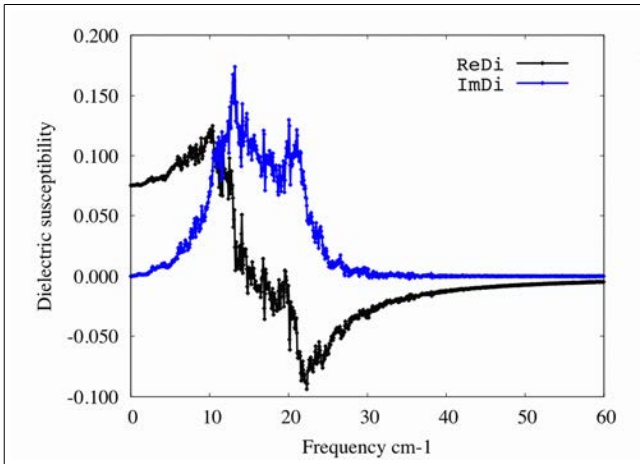


Figure1: Dielectric susceptibility versus frequency for a disordered 10x10x10 PMN-25PT Nanodot at 50K

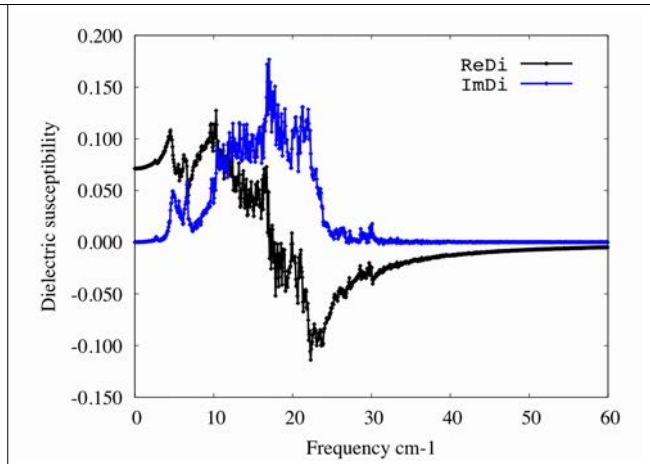


Figure2: Dielectric susceptibility versus frequency for a perfectly ordered 10x10x10 PMN-25PT Nanodot at 50K.

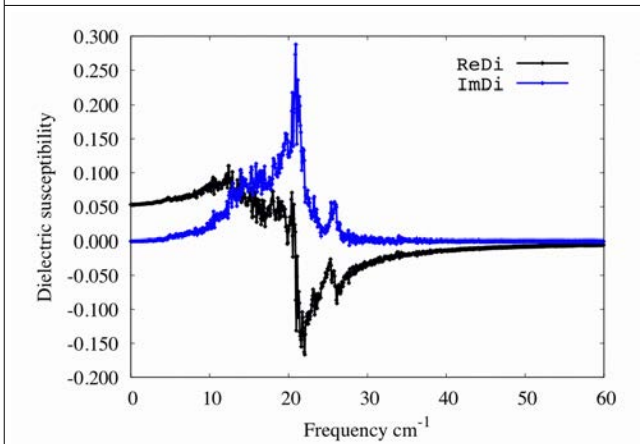


Figure3: Dielectric susceptibility versus frequency at 50K for a disordered 5x5x40 PMN-25PT Nanodot along x-axis at 50K.

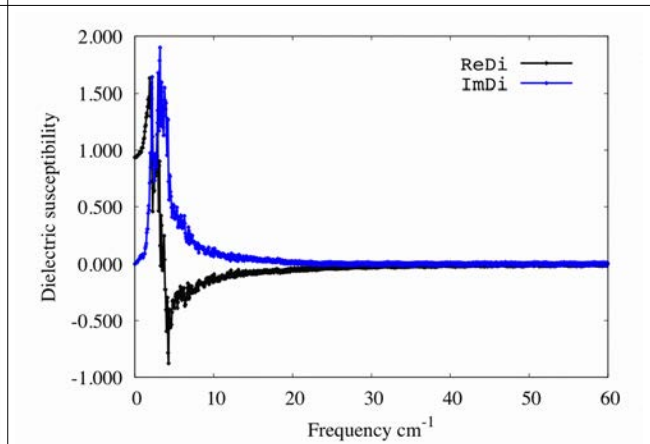


Figure4: Dielectric susceptibility versus frequency at 50K for a disordered 5x5x40 PMN-25PT Nanodot along z-axis at 50K.

Temperature dependence of Ti 1s near-edge spectra in two perovskites: theory and experiment

Eric Cockayne*,¹ Eric L. Shirley,¹ Bruce Ravel,¹ and Joseph C. Woicik¹

¹National Institute of Standards and Technology, Gaithersburg, Maryland 20899 USA

Near-edge spectroscopy is a technique that can extract a wealth of information regarding local atomic geometry.[1] Perovskite systems provide an excellent testing ground for near-edge spectroscopy, as they exhibit a variety of transitions (ferroelectric, antiferroelectric, antiferrodistortive, *etc.*). The Ti 1s near-edge spectra in SrTiO₃ and PbTiO₃ reveal electric-dipole and electric-quadrupole transitions to Ti 4p, 3d and mixed 4p-3d states. Crystal-field-split “pre-edge feature are attributed to 1s-3d transitions and are small compared to the main “edge jump at the onset of the Ti 4p continuum states around 4970 eV. The feature near 4970 eV shows up as a strong peak in the spectrum of PbTiO₃ at room temperature for a field along the tetragonal axis (Fig. 1).[2] This peak is due to the Ti off-centering relative to the surrounding oxygen octahedra in the tetragonal phase and is quantitatively reproduced by calculations within a Bethe-Salpeter equation framework. However, the peak is still present in the PbTiO₃ cubic phase above the transition temperature of about 760 K; Bethe-Salpeter equation predictions based on the average cubic perovskite structure underestimate the peak. Thermal fluctuations must be taken into account.[3]

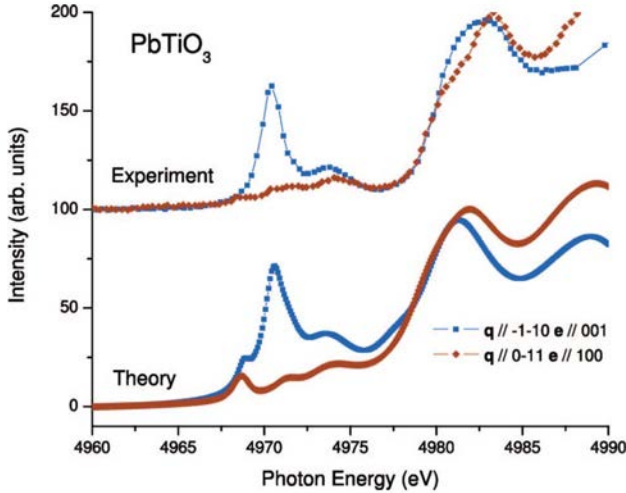


FIG. 1: Experimental PbTiO₃ 1s near-edge spectra compared with Bethe-Salpeter calculations (from Ref. 2).

One way to model thermal fluctuations in perovskites

is through ab initio molecular dynamics (AIMD).[4] We used AIMD to study SrTiO₃ and PbTiO₃. It was found that the generalized gradient approximation PBEsol[5] with a Hubbard correction of $U = 2.3$ eV for oxygen p-states and an artificial pressure of -21 kbar (-2.1 GPa) reproduced the low-temperature structures of BaTiO₃, CaTiO₃, and SrTiO₃ extremely well. PbTiO₃ under these parameters relaxes to a cell with $c/a \approx 1.2$, much larger than experiment, a well known problem with the GGA (intriguingly, it has been suggested that the inclusion of van der Waals forces, neglected here, may strongly affect the calculated c/a ratio[6]). While an unconstrained relaxation of PbTiO₃ is not successful, a fixed-unit-cell AIMD run on PbTiO₃ at room temperature yields an average structure almost identical to experiment. We therefore run all simulations here at the experimental cell parameters. AIMD was performed for 80-atom bcc-type supercells of PbTiO₃ at 300 K, 600 K, and 900 K, and SrTiO₃ at 293 K. The time step was 1.25 fs. Langevin dynamics were used, with a frequency of 2 THz. Each final run of 2.5 ps was performed after a 2 ps initialization run. The time scale was not particularly long, because high-precision convergence in k-points and plane-wave cutoffs were kept for these runs.

The analysis of the MD results was performed using a coordinate transformation to local coordinates around each Ti atom. The local environment of a Ti atom in a perovskite Ti contains seven atoms: the Ti itself and an octahedron of six surrounding O. Under O_h symmetry, the 21 degrees of freedom transform into irreducible representations as follows: $A_{1g} + E_g + T_{1g} + T_{2g} + 3T_{1u} + T_{2u}$. The coordinates were normalized to have magnitude unity in terms of the primitive lattice parameter. Note that the basis set is not complete nor orthogonal for the structure as a whole, but is well-adapted to describe how the local environment affects Ti 1s near-edge spectroscopy. Two important local coordinate displacement patterns are shown in Fig. 2. An example of how the local $1T_{1u}(z)$ coordinate for one specific Ti ion varies over time for different temperatures is shown in Fig. 3.

Defining $\langle \rangle_t$ as an average over time and $\langle \rangle_i$ as an average over sites, we define the mean value of a local coordinate as

$$\bar{x}_\mu = \langle \langle x_{\mu i}(t) \rangle_i \rangle_t, \quad (1)$$

and the root mean square local coordinate as

$$\bar{x}_\mu(rms) = (\langle \langle x_{\mu i}^2(t) \rangle_i \rangle_t)^{1/2}. \quad (2)$$

*eric.cockayne@nist.gov

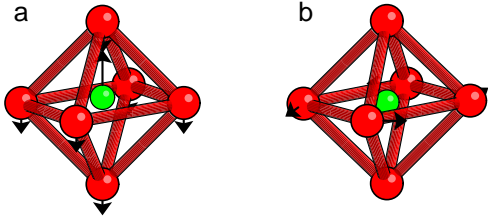


FIG. 2: Two of the local displacement patterns used to define local coordinates.

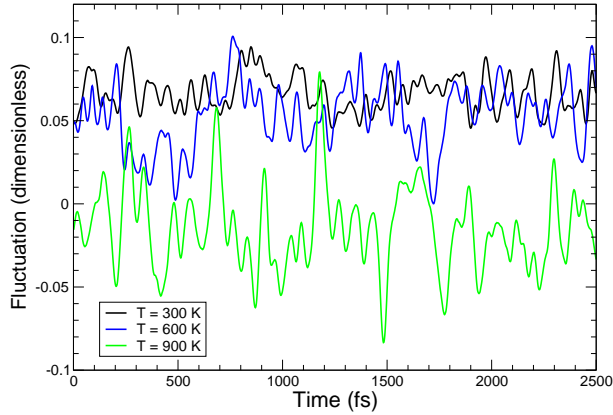


FIG. 3: $1T_{1u}(z)$ fluctuation of one Ti against its octahedral cage versus MD time, at different temperatures.

Results for the root mean square local coordinates are shown in Tables I-II.

The AIMD results were fed into the Bethe-Salpeter equation approach to calculate the near edge spectra. The results show excellent agreement with experiment. Only one type of mode met the criterion of having both a large rms variation from the ideal perovskite structure and a strong spectroscopic signature, namely the $1T_{1u}$ degrees of freedom involving Ti moving relative to the rigid oxygen cage. The intensity of the $PbTiO_3$ 4970 eV peak for electric field parallel to (perpendicular to) the tetragonal axis decreases (increases) as temperature increases, consistent with the changes in the rms fluctuation of $1T_{1u}$ fluctuations along z (x and y) axes (Ta-

TABLE I: Root mean square coordinates $\bar{\mu}(rms)$ for cubic $SrTiO_3$ at temperature 293 K, as computed by ab initio molecular dynamics. The term in parentheses shows one standard deviation uncertainty as calculated using five time subintervals.

| Mode μ | $\bar{\mu}(rms)$ | Mode μ | $\bar{\mu}(rms)$ |
|-----------------|------------------|------------------|------------------|
| A_{1g} | 0.0073(2) | $1T_{1u}(x;y;z)$ | 0.0149(4) |
| $E_g(xy;z)$ | 0.0118(2) | $2T_{1u}(x;y;z)$ | 0.0117(3) |
| $T_{1g}(x;y;z)$ | 0.0460(17) | $3T_{1u}(x;y;z)$ | 0.0226(6) |
| $T_{2g}(x;y;z)$ | 0.0144(4) | $T_{2u}(x;y;z)$ | 0.0225(3) |

TABLE II: Root mean square coordinates $\bar{\mu}(rms)$ for $PbTiO_3$ as a function of temperature, as computed by ab initio molecular dynamics. The term in parentheses shows one standard deviation uncertainty as calculated using five time subintervals.

| Mode μ | $\bar{\mu}(rms)$ | | |
|----------------|------------------|------------|------------|
| | 300 K | 600 K | 900 K |
| A_{1g} | 0.0094(2) | 0.0143(2) | 0.0165(4) |
| $E_g(xy)$ | 0.0143(5) | 0.0217(6) | 0.0275(6) |
| $E_g(z)$ | 0.0198(3) | 0.0255(6) | 0.0275(6) |
| $T_{1g}(x;y)$ | 0.0327(15) | 0.0470(16) | 0.0599(23) |
| $T_{1g}(z)$ | 0.0344(9) | 0.0482(26) | 0.0599(23) |
| $T_{2g}(x;y)$ | 0.0191(5) | 0.0255(7) | 0.0301(5) |
| $T_{2g}(z)$ | 0.0151(4) | 0.0225(7) | 0.0301(5) |
| $1T_{1u}(x;y)$ | 0.0153(1) | 0.0226(5) | 0.0310(3) |
| $1T_{1u}(z)$ | 0.0679(1) | 0.0554(6) | 0.0310(3) |
| $2T_{1u}(x;y)$ | 0.0145(1) | 0.0195(4) | 0.0250(4) |
| $2T_{1u}(z)$ | 0.0130(2) | 0.0196(5) | 0.0250(4) |
| $3T_{1u}(x;y)$ | 0.0246(5) | 0.0379(5) | 0.0454(6) |
| $3T_{1u}(z)$ | 0.0737(4) | 0.0620(11) | 0.0454(6) |
| $T_{2u}(x;y)$ | 0.0218(2) | 0.0329(7) | 0.0400(8) |
| $T_{2u}(z)$ | 0.0207(11) | 0.0313(11) | 0.0400(8) |

ble II). The calculated spectra for $SrTiO_3$ determined from $1T_{1u}$ fluctuations also agree with experiment. The T_{1g} octahedral rotation distortions may influence the spectra at lower temperatures where $SrTiO_3$ undergoes an antiferrodistortive phase transition.

- [1] J. J. Rehr and A. L. Ankudinov, *Coord. Chem. Rev.* **249**, 131 (2005).
- [2] J. C. Woicik, E. L. Shirley, C. S. Hellberg, K. E. Andersen, S. Sambasivan, D. A. Fischer, B. D. Chapman, E. A. Stern, P. Ryan, D. L. Ederer, et al., *Physical Review B* **75**, 140103 (2007), URL <http://dx.doi.org/10.1103/PhysRevB.75.140103>.
- [3] R. V. Vedrinskii, V. L. Kraizman, A. A. Novakovich, P. V. Demekhin, and S. V. Urazhdin, *Journal of Physics: Condensed Matter* **10**, 9561 (1998), URL <http://dx.doi.org/10.1088/0953-8984/10/42/021>.
- [4] M. C. Payne, M. P. Teter, D. C. Allan, T. A. Arias, and J. D. Joannopoulos, *Reviews of Modern Physics* **64**, 1045 (1992), URL <http://dx.doi.org/10.1103/RevModPhys.64.1045>.
- [5] J. P. Perdew, A. Ruzsinszky, J. Tao, V. N. Staroverov, G. E. Scuseria, and G. I. Csonka, *The Journal of Chemical Physics* **123**, 062201 (2005), URL <http://dx.doi.org/10.1063/1.1904565>.
- [6] K. Berland, C. A. Arter, V. R. Cooper, K. Lee, B. I. Lundqvist, E. Schröder, T. Thonhauser, and P. Hyldgaard, *The Journal of Chemical Physics* **140**, 18A539 (2014), URL <http://dx.doi.org/10.1063/1.4871731>.

Towards a current-density implementation for calculating flexoelectric coefficients

Cyrus E. Dreyer* and David Vanderbilt

Department of Physics and Astronomy, Rutgers University, Piscataway, NJ 08845-0849

Massimiliano Stengel

*ICREA-Institució Catalana de Recerca i Estudis Avançats, 08010 Barcelona, Spain,
and Institut de Ciència de Materials de Barcelona (ICMAB-CSIC), Campus UAB, 08193 Bellaterra, Spain*

The flexoelectric effect is the generation of a polarization with the application of a strain gradient, which can be applied by processes such as bending of cantilevers or compression of pyramid-shaped columns. Unlike piezoelectricity, which is only exhibited in certain low-symmetry space groups, flexoelectricity is universal to all insulators, regardless of symmetry or ionicity. Therefore novel devices may be fabricated from well-developed materials which do not contain toxic elements like lead. Also, as devices shrink to the nanoscale, large strain gradients can be present at interfaces, surfaces, or grain/domain boundaries, and the flexoelectric effect will be an important contribution to the properties of such devices.

The bulk flexoelectric tensor elements are given by

$$\mu_{\alpha\beta,\gamma\lambda} = \frac{\partial P_\alpha}{\partial \varepsilon_{\beta,\gamma\lambda}} \quad (1)$$

where P is the induced polarization in the cartesian direction α and $\varepsilon_{\beta,\gamma\lambda}$ corresponds to the gradient of the strain $\varepsilon_{\gamma\lambda}$ in the β direction. Recently, first-principles methodologies were developed to calculate elements of $\mu_{\alpha\beta,\gamma\lambda}$ [1, 2]. The implementations of these methodologies [1, 3] have involved the calculation of the charge-density response to a static perturbation, either the movement of single atoms in a supercell [1], or the collective atomic motion of a long-wavelength acoustic phonon [3]. However, in principle, the bulk charge-density response only contains information about the longitudinal components of the flexoelectric tensor. In order to obtain the transverse components from bulk calculations, it is necessary to calculate the microscopic induced polarization, defined as

$$P_\alpha(\mathbf{r}) = \frac{\partial J_\alpha(\mathbf{r}, t)}{\partial \dot{u}} \quad (2)$$

where J_α is the microscopic current induced in the α direction by the adiabatic motion of a sublattice of atoms at a small velocity, \dot{u} .

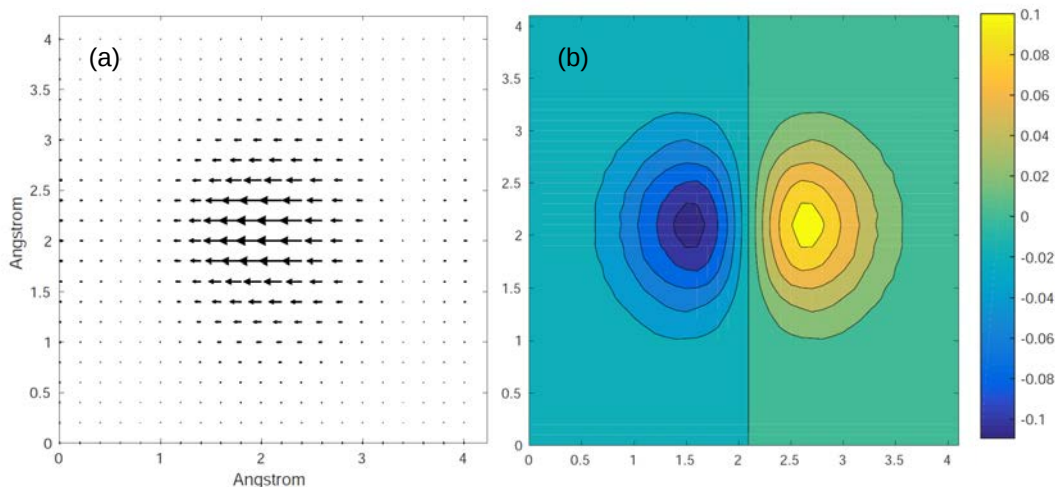


FIG. 1. (a) Polarization density of a He atom in a box induced by a zone center acoustic phonon in the x direction (2D slice through the center of the atom). (b) Divergence of the polarization density in (a), corresponding to the induced charge density.

* email: cedreyer@physics.rutgers.edu

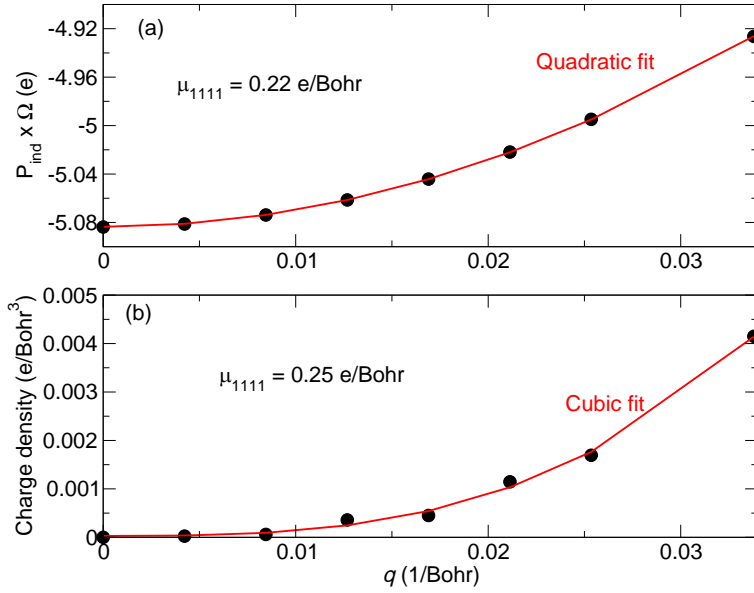


FIG. 2. For SrTiO₃, the induced (a) polarization and (b) charge density from a long wavelength acoustic phonon with wavevector q . A quadratic fit of the current and a cubic fit of the charge gives the clamped-ion longitudinal flexoelectric coefficient μ_{1111} .

Therefore, we are developing a density functional perturbation theory (DFPT) implementation to calculate the microscopic polarization induced by a long-wavelength phonon. DFPT has been demonstrated to be a powerful technique for calculating linear-response properties of materials from primitive-cell calculations, such as phonon dispersions and electron-phonon coupling. For our purposes, a modification to existing DFPT implementations is necessary since the calculation of the microscopic current requires that a time-dependent perturbation be considered. From adiabatic perturbation theory, we can determine the time dependent wavefunction to first order in the velocity of the atoms, $|\partial\psi_n/\partial\dot{u}\rangle$, by solving the Sternheimer equation

$$(E_n - H)|\frac{\partial\psi_n}{\partial\dot{u}}\rangle = -i\hbar|\frac{\partial\psi_n}{\partial u}\rangle \quad (3)$$

where E_n is the energy for state n , H is the DFT Hamiltonian, and $|\partial\psi_n/\partial u\rangle$ is the first order wavefunction induced by the static atomic displacement u , which can be obtained from a normal DFPT calculation. Once we have the first-order adiabatic wavefunction, we can obtain the induced polarization by taking a matrix element of the current density operator.

A simple example of this implementation is provided in Fig. 1, where we plot the polarization density induced by a zone center acoustic phonon (i.e., a rigid displacement) of a He atom in a box, as well as its divergence, which gives the induced charge density.

The flexoelectric coefficients are given by the second derivative of the induced polarization with respect to phonon wavevector q , evaluated at $q = 0$ [2]; we calculate this by finite differences on a mesh of q points around Γ . For example, in Fig. 2 we show a benchmark case for SrTiO₃, where we compute the longitudinal electronic (clamped-ion) flexoelectric coefficient, μ_{1111} , using our current-density implementation [Fig. 2(a)]. We can compare this directly to the charge-density implementation of Ref. 3, where μ_{1111} is determined from the third derivative of the induced charge with respect to q [Fig.2(b)].

Finally, we note that the definition of the current operator and the calculation of its expectation value requires special care in the presence of nonlocal pseudopotentials; this part of the implementation is still in progress.

[1] J. Hong and D. Vanderbilt, Phys. Rev. B **88**, 174107 (2013).

[2] M. Stengel, Phys. Rev. B **88**, 174106 (2013).

[3] M. Stengel, Phys. Rev. B **90**, 201112(R) (2014).

Soft-mode driven nonferroic phase transition in multiferroic BaMnO₃

Stanislav Kamba,¹ Dmitry Nuzhnyy,¹ Maxim Savinov,¹ Pierre Tolédano,² Valentin Laguta,¹ Petr Brázda,¹ Lukáš Palatinus,¹ Fedir Borodavka,¹ Filip Kadlec,¹ Christelle Kadlec,¹ Petr Bednyakov,¹ Viktor Bovtun,¹ Martin Kempa,¹ Jan Drahokoupil,¹ Dominik Kriegner,³ Jan Prokleška,³ Jirka Hlinka,¹ Kamal Chapagain,⁴ Bogdan Dabrowski,⁴ and Veronica Goian¹

¹*Institute of Physics, Czech Academy of Sciences, Prague, Czech Republic*

²*Laboratoire de Physique des Systèmes complexes, Université de Picardie, 80000 Amiens, France*

³*Faculty of Mathematics and Physics, Charles University, Prague, Czech Republic*

⁴*Department of Physics, Northern Illinois University, DeKalb, IL, USA*

Hexagonal BaMnO₃ features a structural phase transition at $T_C=130$ K, as indicated by electron and X-ray diffraction as well as by dielectric and lattice dynamic studies. The high-temperature phase has a polar $P6_3mc$ structure, and the low-temperature $P6_3cm$ phase is ferroelectric (FE) with a unit cell three times larger; thus, the nonequitranslational phase transition is nonferroic. It is driven by an optical soft mode from the Brillouin zone (BZ) boundary [$q = (\frac{1}{3}, \frac{1}{3}, 0)$], observable in the infrared (IR) and Raman spectra below T_C and hardening according to the Cochran law. Upon cooling, permittivity exhibits an unusual linear increase below T_C and a frequency-dependent decrease below 60 K. The FE hysteresis loops become pinched at 25 K and open again at lower temperatures. All these properties are discussed based on the Landau theory. Electron paramagnetic resonance (EPR) spectra and magnetic susceptibility measurements reveal an onset of a one-dimensional antiferromagnetic (AFM) order below ≈ 220 K, which develops fully near 140 K and then it transforms to a three-dimensional AFM order below $T_N \approx 59$ K.

Although ABO₃ compounds usually crystallize in the perovskite structure, BaMnO₃ in the perovskite form is unstable, and it crystallizes in the stabler hexagonal symmetry with face-sharing MnO₆ octahedra. In this paper we deal with the stoichiometric double-layered system which we denote as 2H-BaMnO₃, whose room-temperature crystal structure has raised a long-standing discussion. Some authors claimed that its space group is nonpolar $P6_3/mmc$ ($Z = 2$),¹⁻³ but other structural and vibrational studies proposed a polar $P6_3mc$ structure ($Z = 2$).^{4,5} Also the low-temperature crystal structure was uncertain for a long time. Cussen and Battle,² who had performed structure refinements at 80 K, came to the conclusion that the space group is $P6_3cm$ ($Z = 6$). Only very recently Stanislavchuk *et al.*⁵ confirmed this structure by neutron diffraction, and they found the structural phase transition at $T_C = 130$ K. The same authors investigated also the lattice dynamics of 2H-BaMnO₃ using Raman scattering and far-IR ellipsometry, but they observed no soft mode and a number of modes much lower than that predicted by the factor-group analysis. At low temperatures, 2H-BaMnO₃ exhibits an AFM order, but the Néel temperature T_N is also controversial; Christensen and Ollivier¹ claimed T_N below 2.4 K with spins oriented parallel to the c axis, while a newer work by Cussen and Battle² reported $T_N = 59$ K and the spin directions in the (001) plane.

Our electron and X-ray diffraction studies revealed tripling of hexagonal unit cell below $T_C=130$ K. The low-temperature phase was refined in the $P6_3cm$ space group, but the high-temperature structure can be refined in both nonpolar $P6_3/mmc$ and polar $P6_3mc$ space groups with almost identical R factors. Simultaneously, diffuse scattering appears above 130 K and persists at least up to 170 K, giving evidence about short-range (dynamic)

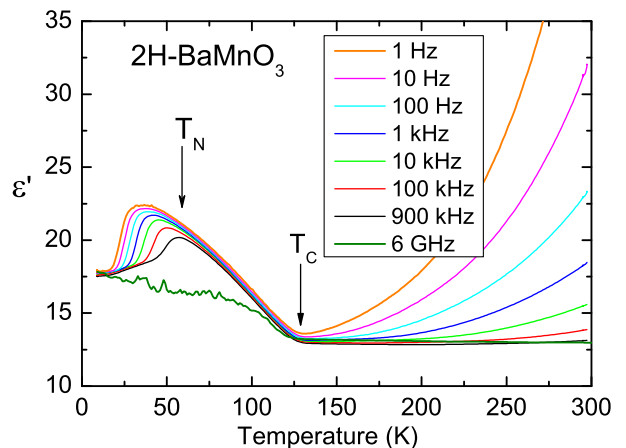


FIG. 1: Temperature dependence of dielectric permittivity measured at various frequencies. The high-temperature dispersion is caused by the Maxwell-Wagner relaxation, the low-temperature relaxor-like behavior comes from slowing-down of the FE domain wall vibrations.

nanoregions with a tripled unit cell, corresponding to a polar $P6_3cm$ structure.

The temperature dependence of the permittivity shows a rather unusual behavior: upon cooling, the high-frequency (0.9 MHz and 6 GHz) permittivity ϵ' is temperature-independent down to T_C , below which ϵ' increases—see Fig. 1. The absence of a peak in $\epsilon'(T)$ at T_C and the gradual increase in ϵ' below T_C remind of second order nonferroic phase transitions,⁷ which would supports the variant of a transition between two polar phases $P6_3mc$ ($Z = 2$) and $P6_3cm$ ($Z = 6$). A hypothetical phase transition from a nonpolar $P6_3/mmc$ ($Z = 2$) to a $P6_3cm$ ($Z = 6$) phase should be improper FE,³ in which case a jump or a small peak in ϵ' is expected at T_C .^{6,7} Below ≈ 60 K, ϵ' decreases, but this decrease is

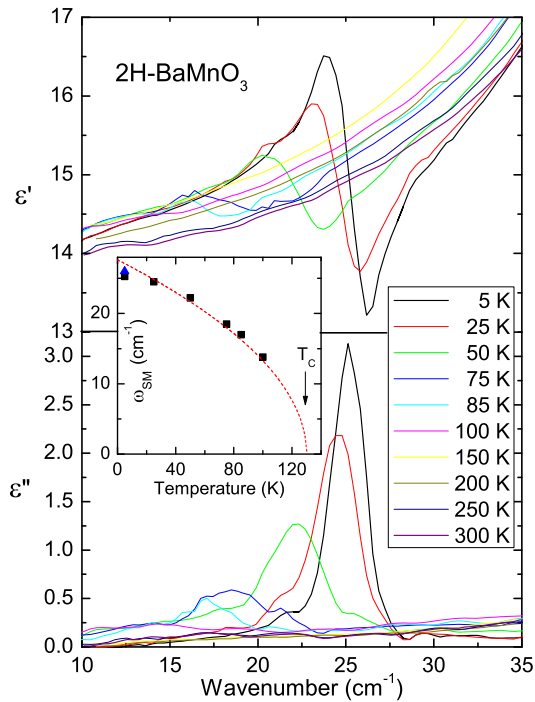


FIG. 2: THz complex dielectric spectra of 2H-BaMnO₃ ceramics, showing activation of a new phonon below $T_C = 130$ K. The temperature dependence of the soft-mode frequency is shown in the inset. The blue point at 5 K corresponds to the mode frequency determined from the Raman spectra.

strongly frequency dependent whereby it reminds of a relaxor FE behavior. In our case, however, the dielectric dispersion is caused by a slowing down of domain-wall vibration, because the relaxation frequencies obtained from the maxima of dielectric losses $\epsilon''(f, T)$ follow the Arrhenius law.

Polarization hysteresis-loop measurements revealed slim S-shaped loops below $T_C=130$ K, but the loops remained open up to 170 K. This can be explained either by relatively high dielectric losses or by persistence of polar nanoclusters with a tripled unit cell up to 170 K. Interestingly, the loops become pinched at $T^* = 26$ K in zero electric field and they open only for $E \neq 0$, which reminds antiferroelectrics. For explanation of this behavior we used the Landau theory.

The lattice dynamics were studied using IR and Raman spectroscopies. The spectra revealed fewer modes than the number predicted by the factor-group analysis. This

provides an evidence that the FE distortion is very small, the newly allowed modes are very weak and therefore they can be hardly seen in the IR and Raman spectra.

We measured the IR-active phonons also using the more sensitive time-domain THz transmission spectroscopy (see Fig. 2); the spectra revealed a weak mode which activates at 100 K near 13 cm^{-1} and it hardens on cooling, reaching the frequency of 26 cm^{-1} at 5 K. Its temperature dependence follows the Cochran law $\omega_{CM} = \sqrt{A(T_C - T)}$ with $T_C = 130$ K (see inset of Fig. 2). This is the soft mode triggering the structural phase transition with tripling of unit cell. Above T_C , this phonon has a wavevector from the BZ boundary with $q = (\frac{1}{3}, \frac{1}{3}, 0)$, so it cannot be observed in the IR or Raman spectra. Below T_C the BZ folds, the phonon wavevector transforms to the BZ center and therefore the soft mode activates in the THz spectra. We observed the same mode also in Raman spectra.

Based on the above-mentioned combination of observed dielectric anomalies, polarization measurements and lattice vibration studies, we can claim that the high-temperature phase is polar $P6_3mc$. Therefore, the nonequitranslational structural phase transition to the low-temperature $P6_3cm$ polar phase must be a nonferroic one. Similar nonferroic phase transitions between two polar phases are rather rare in literature and a similar underdamped soft mode was never reported.

Previous magnetic studies of 2H-BaMnO₃ provided ambiguous result with Néel temperatures ranging from 2 to 200 K.² For that reason we measured magnetic susceptibility $\chi(T)$ and EPR spectra, down to 5 K. The $\chi(T)$ curve measured at 0.05 T does not follow the Curie-Weiss law and reveals two minima near 60 and 220 K. The first value corresponds well to the T_N from Ref. 2; the second anomaly occurs due to an appearance of a short-range one-dimensional magnetic order. The EPR spectra support the same behaviour, because the EPR signal intensity drastically decreases below ≈ 220 K.

In conclusion, our complex structural, dielectric and lattice vibration studies of 2H-BaMnO₃ ceramics revealed an unusual nonferroic phase transition between two polar phases— $P6_3mc$ and $P6_3cm$ —which is driven by a soft mode from the BZ boundary. From magnetic and EPR studies, we identified an AFM phase transition with $T_N \approx 59$ K. Additionally, signatures of one-dimensional or short-range magnetic ordering are present at least up to 220 K.

¹ A. N. Christensen and G. Ollivier, J. Sol. State Chem. **4**, 131 (1972).

² E. Cussen and P. Battle, Chem. Mater. **12**, 831 (2000).

³ J. Varignon and P. Ghosez, Phys. Rev. B **87**, 140403 (2013).

⁴ C. Roy and R. Budhani, Phys. Rev. B **58**, 8174 (1998).

⁵ T. N. Stanislavchuk, A. P. Litvinchuk, R. Hu, Y. H. Jeon,

S. D. Ji, S.-W. Cheong, and A. A. Sirenko, Phys. Rev. B **92**, 134308 (2015).

⁶ A. Levanyuk and D. G. Sannikov, Soviet. Phys. Uspekhi **17**, 199 (1974).

⁷ V. Dvořák, Ferroelectrics **7**, 1 (1974).

“Striped” lanthanum cobaltite films: How strain orders oxygen defects

Axiel Yaël Birenbaum^{*†}

Michael D. Biegalski[†]

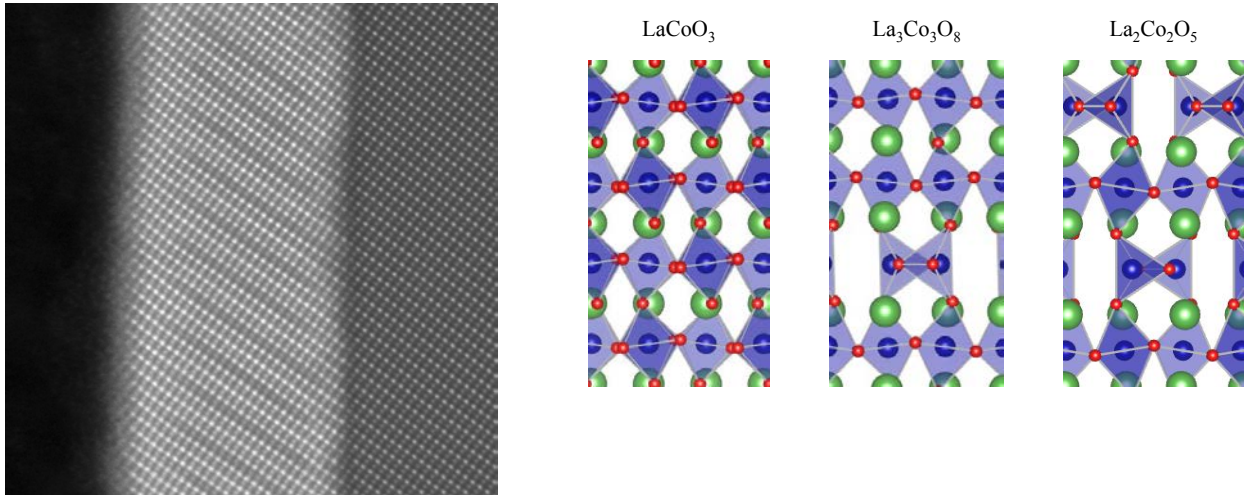
Liang Qiao[‡]

Valentino R. Cooper[†]

Albina Borisevich[†]

Oxygen-deficient metal cobalt oxides have been widely studied for solid oxide fuel cell cathode applications. In order to predict atomic-scale transport pathways, a thorough understanding of its defect properties is crucial. Previous Scanning Transmission Electron Microscopy (STEM) studies, demonstrated that lanthanum cobaltite, grown as thin films on $[100]_{pc}$ oriented perovskites, exhibit spontaneous ordering of oxygen vacancies [1,2]. In addition, the magnetic and spin states of cobalt oxides vary dramatically from one case to another case [3,4].

In this work, we investigate the behavior of $\text{LaCoO}_{3-\delta}$ thin films grown on SrTiO_3 [111]. For these films, STEM studies also reveal ordered vacancy arrangements (see Figure 1a). Here, we use first principles calculations to examine how substrate orientation can be used to shape the anisotropy of oxygen transport. In so doing, we seek to understand the coupling between the structural and electronic properties of $\text{LaCoO}_{3-\delta}$ on SrTiO_3 , induced by oxygen vacancy ordering.



(a) HAADF image of $\text{LaCoO}_{3-\delta}$ thin films (light layer) grown on SrTiO_3 [111] surface (dark layer) showing the distinctive stripe patterns.

(b) Structures of LaCoO_3 , $\text{La}_3\text{Co}_3\text{O}_8$, and $\text{La}_2\text{Co}_2\text{O}_5$. Bulk, 1/4 oxygen deficient, and 1/3 oxygen deficient respectively.

Figure 1: Images and structure of $\text{LaCoO}_{3-\delta}$.

Two oxygen deficient structures are proposed to fit the experimental observations, and hence are the focus of our poster: $\text{La}_3\text{Co}_3\text{O}_8$ with $P2_1$ symmetry, and Brownmillerite $\text{La}_2\text{Co}_2\text{O}_5$. Compared to the bulk LaCoO_3 perovskite, $\text{La}_3\text{Co}_3\text{O}_8$ exchanges one oxygen octahedra layer for a

*email: birenbaumyl@ornl.gov

[†]Oak Ridge National Laboratory, Oak Ridge, Tennessee 37831, United States

[‡]School of Materials, University of Manchester, Oxford Rd, Manchester M13 9PL, UK

tetrahedral layer, and $\text{La}_2\text{Co}_2\text{O}_5$ exchanges two (see Figure 1b). Firstly, we perform a layer-by-layer analysis of the differences between each compositions' structure. This establishes the basis for future study of the dynamics involved going from bulk to $\text{La}_3\text{Co}_3\text{O}_8$ and further to $\text{La}_2\text{Co}_2\text{O}_5$. Secondly, knowing that cobalites' electronic structure is known to be particularly sensitive to coordination and structural changes, such as strain or oxygen defects, we address which magnetic and spin states are present in these structures. This leads to an opportunity to discuss the effect of reduced symmetry in oxygen deficient compounds on cobalt oxide behavior compared to the ideal perovskite environment. Finally, we discuss how epitaxial strain leads to oxygen vacancies forming these distinctive stripe patterns.

Acknowledgements

Research was sponsored by the US Department of Energy (DOE), Ofce of Science, Basic Energy Sciences (BES), Materials Sciences and Engineering Division This research used resources of the National Energy Research Scientific Computing Center, which was supported by the Ofce of Science of the US Department of Energy under Contract No. DE-AC02-05CH11231

References

- [1] Liang Qiao, Jae Hyuck Jang, David J. Singh, Zheng Gai, Haiyan Xiao, Apurva Mehta, Rama K. Vasudevan, Alexander Tselev, Zhenxing Feng, Hua Zhou, Sean Li, Wilfrid Prellier, Xiaotao Zu, Zijiang Liu, Albina Borisevich, Arthur P. Baddorf, and Michael D. Biegalski, *Nano Letters* **15**, 7, pp 46774684 (2015)
- [2] Biškup, Neven and Salafranca, Juan and Mehta, Virat and Oxley, Mark P. and Suzuki, Yuri and Pennycook, Stephen J. and Pantelides, Sokrates T. and Varela, Maria, *Physical Review Letters* **112**, 8 (2014)
- [3] Bernard Raveau, and Md. Motin Seikh, *Handbook of Magnetic Materials* **23**, Pages 161289 (2015)
- [4] Yuichi Yamasaki, Jun Fujioka, Hironori Nakao, Jun Okamoto, Takaaki Sudayama, Youichi Murakami, Masao Nakamura, Masashi Kawasaki, Takahisa Arima, and Yoshinori Tokura, *Journal of the Physical Society of Japan* **85**, 023704 (2016)

Electronic origin of spin-phonon coupling effect in transition-metal perovskites

Hongwei Wang^{1, 2}, Lixin He¹, Hong Jiang³, Cameron C. Steele², and Xifan Wu²

1. Key Laboratory of Quantum Information, University of Science and Technology of China, Hefei, Anhui 230026, China
2. Department of Physics, Temple University, 1925 N 12th Street, Philadelphia, Pennsylvania 19122, USA
3. Beijing National Laboratory for Molecular Sciences, College of Chemistry and Molecular Engineering, Peking University, 100871 Beijing, China

Spin-phonon coupling effect in transition metal perovskites has been identified by the fact that the low-lying phonon modes, as well as the polar ones, are significantly softened when the spin coupling is changed from being antiferromagnetic to ferromagnetic. We study the electronic origins of spin-phonon coupling effect by using SrMnO₃ and BiFeO₃ as examples. In particular, we compute the superexchange interactions via the virtual electronic hopping processes by a recently developed extended Kugel-Khomskii model based on maximally localized Wannier functions, in which the electronic screening is considered by constrained random phase approximation. The spin-phonon coupling effect can be understood as the tendency towards the suppressed superexchange interaction under the structural distortion along the phonon mode. However, the electronic structure plays a crucial role in the above. On one hand, phonon modes that effectively change the hybridization between Mn-3*d* and O-2*p* are found to have strong spin-phonon coupling effect. On the other hand, the rather different details in the virtual hopping processes originating from the distinct electronic configurations in Mn⁴⁺ and Fe³⁺ ions explain the much weaker spin-phonon coupling effect in BiFeO₃ than that of SrMnO₃. Our results bridge the gap between the Goodenough-Kanamori-Anderson phenomenological rule based on metal-oxygen-metal angle only and the electronic structure calculation of materials. Furthermore, it also provides useful guidance to the search for new spin-phonon coupling materials.

Ferroelectric Properties of Off-Stoichiometrically Grown Barium Titanate via Molecular Beam Epitaxy

T. Al. Morgan^{1*}, M. Zamani Alavijeh^{1,2}, G. Story¹, W. Schroeder¹, A. Kuchuk¹, M. Benamara¹ and G. Salamo^{1,2}

1 University of Arkansas, Institute for Nanoscience and Technology (731 W Dickson St., Fayetteville, AR, 72701 USA); **2** University of Arkansas, Physics (Fayetteville, AR, USA)

Even though barium titanate is one of the most investigated ferroelectrics¹ it is still a challenging thin film material to grow using molecular beam epitaxy (MBE)^{2,3}. This is largely because there does not exist a self-limiting growth² approach or corresponding understanding to lock-in stoichiometric growth. The investigation of off-stoichiometric growth of strontium titanate has discovered conditions where SrO layers rearrange^{4,5} and where they do not⁶. However, very few reports⁷⁻¹⁰ on the off-stoichiometric growth of BTO exist. We report on off-stoichiometric growth of barium titanate to understand the limits of BaO mobility within BTO as a potential route to achieve stoichiometric BaTiO₃ thin films.

We have investigated off-stoichiometric growth of BaTiO₃ thin films on STO:Nb (0.5%) using (1) a shuttered-RHEED and (2) co-deposition technique. To understand BaO ability to rearrange, we started with barium rich condition for growth. Shuttered RHEED technique was used to determine the growth temperatures of barium and titanium so that the shutter times would be equal but in a barium rich condition; the equal shutter times made it possible to have equivalent growth times to compare the codeposited samples. The stoichiometry of the films were determined immediately after growth using x-ray photoelectron spectroscopy (XPS) and shown to have excess barium. The samples were then soaked in methanol to remove any excess BaO on the surface⁸ and the Ti/Ba was found to be unity for both samples. The XPS results indicate, rather surprisingly, that excess barium does not incorporate into BaTiO₃ lattice and instead the excess barium accumulates as a BaO layer on the surface. We have discovered that growing in a barium rich regime provides a way to achieve stoichiometric BTO.

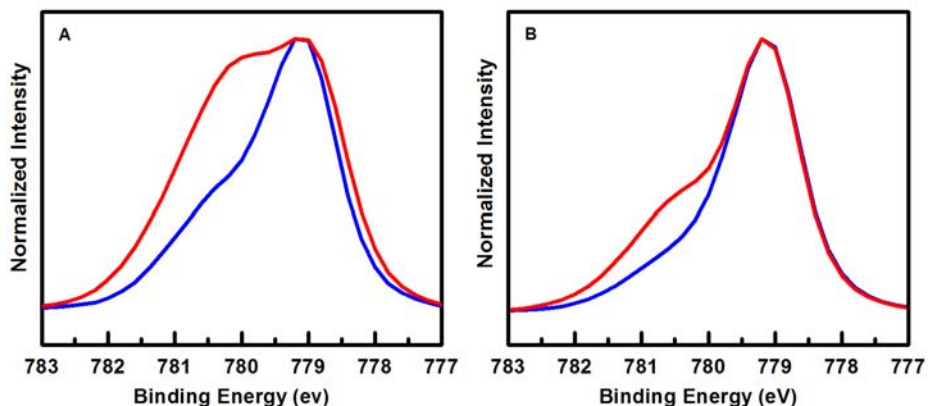


Figure 1 Comparison of XPS Ba Peak change after methanol cleaning of Codeposition (A) and Shuttered RHEED (B) growth technique

*tamorga@uark.edu

To prove this point, we have investigated the ferroelectric properties as a function of growth approach. We have found that excess titanium does incorporate into the lattice when growing in a titanium rich condition. The initial PFM results indicate that excess titanium does not lead to a decrease in piezoelectric coefficient (d_{33}) as seen in Figure 2. More surprisingly, initial PFM measurements show codeposited sample produces a BTO thin film with double the value (6.27 pm/V) as the shuttered RHEED sample. These results suggest that barium rich codeposited barium titanate could be the growth for optimal ferroelectric properties.

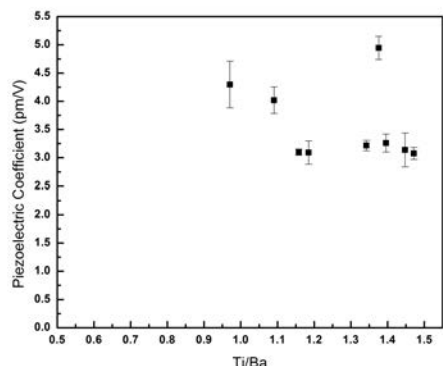


Figure 2 Piezoelectric coefficient (d_{33}) as a function of Ti/Ba and out of plane lattice parameter

1. Forrester, W. F. & Hinde, R. M. Crystal Structure of Barium Titanate. *Nature* **155**, 484–485 (1945).
2. Henini, M. Molecular Beam Epitaxy. 744 (2012). Available at: http://books.google.com/books?id=OPZ5YGXpdC0C&printsec=frontcover&dq=intitle:molecular+beam+epitaxy+from+research+to+mass+production&hl=&cd=1&source=gbs_api.
3. Farrow, R. Molecular Beam Epitaxy. (1995). Available at: https://books.google.com/books/about/Molecular_Beam_Epitaxy.html?id=wToPhW5TZosC.
4. Lee, J. H. *et al.* Dynamic layer rearrangement during growth of layered oxide films by molecular beam epitaxy. *Nature Materials* **13**, 879–883 (2014).
5. Nie, Y. F., Zhu, Y., Lee, C. H. & Kourkoutis, L. F. Atomically precise interfaces from non-stoichiometric deposition. *Nature* **5**, (2014).
6. Brooks, C. M. *et al.* Growth of homoepitaxial SrTiO₃ thin films by molecular-beam epitaxy. *Applied Physics Letters* **94**, 162905 (2009).
7. Suzuki, T., Nishi, Y. & Fujimoto, M. Ruddlesden–Popper Planar Faults and Nanotwins in Heteroepitaxial Nonstoichiometric Barium Titanate Thin Films. *Journal of the American Ceramic Society* **83**, 3185–3195 (2000).
8. Barbier, A. *et al.* Surface composition of BaTiO₃/SrTiO₃ (001) films grown by atomic oxygen plasma assisted molecular beam epitaxy. *Journal Of Applied Physics* **112**, 114116 (2012).
9. Mazet, L. *et al.* Structural study and ferroelectricity of epitaxial BaTiO₃ films on silicon grown by molecular beam epitaxy. *Journal Of Applied Physics* **116**, 214102 (2014).
10. Suzuki, T. & Fujimoto, M. First-principles structural stability study of nonstoichiometry-related planar defects in SrTiO₃ and BaTiO₃. *Journal Of Applied Physics* **89**, 5622–5629 (2001).

*tamorga@uark.edu

An alternative structure of TiO_2 with higher energy valence band edge

Sinisa Coh

sinisa.coh@ucr.edu

UC Riverside, Riverside CA USA

In collaboration with: Peter Y. Yu, Yuta Aoki, Susumu Saito, Steven G. Louie, and Marvin L. Cohen

We propose an alternative structure of TiO_2 anatase that has a higher energy oxygen p -like valence band maximum than the pristine TiO_2 anatase and thus has a much better alignment with the water splitting levels. This alternative structure is unique when considering a large subspace of possible structural distortions of TiO_2 anatase. We propose two ways to access this state experimentally and argue that one of them might have been realized in the recently discovered so-called black TiO_2 .¹

Finding a suitable photocatalytic material that enables sunlight to split water into hydrogen and oxygen has the potential to impact one of the major societal challenges today—clean production of energy. Titanium dioxide (TiO_2) is nearly an ideal photocatalyst for this purpose because it is inexpensive and chemically stable. Unfortunately the electronic band gap of TiO_2 is so large (>3 eV) that it absorbs only $\sim 5\%$ of the solar spectrum. Therefore a large effort has been made to band-engineer TiO_2 so that it can harvest a larger portion of the solar spectrum. As is well established, the valence band of TiO_2 is lower than the water-splitting level by ~ 2 eV, while the conduction band is well aligned with the water-splitting level. Therefore, it seems that the simplest strategy to reduce the band gap of TiO_2 — without affecting its photocatalytic properties — is to move its valence band to a higher energy and leave its conduction band energy intact.

Recently a new form of disordered TiO_2 , so-called black TiO_2 , was fabricated by hydrogenating pure, dopant-free, anatase- TiO_2 nanosized crystals under pressure. Hydrogenation reduced the band gap of anatase TiO_2 from 3.3 eV to 1.5 eV which is a much better match to the solar spectrum. Most importantly, there are experimental indications that this gap reduction was formed by a movement of the valence band while the conduction band was mostly unaffected by the hydrogenation process. Therefore, black TiO_2 has a great potential to be used as an effective photocatalyst, as already demonstrated by Chen et al.²

Detailed high-resolution TEM analysis of black TiO_2 revealed that the centers of the nanocrystals remain in the anatase TiO_2 structure, while only the surfaces of the crystals are modified. However the

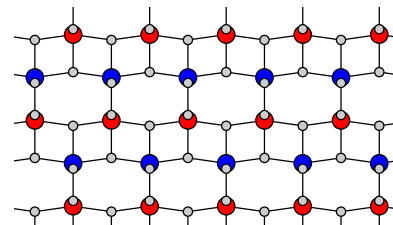


Figure 1: Crystal structure of pristine bulk TiO_2 anatase.

¹ More details on this work can be found in the following preprint arxiv.org/abs/1607.08624

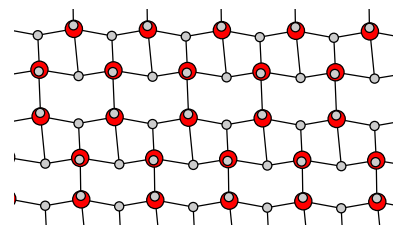


Figure 2: Modified structure of TiO_2 anatase with optimal band alignment. This structure is unstable but derived structures shown in Fig. 3 and 4 are stable.

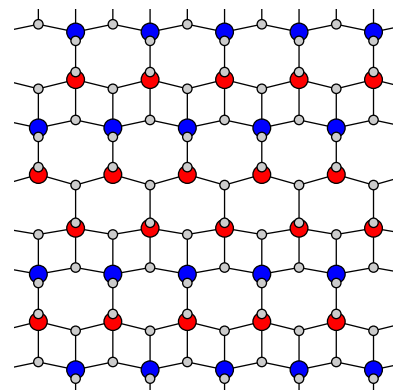


Figure 3: One of the stable structures of TiO_2 with the optimal band alignment for water splitting.

² X. Chen, L. Liu, P. Y. Yu, and S. S. Mao, *Science* 331, 746 (2011).

surface is not completely disordered since after hydrogenation the Raman spectrum shows relatively sharp additional peaks in black TiO₂, even though the overall Raman spectrum is broader. Additional Raman peaks were also found in subsequent studies³ and they could not be associated with any other known polymorph of TiO₂.

The presence of relatively sharp Raman peaks suggests that the hydrogenation might have induced a coherent structural distortion that is periodically repeating on the nanocrystal surface, rather than producing random disorder. Even though extensive electronic and structural measurements have been done on black TiO₂, it remains unknown which structural change — induced by hydrogenation under pressure — might be responsible for the valence band energy shift.

This is the question we address here from a theoretical point of view: *can structural deformation alone move oxygen-p states of TiO₂ to a higher energy and if the answer is yes how could such a deformation be stabilized?*

To answer these questions we introduce an approach that searches over a high-dimensional space of possible coherent structural distortions of TiO₂ anatase and selects coherent structural distortions with a desired electronic band structure. To our surprise, we found a single coherent structural distortion — within a certain subspace — that moves the valence band of TiO₂ to a higher energy without affecting the conduction band minimum (compare Fig. 1 and Fig. 2). We also propose two ways to access this state experimentally (see Figs. 3 and 4) and argue that one of them might have been realized in the recently discovered so-called black TiO₂.

Method

Within the density functional theory framework one conventionally determines the ground-state crystal structure by minimizing the total energy E_{tot} over some structural parameters ζ_i . In this work we will instead start from the fully relaxed TiO₂ anatase structure and then minimize the following function,

$$F(\zeta_i) = E_{\text{tot}}(\zeta_i) + \lambda [-\epsilon_v(\zeta_i) + |\epsilon_c(\zeta_i) - \epsilon_c(0)|]. \quad (1)$$

Here vector ζ_i describes distortions away from the ideal anatase phase and the Kohn-Sham eigenvalues (ϵ_c and ϵ_v) are in principle measured with respect to the vacuum level. With $\lambda > 0$, the second term rewards distortions that move the valence band maximum ϵ_v to higher energies and penalizes those that move the conduction band minimum ϵ_c relative to that of the ideal anatase, $\epsilon_c(0)$.

³ X. Jiang, et al. J.Phys.Chem.C 116, 22619 (2012). Z. Zheng, et al. Chemical Communications 48, 5733 (2012).

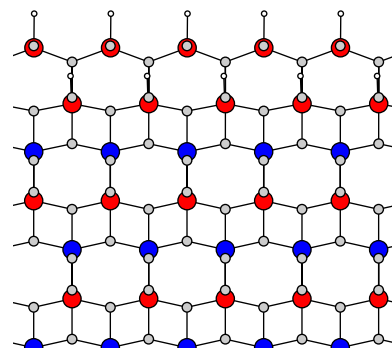


Figure 4: Another stable structure of TiO₂ with the optimal band alignment for water splitting. (Hydrogen atoms used for surface termination are shown as small white circles.)

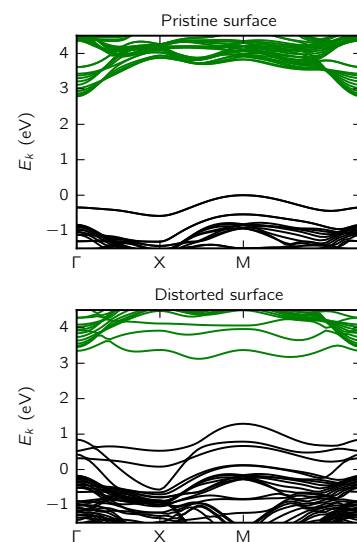


Figure 5: Comparison of the surface band structure without (top) and with (bottom) optimal structural distortion. Vacuum levels in two panels are aligned with each other.

First Principles studies in Oxynitrides at High Pressure

H. Takenaka¹ and R. E. Cohen^{1,2}

¹ *Extreme Materials Initiative, Carnegie Institution for Science, Washington D.C. 20015, USA*

² *Department für Geo-und Umweltwissenschaften, Ludwig-Maximilians-Universitaet, Munich, Germany*

(Dated: December 16, 2016)

Substitution for Pb-based piezoelectric materials is highly desired due to lead toxicity. Lead-free piezoelectric compounds [1–5] have been synthesized over the past decades. The piezoelectrics are composed of complex solid solutions and exhibit their excellent piezoelectric performance mostly near or at their morphotropic phase boundaries, or in textured compounds. Caracas and Cohen theoretically predicted that the tetragonal perovskite structures of YSiO₂N and YGeO₂N exhibit the high spontaneous polarizations and the nonlinear optic coefficients, and are new class of Pb-free piezoelectric materials using the first-principles methods. [6] Single phase of the predicted polar oxynitride perovskites have not been synthesized while oxynitride perovskites have been studied for high dielectrics, visible-light photocatalysts for water splitting, and non-toxic pigments, and colossal magnetoresistance.

Li *et al.* [7], however, proposed tolerance and octahedral factors to search for new possible oxynitrides and concluded YSiO₂N and YGeO₂N cannot form perovskite-type structures in contrast to the first principles methods. Recently, Ahart *et al.* synthesize YSiO₂N at high pressure and temperature. [8] The experimental X-ray diffraction peaks have good agreements with the calculated tetragonal perovskite and hexagonal (P_{6122}) structures [9] and also exhibit unknown structures.

Since pressure-induced structural phases for YSiO₂N and YGeO₂N are not available, we investigate energetically favorable structure performing fully relaxation at given pressures by the density functional theory (DFT) using the pwscf package [10]. We employ GBRV ultra-soft LDA pseudo potentials [11] with a plane-wave and charge density cutoff energy of 40 and 200 Ry, respectively. We use FINDSYM [12] to determine the space groups of our relaxed structures.

Because we obtain 9 and 10 structures for YSiO₂N and YGeO₂N, respectively, we describe denotation of our results of fully relaxed structures. The structures are conventionally distinguished by space groups and the number of atoms in each unit cell is mentioned in parenthesis. For structures in which structural transformation takes place under pressure in a same space group, we assign a number using Roman numerals. We express a perovskite system in which N atoms occupy apical and equatorial sites as NN and NO, respectively, for convenience.

In FIG. 1, we show the relative enthalpies, ΔH and equation of states as a function of pressure for our structures obtained by the DFT. The relative enthalpies, ΔH , are relative to $P_{4/mmm}$ (5) NN. Phase stabilities for YSiO₂N are shown in FIG. 1 a. In YSiO₂N at the ambient pressure, P_{6122} (90) reported by Ouyang *et al.* [9] is most stable. Second stable phase is C_c (10):I forms zig-zag chain structure of nitrogen corner-sharing trigonal pyramid. Third stable phase, most stable perovskite-type structure, is SrTiO₃-type I_{4mcm} (10) NN. C_2 (10) NO is non-polar perovskite and in forth stable phase. The earlier predicted polar YSiO₂N, P_{4mm} (5) NN, is found in fifth stable phase. $P_{4/mmm}$ (5) NN with inversion symmetry and hexagonal P_{63mmc} (10) with face-sharing trigonal pyramids are assigned as sixth since the energy difference is quite small. $P_{\bar{1}}$ (10) contains N-N and O-O edge-sharing octahedra is seventh phase and extremely unstable. At high pressure, the non-perovskites and P_{4mm} (5) NN exhibit instability compared with the other perovskites. The non-perovskite C_c (10):I is transformed to new perovskite-type C_c (10):II NO (non-polar) at 4 GPa. Figure 1 a exhibits coexistence of the P_{4mm} (5) NN and P_{6122} (90) at 18 GPa. Structural transformation from P_{4mm} (5) NN to the $P_{4/mmm}$ (5) NN takes place and the polar tetragonal phase disappears above 18 GPa. Unlike YSiO₂N, YGeO₂N possibly forms P_{6122} (90) and P_{63mmc} (10) at the ambient pressure in Figure 1 b. Most stable perovskite-type structure at the ambient pressure is $C_{2/c}$ (10) NN. The hexagonal P_{6122} (90) exhibits less stable than P_{63mmc} (10) and structural transformation to P_{6122} (30) above 8 GPa. Though Ge atoms enhance phase stability of the P_{4mm} (5) NN up to 20 GPa and the polar phase is favorable compared with $P_{4/mmm}$ (5) NN, the non-polar I_{4mcm} (10) NN is most stable phase above 14 GPa.

Our results indicate no formation of the P_{4mm} (5) NN phase at any pressures. However, YSiO₂N and YGeO₂N can form the single phase of the non-polar I_{4mcm} (10) NN and $C_{2/c}$ (10) NN, respectively. In these phases, O/N ordering is the exactly same as the predicted polar P_{4mm} (5) NN. Since Figure 1 c and d show smooth curvatures of equation of state in the favorable non-polar phases, these structures at high pressure can be quenched into the ambient pressure. The desired piezoelectric Pb(Zr,Ti)O₃ is synthesized at high temperature due to the phase transformation from pyrochlore (paraelectric) to perovskite (ferroelectric) phase. The most stable oxynitride quenched into the ambient pressure can be transformed to the polar P_{4mm} (5) NN by heating up.

In summary, we have examined the pressure-induced phases in YSiO₂N and YGeO₂N. We have shown no straightforward synthesis of the single phase of the polar oxynitrides. Our first-principles studies suggest possibility to achieve the synthesis of the single phase polar oxynitrides.

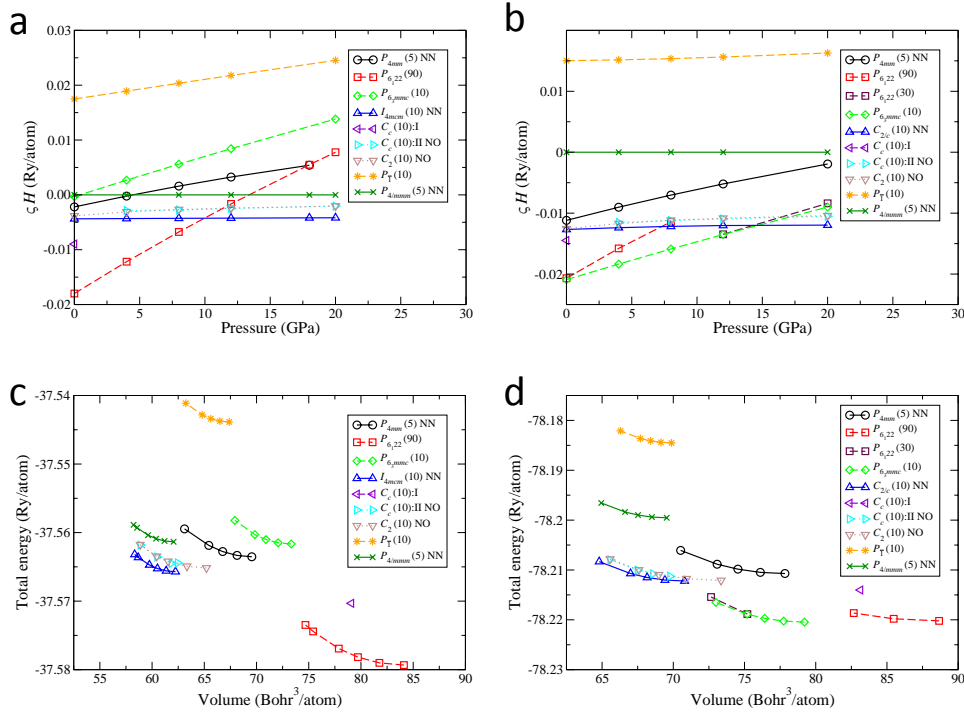


FIG. 1: The relative enthalpies and the equation of states for our calculated structures vs. pressure. The relative enthalpies (a) and (b), and the equation of states (c) and (d) for YSiO_2N and YGeO_2N , respectively. Solid, dotted, dashed lines are NN perovskite, NO perovskite, and non-perovskite structures, respectively.

Acknowledgments

This work was supported by the ONR. We acknowledge support from the Carnegie Institution and the European Research Council Advanced grant ToMCA^T. Computational support was provided by a Challenge Grant from the HPCMO of the U.S. Department of Defense.

-
- [1] T. Takenaka, K.-i. Maruyama, and K. Sakata, *Japanese Journal of Applied Physics* **30**, 2236 (1991).
 - [2] M. D. Maeder, D. Damjanovic, and N. Setter, *Journal of Electroceramics* **13**, 385392 (2004).
 - [3] G.-Z. Zang, J.-F. Wang, H.-C. Chen, W.-B. Su, C.-M. Wang, P. Qi, B.-Q. Ming, J. Du, L.-M. Zheng, S. Zhang, et al., *Applied Physics Letters* **88**, 212908 (2006).
 - [4] T. R. Shrout and S. J. Zhang, *Journal of Electroceramics* **19**, 113126 (2007).
 - [5] W. Liu and X. Ren, *Physical Review Letters* **103** (2009).
 - [6] R. Caracas and R. E. Cohen, *Applied Physics Letters* **91**, 092902 (2007).
 - [7] W. Li, E. Ionescu, R. Riedel, and A. Gurlo, *Journal of Materials Chemistry A* **1**, 12239 (2013).
 - [8] M. Ahart, M. Somayazulu, R. Vadapoo, N. Holtgrewe, Y. Meng, Z. Konopkova, R. J. Hemley, and R. E. Cohen, *Synthesis of polar ordered oxynitride perovskite* (2016), arXiv:1604.03989.
 - [9] L. Ouyang, H. Yao, S. Richey, Y.-N. Xu, and W. Y. Ching, *Physical Review B* **69** (2004).
 - [10] P. Giannozzi, S. Baroni, N. Bonini, M. Calandra, R. Car, C. Cavazzoni, D. Ceresoli, G. L. Chiarotti, M. Cococcioni, I. Dabo, et al., *Journal of Physics: Condensed Matter* **21**, 395502 (19pp) (2009), URL <http://www.quantum-espresso.org>.
 - [11] <https://www.physics.rutgers.edu/gbrv/>.
 - [12] <http://stokes.byu.edu/iso/findsym.php>.

ONR's Research Program on Acoustic Transduction Materials and Devices

Harold C. Robinson, Wallace A. Smith and Carl C.M. Wu
Office of Naval Research
Materials Division, ONR 332
875 North Randolph Street
Arlington, Virginia 22203-1995

Research on innovative materials and device structures is sought that enhances the performance of electro-mechanical transducers used by the Department of Navy to generate, detect and suppress undersea sound waves. The present Office of Naval Research program has two thrusts. The first aims to devise and validate first-principles quantum-mechanical methods to evaluate the properties of materials with structural phase transitions; this will enable the exploration of the properties of new materials in advance of their synthesis. The second focuses on the new high coupling, high-strain relaxor piezoelectric single crystals. Efforts underway aim to produce and characterize these piezocrystals and to design, fabricate and test innovative transducers from them for Navy SONAR systems.

Electric Field Effect on Lead Free Uniaxial Relaxor $\text{Sr}_{0.4}\text{Ba}_{0.6}\text{Nb}_2\text{O}_6$ single crystal Studied by Brillouin Scattering

Md Aftabuzzaman¹, Md Al Helal¹, Jan Dec², Wolfgang Kleemann³, and Seiji Kojima¹

¹Graduate School of Pure and Applied Sciences, University of Tsukuba, Tsukuba, Ibaraki 305-8573, Japan

²Institute of Materials Science, University of Silesia, PL-40-007 Katowice, Poland

³Angewandte Physik, Universität Duisburg-Essen, D-47048 Duisburg, Germany

Email of corresponding author: azamanphy@gmail.com

Uniaxial relaxor ferroelectrics (REFs) with tetragonal tungsten bronze (TTB) structure such as $\text{Sr}_x\text{Ba}_{1-x}\text{Nb}_2\text{O}_6$ (SBN) are technologically important materials owing to their remarkably high dielectric, piezoelectric, pyroelectric, and photorefractive properties [1-3]. These excellent physical properties make them potential candidates for modern applications such as sensors, data storage, lasers, and holography. The unique combination of physical properties and lead free nature make SBN single crystals crucial materials for research. The structural formula of TTB is represented by $(\text{A}1)_2(\text{A}2)_4(\text{C})_4(\text{B}1)_2(\text{B}2)_8\text{O}_{30}$ with corner sharing distorted BO_6 octahedra. In SBN, the A1 sites are occupied only by Sr ions and the A2 sites are occupied by both Ba and Sr ions, while the C sites and one-sixth of all the A sites (A1+A2 sites) are unoccupied and are thus the main source of quenched random fields (RFs). By increasing the Sr content, the Curie temperature, T_C decreases. Consequently the diffusive nature increases due to the increase of the strength of the RFs, which are believed to play a dominant role in the relaxor nature [4]. Generally in REFs, the precursor phenomena of the ferroelectric phase transition are caused by the dominant role of polar nanoregions (PNRs). Recently, the electric field dependences of REFs with TTB structure have been studied and the alignment of static PNRs were observed in the ferroelectric phase [5]. In the present study, the effects of electric field and the temperature dependence of the elastic properties of SBN single crystals were investigated using broadband Brillouin scattering spectroscopy to clarify their critical nature and the related functionality and to get new insight into uniaxial REFs with TTB structure.

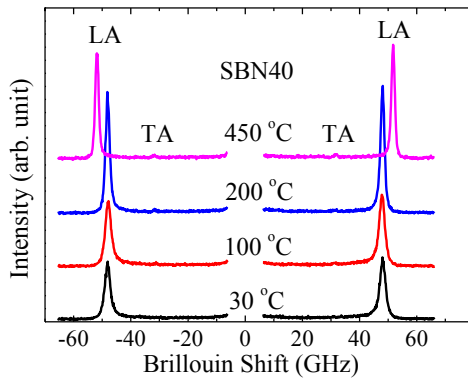


Fig. 1. Brillouin scattering spectra of SBN40 single crystal at selected temperatures under ZFH.

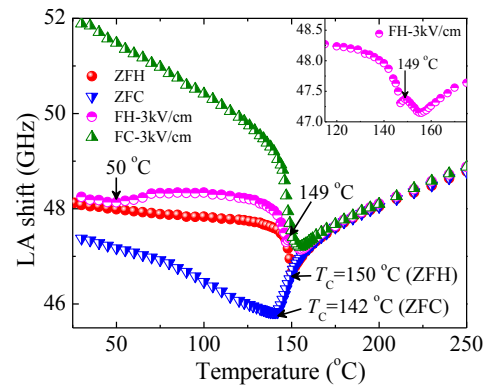


Fig. 2. Temperature dependences of LA shift under constant electric field.

Figure 1 shows Brillouin scattering spectra of a *c*-plate $\text{Sr}_x\text{Ba}_{1-x}\text{Nb}_2\text{O}_6$ ($x = 0.40$, SBN40) single crystal at some selected temperatures under zero field heating (ZFH). The elastic properties

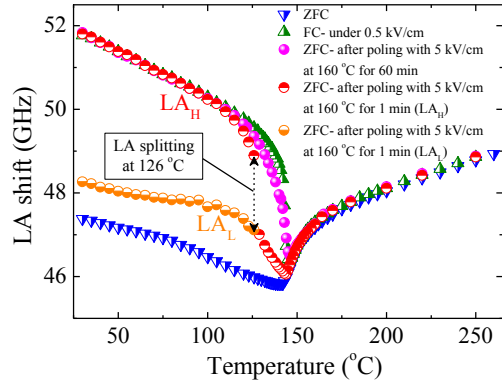


Fig. 3. Temperature dependences of LA shift after poling at 160 °C.

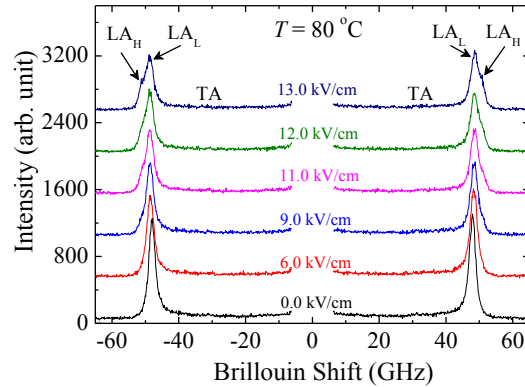


Fig. 4. Electric field dependences of Brillouin scattering spectra at 80 °C.

were studied under zero and externally applied *dc* electric field. In Fig. 2, a remarkable thermal hysteresis was observed in the longitudinal acoustic (LA) shift between ZFH and zero field cooling (ZFC), reflecting the relaxor nature of SBN40. The effect of the electric field along the [001] direction was clearly observed. On field heating (FH) under 3.0 kV/cm (Fig. 2), the alignment of nanodomains at 50 °C and a complete switching of nanodomains to the macrodomain state at 149 °C were observed. At 50 °C the alignment of nanodomains was incomplete due to the formation of cluster glass state [6] induced by random bond interaction between PNRs. The formation of the cluster glass state was confirmed by observing the memory effect after aging in the ferroelectric phase. On field cooling (FC) under 3 kV/cm, a marked increase of LA shift and decrease of thermal hysteresis were observed below T_C . The poling effect of high electric field on static PNRs in the paraelectric phase was investigated. After applying 5 kV/cm electric field for 60 min at 160 °C (*i.e.* below the intermediate temperature, $T^* = 185$ °C), the LA shift during ZFC is comparable to that under FC with 0.5 kV/cm (Fig. 3). Poling under such a high field for 60 min is sufficient to align all static PNRs along the field direction. Therefore, the LA shift becomes similar to that under FC. By decreasing the poling time to 1 min, some of the PNRs switch back, and therefore a splitting of the LA mode was observed below 126 °C. The high-frequency LA mode (LA_H) corresponds to macrodomains induced by the electric field, while the low-frequency LA mode (LA_L) corresponds to nanodomains induced by random fields. Below T_C , upon application of the electric field at constant temperature (Fig. 4), a coexisting state of nano- and macrodomains was also observed at about 9.0 kV/cm. This mixed state persists up to 13 kV/cm due to incomplete switching of the nanodomains into the macro- or single domain state.

References

- [1] R. Blinc, *Advanced Ferroelectricity*, International series of monographs on Physics, Oxford University Press, Vol. 151, 2011.
- [2] A. Glass, *Appl. Phys. Lett.* **13** (1968) 147.
- [3] W. Kleemann, J. Dec, V. V. Shvartsman, Z. Kutnjak, and Th. Braun, *Phys. Rev. Lett.* **97** (2006) 065702.
- [4] K. Suzuki, K. Matsumoto, J. Dec, T. Lukasiewicz, W. Kleemann, and S. Kojima, *Phys. Rev. B* **90** (2014) 064110.
- [5] M. Aftabuzzaman and S. Kojima, *Jpn. J. Appl. Phys.* **55** (2016) 10TC01.
- [6] W. Kleemann, J. Dec, and S. Miga, *Phase Transitions* **88** (2015) 234.

New model of structures and dynamics in perovskite oxide relaxor ferroelectrics

Hiroyuki Takenaka^{1,2}, Ilya Grinberg^{1,3}, Shi Liu^{1,2}, and Andrew M. Rappe¹

¹Department of Chemistry, University of Pennsylvania, Philadelphia PA, 19104

²Geophysical Laboratory, Carnegie Institution of Washington, Washington D.C.,

³Department of Chemistry, Bar-Ilan University, Ramat Gan, Israel

Relaxor ferroelectrics were first discovered in the 1950s and have been a focus of intense research due to their intriguing properties [1]. The model of polar nanoregion (PNR) inside a non-polar matrix has been widely accepted to explain the diffuse phase transitions. Several experimental techniques have been used to prove the PNR model for over the past decades. The numerous X-ray and neutron scattering studies demonstrated that the butterfly shape of the diffuse scattering (DS) was the signature of PNRs. The recent DS experimental studies [2,3], however, raise the subject of revision of the PNR model. In addition, the PNR model has not been useful to define the intermediate phase transition temperature, T^* , to unravel the high piezoelectric performance, and to search for new relaxors. To establish a better model of relaxors is of importance not only to elucidate the origin of the properties but also to provide predictive guidance to synthesize new relaxor materials.

We have used molecular dynamics (MD) simulations for $72 \times 72 \times 72$ (1,866,240 atoms) supercells of $\text{PbMg}_{1/3}\text{Nb}_{2/3}\text{O}_3\text{-PbTiO}_3$ (PMN-PT) to obtain high-resolution DS patterns. We find that our computational DS have good agreements with the experimentally observed DS butterfly and rod shapes around the (100) and (110) Bragg spots [4]. The good agreements indicate that analysis of our MD trajectories may shed light on the unclear features in relaxors.

Inspection of the time-averaged angle correlations for local Pb-O_{12} dipoles reveals the butterfly shape is a signature of 60° multi-domains with their small domain size of 2-10 nm. Below T_b and down to T^* , a weak distance dependence and weak DS intensity emerge. We find on set of formation of domains which dynamically evolve domain size, their positions, and orientations of dipoles with no non-polar matrix. At 400K, below T^* , local dipoles start forming multi-domains with stronger correlations for distances less than 6nm and the domains give rise to stronger DS intensity. From T^* to T_f , the domain size essentially doesn't change. The main changes the correlations inside the multi-domains and reduction of rotation dynamics of domain polarization. Below T_f , the local dipole rotation dynamics are extremely slow and the DS intensity is plateau. It should be noted that our results show no evidence of non-polar matrix below T_b and growth of PNRs below T^* in contrast to the PNR model.

To understand no growth of multi-domain size, we examine autocorrelation function of rotations of local Pb-O_{12} dipoles for sub-group perovskites in PMN-PT. The autocorrelation function only in Mg-rich perovskites still exhibits paraelectric-like rapid rotations down to T_f , while Ti-rich provskites show ferroelectric-like behavior starts below T_b . The local dipoles in the Mg-rich cells decouple with those in their neighbor cells. Thus, the Mg-rich cells act as domain wall sites and this gives rise to formation of the multi-domains. The high density of domain walls give rise to the high piezoelectric performance.

To provide a conceptual picture of the changes in the relaxor through the phase transitions, we have already proposed the analogy found in dielectric response between relaxors and water [5]. We examine the studies of structures and dynamics in water in the literatures in order to more quantitatively show similarities between relaxors and water. The local order parameters for Pb-displacements in PMN-PT are analogous to those for ^1H

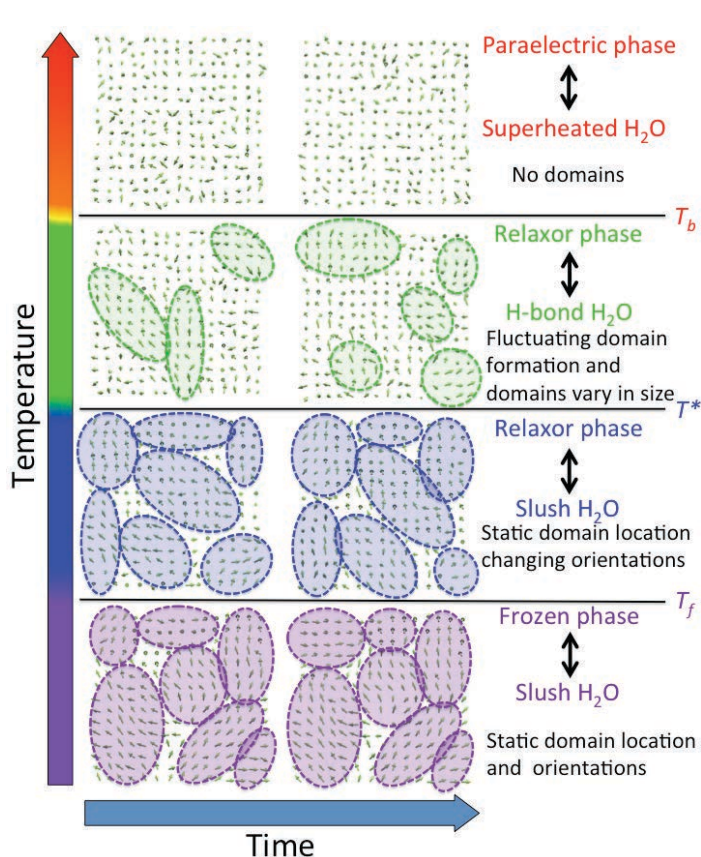


Figure 1: Illustration of our model in PMN-PT using snapshots of MD trajectories.

References:

- 1) A. Bokov and Z.-G. Ye, *J. Mater. Sci.* **41**, 31 (2006).
- 2) A. Bosak, D. Chernyshov, S. Vakhrushev, and M. Krisch, *Acta Cryst.* **A68**, 117 (2012).
- 3) R.G. Burkovsky *et al.*, *Phys. Rev. Lett.* **109**, 097603 (2012).
- 4) M. Matsuura, *et al.*, *Phys. Rev. B* **74**, 144107 (2006).
- 5) H. Takenaka, I. Grinberg, and A. M. Rappe, *Phys. Rev. Lett.* **110**, 147602 (2013).
- 6) M. M. Hoffmann and M. S. Conradi, *J. Am. Chem. Soc.* **119**, 3811-3817 (1997).
- 7) C. Zhang and G. Galli. "Dipolar correlations in liquid water." *J. Chem. Phys.* **141**, 084504 (2014)
- 8) E. Guardia, I. Skarmoutsos and M. Masia, "Hydrogen Bonding and Related Properties in Liquid Water: A Car! Parrinello Molecular Dynamics Simulation Study", *J. Phys. Chem. B* **119**, 8926! 8938 (2015).
- 9) A. K. Soper, "The radial distribution functions of water and ice from 220 to 673 K and at pressures up to 400 MPa", *Chem. Phys.* **258**, 121-137 (2000)
- 10) C. Huang *et al.*, "Wide-angle X-ray diffraction and molecular dynamics study of medium-range order in ambient and hot water", *Phys. Chem. Chem. Phys.* **13**, 19997–20007 (2011).
- 11) P. Kumar, S. V. Buldyrev and H. E. Stanley, "A tetrahedral entropy for water", *Proc. Nat. Acad. Sci.* **106**, 22130–22134 (2009).

chemical shift in water [6]. [7-10] For H₂O and PMN-PT the evolution of the local structure on cooling can be explained by increase of order inside the fixed region boundaries. PMN-PT and H₂O contain several types of local sites that exhibit different structural and dynamic characteristics and different dynamic response properties[8,11]. Thus, we show the picture of our model for the phase transitions in PMN-PT in Figure 1.

In conclusion, we show new model of the phase transitions in PMN-PT with similarity to water. Our results indicate that relaxors have low local domain walls energy due to the decoupling of the local dipole dynamics.

Acknowledgement: This work was supported by the ONR under grant ONR grant: N00014-12-1-1033. The computational support was provided by a Challenge Grant from the HPCMO of the U.S. Department of Defense.

Single Crystal Diffuse Scattering from Ferroelectric $\text{PbZr}_{0.54}\text{Ti}_{0.46}\text{O}_3$

Matthew Krogstad^{1,2}, Peter Gehring³, Jacob Ruff⁴, Feng Ye⁵, Stephan Rosenkranz², Raymond Osborn², Omar Chmaissem^{1,2}, Zuo-Guang Ye⁶, and Daniel Phelan²

¹Department of Physics, Northern Illinois University, DeKalb, IL

²Materials Science Division, Argonne National Laboratory, Argonne, IL

³NIST Center for Neutron Research, Nat'l Inst. of Standards and Technology, Gaithersburg, MD

⁴Cornell High Energy Synchrotron Source, Cornell University, Ithaca, NY

⁵Spallation Neutron Source, Oak Ridge National Laboratory, Oak Ridge, TN

⁶Department of Chemistry and 4D LABS, Simon Fraser University, Burnaby, BC, Canada

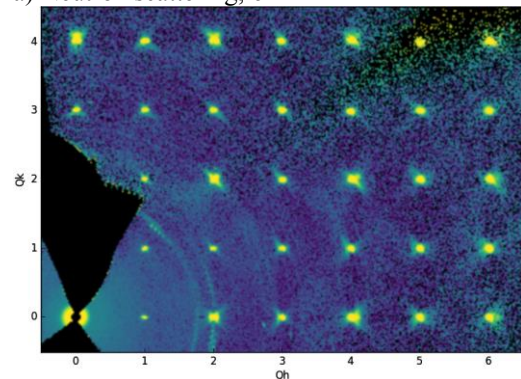
Alloying the ferroelectric PbTiO_3 with the anti-ferroelectric PbZrO_3 produces $\text{PbZr}_{1-x}\text{Ti}_x\text{O}_3$ (PZT), a system featuring a morphotropic phase boundary (MPB) around $x=0.48$. Near this phase boundary, the piezoelectric properties of the system are greatly enhanced, producing some of the more strongly piezoelectric materials currently known. It is thought that this behavior may be related to short-range order phenomena arising from competition between the differing long-range orders of the parent systems. To investigate possible short-range ordering, diffuse scattering measurements were performed on a single crystal of $\text{PbZr}_{0.54}\text{Ti}_{0.46}\text{O}_3$, producing large volumes of reciprocal space intensities from both neutron and x-ray diffraction. Our experiments evidence significant short-range correlations that provide an interesting contrast to related relaxor and ferroelectric systems.

A single crystal of PZT was studied at the ORNL Spallation Neutron Source using CORELLI, an instrument designed to measure elastic diffuse scattering while filtering out inelastic contributions. A small piece of this crystal was taken and etched with HCl to remove any possible surface defects; high energy x-ray diffuse scattering measurements were then performed on this piece at the Cornell High Energy Synchrotron Source (CHESS) using continuous rotation with a fast area detector operating in shutterless mode.

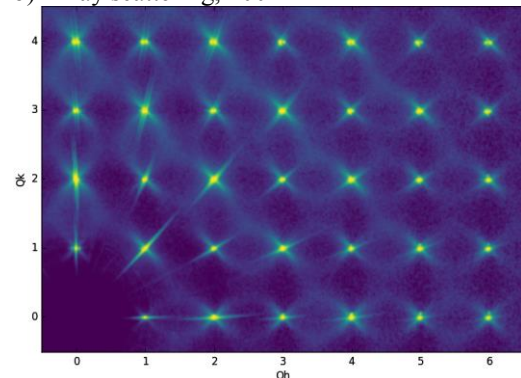
In both studies, butterfly-shaped diffuse scattering commonly associated with polar nanoregions in relaxors was observed, as shown in Figure 1. The intensities of these butterflies are concentrated closer to the Brillouin zone centers than are those of the canonical relaxor $\text{PbMg}_{1/3}\text{Nb}_{2/3}\text{O}_3$; the shapes are more similar to compositions of PMN- x PT in the MPB. When measured with neutrons, these butterflies possess an inter-zone modulation whereby the symmetry alternates between high- q and low- q intensities from zone-to-zone. Sharp R-

Figure 1: Diffuse scattering from PZT in the HK0 plane.

a) Neutron scattering, 6K



b) X-ray scattering, 100K



point superlattice peaks resulting from octahedral rotations and some very broad diffuse scattering between Bragg peaks were also observed. The temperature dependence of these features was investigated, providing a connection between the various types of short-range order and the ferroelectric phase transition in PZT.

The x-ray diffuse scattering from PZT differs from the neutron diffuse scattering in several key respects, and the contrast between the two sheds light on the origin of these features. The butterfly scattering seen as asymmetric in neutron scattering is more symmetric when observed with x-rays. This demonstrates that oxygen atoms play a significant role in determining the local structure. Additionally, the broad scattering between peaks, more easily visualized in $l=n/2$ planes (where n is odd) as shown in Fig. 2, is much more clearly observed with x-rays, with a clear parity structure throughout reciprocal space – the hollow octahedra centered on \mathbf{X} points have a checkerboard pattern of low and high intensity. This scattering, while mostly lacking in temperature dependence, can only arise from local lead displacements which are sensitive to the local environment of surrounding B-site cations. This may be indicative of random electric fields, which could disrupt the well-ordered states of the parent compounds in such a way as to produce the extreme properties seen in this solid solution.

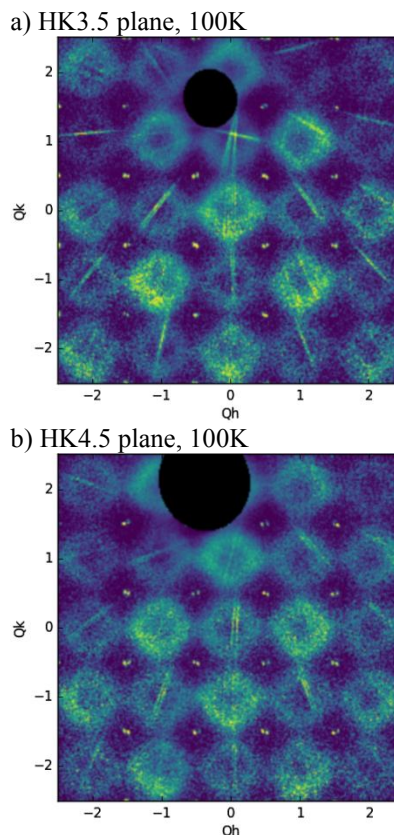
Acknowledgments:

Work at the Materials Science Division at Argonne National Laboratory (M.K.,S.R.,R.O.,D.P.) was supported by the US Department of Energy, Office of Science, Materials Sciences and Engineering Division. Part of the research conducted at ORNL's Spallation Neutron Source was sponsored by the Scientific User Facilities Division, Office of Basic Energy Sciences, US Department of Energy.

krogstad@anl.gov

Argonne National Laboratory
9700 Cass Ave.
Building 223
Argonne, IL 60439

Figure 2: X-ray diffuse scattering indicating size effects between Pb atoms and B site cations



Super-lattice point linking diffuse scattering network and its dynamical mechanism in lead-free NBT-xBT single crystals

Abstract

Neutron and x-ray scattering techniques were used to study $(\text{Na}_{1/2}\text{Bi}_{1/2})\text{TiO}_3$ -xat% BaTiO_3 (NBT-xBT) single crystals near the morphotropic phase boundary (MPB), as a function of both composition and temperature, and including both structural and dynamical aspects. The results revealed a close static and dynamic relationship between M-type and R-type tilts of oxygen octahedra. Furthermore, an unusual band of intensity in the phonon spectra appeared at the MPB, which may play an important role in electromechanical energy transduction in this material. These findings constructed the missing part between the microstructure and the macroscopic functional properties of NBT-xBT.

Atomistic Modelling of Ageing in Ferroelectrics

Jacob B. J. Chapman^{1,2}, R. E. Cohen^{1,3,4}, Anna V. Kimmel^{1,2} & Dorothy M. Duffy¹

`jacob.chapman.13@ucl.ac.uk`

1. Department of Physics and Astronomy, University College London, Gower Street, London, WC1E 6BT, UK

2. Materials Division, National Physical Laboratory, Hampton Road, Teddington, TW11 0LW, UK

3. Geophysical Laboratory, Carnegie Institution of Washington, Washington, DC 20015, USA

4. LMU Munich, Germany

Modern technologies utilising ferroelectric components dominate commercial markets being used from mobile phones, diesel engine drive injectors and sonar to print heads and non-volatile memory [1,2]. The macroscopic mechanical and electronic response of these components to different strength driving fields are known to be affected by structural defects, including vacancies, impurities and grain boundaries [3]. Two of the most widely used perovskite ferroelectrics are $\text{PbZr}_{1-x}\text{Ti}_x\text{O}_3$ (PZT) and $(1-x)\text{Pb}(\text{Mg}_{1/3}\text{Nb}_{2/3})\text{O}_3$ - $x\text{PbTiO}_3$ (PMNPT), which have excellent operating performances and physical properties that can be widely calibrated using aliovalent dopants to produce shifted/pinched P-E loops, increased phase transition temperatures and improved quality factors [4]. However, when large strains are required from these materials for actuators and aerospace electronics, the operating fields approach switching conditions whereby the ferroelectric ages, and reversible domain switching becomes unrecoverable - changing the desired properties of the ferroelectric [1,5].

Ageing is defined as the change in a material's properties over time. It causes severe issues with the operational lifetime of ferroelectric devices, and yet the microscopic mechanisms responsible for aging are still under debate. According to Carl and Härdtl, ageing models can be classified as being a volume, domain or grain boundary effect [6]. In this work, we use large scale classical molecular dynamics with the core-shell model forcefields of Gindele *et al* [7] and Sepliarsky *et al* [8] to model ageing in bulk lead based perovskite composites from dopant-vacancy associates. We show all features of ageing can be reproduced from the 'volume' effects of the associates alone.

Strong evidence from electron paramagnetic spin resonance (ESR) and density functional theory (DFT) calculations have shown dopants such as iron and copper in PZT substitute the B-cations as acceptors, which bind to oxygen vacancies to form thermodynamically stable defect complexes [9,10]. Ren argued that during aging, vacancies diffuse to neighbour sites such that the dipole-moment between the vacancy and acceptor aligns with the domain, which lowers the energy state of the associate [5,11]. To investigate this assumption, we model acceptor-vacancy associates in aged and un-aged conditions. For aged simulated samples, we co-align all defect dipoles and apply a perpendicular driving field returning a double hysteresis response in the P-E loop (Figure 1a, black-diamond). The observation of a double hysteresis is in excellent agreement with experimental studies of aged ferroelectrics [2,5]. We show how, for large enough defect concentrations, at low drive fields the internal bias from the defect complexes re-orientate the polar axis along the ageing axis. Only for moderate fields does the field coerce reorientation parallel to the driving field. This switching from an a-domain to c-

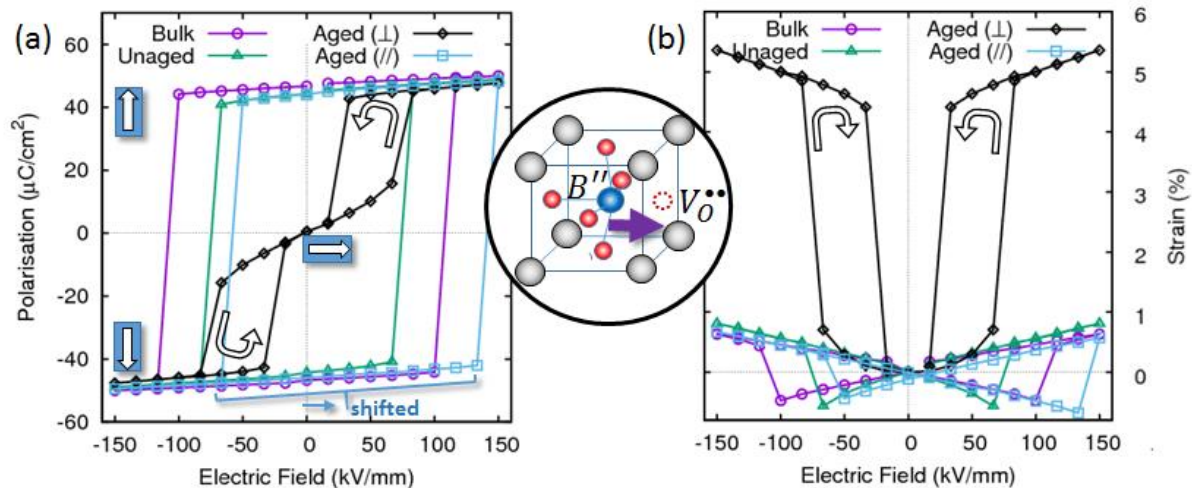


Figure 1. Modelling ageing in Pb-based perovskite ferroelectrics. Hysteresis of (a) polarisation and (b) strain, for defect free bulk (purple-circle), un-aged (green-triangle), ageing perpendicular to applied field (black-diamond) and ageing parallel to driving field (blue-square). Simulations of samples that have been un-aged recover the square P-E hysteresis of the bulk. Aging parallel shifts the P-E hysteresis and breaks the symmetry of the S-E loop. Aging perpendicular pinches the P-E loop, creating a full double hysteresis for large enough defect concentrations, accompanied by a giant recoverable, non-linear strain hysteresis.

domain is associated with a giant recoverable non-linear hysteresis in the strain-electric field curve exceeding 4% (Figure 1b, black-diamond). Again, these calculations are in excellent agreement with the strain-field hysteresis of aged BaTiO₃ [5].

In our ideal un-aged calculations, we set the defect dipoles to be randomly orientated biased such that we have an equal numbers of dipoles aligned with each possible orientation. Under these conditions the square loop of the hard ferroelectric is recovered (Figure 1a, bulk: purple-circle, unaged: green-triangle). Further, we show how aging parallel to the drive field shifts the square hysteresis (Figure 1a, blue-square). In this instance, the internal bias from the associates breaks the degeneracy between the positive and negative poled orientations. We conclude that our model utilising the defect dipoles due to dopant-vacancy associates, reproduces both the double hysteresis, pinching and shifted P-E loops observed in experimental studies and provides fundamental insight into the ageing process at the atomic scale.

- [1] Y. A. Genenko, J. Glaum, M. J. Hoffmann & K. Albe, *Materials Science and Engineering B* **192**, 52 (2015)
- [2] J. Glaum, Y. A. Genenko, H. Kungl, L. A. Schmitt & T. Granzow, *J. Appl. Phys.* **112**, 034103 (2012)
- [3] T. Rojac, S. Drnovsek, A. Bencan, B. Malic & D. Damjanovic, *Phys. Rev. B* **93**, 014102 (2016)
- [4] N. Luo, S. Zhang, Q. Li, Q. Yan, Y. Zhang, T. Ansell, J. Luo, T. R. Shroud, *J. Mater. Chem. C* **4**, 4568 (2016)
- [5] X. Ren, *Nature Mater.* **3**, 91 (2004)
- [6] K. Carl & K.Härdtl, *Ferroelectrics* **17**, 473 (1978)
- [7] O. Gindele, A. Kimmel, M. G. Cain & D. Duffy, *J. Phys. Chem. C* **119**, 17784 (2015)
- [8] M. Sepiarsky, A. Asthagiri, S. R. Phillpot, M. G. Stachiotti & R. L. Migoni, *Current Opinion in Solid State and Materials Science* **9**, 107 (2005)
- [9] P. Erhart, P. Träskelin & K. Albe, *Phys. Rev. B* **76**, 174116 (2007)
- [10] R. A. Eichel et al, *Phys. Rev. Lett.* **100**, 095504 (2008)
- [11] A. V. Kimmel, P. M. Weaver, M. G. Cain & P. V. Sushko, *Phys. Rev. Lett.* **109**, 117601 (2012)

Affiliations 1 & 2 are supported by the EPSRC (EP/G036675/1) via the Centre for Doctoral Training in Molecular Modelling and Materials Science at University College London and the National Measurement Office of the UK Department of Business Innovation and Skills. REC is supported by the ERC Advanced Grant ToMCA_T and by the US ONR.